NEW REACTION PATHS FOR ADVANCED SiAlON/TiN COMPOSITES

BY

PAULINE CALLOCH

A thesis

submitted to Victoria University of Wellington

in fulfilment of the requirements for the degree of

Doctor of Philosophy

in Chemistry

Victoria University of Wellington

2015

Abstract

This thesis demonstrates how selected ceramic additives, including titanium nitride (TiN), impact upon the "chemistry ↔ microstructure ↔ properties" relationship as it applies to composites in the generic Sialon-TiN composite field. Examination and optimisation of this feedback loop enables control of industrially important thermal, electrical and engineering properties of β-Sialon based ceramics.

The effects of a range of additives on the nitridation and sintering of β-Sialon composite bodies have been studied and the chemical and mechanical properties of the sintered bodies have been measured. The additives can be divided in three groups: nitridation additives which improve the yield and the rate of the reaction; sintering aids; and additives that improve resistance to thermal shock. A suite of additives consisting of a mixture of calcium aluminate cement, yttrium aluminium garnet and boron nitride was found to deliver an optimum set of mechanical properties with a fracture toughness achieved of over 4 $MPa.m^{-1/2}$.

This thesis also reports a new reaction path for the formation of a β-Sialon/TiN composite by the reaction bonding of aluminium powder coated with nanosized titania. In this novel technique, the aluminium reacts under an inert atmosphere with titania to form alumina and a Ti_xAl_y intermediate which is then nitrided to form aluminium nitride and titanium nitride. The addition of a suitable silicon phase enables the formation of a β-Sialon phase under nitrogen at high temperature. The TiN was added in the range 1 to 10 wt% (0.6 to 6 vol%).

The effects of milling time on the aluminium powder particle size distribution and reactivity have been studied, with a minimum of two days milling time required to modify the particle shape and reduce melting coagulation during firing. Firing parameters have been optimised, using XRD and MAS-NMR to monitor the samples' composition and SEM to observe their microstructure. The reduction of titania by aluminium was completed at 900 ºC for 4 hours in an argon atmosphere and the nitridation of the titanium aluminide at 1400 ºC for 3 hours in a nitrogen flow. The nitridation and sintering of the β-Sialon/TiN composite were both performed in nitrogen at 1400 ºC and 1600 ºC, respectively. A low level of addition of TiN

(1 wt%) has shifted the composition toward the AlN corner of the Sialon behaviour diagram, forming α-Sialon and AlN polytypes. Other levels of addition in the studied range formed a dense β-Sialon/TiN composite. The TiN inclusions are found at the grain boundaries but are of insufficient volume fraction to form a continuous network in the Sialon matrix.

Mechanical and electrical properties of the newly fabricated β-Sialon/TiN composites have been measured. These properties were generally improved by the highest levels of TiN addition: Young's modulus (up to 210 GPa), hardness (up to 17.7 GPa), fracture toughness (up to 3.3 $MPa.m^{-1/2}$) and compressive strength (up to 188 MPa). However the presence of TiN had no impact on the resistance to thermal shock and electrical conductivity of the β−Sialon.

Finally, the oxidation process for β-Sialon/TiN composites has been observed by a combination of XRD, SEM and Ion Beam Analysis techniques. The results show early enrichment of yttrium and titanium in the first 0.1 µm of the samples' surface; replacement of nitrogen by oxygen to form crystalline phases on the surface and in the glassy phase up to 1.5 µm deep; and, major crystalline and chemical changes in an outer layer of about 100 µm thickness at 1200 ºC. The partial depletion of SiO species from the external sample surface during sintering firing leaves this surface zone more vulnerable to oxidation than the protected body of the ceramic. The oxidation of TiN forms a TiO_2 skin which acts as a protection from further oxidation.

The outcome of this research is a novel reaction path to fabricate new advanced Sialon composites and an improved understanding of the effect of a broad range of additives on the nitridation and sintering behaviour of β-Sialon and β-Sialon/TiN composites.

Publications

One refereed publication from this thesis has been published to date:

- Calloch P., White V., Ryan M., Brown I.W.M. and MacKenzie K.J.D. *Additives to Promote the Nitridation and Sintering of a Sialon Composite*, J Aust Ceram Soc, 2011, **47**[2], pp.74-81.

Presentations

Presentations on the work included in this thesis have been given by the author at four international and national conferences:

- PAC RIM 9, 10-14 July 2011, Cairns (Australia), *Thermal Shock Resistance in Sialon Ceramic Composites*.
- International Symposium on Nitrides (ISNT) 2012, 3-6 June 2012, Saint-Malo (France), *Reaction of a SiAlON-TiN body fabricated from a novel Ti_xAl_y intermediate*.
- AMN-6, 11-15 February 2013, Auckland (New Zealand), *Reaction of a SiAlON-TiN body fabricated from a novel Ti_xAl_y intermediate*.
- New Zealand Conference of Chemical and Materials Engineering (NZCCME) 2013, 25-26 November 2013, Auckland (New Zealand), *Reaction of a SiAlON-TiN body fabricated from a novel Ti_xAl_y intermediate*.

Acknowledgements

First and foremost I would like to thank my supervisor, Ian Brown for giving me the opportunity to study in New Zealand, for his amazing support in the last four years, and for helping me to feel at home at the other side of the world. Thanks also to my co-supervisor Ken MacKenzie for his advice and support.

I would like to express my exceptional gratitude to Martin Ryan for his time, expertise and advice. Thanks in general to Industrial Research Limited/Callaghan Innovation, but especially to Vaughan White, Eugene Stytsenko, Alison Speakman, Sarah Spencer, Ruth Knibbe, Tim Kemmitt, Bill Owers, Conrad Lendrum, Ann Manning, Diego Del Puerto, Neville Baxter, Robert Holt and Neil Milestone for their invaluable technical help, discussions and suggestions.

Thank you to the MacDiarmid Institute for providing financial support, and especially Sarah Dadley and Emily Sullivan.

At GNS Science Gracefield, John Kennedy, Peter Murmu, Jerôme Leveneur and particularly Bill Trompetter have assisted me greatly on part of this project.

Thank you to John Hanna and Gregory Rees from the Solid State NMR Group at the University of Warwick (England) and Aamir Mukhtar at TiDA (Tauranga) for their technical help.

Special thanks to my friends Ina Reichenberger, Katrina Teu, Carole Brown, David Grant-Taylor, Rachael Linklater, Geoff Smith, Matt Sharp, Dave Clarke, Jeremy Wu, Mathias Pommier, Camille Chaumontet, Lise Hégron for their friendship throughout, and especially Anne-Hélène Puichaud who helped me on the proof-reading.

And last but not least, I could not have done this without the unconditional support of my parents Armel and Laurence, my brothers and sister, my grand-mothers and whānau.

Table of Contents

List of Figures

List of Tables

List of Equations

Glossary

CIP Cold isostatic press

CMC Ceramic matrix composite

CVD Chemical vapour deposition

DTA Differential thermal analysis

EDM Electrical discharge machining

EDS Energy dispersive (x-ray) spectroscopy

EFI Extended focal imaging

FAST Field assisted sintering technique

FEG Field emission gun

GPS Gas pressure sintering

HDPE High density polyethylene

HP Hot pressing

HIP Hot isostatic pressing

IBA Ion beam analysis

ICDD The International Centre for Diffraction Data

IPA Isopropyl alcohol

MAS-NMR Magic angle spinning nuclear magnetic resonance

NRA Nuclear reaction analysis

PECS Pulsed electric current sintering

PIGE Particle-induced gamma emission

PIXE Particle-induced X-ray emission

RBS Rutherford backscattering

SEM Scanning electron microscopy/microscope

SPS Spark plasma sintering

SSB Silicon surface barrier

TGA Thermogravimetric analysis

WURST-QCPMG Wideband uniform rate and smooth truncation - Quadrupolar Carr-Purcell-Meiboom-Gill

XRD X-ray diffraction

YAG Yttrium aluminium garnet

Chapter One: Introduction to Sialon Ceramics

In an early definition only clay based materials hardened by heating were considered as ceramics. They were first used in a cultural or religious way, for example as iconic statues, then in domestic applications from about 25,000 BC. Although they were not initially classified as ceramics, glass, cements and refractories have been invented and used for many centuries. Since the 1970s', the term "Ceramics" has been broadened to include virtually every covalent non-metallic inorganic material. This definition includes very different materials and gives ceramics a wide range of properties and possibilities of use.

Nitrogen based ceramics have been developed[1] in the last decades to take advantage of their remarkable thermo-mechanical properties. Silicon nitride (Si_3N_4) is known for its high strength, high decomposition temperature, excellent thermal shock and wear-resistance, low coefficient of friction and resistance to corrosive environments. Most of these very desirable properties come from the covalent-bonded structure of silicon nitride. This characteristic gives a very low diffusivity to this material and so it cannot be fully densified by classic sintering. Reaction-bonding, hot-pressing, hot isostatic pressing and gas-pressure sintering processes densify silicon nitride but they require more expensive processing and do not allow fabrication of complex shapes.

Sialon (Si-Al-O-N) is a class of nitrogen ceramics used as refractories in the molten metal industry as well as for a large range of engineering applications such as cutting tools, spray nozzles or ballistic ceramic armour. Sialon is formed from silicon, aluminium, oxygen and nitrogen but can be considered to be a solid solution of silicon nitride, aluminium nitride (AlN), silica (SiO_2) and alumina (Al_2O_3). The behaviour diagram constructed by Ekström et al.[2] in Figure 1.1 shows the Sialon phases which are of most interest. Each phase presents different strengths and weaknesses that will be detailed later in Chapter 2.

This work develops a new Sialon ceramic fabrication process that addresses the "chemistry ↔ microstructure ↔ properties" relationship. Essentially this is a feedback loop where the effect of changing the ceramic chemistry modifies the ceramic microstructure, which in turn results in a particular suite of properties (physical, chemical, electrical, etc.). The overall goal of this thesis is to examine how selected ceramic additives, including titanium nitride (TiN), impact upon this feedback loop and enable control of industrially important thermal, electrical and engineering properties of β-Sialon based ceramics.

In recent years, composite Sialon bodies with the high thermal and electrical conductivity additive TiN have been developed (See Section 2.3). Some other titanium compounds, such

as TiC, TiCN and TiB_2 or some oxide ceramic additives may also be suitable and compatible and enhance thermal and electrical conductivity. Although there is some previous work on such materials, it is restricted to direct blending of pure phase materials and fails to exploit or address the opportunities for extensive variation of the base Sialon composition and the efficient formation of new composites by smart reaction path design, including *in situ* fabrication of the high conductivity phase.

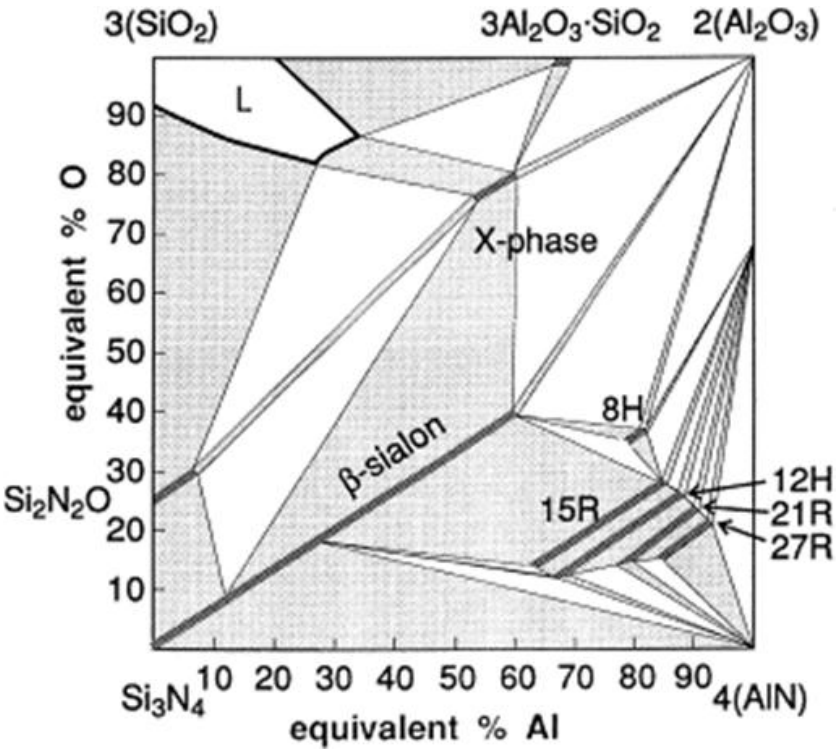

Figure 1.1: The Si–Al–O–N behaviour diagram at temperatures of 1700–1730 ºC from Ekström et al[2].

This project adopts a staged approach with an initial focus on (1) developing process chemistry routes to synthesise new powder composite phases; (2) forming densified bodies from these powders; (3) examination of the microstructure of densified materials, including optimising the variables that control densification and sintering; and (4) the measurement of selected relevant properties (thermal parameters, electrical conductivity, oxidation resistance and physical properties such as strength, hardness and toughness).

1.1 Reaction Paths

A new reaction path has been designed to fabricate Sialon composites using key techniques of thermal analysis (monitoring mass and thermal changes). Parallel experiments in controlled atmosphere tube furnaces have enabled study of the high temperature reactions of

materials for phase analysis by X-Ray Diffraction (XRD). Conventional Sialon ceramic chemistry uses combinations of pure phase materials to generate a Sialon of a specific composition:

e.g. $\frac{(6-z)}{3}Si_3N_4 + \frac{z}{3}Al_2O_3 + \frac{z}{3}AlN \rightarrow Si_{6-z}Al_zO_zN_{8-z}\ (0 \leq z \leq 4.2)\quad (\beta - \text{Sialon})$ (Eq 1.1)

or $\frac{(2-x)}{4}Si_3N_4 + \frac{(2-x)}{4}SiO_2 + \frac{x}{2}Al_2O_3 \rightarrow Si_{2-x}Al_xO_{1+x}N_{2-x}\ (0 \leq x \leq 0.4)\quad (O - \text{Sialon})$

(Eq 1.2)

The approach was developed to use different existing reaction routes to Sialon formation, based on the knowledge of processes such as carbothermal reduction[3], silicothermal reduction[4] and aluminothermal reduction[5] , in which carbon, silicon metal and aluminium metals are used to reduce the oxygen content of source materials such as silica, alumina and pure clay mineral phases (e.g. $Al_2O_3.2SiO_2.2H_2O$). A new approach presented in this research initiates the Sialon formation reaction by coating powder particles (aluminium, silicon or silicon nitride) with a sol-gel derived titanium compound. In this method, the Sialon body and the titanium phase form in two reactions to create a uniformly dispersed ceramic/titanium phase composite.

The reactions are undertaken under nitrogen or argon conditions, as suits the particular chemistry being sought. Magic Angle Spinning Nuclear Magnetic Resonance (MAS-NMR) analysis of ^{27}Al, ^{29}Si, ^{11}B and, $^{47,49}Ti$ enable detailed examination of the changing role of key species as the reaction chemistry proceeds. In some cases, a thermodynamic assessment of the reactants, using a commercial software[6], gives guidance as to the likely reaction products and their respective thermal stability regimes.

It is known that high energy milling accelerates phase chemistry and early microstructure development in reactive powder raw materials and this approach is one of the considered reaction options. It facilitates a nanomaterials approach to Sialon precursor powder formation, but this benefit is usually short lived as the highly reactive, high surface area powders lead to rapid grain growth at elevated temperature for no clear advantage.

1.2 Densification

Powder bodies are fabricated into test specimens (discs, bars, etc) using uniaxial and isostatic pressing, then fired in controlled atmosphere furnaces to achieve densification. The introduction of sintering aids is critical to assure adequate densification. The selection of

sintering aids depends on the specific composite under consideration, but includes Y_2O_3, CaO, MgO and other materials. The role of the sintering aids is to provide liquid phase assistance to the densification process. The success of sintering is determined by measurements of density, apparent porosity and shrinkage. The nature of the phases formed is determined by XRD. The results of the densification study feeds back to chemical modifications in step 1 (developing process chemistry routes). Instability of the surface layers of the densified Sialon ceramics may dictate that some specimens are sintered using a protective powder bed, to minimise silicon loss via high temperature SiO evaporation from the specimen surface.

1.3 Microstructure

Characterisation of the microstructure of sintered Sialon composites is critical to the optimisation process, since the microstructure controls the physical properties. Most particularly, the nature of some intergranular phases controls specific properties (e.g. oxidation resistance) and these measurements are key to observing, characterising and analysing such phases. Methodologies for microstructure examination and assessment are described in Section 3.9.

1.4 Measurement of Chemical and Physical Properties

Physical and chemical property measurements are undertaken using specifically shaped specimens (discs, bars) according to the test procedure required. Polished surfaces (3 microns surface finish) are required for indentation hardness and fracture toughness measurements. Bars are required for 3 or 4 point modulus of rupture measurement although edge compression testing on discs (the 'Brazil' test, See Section 3.11) gives a good indication of comparative strength. Ideally, a test facility using the Flash Laser method would enable the measurement of the thermal conductivity at high temperature (up to 1500 ºC). As a short term proxy, the effect of thermal quenching of specimens using the change in their measured strength is used as a guide. Oxidation behaviour of the materials is assessed following heat treatment in air of polished specimens. The effects can be observed and quantified using a range of Ion Beam Analysis (IBA) facilities, detailed in Section 3.8. A combination of Particle-Induced Gamma Emission (PIGE), Nuclear Reaction Analysis (NRA) and Rutherford Backscattering (RBS) techniques enables tracking of the surface diffusion behaviour of all key Sialon atomic species (Si, Al, O, N, Ti and Y). The combination of

thermal and IBA experiments give detailed information regarding the diffusion and oxidation rate kinetics.

Overall, a feedback loop via steps (1)-(4) (refer page 3) enables examination of the "chemistry ↔ microstructure ↔ properties" relationship as it applies to composites in the generic Sialon-TiN composite field. The outcome is a novel reaction path to fabricate new advanced Sialon composites and an improved understanding of the effect of a broad range of additives on the nitridation and sintering behaviour of β-Sialon and β-Sialon/TiN composites. In this context, the analysis of phase composition and microstructure is complemented by measurement of specific physical, chemical and materials properties, including thermal shock resistance, hardness, fracture toughness, compressive strength, Young's modulus and oxidation resistance.

1.5 Chapter One Bibliography

1. Jack, K.H., *Sialons and related nitrogen ceramics*. J Mater Sci, 1976, **11**[6], pp. 1135-58.
2. Ekström, T. and Nygren, M., *SiAlON Ceramics*. J Am Ceram Soc, 1992, **75**[2], pp. 259-76.
3. Lee, J.G., Casarini, R., and Cutler, I.B., *Sialon derived from clay to provide an economical refractory material*. Ind Heat, 1976, **43**[4], pp. 50-53.
4. White, G.V., *New synthesis routes for sialon and sialon ceramics*. Key Eng Mat, 2001, **206-213**, pp. 51-54.
5. Mazzoni, A.D. and Aglietti, E.F., *Aluminothermic reduction and nitriding of high silica materials (diatomite and bentonite) minerals*. Appl Clay Sci, 2000, **17**, pp. 127-40.
6. Software *HSC Chemistry 7.1*, Outotec. Finland.

Chapter Two: Literature Review

The literature review is divided in seven distinct sections. The first presents Sialon ceramics and introduces their main chemical and physical properties. The second introduces the reaction paths and densification methods used in research and industry. The third section discusses the reinforcing of silicon nitride ceramics (silicon nitride, silicon oxynitride and Sialon) with particles, whiskers or fibres. The fourth section describes the development of thermal and electrical conductivity research in silicon nitride ceramics. The fifth section reports the different techniques used in the measurement of oxidation resistance of silicon nitride ceramics. The sixth section gives an overview of the current knowledge on aluminium/titanium alloys, their formation, densification and properties. The final section focuses on the different parameters having an effect on the Sialon reaction rate or yield, on the densification of the Sialon body and its microstructure or on its mechanical properties.

2.1 Sialon Ceramics

The solid solubility of Al_2O_3 in Si_3N_4 was first reported by Oyama et al.[1] in 1971 and Jack and Wilson in 1972[2]. Sialon phases are divided in five classes: α-Sialon, β-Sialon, O-Sialon, X-Phase and AlN polytypes. Each phase is described by a composition range over which its structure is stable.

Sialon ceramics are used as refractories in the molten metal industry and for a large range of engineering applications such as cutting tools and spray nozzles due to their superior mechanical properties such as high strength, high decomposition temperature, excellent thermal shock and wear-resistance, low coefficient of friction and resistance to corrosive environments. These mechanical and chemical performances are closely related to the microstructures, chemical composition and fabrication process. Overall, α-Sialon contains a metal cation in addition to the four Sialon elements and is known for high hardness; β-Sialon is widely regarded as having high fracture toughness; O-Sialon is easily manufactured relative to silicon nitride and is resistant to oxidation; X-Phase is regarded as having inferior mechanical properties.

2.1.1 α-Sialon

The α-Sialon structure is based on that of α-Si_3N_4. Its unit-cell contains four silicon nitride units and can be described by the formula $Re_{m/p}Si_{12-m-n}Al_{m+n}O_nN_{16-n}$ where Re^{p+} represents a stabilising cation (commonly a rare earth), m and n are the numbers of Si-N bonds substituted by the Al-N and Al-O bonds respectively. The α-Sialon phase is stabilised by a metal cation

such as Y, Li, Na, Mg, Ca or by a rare earth ion such as Nd, Sm, Gd, Dy, Er, Yb, Lu which maintains the electron balance. Figure 2.1 shows the α-Sialon plane in the Re-Si-Al-O-N phase diagram or Janecke prism[3] and the limited area of stability of the single phase in the plane $Si_3N_4 \cdot 4/3(AlN \cdot Al_2O_3)$-Re·3AlN. The size of this area of stability is influenced by the nature of the stabilising cation and the temperature: it is smaller for larger rare-earth cations and at lower temperature[4].

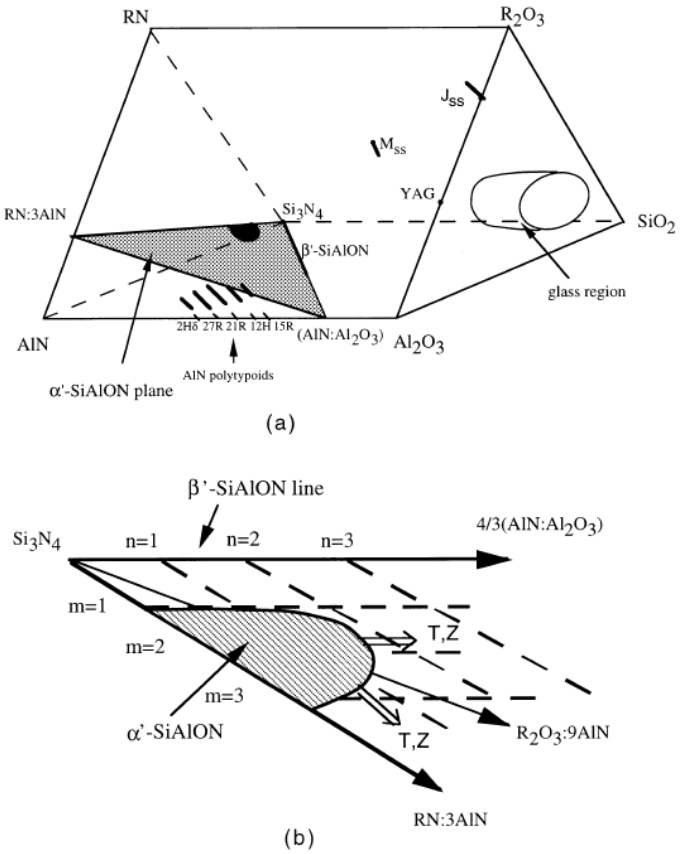

Figure 2.1: (a) Janecke prism showing the α-Sialon plane ; (b) α-Sialon plane with α-Sialon single phase stability region from Rosenflanz et al.[3].

The nature of the cation also influences the yield and rate of precipitation of the α-Sialon phase as well as the amount of intermediate phase. The smaller the cation the higher the α-Sialon precipitation yield[3]. This observation is not due to changes in liquid viscosity because for alumino-silicates containing rare-earth cations the viscosity increases with decreasing ionic size[3, 5]. The lighter the cation the more intermediate phases are formed[6-8]. The volume of these phases is reduced as the temperature is decreased for every cation. However, the rate of this decrease is faster with heavier cations.

The lattice parameters of α-Sialons are strongly dependent on m but only slightly on n. This is due to the significant difference between the bond lengths of Si-N (1.75 Å) and Al-N (1.87 Å) whereas the Si-N bond length is comparable to that of Al-O (approximately 1.75 Å)[4].

α-Sialons slowly grow in equiaxial grains which confer high hardness (typically 19-20 GPa) but poor fracture toughness (typically 2-4 $MPa.m^{1/2}$). The latter has been shown to be improved by developing elongated grains[9] to increase the crack path length and reduce the impact of the weaker intergranular amorphous phase. Different techniques have been investigated for α-Sialon grain elongation by controlling their nucleation and growth. Two stage processes can achieve the elongation as nuclei are formed at low temperature and grain growth occurs at higher temperature [10, 11] as well as through the addition of seed crystals to provide growth from nuclei in a one-step process[12].

In principle it is possible to form an α-Sialon body without any boundary glass phase due to the ability of this material to integrate the additives into the crystal structure; in practice, it is very difficult to prepare a single phase α-Sialon without a residual glassy phase. The mechanical properties of the α-Sialon sharply deteriorate after 900-1100 ºC which is the normal glass transition temperature range of the residual Re-Si-Al-O-N glassy phase. Otherwise, α-Sialons have a low thermal expansion[13] and a high thermal conductivity[14] which give them good thermal shock resistance.

2.1.2 β-Sialon

β-Sialons are formed by equivalent substitution of Al-O for Si-N bonds and present an hexagonal structure based on the β-Si_3N_4 structure of MX_4 tetrahedra (M = Si, Al ; X = O, N) in which each metal atom is coordinated to four X atoms and each X atom to three metal atoms. They can be described by the formula $Si_{6-z}Al_zO_zN_{8-z}$ where z can vary from 0 to 4.2[15].

The microstructure of the β-Sialons consists of elongated hexagonal grains with a typical ratio in the range 4 to 10. This shape is believed to be due to the anisotropic growth of grains because of the difference between the chemical potential between the facets[16]. A study has shown that the grain size increases with the z-value and that the XRD peaks are shifted to lower diffraction angles as the z-value increases due to expanded lattice parameters when more aluminium and oxygen are substituted in the silicon nitride[17]. The crystal structure of

β-Sialon is represented in Figure 2.2 and shows the three dimensional covalent framework that leads to enhanced engineering properties.

Unlike silicon nitride, β-Sialons can be fully densified by conventional ceramic techniques such as pressing or extrusion followed by sintering in a nitrogen atmosphere. An amorphous phase is created at the grain boundaries and the mechanical properties of the material are greatly dependant on the properties of this phase. Their elongated grain shape gives β-Sialons a higher fracture toughness (typically 3-6 $MPa.m^{1/2}$) than silicon nitride and the highest fracture toughness of all the Sialon phases[18]. Its oxidation resistance is also better than that of silicon nitride because of the formation of a thin layer of mullite ($2SiO_2.3Al_2O_3$) on the exposed surface. Finally, it is compatible with molten metals such as steel, iron and most especially aluminium[19].

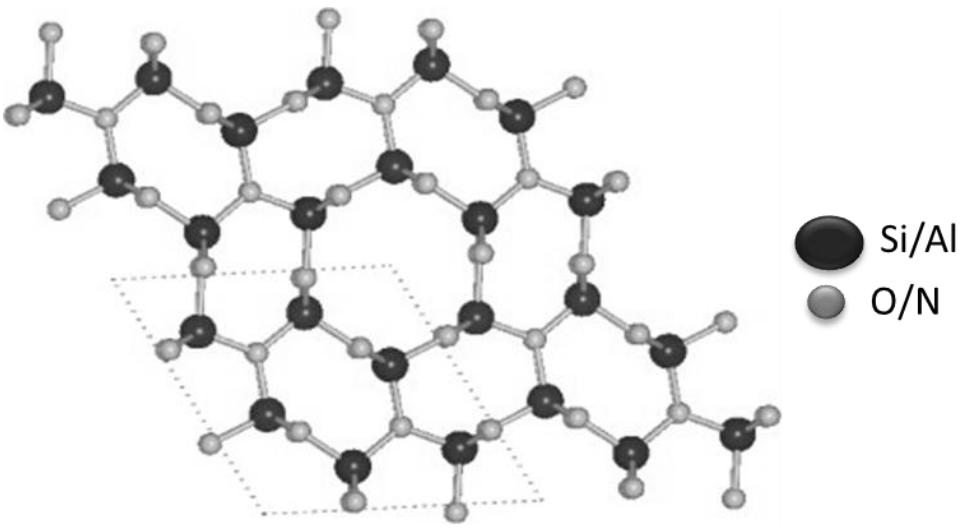

Figure 2.2: β-Sialon crystal structure[20].

Suzuki et al.[21] have shown that β-Sialons reach an optimum in their properties with a low z-value (around 0.5). Above z = 1, the mechanical properties decline, with a decrease in strength and toughness and an increase in the thermal expansion.

2.1.3 α/β-Sialon Composites

Making use of the α to β-Sialon transformation is a good way to change the microstructure and the phase content without the help of additives which may result in a weaker glassy phase. This reaction is a reconstructive transformation which needs a high energy to break the Si-N bonds. It happens when an α-Sialon formed at high temperature is held at a lower temperature. The reaction starts at 1400 ºC and completes in the presence of a necessary liquid phase[22] at about 1800 ºC.

The α-Sialons stabilised with light rare earths will transform more easily than the ones stabilised with heavier cations[3]. The α-Sialons situated in the middle of the α-Sialon region are also more stable than those near the border and especially near the β-Sialon field[4] (see Figure 2.1).

Controlling the α/β ratio in such composites allows the control of the material properties. For example a high content of α-Sialon increases the hardness, whereas the fracture toughness decreases[23]. The advantage of this transformation is that it allows the control of physical properties by a straight forward heat treatment.

2.1.4 O-Sialon

Compared with silicon nitride and the other Sialon phases, O-Sialon exhibits the best oxidation resistance because of its high oxygen content. It can be described by the general formula $Si_{2-x}Al_xO_{1+x}N_{2-x}$ where x ranges from 0 to 0.4[24]. O-Sialons have a similar but more expanded structure than silicon oxynitride (Si_2N_2O), an orthorhombic crystal structure consisting of SiN_3O tetrahedra linked together to form the 3D network[25].

The oxidation resistance of O-Sialon is remarkable with no oxidation detected before 1200 ºC and a nitrogen diffusion controlled oxidation process active between 1200 and 1450 ºC[26].

O-Sialon is not easy to form by reaction sintering as it starts to decompose at a temperature very close to its sintering temperature. However, the addition of sintering aids enables formation of a liquid phase which promotes the reaction at lower temperature. However, these additives considerably degrade the oxidation resistance of the O-Sialon[27, 28]. Yttrium oxide additives form refractory intergranular glass phases and are a suitable choice for improving physical properties, such as fracture toughness[29].

When the temperature increases, O-Sialon can be converted to β-Sialon with loss of silica by evaporation[30]. This reaction is completed between 1770 and 1820 ºC[31].

2.1.5 X-Phase

The X-Phase exists in a small region of the diagram between mullite and silicon nitride. It has a similar structure to mullite. Many formulae describing the X-Phase are reported in the literature from $SiAlO_2N$ to $Si_{16.9}Al_{22.7}O_{48.8}N_{11.6}$ but $Si_{12}Al_{18}O_{39}N_8$ seems commonly accepted[32]. As well as its position on the behaviour diagram, its unit cell is a matter of disagreement: Jack[19] reported it as monoclinic, Zangvil[33] and Thompson[34] as triclinic and Gugel[35] as orthorhombic.

A possible mechanism of formation of the X-Phase by hot pressing of Si_3N_4-Al_2O_3-SiO_2 powders mixtures has been reported by Zhou[32] in which the alumina and silica form a viscous oxynitride glass with the silica layer around the α-Si_3N_4 particles. At higher temperature, α-Si_3N_4 dissolves into the melt which will crystallise as X-Phase during cooling below 1650 ºC.

The X-phase is probably the least studied Sialon phase because it exhibits the poorest mechanical properties of all Sialon phases with a hardness of about 15 GPa, a fracture toughness of 1.2 MPa.m^{½} and a thermal expansion coefficient of $4x10^{-6}$ ºC^{-1} (data from Sheppard et al.[36]).

2.1.6 AlN Polytypes

The AlN polytypes are situated in the AlN corner of the Sialon phase diagram (See Figure 1.1). They are all based on the AlN wurtzite structure with either a hexagonal or rhombohedral unit-cell. Table 2.1 gives the metal M / non-metal X atomic ratio in the different AlN polytypes. The Ramsdell notation[37] used to name AlN polytypes is composed of a number and a letter that refers to the number of close-packed Al-N double layers in the unit cell and the crystal structure respectively. When 9/10 < M/X < 1, it is assumed that the extra non-metallic atoms are taken up in the 2H phase forming the $2H^{\delta}$ structure, which is essentially the 2H structure with an elongated c-parameter.

AlN polytypes	8H	15R	12H	21R	27R	$2H^{\delta}$	2H
M/X ratio	4/5	5/6	6/7	7/8	9/10	>9/10	1/1

Table 2.1: Atomic ratio in the different AlN polytypes[19]

These phases grow in fibrous elongated grains and therefore may potentially contribute to the reinforcement of composite Sialons.

2.1.7 Applications

The Sialon phases are used in the molten metal manufacturing industries, including foundries, as casting tubes or thermocouple protectors. They have been chosen for their high resistance to oxidation and compatibility with molten metals[18] like aluminium or steel. Moreover, Sialon ceramics present a lower thermal expansion coefficient than most ceramic materials such as $3.4x10^{-6}$ ºC^{-1} for β-Sialon z = 0.5[21], which give them a good thermal shock resistance.

These nitrogen ceramics are also used for their high hardness and fracture toughness in ballistic ceramic armour[38]. They are even more suitable for this application since their density is low, usually around 3 $g.cm^{-3}$, in comparison with steel or even alumina ceramics ($\rho \sim 4$ $g.cm^{-3}$) and can be made from low cost raw materials.

To a lesser extent, Sialon ceramics are also used for their wear resistance as milling media and as cutting tools (such as indexable inserts) for metals, where they complement carbide-based tools. Recently, Yamada et al.[39] exhibited the optical properties of a high purity α−Sialon phosphor. Combined with its mechanical and chemical properties this phosphor material is a candidate in applications such as medicine or communications.

2.2 Reaction Paths and Densification of Sialon Materials

2.2.1 Traditional Liquid Phase Sintering

The first process used to fabricate Sialon was the sintering of a silicon nitride powder with one or several pure phases from the phase diagram (Al_2O_3, AlN or SiO_2) and a rare earth in the α-Sialon case. This produces the purest and the densest Sialon body but it is also extremely energy and time consuming. Moreover, silicon nitride is an expensive raw material.

At a temperature between 1000 and 1400 ºC, an eutectic liquid phase forms from the reaction of the oxides Al_2O_3, SiO_2 (which can also come from the oxygen-rich layer always found at the Si_3N_4 surface) and Re_xO_y, if present. The presence of impurities and nitrogen will change this temperature[40] as well as the nature and concentration of the rare earth[41].

After the formation of the liquid phase, the silicon nitride starts to dissolve in it to form an oxynitride liquid phase at about 1380 ºC[42]. The precipitation of the Sialon phase occurs immediately after. The reaction continues until 1800 ºC when it nears completion.

The liquid phase formed during this reaction will stay at the grain boundaries in the final material. In the α-Sialon case, the cations residual in the intergranular liquid can be incorporated in the Sialon structure to create a pure phase.

The densification of the Sialon body occurs according to classical and well documented ceramic densification process knowledge[43] including the closing of pores and the growth and coalescence of the Sialon grains.

2.2.2 Carbothermal Reduction

The carbothermal reduction technique for Sialon synthesis was first described by Lee *et al.*[44] in 1976. It uses low cost raw materials such as clay and carbon black and produces carbon monoxide as a waste gas product.

The starting conditions used by Lee et al. led to the formation of a β-Sialon with a z-value of 3 (See Equation 2.1). But with the addition of silica, alumina, silicon or a rare earth oxide, every Sialon phase can be produced. Equation 2.2 gives the example of the β-Sialon of any z−value, which is of most interest in this study.

$$\frac{3}{2}[Al_2O_3 \cdot 2SiO_2] + \frac{15}{2}C + \frac{5}{2}N_2 \rightarrow Si_3Al_3O_3N_5 + \frac{15}{2}CO \qquad \text{(Eq 2.1)}$$

Metakaolin β-Sialon (z=3)

$$\frac{z}{2}[Al_2O_3 \cdot 2SiO_2 \cdot 2H_2O] + (6-2z)Si + \frac{5z}{2}C + \frac{8-z}{2}N_2 \rightarrow Si_{6-z}Al_zO_zN_{8-z} + \frac{5z}{2}CO + zH_2O$$

Kaolin Clay β-Sialon (generic) (Eq 2.2)

The carbothermal reduction reaction occurs in three steps. From 950 °C, the clay decomposes into mullite and silica[45] (Equation 2.3). Then silica is reduced by carbon to form silicon carbide (SiC) and carbon monoxide (CO) or carbon dioxide (CO_2). Equations 2.4 and 2.5 happen simultaneously. This silicon carbide phase has not always been detected and its presence seems to depend on the carbon content[46]. Finally, mullite, silicon carbide, carbon and, in the β-Sialon case, silicon react in a nitrogen atmosphere to form the Sialon and more carbon monoxide (Equation 2.6). These reactions occur before 1450 ºC[44].

$$\frac{z}{2}(Al_2O_3.2SiO_2.2H_2O) \rightarrow \frac{z}{6}Al_6Si_2O_{13} + \frac{2}{3}zSiO_2 + zH_2O_{(g)} \qquad \text{(Eq 2.3)}$$

$$\frac{2}{3}zSiO_2 + 2zC \rightarrow \frac{2}{3}zSiC + \frac{4}{3}zCO_{(g)} \qquad \text{(Eq 2.4)}$$

$$\frac{2}{3}zSiO_2 + \frac{4}{3}zC \rightarrow \frac{2}{3}zSiC + \frac{2}{3}zCO_{2(g)} \qquad \text{(Eq 2.5)}$$

$$\frac{z}{6}Al_6Si_2O_{13} + \frac{2}{3}zSiC + \frac{z}{2}C + (6-2z)Si \xrightarrow{N_2} Si_{6-z}Al_zO_zN_{8-z} + \frac{7}{6}zCO_{(g)} \qquad \text{(Eq 2.6)}$$

2.2.3 Silicothermal Reduction

The silicothermal reduction route allows the formation of all Sialon phases at lower temperatures than via liquid phase sintering. Similarly to carbothermal reduction, it uses low cost raw materials but does not produce any unwanted waste gases. The starting clay is responsible for the decrease of reaction temperature. It is a plastic material, which helps with

the material shaping before firing, effectively combining the benefits of traditional processing with advanced ceramic manufacture.

Sheppard et al.[47] described the mechanism of formation of the X-Phase by this method: starting materials are clay (halloysite or kaolin), silicon and aluminium hydroxide ($Al(OH)_3$) dehydroxylated to form alumina. Between 885 and 1000 ºC, the clay decomposes producing mullite and amorphous silica (as in Equation 2.3). The nitridation of silicon starts at 1100 ºC. Then the alumina and the silica react between 1250 and 1300 ºC as a second source of mullite. The latter reacts with silicon nitride to form the X-Phase. Some O-Sialon has been detected during the process and is thought to be an intermediate phase in the last reaction step.

These same authors suggested an alternative reaction mechanism[48]: from the same starting materials, the clay decomposes then the resulting silica reacts with silicon and the nitrogen atmosphere to form a silicon oxynitride which will later form the Sialon by reacting with alumina and mullite.

White[49] fabricated α and β-Sialons using aluminium nitride following Equations 2.7 and 2.8.

α-Sialon:

$$0.0064(Al_2O_3.2.4SiO_2.2.2H_2O) + 10.45Si + 1.37AlN + 7.06N_2 + LiF \rightarrow LiSi_{10.6}Al_{1.5}O_{0.5}N_{15.5} + 0.25SiF_{(g)} + 0.14H_2O_{(g)} \quad \text{(Eq 2.7)}$$

β-Sialon (z = 0.5) at 1350 ºC:

$$0.0064(Al_2O_3.2.4SiO_2.2.2H_2O) + 5.35Si + 0.37AlN + 2.57N_2 \rightarrow Si_{5.5}Al_{0.5}O_{0.5}N_{7.5} + 0.14H_2O_{(g)} \quad \text{(Eq 2.8)}$$

However, the porosity measured on samples fabricated with this method is very high (30−40 %). Moreover, during pressureless sintering, the nitridation of silicon requires a very long time to achieve completion.

2.2.4 Reaction Bonding

The Reaction Bonding technique uses the same raw materials as the traditional liquid phase sintering except that the expensive silicon nitride is replaced by the cheaper silicon metal. The first step of this method is to nitride the silicon in a nitrogen controlled atmosphere to form silicon nitride. The following steps depend on the other raw materials used.

Several reaction bonding methods have been reported. The excellent mechanical properties characteristic of the Sialon ceramics are not always achieved due to the presence of pores and residual silicon.

Peelamedu et al.[50] report a three stage process starting with silicon metal and aluminium nitride using a nitrogen and oxygen controlled atmosphere. First the silicon is nitrided to form silicon nitride. Then AlN is incorporated in the Si_3N_4 structure and finally the electronic imbalance created (tetravalent Si replaced by trivalent Al) attracts the oxygen from the atmosphere in the lattice. This study notes that with an AlN/Si ratio higher than 0.66, only β−Sialon is formed.

A mix of aluminium, silicon and alumina can also be used as a starting mixture[51]. The aluminium and silicon are nitrided at 900 ºC and 1050 ºC, respectively, and then react with the alumina to form a β-Sialon (z = 2). A β-Sialon with a z value of 1.0 has been detected as a reaction intermediate.

Sintering aids are usually added to the starting mixture, mainly to help with the nitridation of silicon and the densification by lowering the temperature of formation of a liquid phase and increasing its volume. Yttria is commonly used but Hyuga et al.[17] also fabricated a dense β−Sialon by pressureless reaction bonding with the help of the inexpensive ZrO_2 while Eser et al.[52] sintered a β-Sialon (z = 2) without pressure and using a low amount of yttria with high energy milled starting powders.

2.2.5 Gas Pressure Sintering

Gas Pressure Sintering (GPS) is a laboratory and industrial technique for the mass production of Sialon using nitrogen pressure during the synthesis and the sintering up to 20 MPa to force the gas reactant into the porous green sample while applying an isostatic mechanical pressure at the same time. The high consumption of nitrogen that this technique requires makes it expensive but the reactions can reach completion quickly which alters the cost benefit more favourably.

In a recent study, Rouquié[53] has shown that an overpressure of 0.7 MPa of nitrogen is sufficient to convert a minimum of 90 % of the silicon to silicon nitride after 1 hour at 1400 ºC.

2.2.6 Hot Pressing and Hot Isostatic Pressing

Hot Pressing (HP) and Hot Isostatic Pressing (HIP) as well as post-hot isostatic pressing are very effective processing techniques to densify powder compacts without or with only small amounts of sintering aids by applying a mechanical pressure to the sample during the synthesis and the sintering[54, 55]. Typically hot pressing is a uniaxial process carried out using a solid graphite die, whereas hot isostatic pressing uniformly delivers pressure all over the sample surface, most commonly via a hot gas medium compressing a metal clad ('canned') sample.

Santos et al.[56] sintered α-Sialon/SiC composites by uniaxial hot-pressing at 1750 ºC for 30 minutes under 20 MPa and obtained good mechanical properties such as fracture toughness of 5 $MPa.m^{1/2}$ and hardness of 21.5 GPa.

Applying pressure during the synthesis of an α-Sialon changes the grain shapes by making them more elongated[57] even though the same study also showed that pressure does not have any effect on the speed of formation of the grains.

2.2.7 Spark Plasma Sintering

Spark Plasma Sintering (SPS), also known as Field Assisted Sintering Technique (FAST) or Pulsed Electric Current Sintering (PECS) is a low temperature and very fast sintering technique in which the heating rate can reach up to 600 ºC/min. A SPS furnace applies pulsed direct current through the sample which creates a local spark discharge at the surface of the particles. This technique densifies the samples in a few minutes. By acting directly inside the sample, it avoids the problem of shell formation and reduces the weight loss by evaporation as it is a very fast process.

The sample material's electrical conductivity, the die wall thickness and the presence of graphite papers used to prevent direct contact between graphite parts and the specimen and used to guarantee electrical contacts between all parts are important parameters that have a great influence on the temperature distribution inside the sample[57, 58].

However, this technique is primarily a research tool as it sinters only small sized samples and is highly energy consuming.

2.3 Reinforced Silicon Nitride Ceramics

Silicon nitride ceramics are used for their high strength, hardness and thermal stability. The need for improvement of their fracture toughness and resistance to thermal shock has led to the development of reinforced silicon nitride ceramics by the introduction of whiskers, fibres or particles.

Sintering additives have been widely studied to minimise the weakening of the ceramic matrix by the introduction of an intermediate phase while improving the Sialon precipitation and its densification. The effects of a range of these additives is detailed in section 2.7.2.

The addition of silicon carbide particles in the silicon nitride ceramic matrix has been used as a reinforcing method for more than forty years[59]. However, the addition of silicon carbide as uniformly sized particles does not improve noticeably the properties of the matrix[60, 61].

Generally, nitride additives are more compatible with silicon nitride than carbides[62]. Recently, some studies have investigated the introduction of conducting titanium species such as TiN or TiCN into silicon nitride or sialon ceramics composites[63-65], improving not only the thermal and electrical conductivities[63, 66] but also the mechanical properties[67-69]. These titanium species can be produced in-situ[70, 71] or mixed with the Sialon powder before sintering[66, 72]. When produced in-situ, the titanium species are usually made from TiO_2 mechanically mixed with a reducing agent and Si_3N_4 or pre-made Sialon, or by directly coating the particles. The nitridation of TiO_2 starts at 1150 ºC and is complete by 1450 ºC[73]. There is a critical size (approximately one micron) for the TiO_2 under which the TiN formed is of a similar size to the starting submicron TiO_2 but over this critical size the TiN particles formed are smaller than the starting TiO_2 because of the stress induced by the volume change during the TiO_2 to TiN reaction[73]. Krnel et al[71] have observed the segregation of TiN particles in β-Sialon/TiN composites formed from TiO_2-coated Si_3N_4 and TiN-coated Si_3N_4.

2.4 Electrical and Thermal Conductivity in Nitrogen Ceramics

2.4.1 Electrical Discharge Machining (EDM)

Electrical Discharge Machining is an industrial shaping method for electrically conductive materials. The material to be shaped (workpiece) is placed in a dielectric bath such as distilled water, kerosene or other oil-based dielectric liquid. The other electrode, named the tool, can move along three dimensions. The tool is usually made of copper or graphite. Figure

2.3 shows a simplified EDM installation. An electrical potential with a very large voltage range (typically 5 to 200 V D.C.) is applied between the two electrodes. When the distance between the two electrodes is reduced, the intensity of the electric field between them becomes greater than the strength of the dielectric liquid which breaks down. The current then flows between the electrodes in sparks and material is removed from both electrodes. The tool can take different forms such as wires to allow almost any kind of shaping with a maximum precision of a few microns.

Some recent studies have demonstrated that EDM can also be applied to non-conductive materials. Ceramics being insulators with a typical resistivity above 10^5 Ω.m are not suitable for the traditional EDM technique as it requires two conductive electrodes. This problem has been addressed by several means. Firstly, an assisting electrode, which is a thin (1-2 mm) and flat piece made of a conducting material such as copper or nickel[74-76], can be used. Because this electrode is thin and placed closely to the workpiece, when the distance between the tool and the assisting electrode reaches the sparking distance, the energy and heat produced are also applied to the workpiece. Another method is to add a large amount of an electrically conductive phase to the ceramic matrix. For example, Wei[77] successfully shaped SiC ceramic matrix composites (CMC) with EDM by infiltrating silicon in the matrix and, Liu[78] optimised EDM parameters to fabricate micro gas turbine impellers from Si_3N_4-TiN composites with 30-40 vol% TiN.

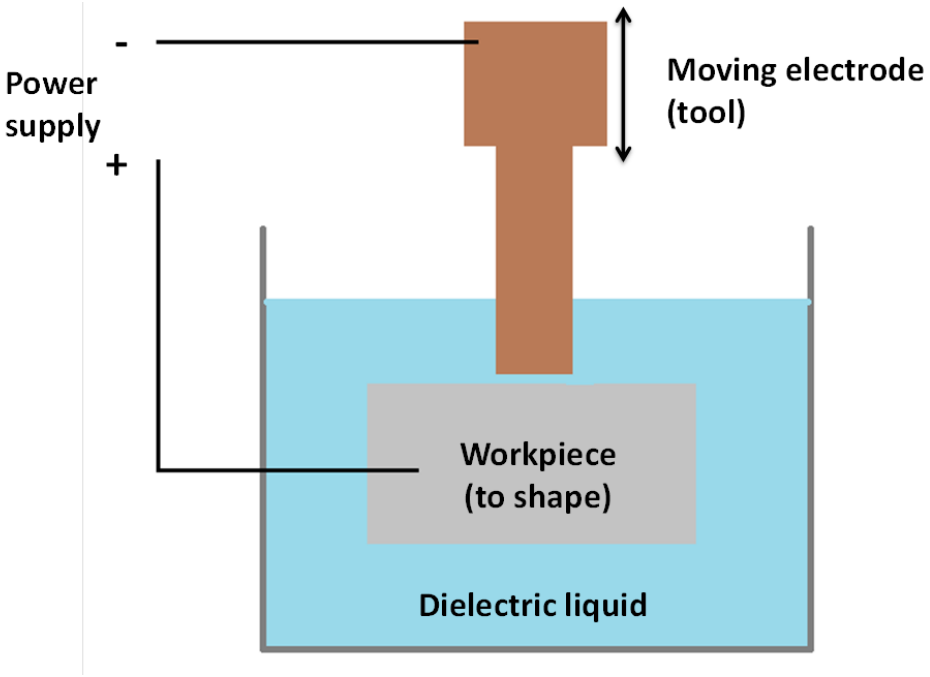

Figure 2.3: Electrical Discharge Machining equipment.

2.4.2 Electrical Conductivity

Sialon ceramics are extremely difficult to shape using conventional manufacturing techniques and are restricted to simple shapes such as tubes or rings. They are non-conducting materials with an electrical resistivity in the order of 10^{13} Ω.m (See Figure 2.4). If an electrically conductive phase can be introduced in the Sialon matrix, Electrical Discharge Machining (EDM) techniques could be used to shape Sialon to form more complex objects (see Section 2.4.1).

Sialon ceramics, like most ceramics, are insulators with an electrical conductivity in the order of 10^{-13} $S.m^{-1}$[79]. TiN is classified as a semi-conductor with an electrical conductivity in the order of 10^{-1} $S.m^{-1}$[79], almost metal-like. The electrical conductivity of Sialon ceramics is greatly improved by the presence of a continuous network of conductive titanium compounds[71] to a value which is always reported to be of the same magnitude, regardless of the nature of the titanium species or the fabrication process. The electrical conductivity of a material is traditionally determined by measuring the A.C. resistance of this material between two electrodes. For example, Ayas et al.[66] measured the electrical resistivity of an α−β−Sialon/TiCN composite by using the two probes method at room temperature with gold electrodes deposited on both sides of the samples. The electrical resistivity of this Sialon body ($1x10^{13}$ Ω.m) was reduced to $18x10^{-4}$ Ω.m with 5 vol% nanosized TiCN spray coated on the Sialon particles. The percolation threshold depends on the electrically conductive phase used and the way it is mixed into the ceramic matrix. Electrical conductivity has been achieved with a minimum of 20 vol% TiN chemically coated on the Si_3N_4 particles[70].

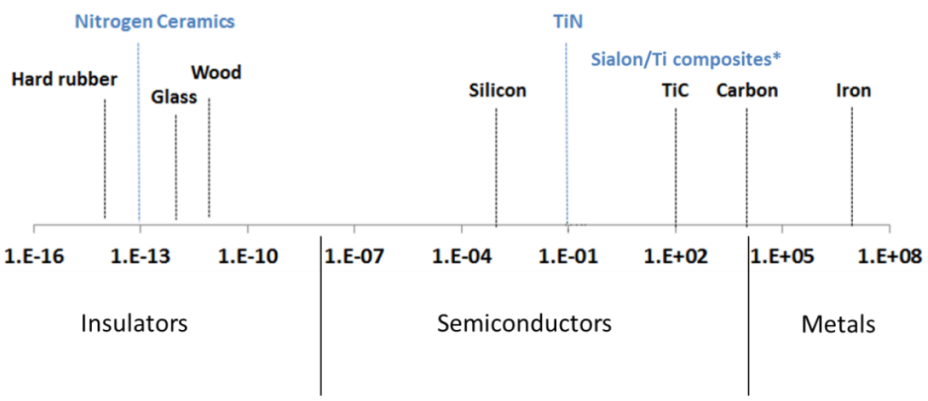

Figure 2.4: Electrical conductivity at room temperature ($S.m^{-1}$).

Data from Materials Science and Engineering Handbook[79].

** Data example from Ayas et al.[66]*

2.4.3 Thermal Conductivity and Thermal Shock Resistance

Sialon ceramics show a variety of improved properties compared to the silicon nitride on which they are based. However, the thermal shock properties of the Sialon ceramics do not achieve the performance of silicon nitride. Inomata[80] showed that the aluminium and oxygen incorporated in the Si_3N_4 matrix are responsible for the reduction of the thermal conductivity. Mitomo et al.[81] measured the thermal conductivity of an α-Sialon and found it to be between 1.7 and 2.1×10^{-2} $cal.cm^{-1}.s^{-1}.K^{-1}$ (7-8.8 $W.m^{-1}.K^{-1}$ with 1 cal = 4.184 J). The value for the β−Sialon can vary between 5.5[82]and 12.5[83] $W.m^{-1}.K^{-1}$. Liu et al.[84] demonstrated that the thermal conductivity of an α/β-Sialon composite followed the equation $k = 12.46 - 0.043f$ where f is the weight percentage of α-Sialon.

Good resistance to thermal shock can be achieved by reducing the thermal expansion coefficient or increasing the thermal conductivity but usually it is achieved by increasing the strength or toughness. For example, Pettersson et al.[85] improved the toughness and the thermal shock resistance of an α/β-Sialon composite by increasing the amount of β-Sialon and yttria. The first has a better fracture toughness than the α-Sialon and improves the overall fracture toughness of the composite while the latter improves the fracture toughness of the amorphous phase, usually by encouraging crystallisation of refractory phases such as yttrium aluminium garnet (YAG, $Y_3Al_5O_{12}$) from this phase.

2.5 Oxidation Resistance of Silicon Nitride Ceramics

Silicon nitride is protected from oxidation by the formation of a superficial layer of silica. It has a very slow rate of oxidation, even slower than other silicon compounds because of a sub-layer of silicon oxynitride (Si_2N_2O) between the silicon and the silica layer[86]. However, to assist the sintering of silicon nitride, oxides such as Y_2O_3 or Al_2O_3 are used, forming a glassy phase at the silicon nitride grain boundaries. In this glassy grain boundary phase, the transport of oxygen by diffusion is faster[87] and therefore the grain boundary phases are the weakest point of the material. However, Cubicciotti et al.[88] have shown that yttria partially protects silicon nitride from oxidation by forming a protective sub-layer to the oxidation layer composed of $Y_2Si_2O_7$ crystals.

Traditionally, the oxidation resistance of silicon nitride based ceramics is quantified by the measurement of the weight gain as a function of time and temperature[86, 89]. Changes in

microstructure are also followed by SEM[72] and the composition of crystalline phases assessed by XRD. MAS-NMR can also be used to follow the behaviour of the intergranular phases[90], particularly those phases in which ^{29}Si or ^{27}Al nuclei can be monitored.

Ion beam analysis (IBA), combined with XRD, is an uncommon technique used to follow the movement of atoms on the sample surface during the oxidation. Vickridge et al.[91] and Brown and al.[92] have studied the oxidation resistance of Sialon ceramics using different IBA techniques which detect the changes in concentration of the atoms in the Y-Si-Al-O-N system. Unlike the other techniques mentioned above, IBA techniques can detect the earliest stages of oxidation as these tools have a sensitivity of few ppm and can measure the thickness of the oxidation layer. IBA techniques are also fast and non-destructive.

Generally, like silicon nitride, the Sialon grains are unaffected or barely affected by oxidation because of their very low self-diffusivity. The diffusion of oxygen and replacement of nitrogen through the intergranular phase is the main oxidation mechanism and is accompanied of the formation of mullite and silica[86, 90-92], though the formation of crystalline silica is not always observed[90]. The presence of intermediate phases such as YAG leads to the formation of other intergranular phases such as yttrium silicates[91, 92].

2.6 Al/Ti Composites

Aluminium metal is not a common starting material in Sialon ceramic fabrication as the low melting temperature of this material risks early phase segregation during thermal processing. Aluminium is usually added as alumina, clay or aluminium nitride in the Sialon green mix. However at high temperature and under an inert atmosphere, aluminium metal reduces titania to form alumina and a titanium aluminide intermetallic phase but it cannot reduce it to pure titanium[93]. The final stoichiometry of the titanium aluminide depends on the initial Al/Ti ratio[94-96] and the possible phases are AlTi, Al_3Ti and $AlTi_3$. The reaction path shows that Al_3Ti is always formed between 500 and 650 ºC then transforms to another stoichiometry if the initial composition allows it[95]. Figure 2.5 shows the final composition of the alloy as a function of the initial Al:TiO_2 ratio.

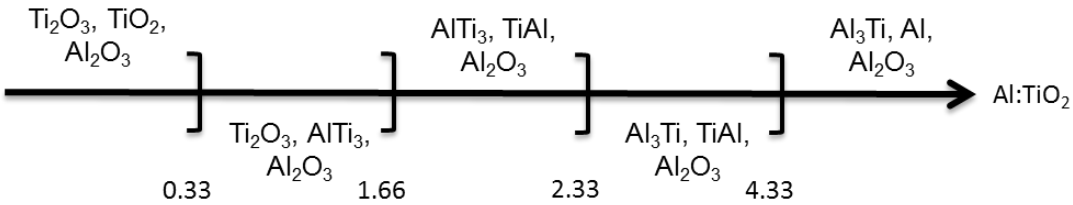

Figure 2.5: Composition of titanium aluminides after firing at 800 ºC in vacuum with changing initial Al:TiO_2 ratio from Gaus et al.[95].

The starting powder particle size and pre-firing treatment affect both the reaction temperature and the product microstructure. For example, Gaus et al.[95] and later Wang et al.[97] reported the formation of Al_3Ti in a needle shape after mechanical shaping of the aluminium particles which act as nuclei for growth of the needles.

This reaction can also be controlled by using a slow heating rate between 400 and 700 ºC because its enthalpy is low (ΔH = -478.2 kJ.mol^{-1}). Using small sized samples compacted at high pressure and increasing the heat removal by using a high thermal conductivity inert gas, such as helium, neon or argon, also improves control of the reaction between aluminium and titania.

The mechanisms of formation of the titanium aluminides Al_3Ti, AlTi and $AlTi_3$ have been described by Feng et al.[94] (Equation 2.9), Pan et al.[96] (Equation 2.10), and Gaus et al.[95] (Equation 2.11), respectively:

$$13Al + 3TiO_2 \rightarrow 3Al_3Ti + 2Al_2O_3 \quad \text{(Eq 2.9)}$$

$$7Al + 3TiO_2 \rightarrow 3TiAl + 2Al_2O_3 \quad \text{(Eq 2.10)}$$

$$5Al + 3TiO_2 \rightarrow AlTi_3 + 2Al_2O_3 \quad \text{(Eq 2.11)}$$

In a differential thermal analysis (DTA) curve obtained by heating an Al/TiO_2 powder in argon atmosphere, an endothermic peak appears at about 660 ºC due to the aluminium melting. Exothermic peaks observed between 500 and 1500 ºC correspond to the formation of the titanium aluminide and alumina following these equations for the Al_3Ti reaction path[94]:

$$2Al + 3TiO_2 \rightarrow 3TiO + \gamma - Al_2O_3 \quad \text{(Eq 2.12)}$$

$$2Al + 3TiO_2 \rightarrow 3TiO + \alpha - Al_2O_3 \quad \text{(Eq 2.13)}$$

$$11Al + 3TiO \rightarrow 3Al_3Ti + \alpha - Al_2O_3 \quad \text{(Eq 2.14)}$$

Al_3Ti melts at about 1220 ºC[98].

Once formed, these intermetallic phases can be nitrided to give aluminium nitride and titanium nitride. There is no evidence than the nitridation of the titanium aluminide following

the Equation 1.17 has been reported in the literature but it is strongly thermodynamically driven by a high enthalpy of reaction ΔH = -1121.54 kJ and a free energy of reaction ΔG = -485.77 kJ at 1400 ºC[99].

$$Al_3Ti + 2N_{2\,(g)} \rightarrow 3AlN + TiN \qquad \text{(Eq 2.15)}$$

2.7 Influence of Synthesis Parameters

2.7.1 Powder Bed

Powder beds are primarily used to reduce the weight loss through limiting evaporation of SiO during firing by creating an SiO-rich gas equilibrium in a close region around the sample. Barris et al.[100] found that a 1:1 ratio Si_3N_4:O-Sialon or 1:2 ratio BN:O-Sialon considerably reduces the thick and porous surface layer of β-Sialon formed on O-Sialon samples. However, the ideal powder bed composition depends on the nature of the Sialon formed and the composition of the sample.

Calis et al.[101] used powder beds to form a new kind of Sialon composite by encouraging the formation of a hard α-Sialon shell around a tough β-Sialon core in order to give to the composite the high mechanical properties of both phases.

2.7.2 Sintering Additives

Sintering aids are not necessary to form and densify Sialon bodies[102, 103] but when they are used the completion of reaction as well as the mechanical and chemical properties usually can reach higher levels. Rare earth oxides and metal oxides such as iron oxides (Fe_2O_3 and Fe_3O_4), alumina, zirconia or calcium hydroxide are the most common sintering aids[17, 50, 104]. They enhance the nitridation of silicon by reducing the reaction temperature and by reacting with the silica layer present at the surface of the silicon particles. They also improve the densification by melting to form the liquid phase necessary to assist this process.

Iron can be introduced as a metal[50] or an oxide[105]. Iron promotes the nitridation of silicon by removing the silicon oxide film present on the silicon grains to form $FeSi_2$ which is liquid at the reaction temperature. However, the migration of iron compounds introduces porosity which lowers the mechanical properties of the material[17].

Alumina is the most commonly used additive for the sintering of silicon nitride as it reduces the eutectic temperature by 200-300 ºC and enhances the formation of β-Si_3N_4 over α−Si_3N_4[106].

The addition of zirconia decreases the initial reaction temperature of the silicon nitridation[17] and increases the yield of reaction.

Below 1 wt% addition, calcium enhances the nitridation of silicon[107]. The combination of high temperature and calcium addition gives a high yield of conversion.

Yttria is widely used to enhance the silicon nitridation reaction and forms a liquid phase to assist the Sialon sintering[108].

Mandal et al.[104] lists the required characteristics of a good Sialon sintering aid: the eutectic temperature of the oxide containing liquid should be lower than the formation temperature of the Sialon but not too low in order to maintain good creep resistance; the intermediate phase produced should be formed at as low a temperature as possible and have good resistance to oxidation; finally, a high nitrogen solubility in this liquid phase is desirable as it can reduce the nitrogen diffusion through the sample and facilitate the nitridation reaction.

2.8 Critical Findings / Gaps in the Knowledge

2.8.1 State of knowledge

Nitrogen ceramics include a variety of materials with different properties such as high hardness and fracture toughness or resistance to oxidation and molten metals. Nitrogen ceramic composites or nitrogen ceramic matrix composites have been fabricated to combine the performance of each phase and to obtain materials with appropriate properties for various applications such as refractories for molten metal industries, cutting tools and wear resistant components.

Because the properties of a material depend mainly on its density and microstructure, processing methods, additives and firing conditions have been studied to achieve the desired properties. In the case of Sialons, yttrium aluminium garnet is recognised as a good sintering additive.

Sialon bodies can be fabricated by different methods that directly use the compounds present on the phase diagram corners or by forming them during processing (e.g. Si_3N_4 can be formed from Si in the first stage of the sialon nitridation). The method used depends on the quality to be achieved and the acceptable fabrication costs for the application.

In recent years, high performance composite Sialon bodies with the high electrical conductivity additive TiN have been developed. They make the use of new machining methods (e.g. EDM) possible and open new applications for Sialons, such as heaters,

conducting cutting tools or structural components. The TiN phase is usually mixed with pre-synthesised Sialon powder or formed *in-situ* in the Sialon or the silicon nitride raw material by nitridation of TiO_2.

The resistance to oxidising environment is a crucial property for a refractory material. The oxidation resistance of Sialon phases and its kinetics have been observed and calculated by different techniques from SEM observation to IBA techniques that consider the atomic movements at the surface.

Finally, Al metal is not a common raw material in the fabrication of Sialon bodies and examination of the metallurgical field of Al/Ti composites has shown that TiO_2 cannot be reduced to the metal by Al but together they form a family of alloys at the low temperature of 900 ºC. This prompts a solution to one of the key questions addressed in the next paragraph, namely the efficient formation of Sialon/TiN composite via a smart reaction path design.

2.8.2 Key research questions

Several unanswered questions are raised from the literature review presented in this chapter:

- In the objective of cost-effective fabrication of high performance Sialon bodies, the use of mixes of silicon and alumina with nitridation and sintering additives to form Sialon composites has not been systematically studied. It is proposed that the use of β−Sialon in Sialon composites instead of other Sialon phases will improve strength and fracture toughness, leading to improvement in thermal shock resistance.
- An efficient formation of Sialon/TiN composite via a smart reaction path design, including *in situ* fabrication of the high conductivity phase, which uses inexpensive raw materials and forms a homogenous mix could be developed. This new process would not be restricted to direct blending of pure phase materials and would address the opportunities for extensive variation of the base Sialon composition.
- There is no evidence than the nitridation of titanium aluminides has been reported in the literature. It is strongly thermodynamically driven but a study of the influence of kinetics on this conversion would add to the knowledge of the Al/Ti composites field.
- The oxidation resistance of Sialon/TiN composites is a poorly covered area of the studies on Sialon materials. Helped by the literature on oxidation of Sialon pure phases and a reference sample, the behaviour of newly formed Sialon/TiN composites in oxidising conditions could be studied by a combination of traditional techniques such as XRD and SEM observation, as well as the less commonly used IBA

techniques. The latter should bring new type of information to the oxidation resistance study because it allows the observation of very small atomic movements in crystalline and amorphous phases.

2.9 Objectives of this Research

The overall goal of this study is to improve understanding of the effects of additives on the synthesis, phase composition, microstructure and properties of β-Sialon and β-Sialon/TiN composite ceramics by:

- Observing the effect of a range of additives on the nitridation and sintering behaviour, and the chemical and mechanical properties of a β-Sialon composite. In this study yttrium aluminium garnet (YAG), is added as sintering aid; boron nitride (BN) is added to lower the elastic modulus; Fe_2O_3, TiO_2, ZrO_2, $Ca(OH)_2$, presynthesised β/O-Sialon, gibbsite ($Al(OH)_3$) and a refractory calcium aluminate cement are added to improve nitridation yield and rate.
- Developing a new fabrication method for β-Sialon/TiN composites using uncommon yet inexpensive raw materials based on aluminium reduction of titania, leading to the *in situ* fabrication of the electrically conductive TiN phase.
- Evaluating the effect of TiN addition on β-Sialon physical, chemical and materials properties, namely phase composition, microstructure, porosity, density, Young's modulus, hardness, fracture toughness, compressive strength, resistance to thermal shock and electrical conductivity.
- Measuring the oxidation resistance of β-Sialon/TiN composites using Ion Beam Analysis techniques supported by X-Ray Diffraction methods.

This study involves the development and application of multiple skills and tools across the field of ceramic materials science, underpinned by knowledge drawn from the core disciplines of chemistry, physics and metallurgy.

2.10 Chapter Two Bibliography

1. Oyama, Y. and Kamigaito, O., *Solid Solubility of Some Oxides in Si_3N_4*. Japan J. Appl. Phys., 1971, **10**, pp. 1637.
2. Jack, K.H. and Wilson, W.I., *Ceramics based on the Si-Al-O-N and Related Systems*. Nature Phys Sci, 1972, **238**, pp. 28-29.
3. Rosenflanz, A. and Chen, I.W., *Kinetics of Phase Transformations in SiAlON Ceramics: I. Effects of Cation Size, Composition and Temperature*. J Eur Ceram Soc, 1999, **19**, pp. 2325-35.
4. Rosenflanz, A. and Chen, I.W., *Phase relationships and stability of α'-SiAlON*. J Am Ceram Soc, 1999, **82**[4], pp. 1025-36.
5. Shelby, J.E. and Kohli, J.T., *Rare-earth aluminosilicate glasses*. J Am Ceram Soc, 1990, **73**[1], pp. 39-42.
6. Slasor, S. and Thompson, D.P., *Preparation and characterization of yttrium α'-SiAlONs.* In Non-oxide Technical and Engineering Ceramics 1986, ed. by S. Hampshire. Elsevier Applied Science Barking, UK, pp. 223-30.
7. Hampshire, S., O'Reilly, K.P.J., Leigh, M., and Redington, M., *Formation of α-SiAlONs with neodymium and samarium modifying cations.* In High-Tech Ceramics 1987, ed. by P. Vincenzini, Elsevier, Amsterdam, pp. 933-40.
8. O'Reilly, K.P.J., Redington, M., Hampshire, S., and Leigh, M., *Parameters affecting pressureless sintering of α-SiAlONs with lanthanide modifying cations*. Mater Res Soc Symp Proc 1992, **287**, pp. 393-98.
9. Liu, G., Chen, K., Zhou, H., Ning, X.G., Pereira, C., and Ferreira, J.M.F., *Fabrication of yttrium-stabilized α-SiAlON powders with rod-like crystals by combustion synthesis*. J Mater Sci, 2006, **41**[18], pp. 6062-68.
10. Kushan, S.R. and Mandal, H., *Effects of different Si_3N_4 starting powders and sintering conditions on the grain morphology and mechanical properties of α-SiAlON ceramics*. Key Eng Mat, 2001, **206-213**[I], pp. 417-20.
11. Shin, I.H. and Kim, D.J., *Growth of elongated grains in α-SiAlON ceramics*. Mater Lett, 2001, **47**, pp. 329-33.
12. Kim, J., Rosenflanz, A., and Chen, I.W., *Microstructure control of in-situ-toughened α-SiAlON ceramics*. J Am Ceram Soc, 2000, **83**[7], pp. 1819-21.
13. Okamoto, T. and Ukyo, Y., *Thermal expansion coefficient of Y-α'-sialon*. J Mater Sci, 1997, **32**[9], pp. 2473-77.
14. Mitomo, M., Hirosaki, N., and Mitsuhashi, T., *Thermal conductivity of α-sialon ceramics*. J Mater Sci Lett, 1984, **3**[10], pp. 915-16.
15. Ekström, T., Käll, P.O., Nygren, M., and Olsson, P.O., *Dense single-phase β-sialon ceramics by glass-encapsulated hot isostatic pressing*. J Mater Sci, 1989, **24**[5], pp. 1853-61.
16. Kitayama, M., Hirao, K., Toriyama, M., and Kanzaki, S., *Modeling and simulation of grain growth in Si_3N_4-I. Anisotropic Ostwald ripening*. Acta Mater, 1998, **46**[18], pp. 6541-50.
17. Hyuga, H., Yoshida, K., Kondo, N., Kita, H., Sugai, J., Okano, H., and Tsuchida, J., *Fabrication of presureless sintered dense β-SiAlON via a reaction-bonding route with ZrO_2 addition*. Ceram Int, 2009, **35**[5], pp. 1927-32.
18. White, G.V., Sheppard, C.M., Bowden, M., Ryan, M., Barris, G.C., Cooper, M., and Chen, C.Y., *Precision cast sialon-bonded silicon carbide for molten metal refractory applications*. Journal of the Australian Ceramic Society, 2007, **43**[1], pp. 24-31.

19. Jack, K.H., *Sialons and related nitrogen ceramics*. J Mater Sci, 1976, **11**[6], pp. 1135-58.
20. Xie, R.J. and Hirosaki, N., *Silicon-based oxynitride and nitride phosphors for white LEDs-A review*. Sci Technology Adv Mat, 2007, **8**[7-8], pp. 588-600.
21. Suzuki, S., Nasu, T., Hayama, S., and Ozawa, M., *Mechanical and Thermal Properties of β'-Sialon Prepared by a Slip Casting Method*. J Am Ceram Soc, 1996, **79**[6], pp. 1685.
22. Mandal, H. and Thompson, D.P., *Mechanism for Alpha to/from Beta Sialon Transformation*. Proc. Fourth ECerS, 1995, **2**[2], pp.2-6.
23. Jones, M.I., Hirao, K., Hyuga, H., Yamauchi, Y., and Kanzaki, S., *Wear properties of Y–α/β composite sialon ceramics*. J Eur Ceram Soc, 2003, **23**[10], pp. 1743-50.
24. Barris, G.C., Brown, I.W.M., Ekström, D.P., White, G.V., Cooper, M.T., and Hodren, G.M., *Reaction Bonded O'-Sialon and O'-Sialon-Silicon Carbide*. J Aust Ceram Soc, 1997, **33**[1-2], pp. 15-20.
25. Ekström, T. and Nygren, M., *SiAlON Ceramics*. J Am Ceram Soc, 1992, **75**[2], pp. 259-76.
26. Brown, I.W.M., *Advanced ceramic research at industrial research limited*. Adv Eng Mat, 2002, **4**[1-2], pp. 53-70.
27. Bergman, B. and Heping, H., *The influence of different oxides on the formation of Si_2N_2O from SiO_2 and Si_3N_4*. J Eur Ceram Soc, 1990, **6**[1], pp. 3-8.
28. Huang, Z.K., Greil, P., and Petzow, G., *Formation of Silicon Oxynitride from Si_3N_4 and SiO_2 in the Presence of Al_2O_3*. Ceram Int, 1984, **1**, pp. 14-17.
29. Ekstrom, T., *Sialon ceramics sintered with Yttria and rare earth oxides*. Proc. Materials Research Society Symposium Proceedings, 1993, **287**[pp.121-32.
30. Rouquié, Y. and Jones, M.I., *Formation and densification of SiAlON materials by reaction bonding and silicothermal reduction routes*. Proc. IOP Conference Series: Materials Science and Engineering, 2011, **18**.
31. Ma, B.Y., Yu, J.K., Liu, T., and Yan, Z.G., *Preparation of β-Sialon/ZrN bonded corundum composites from zircon by nitridation reaction sintering process*. J Cent South Univ Technol, 2009, **16**[5], pp. 725-29.
32. Zhou, Y., *Preparation and properties of X-Sialon*. J Mater Sci, 1995, **30**, pp. 4584-90.
33. Zangvil, A., *The structure of the X phase in the Si-Al-O-N alloys*. J Mater Sci, 1978, **13**[6], pp. 1370-74.
34. Thompson, D.P., In *Progress in Nitrogen Ceramics*. Ed. by F.L. Riley, Martinus Nijhoff, The Hague, Netherlands, 1983, pp. 375.
35. Gugel, E., Petzenhauser, I., and Fickel, A., *X-Ray Investigation of the System Si_3N_4-Al_2O_3 (On the Question of a 'Second' Phase in the System Al-Si-O-N)*. Powder Metall Int, 1975, **7**[2], pp. 66.
36. Sheppard, C.M., MacKenzie, K.J.D., and Ryan, M.J., *The Physical Properties of Sintered X-Phase Sialon Prepared by Silicothermal Reaction Bonding*. J Eur Ceram Soc, 1998, **18**, pp. 185-91.
37. Ramsdell, L.S., *Studies on Silicon Carbide*. Am Mineral, 1947, **32**, pp. 64-82.
38. Yeckley, R.L., *Alpha-Beta Sialon Ballistic Ceramic Armor*. Patent, 2008.
39. Yamada, T., Yamao, T., and Sakata, S., *Development of SiAlON -From Mechanical to Optical Applications-*. Key Eng Mat, 2007, **352**, pp. 173-78.
40. Hampshire, S. and Jack, K.H., In *Progress in Nitrogen Ceramics*. Ed. by F.L. Riley, Martinus Nijhoff, The Hague, Netherlands, 1983, pp. 225.
41. Sun, W.Y., Wu, F.Y., and Yan, D.S., *Studies of the formation of α' and α'-β' sialon*. Mater Lett, 1987, **6**[1-2], pp. 11-15.

42. Cao, G.Z., Metselaar, R., and Ziegler, G., *Formation and densification of α'-sialon ceramics*. Ceramics Today - Tomorrow's Ceramics. Proc.7th Int. Meeting on Modern Ceramics Technologies (7th CIMTEC - World Ceramics Congress). Part B Montecatini Terme, Materials Science Monographs, 66B (Elsevier Science Publishing Co.Inc.), 1990, pp. 1285-93.
43. Kingery, W.D., Bowen, H.K., and Uhlmann, D.R., In *Introduction to Ceramics - 10. Grain Growth, Sintering and Vitrification*. Ed. by Wiley-Interscience Publication, New York, 1976, pp. 448.
44. Lee, J.G., Casarini, R., and Cutler, I.B., *Sialon derived from clay to provide an economical refractory material*. Ind Heat, 1976, **43**[4], pp. 50-53.
45. MacKenzie, R.C., In *The differential thermal investigation of clays*. Ed. by Mineralogical Society (Clay minerals Group), London, 1957, pp. 98-139.
46. Xu, L.H., Lian, F., Zhang, H., Bi, Y.B., Cheng, K., and Qian, Y.B., *Optimal design and preparation of beta-SiAlON multiphase materials from natural clay*. Materials and Design, 2006, **27**[7], pp. 595-600.
47. Sheppard, C.M., MacKenzie, K.J.D., Barris, G.C., and Meinhold, R.H., *A New Silicothermal Route to the Formation of X-Phase Sialon: The Reaction Sequence in the Presence and Absence of Y_2O_3*. J Eur Ceram Soc, 1997, **17**, pp. 667-73.
48. Sheppard, C.M. and MacKenzie, K.J.D., *Silicothermal Synthesis and Densification of X-Sialon in the Presence of Metal Oxide Additives*. J Eur Ceram Soc, 1999, **19**, pp. 535-41.
49. White, G.V., *New synthesis routes for sialon and sialon ceramics*. Key Eng Mat, 2001, **206-213**, pp. 51-54.
50. Peelamedu, D.R. and Kalya, J.R., *Preparation and Characterization of Single-Phase B-SiAlON*. J Am Ceram Soc, 1995, **78**[2], pp. 395-400.
51. Chen, Q., Wu, J., He, X., and Cao, J., *Preparation of β-Sialon Powder at Low Temperature*. Key Eng Mat, 2005, **280-283**, pp. 1245-48.
52. Eser, O. and Kurama, S., *A comparison of sintering techniques using different particle sized β-SiAlON powders*. J Eur Ceram Soc, 2012, **32**, pp. 1343-47.
53. Rouquié, Y., Jones, M.I., Brown, I.W.M., and White, G.V., *Influence of nitrogen overpressure on the nitridation, densification and formation of β-SiAlONs produced by silicothermal reduction*. J Eur Ceram Soc, 2013, **33**[4], pp. 859-67.
54. Hunold, K., *Hot Isostatic Pressing of High Temperature Ceramics*. Ceram Int, 1985, **34**, pp. 38-43.
55. Jiang, D.L., She, J.H., Tan, S.H., and Greil, P., *Strenthening of silicon carbide ceramics by surface nitridation during hot isostatic pressing*. J Am Ceram Soc, 1992, **75**[9], pp. 2586-89.
56. Santos, C., Kelly, C.A., Ribeiro, S., Strecker, K., Souza, J.V.C., and Silva, O.M.M., *α-SiAlON-SiC composites obtained by gas-pressure sintering and hot pressing*. J Mater Process Tech, 2007, **189**, pp. 138-42.
57. Salamon, D., Shen, Z., and Sajgalik, P., *Rapid formation of α-sialon during spark plasma sintering: Its origin and implications*. J Eur Ceram Soc, 2007, **27**, pp. 2541-47.
58. Suárez, M., Fernández, A., Menéndez, J.L., Torrecillas, R., Kessel, H.U., Hennicke, J., Kirchner, R., and Kessel, T., In *Challenges and Opportunities for Spark Plasma Sintering: A Key Technology for a New Generation of Materials, Sintering Applications*. Ed. by D.B. Ertug, InTech, DOI: 10.5772/53706, 2013, pp. 319-342.
59. Lange, F.F., *Effect of Microstructure on Strength of Si//3Ni//4-SiC Composite System*. J Am Ceram Soc, 1973, **56**[9], pp. 445-50.

60. Buljan, S.T. and Baldoni, J.G., Mater Sci Forum, 1989, **47**, pp. 249.
61. Greskovich, C. and Palm, J.A., *Observations on the Fracture Toughness of β-Si_3N_4-βSiC Composites*. J Am Ceram Soc, 1980, **63**[9-10], pp. 597-99.
62. Gogotsi, Y.G., *Particulate silicon nitride-based composites*. J Mater Sci, 1994, **29**[10], pp. 2541-56.
63. Duan, R.G., Kuntz, J.D., Garay, J.E., and Mukherjee, A.K., *Metal-like electrical conductivity in ceramic nano-composite*. Scripta Mater, 2004, **50**, pp. 1309-13.
64. Xu, F., Wen, S., Nordberg, L.O., and Ekstrom, T., *TEM study of Y-doped α-SiAlON composite with 10vol% TiN particulates*. Mater Lett, 1998, **34**, pp. 248-52.
65. Xu, J., Zhang, B., Li, W., Zhuang, H., and Jiang, G., *Pressureless sintering of TiN/Y-(α/β)-sialon ceramics from SHS powder*. Ceram Int, 2006, **32**, pp. 599-602.
66. Ayas, E. and Kara, A., *Novel electrically conductive α-β Sialon/TiCN composites*. J Eur Ceram Soc, 2011, **31**, pp. 903-11.
67. Duan, R.G., Roebben, G., Vleugels, J., and Van der Biest, O., *Optimization of microstructure and properties of in-situ formed β-O-Sialon-TiN composite*. Mat Sci Eng A-Struct, 2006, **427**, pp. 195-202.
68. Jiang, T., Xue, X.X., Li, Z.F., and Duan, P.N., *High temperature oxidation behavior of electroconductive TiN/O'-Sialon ceramics prepared from high titania slag-based mixture*. T Nonferr Metal Soc, 2011, **21**[12], pp. 2638-43.
69. Shimada, S. and Kato, K., *Coating and spark plasma sintering of nano-sized TiN on Y-α-sialon*. Mat Sci Eng A-Struct, 2007, **443**, pp. 47-53.
70. Gao, L., Li, J., Kusunose, T., and Niihara, K., *Preparation and properties of TiN-Si_3N_4 composites*. J Eur Ceram Soc, 2004, **24**[2], pp. 381-86.
71. Krnel, K., Maglica, A., and Kosmac, T., *β-Sialon/TiN nanocomposites prepared from TiO_2-coated Si_3N_4 powder*. J Eur Ceram Soc, 2008, **28**[5], pp. 953-57.
72. Çelik, A., Ayas, E., Halil, E., and Kara, A., *Oxidation behavior of electrically conductive α/β Sialon composites with segregated network of TiCN*. J Eur Ceram Soc, 2012, **32**[7], pp. 1395-403.
73. Ueno, K., Inoue, T., Sodeoka, S., Suzuki, M., Ishikawa, H., Uchiyama, K., and Inui, T., *Si_3N_4-Matrix Composite with TiN Particles Formed by In-situ Reaction*. J Ceram Soc Jpn, 1997, **105**[4], pp. 304-07.
74. Mohri, N., Fukuzawa, Y., Tani, T., Saito, N., and Furutani, K., *Assisting Electrode Method for Machining Insulating Ceramics*. Annals of the CIRP, 1996, **45**[1], pp. 201-04.
75. Fukuzawa, Y., Gotoh, H., Mohri, N., and Tani, T., *Line swept surface generation on insulating ceramics by wire electrical discharge machining*. J Aust Ceram Soc, 2005, **41**[1], pp. 17-21.
76. Guo, Y.F., Bai, J.C., Deng, G.Q., and Lu, Z.S., *High Speed Wire Electrical Discharge Machining (HS-WEDM) phenomena of insulating Si_3N_4 ceramics with assisting electrode*. Key Eng Mat, 2007, **339**, pp. 281-85.
77. Wei, C., Zhao, L., Hu, D., and Ni, J., *Electrical discharge machining of ceramic matrix composites with ceramic fiber reinforcements*. Int J Adv Manuf Technol, 2013, **64**[1-4], pp. 187-94.
78. Liu, K., Reynaerts, D., and Lauwers, B., *Influence of the pulse shape on the EDM performance of Si_3N_4–TiN ceramic composite*. CIRP Annals - Manufacturing Technology, 2009, **58**[1], pp. 217-20.
79. *Materials Science and Engineering Handbook*. Ed. by CRC Press LLC.
80. Inomata, Y., *Energy and Ceramics*. Proceedings of 4th International Meeting in Modern Ceramics Technologies, P. Vincenzini (Elsevier Sci. Pub.), 1980, pp. 706.

81. Mitomo, M., Hirosaki, N., and Mitsuhashi, T., *Thermal conductivity of α-sialon ceramics*. J Mater Sci Lett, 1984, **3**, pp. 915-16.
82. Sivakumar, R., Aoyagi, K., and Akiyama, T., *Thermal conductivity of combustion synthesized β-sialons*. Ceram Int, 2009, **35**, pp. 1391-95.
83. Chatfield, C., Ekstrom, T., and Mikus, M., *Microstructural investigation of alpha-beta yttrium sialon materials*. J Mater Sci, 1986, **21**, pp. 2297-307.
84. Liu, D.M., Chen, C.J., and Lee, R.R., *Thermal diffusivity/conductivity in SiAlON ceramics*. J Appl Phys, 1995, **77**[2], pp. 494-96.
85. Pettersson, P., Shen, Z., Johnsson, M., and Nygren, M., *Thermal shock resistance of α/β-sialon ceramic composites*. J Eur Ceram Soc, 2001, **21**, pp. 999-1005.
86. Persson, J. and Nygren, M., *The oxidation kinetics of β-sialon ceramics*. J Eur Ceram Soc, 1994, **13**[5], pp. 467-84.
87. Clarke, D.R., *Thermodynamic mechanism for cation diffusion through an intergranular phase.* In Progress in Nitrogen Ceramics 1983, ed. by Martinus Nijhoff, The Hague, Netherlands, pp. 421-26.
88. Cubicciotti, D. and Lau, K.H., *Kinetics of Oxidation of Yttria Hot-pressed Silicon Nitride*. J Electrochem Soc, 1979, **126**[10], pp. 1723-28.
89. Persson, J., Käll, P.O., and Nygren, M., *Parabolic-non-parabolic oxidation kinetics of Si_3N_4*. J Eur Ceram Soc, 1993, **12**[3], pp. 177-84.
90. Shimada, S., Aoki, T., Mackenzie, K.J.D., Okutani, T., and Shimokawa, K., *Oxidation and mechanical behavior of carbothermal β-SiAlON ceramics*. J Ceram Soc Jap, 1999, **107**[9], pp. 786-90.
91. Vickridge, I.C., Brown, I.W.M., Ekstrom, T.C., and Trompetter, W.J., *Ion Beam analysis of sialon ceramics*. Nucl Instrum Meth B, 1996, **118**, pp. 608-12.
92. Brown, I.W.M., Barris, G.C., Sheppard, C.M., Trompetter, W.J., and Vickridge, I.C., *Use of IBA techniques for the measurement of oxidation processes in sialon ceramics*. Mod Phys Lett B, 2001, **15**[28-29], pp. 1305-13.
93. Ying, D.Y., Zhang, D.L., and Newby, M., *Solid-state reactions during heating mechanically milled Al/TiO_2 composite powders*. Metall Mater Trans A, 2004, **35**[7], pp. 2115-25.
94. Feng, C.F. and Froyen, L., *Formation of Al_3Ti and Al_2O_3 from an Al-TiO_2 system for preparing in-situ aluminium matrix composites*. Compos Part A-Appl S, 2000, **31**, pp. 385-90.
95. Gaus, S.P., Harmer, M.P., Chan, H.M., Caram, H.S., Bruhn, J., and Claussen, N., *Alumina-Aluminide Alloys (3A) Technology: II, Modeling of Ti_xAl_y-Al_2O_3 Composites Formation*. J Am Ceram Soc, 2000, **83**[7], pp. 1606-12.
96. Pan, J., Li, J.H., Kukunaga, H., Ning, X.G., Ye, H.Q., Yao, Z.K., and Yang, D.M., *Microstructural study of the interface reaction between titania whiskers and aluminium*. Compos Sci Technol, 1997, **57**, pp. 319-25.
97. Wang, X., Jha, A., and Brydson, R., *In situ fabrication of Al_3Ti particle reinforced aluminium alloy metal-matrix composites*. Mat Sci Eng A-Struct, 2004, **364**, pp. 339-45.
98. Zhang, D.L., Ying, D.Y., and Munroe, P., *Formation of Al_2O_3 during heating an Al/TiO_2 nanocomposite powder*. J Mater Res, 2005, **20**[2], pp. 307-13.
99. Software *HSC Chemistry 7.1*, Outotec. Finland.
100. Barris, G.C., Ryan, M.J., and Brown, I.W.M., *Densification and properties of clay derived O'-sialon powder*. Key Eng Mat, 1999, **159-160**, pp. 229-34.
101. Calis, N., Reyhan Kushan, S., Kara, F., and Mandal, H., *Functionally graded SiAlON ceramics*. J Eur Ceram Soc, 2004, **24**[12], pp. 3387-93.

102. Aoyagi, K., Hiraki, T., Sivakumar, R., Watanabe, T., and Akiyama, T., *Mechanically Activated Combustion Systhesis of β-$Si_{6-z}Al_zO_zN_{8-z}$ (z=1-4)*. J Am Ceram Soc, 2007, **90**[2], pp. 626-28.
103. Sivakumar, R., Aoyagi, K., and Akiyama, T., *Effect of mechanically activated raw materials on β-sialon formation by combustion systhesis*. J Mater Res, 2007, **22**[10], pp. 2863-67.
104. Mandal, H., Camuscu, N., and Thompson, D.P., *Comparison of the effectiveness of rare-earth sintering additives on the high temperature stability of alpha-sialon composites*. J Mater Sci, 1995, **30**[23], pp. 5901-09.
105. Kaga, Y., Jones, M.I., Hirao, K., and Kanzaki, S., *Fabrication of elongated α-SiAlON via a reaction-bonding process*. J Am Ceram Soc, 2004, **87**[5], pp. 956-59.
106. Mitomo, M., *Effect of Fe and Al additions on nitridation of silicon*. J Mater Sci, 1977, **12**[2], pp. 273-76.
107. Tanaka, I., Igashira, K.i., Okamoto, T., Niihara, K., and Cannon, R.M., *High-temperature fracture mechanism of low-Ca-doped silicon nitride*. J Am Ceram Soc, 1995, **78**[3], pp. 673-79.
108. Brown, I.W.M., Pompe, R., and Carlsson, R., *Preparation of Sialons by the Nitrided Pressureless Sintering (NPS) Technique*. J Eur Ceram Soc, 1990, **6**, pp. 191-200.

Chapter Three: Equipment, Instruments and Methods

This second chapter presents the equipment and methods used in this work:

- systematic steps in the development of powder mixes and sample preparation,
- firing techniques including furnace descriptions and firing processes,
- chemical and physical properties measurement techniques and their application to samples of different nature (in this case: metal/composite/ceramic, homogeneous/heterogeneous, porous/non-porous).

In the following chapters, when mentioned, these methods are not necessarily restated in all details. For a full description of an experiment, please refer to the corresponding section in this chapter.

3.1 Raw Materials and Compositions

Table 3.1 gives a list of all the raw materials and products used in this work. The compositions mentioned in this thesis are listed in Table 3.2.

Compound	Purity, Supplier	Notes
Al	99.7 %, TLS Technik	Spherical particle -25 µm
AlN	≥ 98 %, H.C. Starck	Grade A
Al_2O_3 HPA-0.5	99.7 %, Ceralox	$D_{50} \approx 0.6$ µm
Calcined Al_2O_3	98 %, Alcoa	
BN	99 %, Shenzhen Chinary Co., Ltd	Hexagonal
$Ca(OH)_2$	May & Baker $Ca(OH)_2$	
CA-25C	Alcoa Calcium Aluminate Cement	Casting Grade
Fe_2O_3	Ferric Oxide Fine Chemicals	
Gibbsite	99 %, Henan Victory Industry Co.	$D_{50} \approx 3$ µm
Presynthesised β and O-Sialon	IRL	Synthesised by team member at IRL in 2005
Silicon metal	Grade 4D, Sicomill Permascand	$D_{50} \approx 7.6$ µm
TiO_2	TIONA 505-T27	
Titanium (IV) Isopropoxide	97 %, Aldrich Chemistry	
Y_2O_3	99.9 %, H.C. Starck Grade C	Trace of Al, Ca and Fe
ZrO_2	99 %, TOSOH Co.	Grade TZ-0
IPA	Drum solvents	
Ethanol		
Argon	> 99.9 %, BOC	Welding Grade, Compressed
Nitrogen	> 99.9 %, BOC	Industrial Grade, Oxygen free, Compressed

Table 3.1: List of raw materials.

Sample number	Sialon type	Sintering Aid (wt%)	BN (wt%)	Additive (wt%)
1	β-Sialon / X-Phase	-	1.5 %	-
2	β-Sialon / X-Phase	13 % YAG	1.5 %	-
3	β-Sialon / X-Phase	5 % YAG	0 %	-
4	β-Sialon / X-Phase	5 % YAG	1.5 %	-
5	β-Sialon / X-Phase	5 % YAG	9 %	-
6	β-Sialon / X-Phase	5 % YAG	18 %	-
7	β-Sialon / X-Phase	5 % YAG	9 %	0.7 % Fe as Fe_2O_3
8	β-Sialon / X-Phase	5 % YAG	9 %	1.5 % Fe as Fe_2O_3
9	β-Sialon / X-Phase	5 % YAG	9 %	2.9 % Fe as Fe_2O_3
10	β-Sialon / X-Phase	5 % YAG	9 %	5 % TiO_2
11	β-Sialon / X-Phase	5 % YAG	9 %	5 % $Ca(OH)_2$
12	β-Sialon / X-Phase	5 % YAG	9 %	5 % $Ca(OH)_2$ from CA-25C
13	β-Sialon / X-Phase	5 % YAG	9 %	5 % ZrO_2
14	β-Sialon / X-Phase	5 % YAG	9 %	10 % Premade Sialon
15	β-Sialon / X-Phase	5 % YAG	9 %	Heated Gibbsite
16	β-Sialon / X-Phase	5 % YAG	1.5 %	5 % $Ca(OH)_2$ from CA-25C
17	β-Sialon / X-Phase	5 % YAG	4 %	5 % $Ca(OH)_2$ from CA-25C
18	β-Sialon / X-Phase	5 % YAG	5.8 %	5 % $Ca(OH)_2$ from CA-25C
19	β-Sialon / X-Phase	5 % YAG	7.7 %	5 % $Ca(OH)_2$ from CA-25C
20	β-Sialon / X-Phase	5 % YAG	10.6 %	5 % $Ca(OH)_2$ from CA-25C
21	β-Sialon	5 % YAG	0 %	-
22	β-Sialon	5 % YAG	0 %	1 % TiN
23	β-Sialon	5 % YAG	0 %	3 % TiN
24	β-Sialon	5 % YAG	0 %	10 % TiN

Table 3.2: List of samples compositions.

3.2 Powder Mixture Preparation

3.2.1 Mixing and Milling

Most of the raw materials used in this study were powders with a particle size distribution in the range 1-100 µm. In order to create a reactive starting mix, the raw materials were milled together to achieve a homogeneous powder. Each raw material was weighed into a separate container and transferred into a dry and clean high-density polyethylene (HDPE) milling bottle (250, 500 or 1000 mL) with about 1/3 of the bottle volume filled by 10 mmØ zirconia or silicon nitride milling balls and isopropyl alcohol (IPA) to cover the balls. Zirconia milling balls were used in the milling process of aluminium to avoid silicon contamination and silicon nitride milling balls were used for all other mixes. The bottle rotated on the mill overnight, approximately 16 hours, except for extended milling trials. Once milled the slurry could be poured into a special flask designed for a rotary evaporator (See 3.2.3) and as much mixture as possible was rinsed out of the milling bottle using IPA.

3.2.2 Milling with a Bouncing Ball System

As part of the fabrication process, some disc samples needed to be ground to powder after being fired in order to be mixed with other reactants.

A tungsten carbide mortar and ball (See Figure 3.1) has been especially designed to be able to easily grind hard and tough samples such as nitrogen ceramics. A sample was placed in the mortar and the ball was put on top. A cap covered the mortar and the whole system was secured on a vibrating plate. The vibrations bring the ball into a bouncing movement that shatters and crushes the softer sample.

Typically, the vibrating plate was set to a medium speed so the ball bounces several millimetres but does not jump as high as the cover level. Samples were reduced to a feed stock for ball milling in about 30 minutes to an hour.

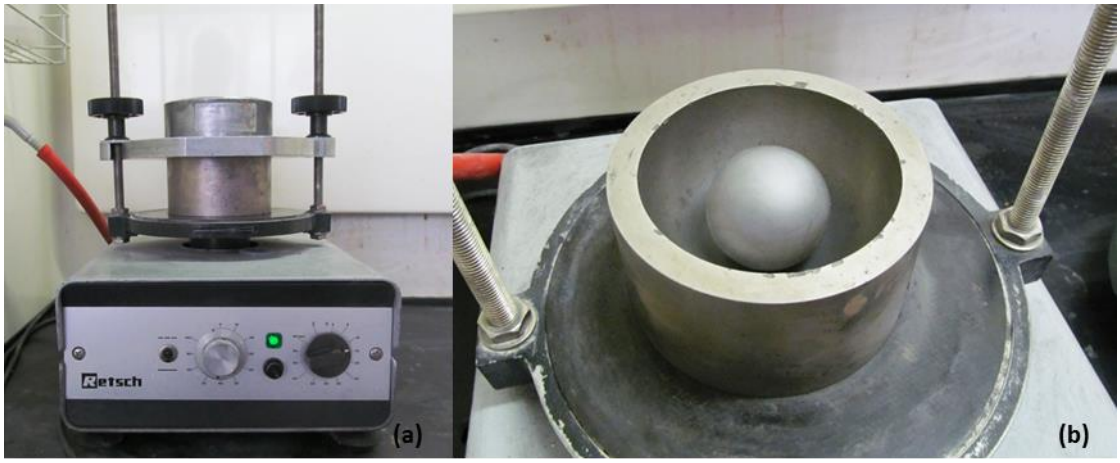

Figure 3.1: (a) Tungsten Carbide bouncing ball with steel cover on a vibrating plate. (b) Tungsten Carbide bouncing ball and mortar.

3.2.3 Rotary Evaporator

When necessary, the powder was extracted from the IPA by rotary evaporation. The rotary evaporator equipment is shown in Figure 3.2. The lid was clamped onto a rotary evaporator flask with the suspension in it and the water bath was set to 50 ºC. The flask was attached to the rotary evaporator, vacuum was applied, and the flask was set rotating at low speed until all liquid has evaporated. The resulting powder was scraped out of the flask and passed through a 710 µm sieve in order to break up aggregates and form granules for pressing. This sieve size has been chosen to stop dusting and loss of fine particles. These soft aggregates are readily broken by pressing.

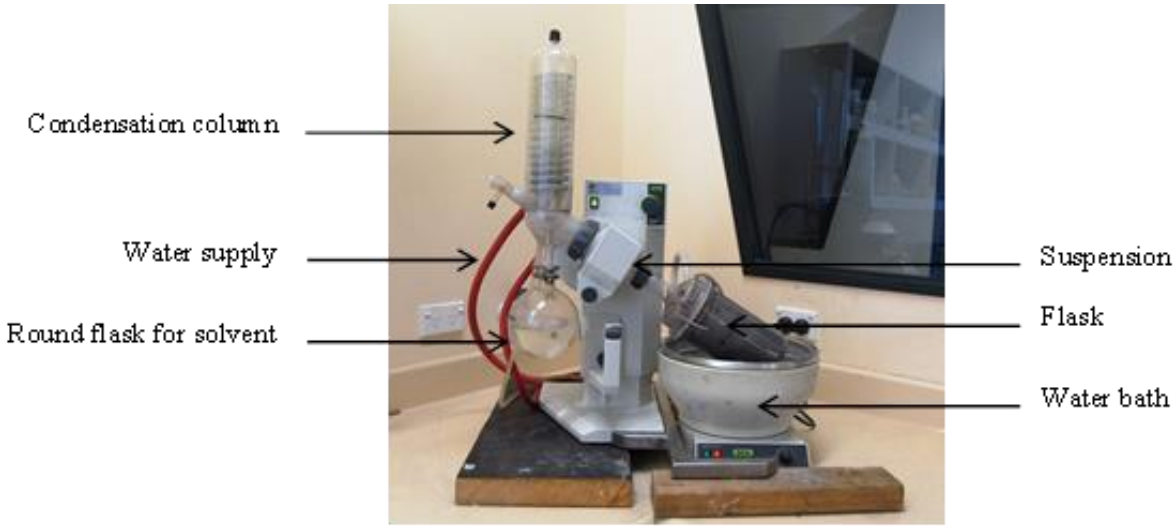

Figure 3.2: Rotary evaporator in use (Sialon mix in IPA).

For safety reasons, the milled aluminium powder was not evaporated as it is highly sensitive to oxidation and hydrolysis when dry and could spontaneously ignite.

3.2.4 Sol-gel inspired Coating of Aluminium Powder

The sol-gel coating process of aluminium powder by titania used in this work is a similar method to the classic sol-gel technique but the process was adapted to stop the formation of a gel which is not necessary for this coating process. The method is largely inspired by the work described by Gao et al.[1] and Krnel et al.[2] but it has been mentioned in other research reports.

The aluminium powder (typically a few grams) was introduced in a round bottom flask with a magnetic stirrer and about 100 mL of IPA including the IPA used for its milling. Titanium isopropoxide was introduced in the flask (See Annex I for the details on the quantities introduced). All these steps were undertaken relatively quickly and the flask was immediately closed with a rubber top to reduce the exposure of the compounds to air. The resultant suspension was mixed for about an hour to allow the titanium isopropoxide to attach to the aluminium particles surfaces.

Once the aluminium and the titanium isopropoxide were thoroughly mixed, the latter was hydrolysed to form titania (see Equation 3.1). The calculated amount of water was diluted in about 50 mL of IPA then introduced in the opened flask at the rate of a dozen drops every 5 minutes for the first 2 mL to avoid an uncontrollable hydrolysis which would result in the formation of a gel, then added progressively faster and faster. The mix was left stirring for another half an hour to complete the hydrolysis of the titanium isopropoxide.

$$\mathrm{Ti(OCH(CH_3)_2)_4 + 2H_2O \rightarrow TiO_2 + 4(CH_3)_2CHOH} \qquad \text{(Eq 3.1)}$$

Titanium Isopropoxide IPA

A vacuum filter, using grade 1 qualitative filter paper, was used to remove the solvent and the powder was washed with ethanol then dried overnight in a vacuum oven at about 50 ºC.

3.3 Preparation of Disc Samples

3.3.1 Uniaxial Press

Two different types of discs were pressed: samples with a 10 mmØ for the thermogravimetric analysis due to the size of the sample holder as well as for some early experiments and, samples with a 20 mmØ for every other experiment. Figure 3.3 shows the uniaxial press and

the dies used in this work. The powder was loaded into a cylindrical metal die, spread evenly and the plunger introduced. Then the die was placed onto the uniaxial press, pumped up to about 15 MPa pressure on the pellet and held at this for around 30 seconds, then slowly released. A pressure of 15 MPa is sufficient to form robust pellets but not to create over-compression of the pellet faces.

Figure 3.3: Uniaxial Press and dies.

3.3.2 Cold Isostatic Press (CIP)

A cold isostatic press (shown in Figure 3.4) allows uniform pressing of samples from every direction by applying the pressure to a liquid in which the sample is kept. The cold isostatic press used in this work has a 14 L Fluitron pressure chamber (SO#9202-4967). It works with ethylene glycol as an hydraulic compression oil so the samples need to be protected from this liquid. Samples were introduced in a latex balloon with the help of a special tool ("Elastrator") represented in Figure 3.5 to make the balloon opening wider then vacuum was created inside the balloon and it was sealed with a simple knot. The balloon was suspended on a metal wire and placed into the pressing cage. The balloons and cage were placed in the CIP chamber, ensuring that the samples were immersed in the compression liquid.

Samples were pressed at a chosen pressure (40 to 200 MPa) for 60 seconds. After pressing, balloons were easily rinsed with water as ethylene glycol is highly water soluble and left on absorbing paper to dry.

The aluminium coated with titania samples were pressed in the uniaxial press but were not pressed in the CIP because they do not need to be densified, as further addition of a silicon species is required to form the Sialon phase.

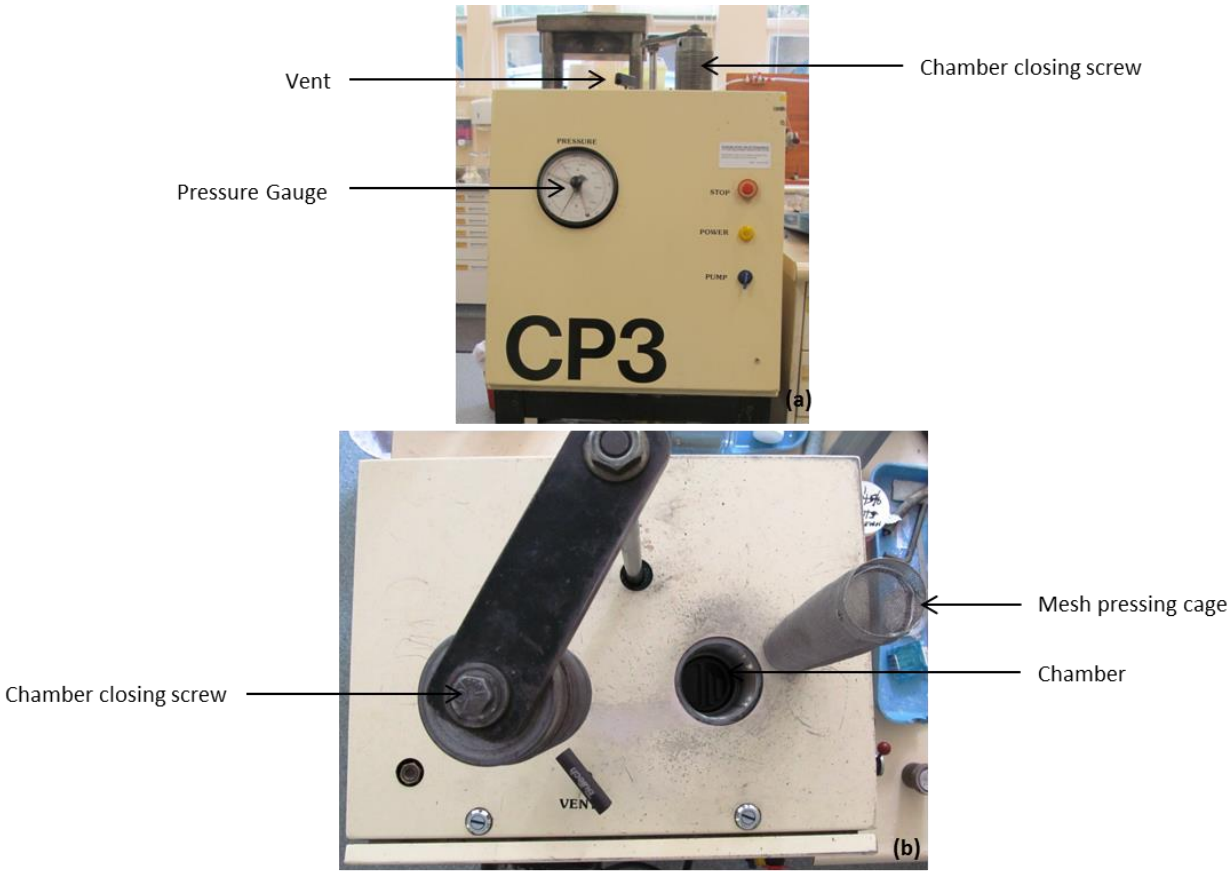

Figure 3.4: Cold Isostatic Press (a) Front view and, (b) Top view with mesh pressing cage.

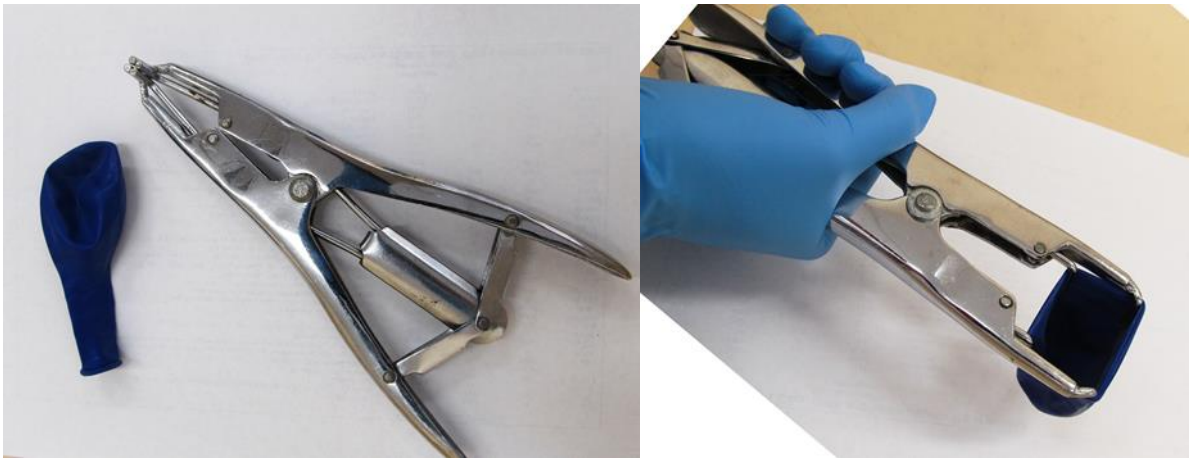

Figure 3.5: Elastrator Applicator used to enlarge the rubber balloons opening.

3.3.3 Firing Equipment

A number of ovens and furnaces have been used in this project to create the desired firing conditions for the different synthesis and sintering methods required (See Figure 3.6):

a. A vacuum oven (Precision Scientific Model 19, GCA Corporation) to evaporate residual solvents in mix and discs samples with a maximum temperature of 150 ºC, a maximum vacuum of 18 kPa and a volume of 10^{-2} m^3. The oven is connected to a pump that is equipped with filters made to deal with solvents to avoid contamination in the vacuum system. Note that the vacuum applied to the chamber does not reach its maximum when the samples are wet as the evaporation of the solvents increases the pressure in the oven.
b. An Amalgams CH5 air furnace with a maximum temperature of 1400 ºC and a capacity of $7.5.10^{-2}$ m^3 for firings that do not require a controlled atmosphere.
c. An Amalgams HT2-5 alumina tube furnace for temperatures up to 1400 ºC under a maximum of 1 atm of argon or nitrogen, or vacuum. The tube can also be closed with Kaowool® (refractory ceramic fibrous material used for thermal insulation) for firing in oxidising atmosphere. The samples are placed in alumina boats and the furnace can contain a maximum of five 20 mmØ samples.
d. A home built vertical tube furnace of 45 cm height and a maximum temperature of 1000 ºC. This furnace is used to apply a thermal shock to the samples, which are suspended inside the hot tube above a bucket of water at ambient temperature.
e. A hot press furnace (Thermal Technology Group 1400 Laboratory Hot Press, model HP20-1000-3060) for temperatures up to 1800 ºC in argon or nitrogen, or vacuum and

uniaxial force up to 10,000 kg. The 19 mm and 25 mm dies available are made of dense graphite and can contain three disc samples separated by BN layers. Note that the maximum pressure indicated depends on the die used and the size of the sample.

f. An Elatec® Vertivac Laboratory Vacuum Furnace controlled atmosphere furnace (nitrogen, argon or vacuum) for temperatures up to 2000 ºC. The advantage of this high volume furnace (up to 4.10^{-2} m^3 depending on the crucible used) is that it can contain a high number of samples in graphite pots.

Figure 3.6: Different furnaces available (a) Vacuum oven (b) Amalgams air chamber furnace, (c) alumina tube furnace, (d) vertical tube furnace, (e) graphite hot press furnace and, (f) Elatec high capacity graphite furnace.

3.3.4 Discs Sample Cutting

To observe the samples core, a Struers Accutom-5 saw (See Figure 3.7) was used as a cutting tool. Samples were placed flat in the sample holder and well tightened to eliminate movement during the cutting. The wheel used was a 452CA 10 cmØ diamond wheel for sintered carbide

and hard ceramics. The cutting program was set depending on the sample size but the cutting speed was always set to the minimum of 0.005 mm.s^{-1} to avoid overheating and fracture. The lubricant projected on the wheel was composed of one part Struers Corrozip-LF (anti-corrosion and heating lubricant for cutting tools based on triethanolamine) for twenty-five parts water.

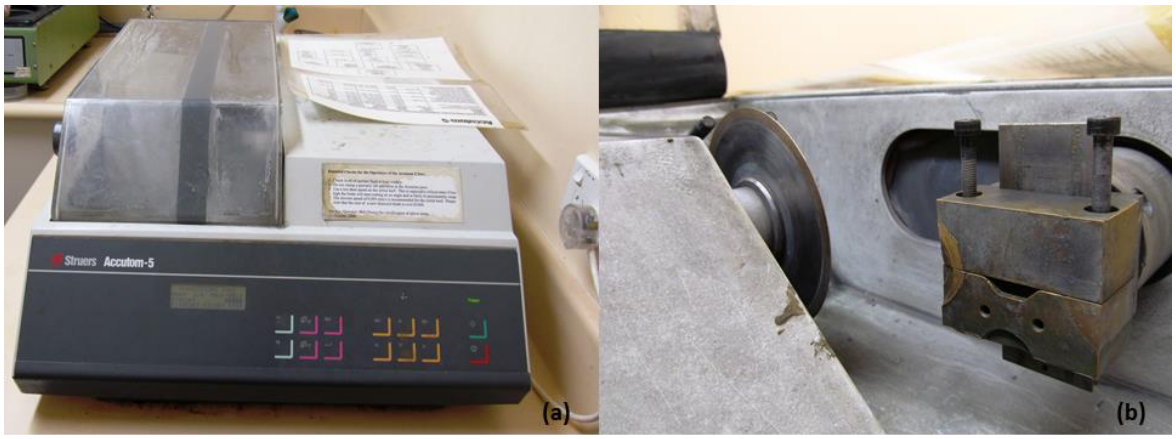

Figure 3.7: (a) Struers Accutom-5 Saw and, (b) Diamond wheel with sample holder.

3.3.5 Discs Sample Encapsulation and Polishing

For polishing, samples were encapsulated in Bakelite or epoxy resin, stuck to a support with wax or simply held against the polishing disc depending on the quality of polishing desired.

To encapsulate a sample in bakelite, it was placed in a Struers LaboPress-3 (See Figure 3.8) with the surface to be observed facing down. It was then covered with about 30 mL of bakelite Struers Multifast and pressed at 20 kN and 180 ºC for five minutes then cooled down for another five minutes.

To encapsulate in epoxy resin, a dry sample was placed in an encapsulating mould with the surface to be observed facing down. A mix of 25 Struers Epofix resin:3 Struers Epofix hardener was poured over the sample and the whole system was placed into a desiccator and evacuated twice for five minutes to remove all the air in the liquid resin. The resin was left to set overnight.

To attach sample with wax, the support (a simple nylon cylinder) and the sample were heated at 140 ºC on a hot plate. A wax stick was applied against the hot support and the sample is immediately pressed against it. The support and sample were left to cool down for a few minutes before polishing.

Encapsulated and wax-attached samples were placed on a Struers LaboPol-5 with a Struers LaboForce-3 sample holder (See Figure 3.9) at 100 rpm. Table 3.3 shows the polishing time for each disc. Polishing time was adapted to the hardness of each sample. To simply grind the sample surface, a polishing bench equipped with SiC paper (See Figure 3.9) was used. In this case, samples were simply held by hand against the polishing discs.

Figure 3.8: Encapsulating equipment Struers LaboPress-3

Polishing disc	Minimum / maximum time (min)	Lubricant
MD-Piano 20 mmØ #80	0.5 / 10	Water
MD-Piano 20 mmØ #120	1 / 10	
MD-Piano 20 mmØ #220	1 / 10	
Polishing cloth with DP-Stick P 15 µm	30 / 45	Mix of ethanol, IPA and ethylene glycol
Polishing cloth with DP-Stick P 6 µm	30 / 45	
Polishing cloth with DP-Stick P 3 µm	30 / 45	
Polishing cloth with DP-Suspension 1 µm	0 / 60	

Table 3.3: Polishing discs, time and lubricants.

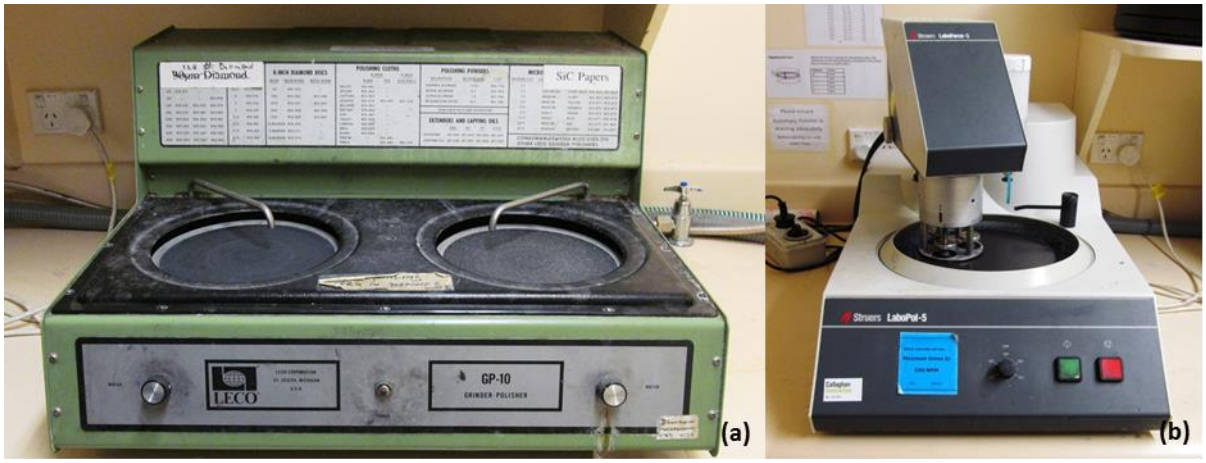

Figure 3.9: Polishing equipment: (a) Polishing bench with SiC paper discs and, (b) Polishing machine.

3.4 Measurement of Volume, Porosity and Density

The mass, height and weight of the samples were measured before and after firing. To measure density and porosity, the samples were kept under vacuum for 1 hour, then water was added to the container while under vacuum, and maintained for another hour (See Figure 3.10). This ensured thorough infiltration by water into the pore structure of the sample. The pressure was removed and the samples left immersed under water for at least 15 minutes before being weighed. The samples were weighed suspended in water then wiped with a wet towel to remove excess surface moisture and weighed in air. The densities and open porosity were calculated using Archimedes Principle. The density was compared with the theoretical Sialon density and the closed porosity was calculated.

$$\text{Apparent porosity} = \frac{\text{Volume of open pores}}{\text{Vol.of solid material+vol.of (closed+open pores)}} = \frac{(W_W - W)}{W} * 100 \qquad \text{(Eq 3.2)}$$

$$\text{Apparent density} = \frac{\text{Dry weight of the porous material}}{\text{Vol.of solid material+vol.of closed pores}} = \frac{W}{(W - W_S)} * D * 100 \qquad \text{(Eq 3.3)}$$

$$\text{Bulk density} = \frac{\text{Dry weight of the porous material}}{\text{Vol.of solid material+vol.of (closed+open pores)}} = \frac{W}{(W_W - W_S)} * D * 100 \qquad \text{(Eq 3.4)}$$

$$\text{Closed porosity} = \text{Bulk density} * \left(\frac{1}{\text{Apparent density}} - \frac{1}{\text{Theoretical density}}\right) * 100 \qquad \text{(Eq 3.5)}$$

Where W is the weight of the dry sample, D is the density of water at measurement temperature, W_W is the weight of the sample with open pores filled with water after vacuum impregnation and W_S is the weight of the sample suspended in water after vacuum impregnation.

Figure 3.10: Porosity and density equipment.

3.5 Chemical composition

3.5.1 Phase Composition by X-ray Diffraction (XRD)

The ground surfaces and powders were examined by XRD to determine the composition of the crystalline phases. To prepare bulk samples for XRD, the discs were ground on SiC paper to remove any surface reaction layer and the powder samples were hand ground in an agate mortar and packed into a sample holder.

X-ray diffraction measurements on bulk samples were carried out on a Bruker D8 Advance diffractometer configured as a parallel beam instrument with a 60 mm incident beam Goebel mirror and a 0.23 degree parallel plate collimator in front of a NaI scintillation counter. Cobalt K alpha radiation was used. The 2θ range observed was typically 10 to 80º with 0.05 degree step intervals but could be extended as far as 150º if necessary.

Powder samples were analysed with a Philips PW1700 series diffractometer running cobalt K alpha radiation from a long fine focus tube. The instrument was equipped with 1 degree effective divergence slit, 0.2 mm receiving slit, 1 degree antiscatter slit, incident and diffracted beam Soller slits, graphite diffracted beam monochromator and Xe-filled gas proportional counter. The sample was front-loaded for analysis with 0.05 degree step interval between 10 and 80º.

Approximate proportions of the different Sialons phases were calculated using templates, which compare the most intense peak heights to calculate the percentages. If the highest peak for a phase was overlapped with the peak of another phase the corrected height was calculated from a lower peak, using the intensity ratio recorded for that phase in the International Centre for Diffraction Data (ICDD) database (See Annex II). The z-values of

β−Sialons were also calculated using a template, which compares the exact position of the peaks at 2θ ≈ 15° and 2θ ≈ 38.5° (See Annex III). Silicon metal was used as an internal angle calibrant when necessary.

3.5.2 Composition by MAS-NMR

When a material is not crystalline, XRD analysis is unable to give useful structural or phase information. Analysis using Solid State Magic Angle Spinning Nuclear Magnetic Resonance (MAS-NMR) can be applied to atoms with a spin number greater than zero such as Al (spin = 5/2) or Si (spin = 1/2). The nucleus absorbs the magnetic wave with a characteristic frequency. To return to equilibrium, it creates an electromagnetic wave, which can be detected and interpreted to yield information about the immediate environment of the atom. From this the nature of bonding can often be deduced by comparison with samples of known structure.

Callaghan Innovation operates a Bruker Avance III500 spectrometer shown in Figure 3.11 using an 11.7 T magnet and Doty Scientific XC probes. The measurement settings were adapted to the element analysed.

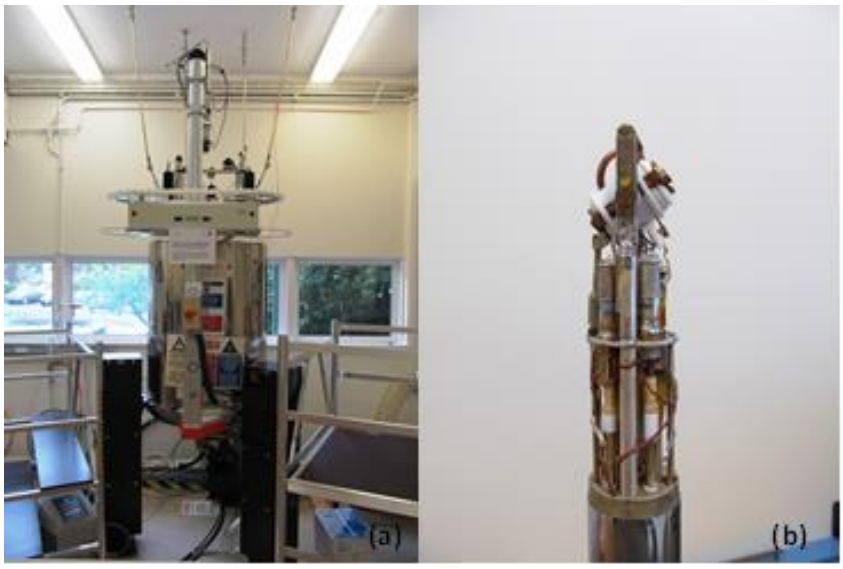

Figure 3.11: (a) Bruker Avance III500 Spectrometer and, (b) top of the silicon probe with the sample holder tilted to the Magic Angle (54.7º).

A number of elements can be analysed by NMR. In this project, the isotopes of most interest were:

- ^{27}Al which has a high sensitivity nucleus that yields broad lines over a wide chemical shift range. It has a 100 % natural abundance, its spin is 5/2 and it is quadrupolar. The emitted signal width is increased with asymmetry in the environment.
- ^{29}Si has a spin of ½ and is therefore not subject to quadrupolar peak broadening and distortion. Despite its low abundance (about 4 %), ^{29}Si gives good intensity spectra. It also has a slow relaxation rate which means that the measurement needs to be longer to obtain a good signal/noise ratio.
- ^{89}Y NMR is commonly used to investigate the content of the Sialon glassy phase when yttria is used as a sintering aid. The disorder of this phase can make the spectra broader and the relaxation time longer but a small addition of paramagnetic rare earth ions, such as Eu^{3+}, can improve the detection of ^{89}Y. This isotope also has a 100 % natural abundance.
- ^{11}B has a high natural abundance of 80.42 %, its sensitivity is good and its relaxation time relatively fast. These characteristics make ^{11}B MAS-NMR easy to process even though an asymmetrical environment makes the spectra broad.
- Titanium has two NMR active isotopes: ^{47}Ti and ^{49}Ti. They have very similar characteristics such as large quadrupolar moments and similar nuclear gyromagnetic ratios which give them really close resonance frequencies, only 9 kHz apart in a 14.1 T magnetic field. This results in the superposition of the two resulting spectra and imposes great difficulties in interpretation.

There is no probe able to tune at the correct frequency for ^{89}Y MAS-NMR available at Callaghan Innovation but The University of Warwick (England) has NMR equipment with a 21 T magnet and a yttrium compatible probe. The magnetic field available in Warwick also has the potential to separate the resonance frequencies of the two titanium isotopes in order to separate the resulting spectra from each other.

3.6 Particle Size Distribution Analysis

The particle size distribution of powders was measured with a Shimadzu Sald-2001 instrument using laser diffraction (wavelength 680 nm, 2.5 mW) with the Mie light scattering theory[3] and a variable refractive index. Measurements were made using water or IPA as a

liquid medium with ultrasonic agitation applied to the sample for two minutes to break up any aggregates.

This measurement gives information to enable the understanding of the effect of grain size on reactivity, densification and microstructures.

3.7 Ultrasonic Evaluation of Young's Modulus

Measurement of both longitudinal wave and transverse wave sound velocities in a solid sample permits a straightforward calculation of Poisson's ratio and Young's modulus, shear and bulk moduli[4]. The method requires that the dimensions of the sample exceed the wavelength of sound by at least a few times, so in this work, ultrasonic frequencies from a 10 MHz probe in pulse-echo mode using a Krautkrämer USIP11 Crack Detector were used. The probe was applied directly to 15 mm diameter sample discs polished to have plane parallel faces about 6 mm apart for measurement of longitudinal wave transit times or equivalent steel distances, and via a shaped block (inducing a mode change due to total internal reflection) for measurement of transverse wave transit times (See Figure 3.12). These times were combined with independent measurement of disc thickness and bulk density to yield velocities and thus Poisson's ratio and Young's modulus.

Where reliable transverse wave measurements could not be obtained, Young's moduli were estimated for the Sialon samples using the longitudinal wave sound velocities. The Krautkrämer USIP11 Crack Detector was used in pulse echo mode and in 'pitch and catch' mode with a 5 MHz probe. The instrument display was calibrated with 25 mm of steel full scale, and measurements produce an equivalent steel thickness which could be used to estimate Young's modulus using the following equation:

$$E = \rho * (v_s * \frac{l_c}{l_s})^2 \qquad \text{(Eq 3.6)}$$

Where E is the Young's modulus; ρ is the bulk density; l_c is the thickness of the ceramic sample; l_s is the equivalent thickness of steel and, v_s is the speed of sound in steel (5.94 km.s^{-1}).

Equation 3.7 was used to calculate Young's Modulus from the longitudinal wave transit time and an estimated Poisson's ratio.

$$E = \rho * (H/\Delta t_l)^2 * (1 - 2\nu^2)/(1 - \nu) \quad \text{(Eq 3.7)}$$

Where H is the sample thickness; Δt_l is the longitudinal wave transit time; and ν is the estimated Poisson's ratio.

Where a transverse wave measurement was obtained, Poisson's ratio and Young modulus were calculated with equations 3.8 and 3.9, respectively.

$$\nu = (0.5 - \left(\frac{\Delta t_l}{\Delta t_t}\right)^2)/(1 - \left(\frac{\Delta t_l}{\Delta t_t}\right)^2) \quad \text{(Eq 3.8)}$$

$$E = \rho * 4H^2 * (3 - 4\left(\frac{\Delta t_l}{\Delta t_t}\right)^2)/(\Delta t_t{}^2 - \Delta t_l{}^2) \quad \text{(Eq 3.9)}$$

Where Δt_t is the transverse wave transit time.

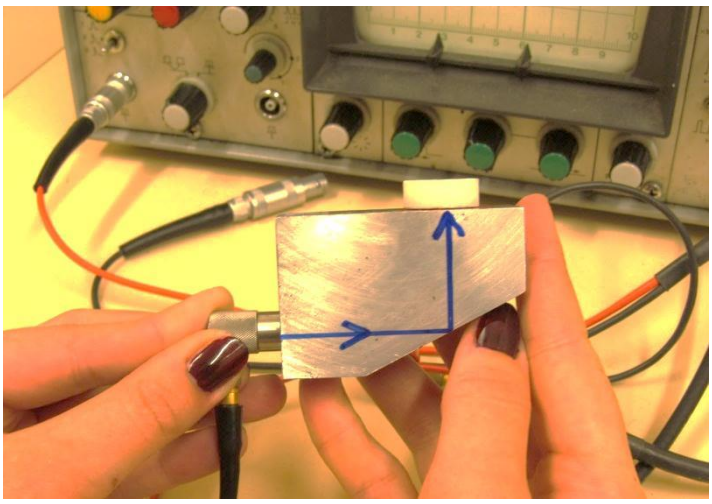

Figure 3.12: Measurement of transverse wave transit times via a shaped steel block.

3.8 Oxidation Resistance by Ion Beam Analysis (IBA)

Ion Beam Analysis includes a range of techniques based on the interaction, at both the atomic and the nuclear level, between accelerated charged particles and the studied material. When a charged particle moving at high speed strikes a material, it interacts with the electrons and nuclei of the material atoms, slows down and possibly deviates from its initial trajectory. This can lead to the emission of particles or radiation whose energy is characteristic of the elements which constitute the sample material. Therefore IBA techniques can determine the variation in the elemental composition in the surface of a material.

A range of IBA equipment is available at GNS Science in Gracefield, Lower Hutt (See Figure 3.13). The IBA method uses a particle accelerator to inject the nuclei of light atoms such as hydrogen, deuterium or helium into the surface particles (at 0.75-3 MeV), producing nuclei,

gamma rays or X-rays. Through use of a combination of IBA techniques including Particle-Induced X-Ray Emission (PIXE), Particle-Induced Gamma Emission (PIGE), Rutherford Backscattering (RBS) and Nuclear Reaction Analysis (NRA), each of the key Sialon elements (Si, Al, O, N, Y) can be analysed as a surface depth profile, enabling a detailed understanding of oxidation induced atomic mobility[5].

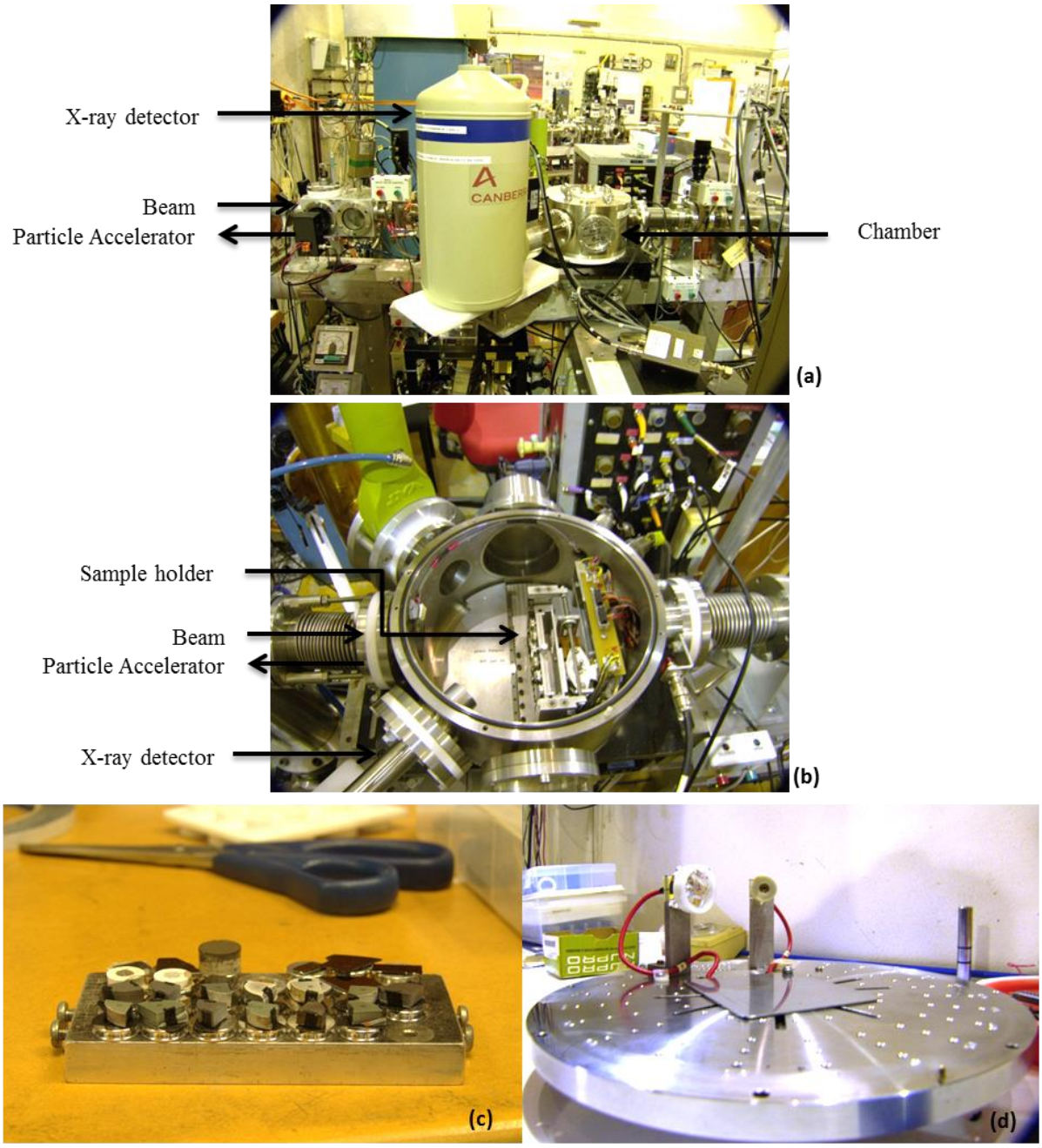

Figure 3.13: IBA equipment. (a) Chamber, (b) Open chamber,(c) Samples on sample holder and, (d) Detectors in the chamber lid.

3.9 Scanning Electron Microscopy (SEM)

Samples were examined using the Callaghan Innovation electron microscopes. Low magnifications imaging and energy dispersive X-ray spectroscopy (EDS) were done with an FEI Quanta 450 scanning electron microscope equipped with a tungsten filament. For high magnification (> 30,000), an FEI Nova NanoSEM 450 field emission gun (FEG) was used.

When quantitative results were required, a ZAF correction has been applied using the EDS software[6]. The ZAF correction is a mathematical adjustment to the analysis, taking into account the effects of atomic number, absorption and fluorescence[7] on the elemental concentration.

For this analysis, samples were ground flat on a 80, 120 then 220 grit resin bonded diamond wheel for a few minutes each (polishing time depended on the softness of the material and softer materials could be ground for only 30 seconds on each disc). Samples were then polished with 15, 6 and 3 µm diamond paste for a minimum of 30 minutes each on a Struers Labo Pol 5, planetary grinding and polishing machine. Each sample was placed on a disc of carbon tape and stuck to a single support. Except for the aluminium powder and fragile oxidised surfaces, every sample observed by electron microscopy was carbon coated to avoid surface charging.

The Nova SEM uses a higher vacuum than the Quanta and samples needed to be prepared with more care. To avoid contamination of the chamber, samples were placed for at least an hour in a desiccator before being introduced in the SEM.

Observation parameters were dependant on the sample and the measurement undertaken: voltage was tested for every material observed to obtain the best focus (between 20 and 30 keV) ; working distance (10-15 mm for imaging, 5-10 mm for EDS) and spot size (around 3 for imaging, around 7 for EDS) were adapted to the individual measurement.

3.10 Hardness and Fracture Toughness Measurement

Hardness and toughness were measured using the Vickers indentation method[8] on a polished surface. Samples were supported in bakelite and polished down to 3 µm.

A standard Vickers diamond indenter (shown in Figure 3.14) was pressed into the polished sample with force equivalent to a 10 kg mass. Five indents were made in each sample separated for at least 3 mm from each other. The samples were immediately viewed under a

microscope to measure the length of the inside diagonals, and the lengths of the cracks extending from the indent corners (See Figure 3.15). When the indent is observed on the surface, one crack appears to originate from each corner of the indent. Figure 3.15 illustrates how the cracks propagate under the surface, under the indent and shows that one indent actually creates two cracks rather than four.

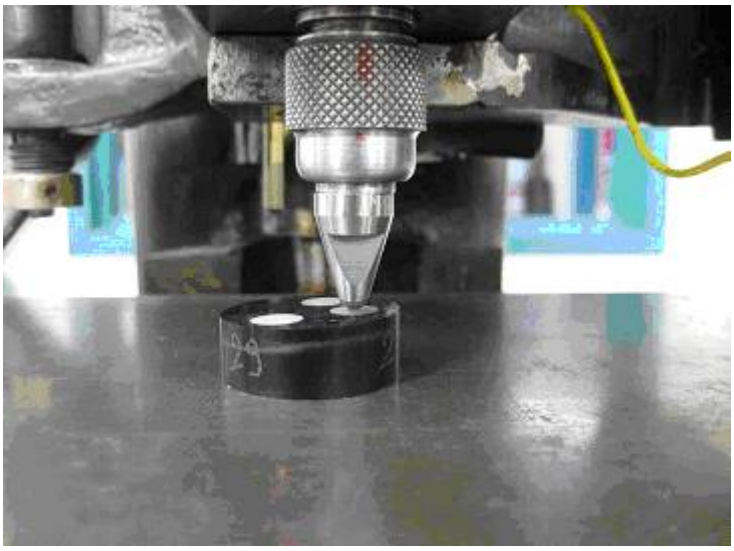

Figure 3.14: Vickers diamond indenter on a bakelite cylinder containing three samples.

Hardness was calculated using the Vickers formula (Equations 3.10 and 3.11). The toughness was calculated using the Miyoshi formula (Equation 3.12).

Vickers Hardness (H_v) in GPa:

$$H_v = \frac{2P\sin\left(\frac{136}{2}\right)}{a^2} = \frac{1.854P}{a^2} \qquad \text{(Eq 3.10)}$$

Where P is the applied load in kg and a is the arithmetic mean of the length of the two diagonals of the indent in mm.

To convert this result to SI units, the following equation can be used:

$$H_v = \frac{0.189P}{a^2} \qquad \text{(Eq 3.11)}$$

Indentation Fracture Toughness (K_c) in MPa.m$^{-1/2}$:

$$K_c = 0.018\left(\frac{E}{H_v}\right)^{\frac{1}{2}}\frac{P}{c^{\frac{1}{2}}} = 0.0264aE^{1/2}\frac{P}{c^{\frac{1}{2}}} \qquad \text{(Eq 3.12)}$$

Where c is the arithmetic mean of the length of the two cracks created by the indent in mm.

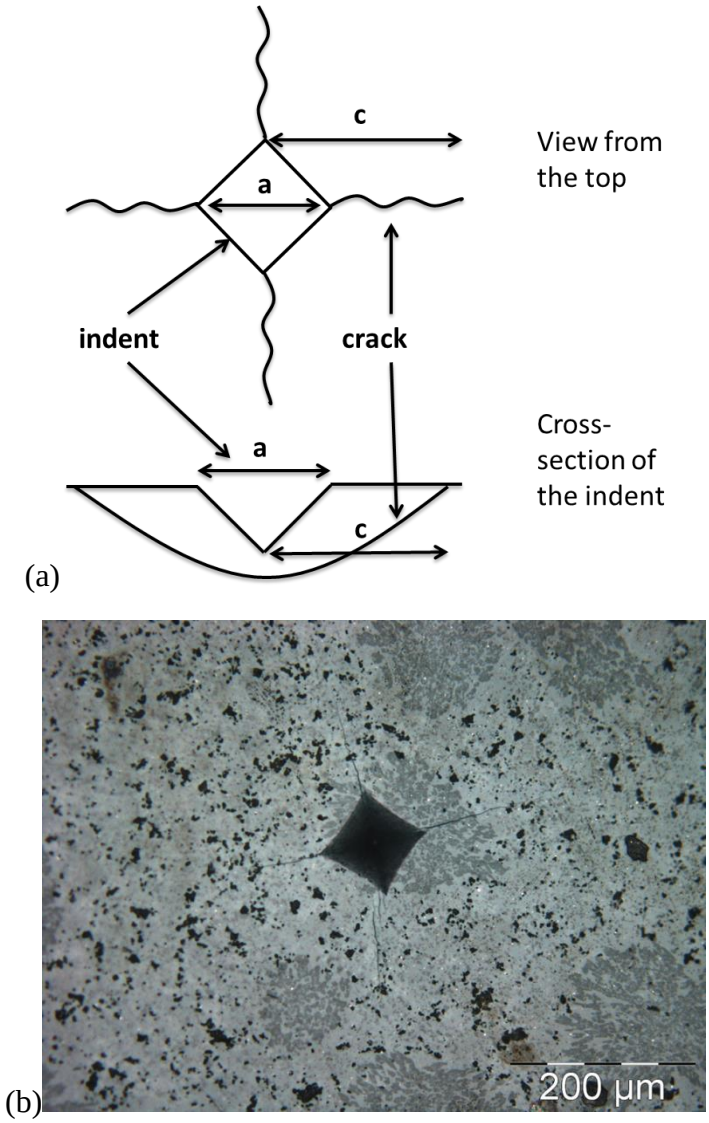

Figure 3.15: (a) Schematic and (b) light microscope image illustrating the cracks from the indent.

3.11 Compressive Strength Measurement: Brazil Test

The method chosen to monitor strength is a diametral compression test, frequently referred to as the "Brazil Test"[9]. The sample was compressed diametrically between two flat platens. The testing was performed using an Instron 1225 universal tester (See Figure 3.16). Pieces of thin card were placed between the sample and the machine to decrease the impact of any potential irregularity in the sample surface. All tests were run at 1 $mm.min^{-1}$ loading rate. This test is designed to measure the tensile stress that is developed when a solid disk is subjected to diametric loading. The maximum tensile stress, σ_{max}, exists over a substantial part of the loaded diameter and is represented by:

$$\sigma_{max} = \frac{2P}{\pi L h} \quad \text{(Eq 3.13)}$$

Where P is the maximum load in N, L is the length of the sample diameter in mm, h is the thickness of the sample in mm.

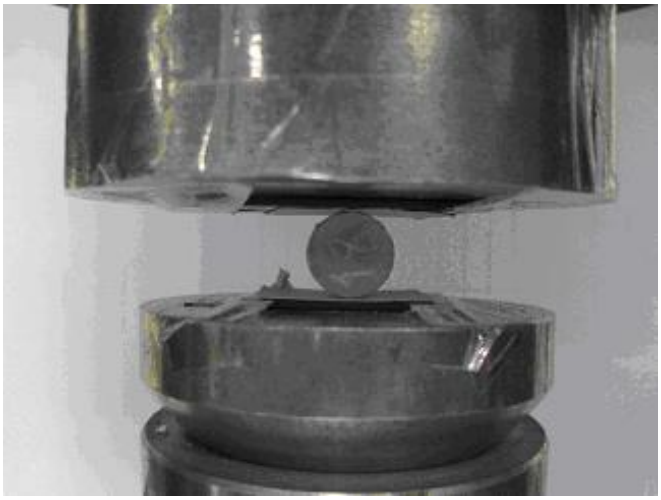

Figure 3.16: Brazil test with an Instron force test instrument.

3.12 Electrical Conductivity Measurement

The electrical conductivity σ measurement can be made by a two-probe method which consists of applying a potential through an electrode on one side of the sample and measuring the intensity of the current at the other side through a second electrode (see Figure 3.17). The result is then calculated using the following equation:

$$\sigma\ (\mathrm{S.m^{-1}}) = \frac{\ell}{\rho\ (\Omega.\mathrm{m})} = \frac{I}{V} \times \frac{\ell}{A} \quad \text{(Eq 3.14)}$$

Where ℓ is the distance between the electrodes in m, ρ is the electrical resistivity, I is the intensity of the current, V is the applied voltage and A is the cross section in m^2.

The electrodes can be made of gold, silver or Aquadag® (a high density colloidal graphite) depending on the measurement temperature and the porosity of the sample.

However, above a certain potential which depends on the distribution of the conducting particles in the materials and the quality of the contact between the electrodes and the sample, an accumulation of charge in a limited volume of the sample can occur and create an heterogeneous resistivity of the material. This effect called Space Charge Limited Current is detected by a non-linear response of the material to this measurement. To avoid the phenomenon, the four-probe method can be used. The applied potential and measured

intensity are the same as in the two-probe method but the potential used to calculate the electrical conductivity is a difference of potential between two points situated on the perpendicular surface (See Figure 3.18).

$$\sigma\ (\mathrm{S.m^{-1}}) = \frac{\ell}{\rho\ (\Omega.\mathrm{m})} = \frac{\mathrm{I}}{(\mathrm{V_2}-\mathrm{V_1})} \times \frac{\ell_0}{\mathrm{A}} \qquad \text{(Eq 3.15)}$$

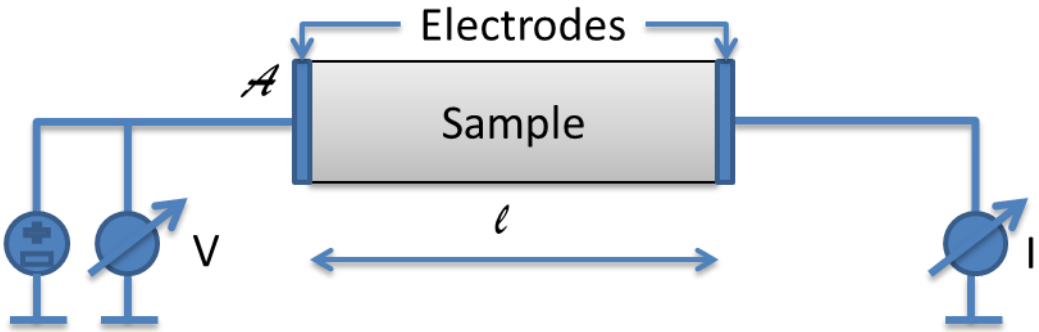

Figure 3.17: Two-probe method for electrical resistivity measurement.

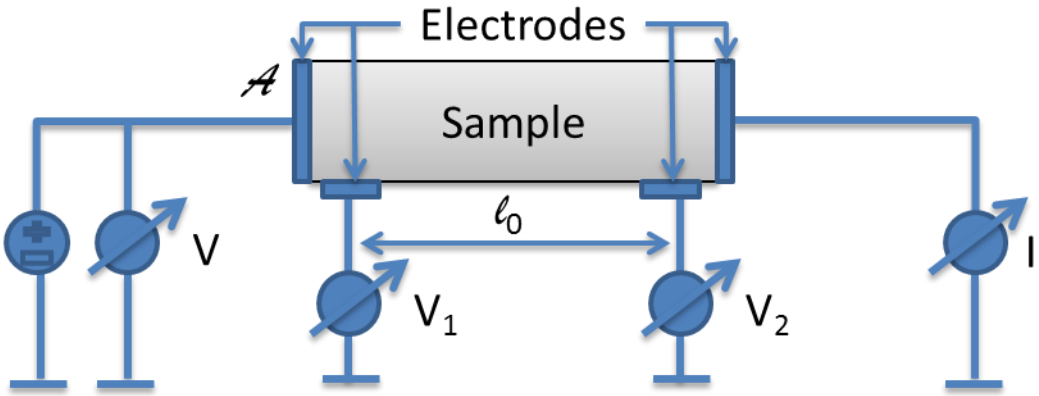

Figure 3.18: Four-probe method for electrical resistivity measurement.

3.13 Health & Safety Issues

As a basic personal protection, a lab coat, latex gloves and safety glasses were used in the laboratory. A number of health and safety issues have been encountered during this project:

3.13.1 Manual Handling

Some equipment used in this project was very heavy. As a general rule, if the object could be carried, it was done with great care and as rarely as possible; if the object was too heavy to be transported, helped was asked to another person. Heavy equipment includes the Instron 1225 universal tester (sample support in particular), the tungsten carbide bouncing ball, barrels of

powder and gas bottles. The transportation of the latter required a special training and was never made under rain, frost conditions or at night.

3.13.2 Cutting Hazards

Working with hard and tough materials requires the use of sharp and strong cutting tools. Generally, cutting equipment is fitted with security systems such as the diamond saw which cannot operate when its cover is open. But samples need to be manually pressed against the grinding paper on the polishing bench (See Figure 3.9). SiC paper is very abrasive and can easily cut skin. Gloves were used and samples were hold as far from the disc as possible.

NMR equipment contains strong magnets and no metal object, such as scalpels used for sample preparation, should be brought to within a couple of metres of the instrument.

3.13.3 Temperature Hazards

High temperature furnaces are well insulated and many have a coolant water system, so they do not represent any danger while closed. Opening in normal conditions was undertaken at a temperature below 100 ºC with heat-resistant gloves. When the furnace needed to be opened at higher temperature (for quenching experiment), glasses with optical filters were used as a protection against radiation from the glowing hot chamber.

3.13.4 Toxic Chemicals

Most of the products and materials used in this study were non-toxic.

Latex gloves needed to be replaced by nitrile gloves to manipulate the aluminium powder as it was found to penetrate through the former. Dust masks were used for manipulation of powders, particularly aluminium which is very light and floats in air easily. Solvent manipulation was made under a fume hood.

When fabricating Sialon composites by carbothermal reduction, a non-negligible amount of carbon monoxide was formed. A carbon monoxide detector was used at all time and tested regularly.

Technical and safety training was undertaken for safe operation of the following machines: Accutom-5 diamond saw, Shimadzu Sald-2001 Particle Size Distribution Analyser, Instron 1225 universal tester, Vickers Indenter, Struers, NMR equipment, both X-ray diffractometers and both SEMs.

3.14 Chapter Three Bibliography

1. Gao, L., Li, J., Kusunose, T., and Niihara, K., *Preparation and properties of TiN-Si_3N_4 composites*. J Eur Ceram Soc, 2004, **24**[2], pp. 381-86.
2. Krnel, K., Maglica, A., and Kosmac, T., *β-Sialon/TiN nanocomposites prepared from TiO_2-coated Si_3N_4 powder*. J Eur Ceram Soc, 2008, **28**[5], pp. 953-57.
3. Van de Hulst, H.C., In *Light Scattering by Small Particles*. Ed. by John Wiley & Sons, New York, 1981, pp. 115.
4. Krautkkrämer, J. and Krautkkrämer, H., *Measurement of Acoustic Velocity.* In Ultrasonic Testing of Materials - Translation of the Second Revised German Edition 1969, ed. by Springer International Student Edition, Berlin, pp. 460-66.
5. Brown, I.W.M., Barris, G.C., Sheppard, C.M., Trompetter, W.J., and Vickridge, I.C., *Use of IBA techniques for the measurement of oxidation processes in sialon ceramics*. Mod Phys Lett B, 2001, **15**[28-29], pp. 1305-13.
6. Software *TEAM 3.1*, EDAX. USA.
7. Goldstein, J.I., Newbury, D.E., Echlin, P., Joy, D.C., Romig, A.D.J., Lyman, C.E., Fiori, C., and Lifshin, E., In *Scanning Electron Microscopy and X-Ray Microanalysis Second Edition*. Ed. by P. Press, New York and London, 1992, pp. 405-413.
8. Anstis, G.R., Chantikul, P., Lawn, B.R., and Marshall, D.B., *A Critical Evaluation of Indentation Techniques for Measuring Fracture Toughness: I, Direct Crack Measurements*. J Am Ceram Soc, 1981, **64**[9], pp. 533-38.
9. ASTM D3967-08, Standard Test Method for Splitting Tensile Strength of Intact Rock Core Specimens, International, A., West Conshohocken, PA, 2008, www.astm.org.

Chapter Four: Nitridation of a Sialon Composite and the Role of Sintering Additives

This chapter examines the effect of a range of additives on the nitridation and sintering of β-Sialon composite bodies. It is proposed that the use of β-Sialon in Sialon composites instead of other Sialon phases will improve strength and fracture toughness, leading to improvement in thermal shock resistance.

To fabricate β-Sialon ceramics the commonly used route is to mix and sinter appropriate mixtures of the four compounds at the corners of the Sialon behaviour diagram – SiO_2, Al_2O_3, AlN and Si_3N_4 (See Figure 4.1). These are refractory, strongly covalently bonded materials which must be heated to very high temperature (> 1750 ºC) to react to form Sialon. The use of silicon metal powder, which forms Si_3N_4 when heated under nitrogen, reduces the temperature required to form Sialon to 1400 ºC. The use of AlN brings problems for commercial production: it forms toxic ammonia when wet making it challenging to use and store, as well as being expensive. The use of SiO_2 introduces oxygen which, if not balanced by AlN, must be removed by other means such as carbothermal reduction, also inconvenient as it produces significant amounts of carbon monoxide as a waste and may leave residual carbon in the ceramic body.

To achieve fully dense Sialon bodies with improved mechanical properties, rigorous sintering techniques are required, including the use of chemical additives to assist both nitridation and sintering.

In this study, Sialon formulations have been designed from two component mixtures of silicon and alumina (Al_2O_3). The effect of a range of additives on synthesis and sintering has been explored. The additives can be divided into three groups:

- Nitridation additives which improve the yield and the rate of the reaction,
- Sintering aids,
- Additives that improve resistance to thermal shock.

4.1 Methods and Procedures

4.1.1 Compositions

Sialon composites have been prepared with a target composition situated on the behaviour diagram diagonal Si_3N_4-Al_2O_3 located vertically above the β-Sialon z = 2 composition. This particular composition has been chosen from a previous study[1] because it gives the best reaction yield and mechanical properties for this two-component Sialon composite. The location of this composition, labelled A on the Sialon behaviour diagram is illustrated in Figure 4.1.

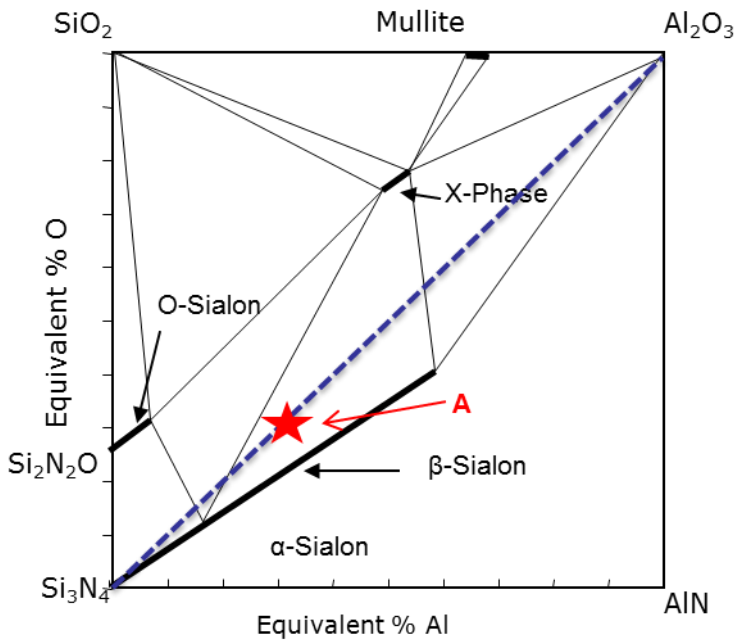

Figure 4.1: Starting composition A on the Sialon behaviour diagram at 1750 ºC.

A wide range of additives has been added to this basic composition: Yttrium Aluminium Garnet (YAG), added as single oxides Al_2O_3 and Y_2O_3, is a common sintering aid for Sialons[2-4]; boron nitride (BN) was added in different amounts to lower the elastic modulus. At the same time, nitridation additives were tested including Fe_2O_3, TiO_2, ZrO_2, $Ca(OH)_2$, ground pre-sintered β/O-Sialon, $Al(OH)_3$ (gibbsite) and, a refractory calcium aluminate cement based on $CaAl_2O_4$ (CA-25C, 'Casting' grade). The latter is a high purity calcium aluminate cement containing about 80 % Al_2O_3 and 18 % CaO. The Casting grade of this cement has been used to improve the strength of the green samples.

The different compositions used are displayed in Table 4.1.

Sample number	Sintering Aid (wt% - vol%)	BN (wt% - vol%)	Additive (wt% - vol%)
1	-	1.5 wt% - 2 vol%	-
2	13 wt% - 9.4 vol% YAG	1.5 wt% - 2 vol%	-
3	5 wt% - 3.3 vol% YAG	-	-
4	5 wt% - 3.3 vol% YAG	1.5 wt% - 2 vol%	-
5	5 wt% - 3 vol% YAG	9 wt% - 10 vol%	-
6	5 wt% - 3 vol% YAG	18 wt% - 18.7 vol%	-
7	5 wt% - 3 vol% YAG	9 wt% - 10 vol%	0.7 wt% - 0.3 vol% Fe as Fe_2O_3
8	5 wt% - 3 vol% YAG	9 wt% - 10 vol%	1.5 wt% - 0.6 vol% Fe as Fe_2O_3
9	5 wt% - 3 vol% YAG	9 wt% - 10 vol%	2.9 wt% - 1.1 vol% Fe as Fe_2O_3
10	5 wt% - 3 vol% YAG	9 wt% - 10 vol%	5 wt% - 2.2 vol% TiO_2
11	5 wt% - 3 vol% YAG	9 wt% - 10 vol%	5 wt% - 2.2 vol% $Ca(OH)_2$
12	5 wt% - 3 vol% YAG	9 wt% - 10 vol%	5 wt% - 2.2 vol% $Ca(OH)_2$ from CA-25C
13	5 wt% - 3 vol% YAG	9 wt% - 10 vol%	5 wt% - 1.8 vol% ZrO_2
14	5 wt% - 2.9 vol% YAG	9 wt% - 10 vol%	10 wt% - 6.4 vol% ground pre-sintered Sialon
15	5 wt% - 3 vol% YAG	9 wt% - 10 vol%	Heated $Al(OH)_3$ as a raw material
16	5 wt% - 3.3 vol% YAG	1.5 wt% - 2 vol%	5 wt% - 2.2 vol% $Ca(OH)_2$ from CA-25C
17	5 wt% - 3.3 vol% YAG	4 wt% - 4.9 vol%	5 wt% - 2.2 vol% $Ca(OH)_2$ from CA-25C
18	5 wt% - 3.3 vol% YAG	5.8 wt% - 6.8 vol%	5 wt% - 2.2 vol% $Ca(OH)_2$ from CA-25C
19	5 wt% - 3.3 vol% YAG	7.7 wt% - 8.8 vol%	5 wt% - 2.2 vol% $Ca(OH)_2$ from CA-25C
20	5 wt% - 3.3 vol% YAG	10.6 wt% - 11.7 vol%	5 wt% - 2.2 vol% $Ca(OH)_2$ from CA-25C

Table 4.1: Initial sample formulations as a percentage of the Sialon final mass.

The standard green mix was composed of silicon, alumina and yttrium oxide equivalent to 5 wt% of YAG in the final Sialon (sample 3 in Table 4.1).

Four major composition families were investigated (all added compound masses including those in Table 4.1, are expressed as a percentage of the final Sialon mass):

- Samples 1 and 2 were prepared to examine the effect of YAG addition for a fixed 1.5 wt% BN content.

- Samples 3 to 6 use standard 5 wt% YAG and examine variations in BN content.
- Samples 7 to 15 use standard 5 wt% YAG and 9 wt% BN and examine a range of nitridation additives.
- Samples 16 to 20 use standard 5 wt% YAG and 5 wt% $Ca(OH)_2$ as CA-25C and examine the effect of a more defined range of BN addition.

4.1.2 Powder Preparation and Fabrication of Test Specimens

Powder mixes were prepared as described in Sections 3.2.1 and 3.2.3 using silicon nitride milling balls and IPA for the milling.

Two different types of discs were pressed: approximately 1 g samples of 10 mmØ and approximately 3 g samples of 20 mmØ. Each pellet was uniaxially pressed to 15 MPa and held at this pressure for around 30 seconds. The pellets were transferred to latex balloons and cold isostatically pressed in ethylene glycol at 40 MPa for 60 seconds.

Samples for thermogravimetric analysis (TGA) were pressed in the uniaxial press but were not CIPped.

Further details of the powder preparation and fabrication methodology are expanded in Chapter 3.

4.1.3 Nitridation and Sintering Technique

Firings were carried out in a high temperature graphite furnace (See Figure 3.6.f) using a graphite crucible with a nitrogen atmosphere at a flow rate of 0.5 $L.min^{-1}$ per gram of sample.

The nitridation firings create the Sialon phase chemistry and can also assist densification of the sample. They were carried out with a schedule including two holds at 1200 ºC and 1350 ºC to better understand the reaction behaviour at intermediate firing temperatures.

The samples were nitrided at 1400 ºC on a powder bed layer containing O and β-Sialon in a ratio of 1:2 and, if included in the sample, 10 % of the total weight of BN.

The nitridation schedule was programmed to be 120 minutes to 1200 ºC, hold 4 hours; 30 minutes to 1350 ºC, hold 4 hours; 10 minutes to 1400 ºC, hold 4 hours; then allowed to cool to ambient temperature at a maximum rate of 10 $ºC.min^{-1}$.

The sintering schedule was designed to reduce the porosity and complete the densification. The samples were covered by the O/β Sialon powder bed (designed to repress SiO loss) that also included 10 wt% BN to inhibit bed sintering.

The sintering schedule was programmed to be 160 minutes to 1600 ºC, hold 6 hours; or 170 minutes to 1700 ºC, hold 6 hours; then cooling to ambient temperature at a maximum rate of 10 ºC.min^{-1}.

Firing schedules are represented in Figure 4.2. The cooling down phase was actually slower than this trend line below approximately 600 ºC due to the thermal mass of the furnace.

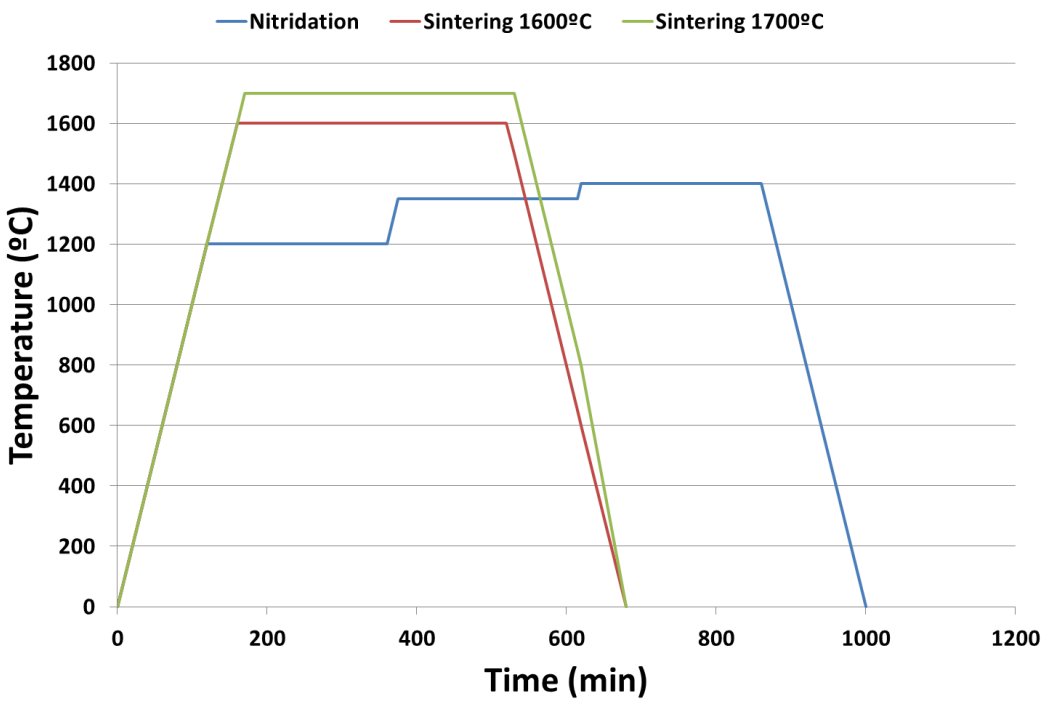

Figure 4.2: Nitridation and sintering schedules.

Further details of the nitridation and sintering methodology are expanded in Section 3.3.3.

4.1.4 Material Property Measurement

The property measurement methodology précised in this section provides only the experiment details specific to Chapter 4.

Phase composition by XRD was analysed using the Bruker D8 Advance diffractometer for bulk samples and the Philips PW1700 series diffractometer for powder mixes or very thin bulk samples (H < 3 mm). Spectra were collected between 10 and 80º 2θ.

^{11}B MAS NMR spectra were obtained at 11.7 T with a Bruker Avance III500 spectrometer using a 4 mm Doty Scientific XC probe at a spinning speed of approximately 17 kHz. Spectra were collected at a frequency of 160 MHz, at a spectral width of 300 kHz, using a 1 μs π/8 pulse for solution, an acquisition rate of 0.014 s and a delay of 1 s. The ^{11}B MAS NMR spectra were referenced to $BF_3.Et_2O$.

The Young's modulus was estimated using Equation 3.7 or 3.9 depending on the success of transverse wave measurement.

Other measurements, such as porosity and density, SEM sample preparation, compressive strength, and fracture toughness and hardness, were conducted as described in Chapter 3.

4.2 Results and Discussion

4.2.1. Phase Development

4.2.1.1 Yttrium Phase Behaviour

The phase composition of sample 2 (13 wt% YAG, 1.5 wt% BN) was observed by XRD. This sample contains about three times more yttrium than the standard amount so as to reveal the yttrium phase XRD peaks above the background. Every firing followed the nitridation schedule (See Figure 4.2), and the composition was observed every 50 ºC between 1000 and 1400 ºC. A new sample was used for every firing. Figure 4.3 shows the crystalline composition of sample 2 on its surface and in its body as a function of temperature. Selected XRD patterns that support this analysis are displayed in Annex IV.

The surface and the body of the sample react very differently. In the first reaction step, yttria (Y_2O_3) reacts with the (impurity) silica (SiO_2) on the surface of the silicon particles to form yttrium silicate (Y_2SiO_5) at 1050 ºC on the sample surface and at 1100 ºC in the body, probably because of thermal diffusion through the sample. By 1100 °C crystalline yttria is no longer detectable by XRD.

Second, on the surface of the sample, the yttrium silicate reacts at 1150 ºC with more silica to form yttrium disilicate ($Y_2Si_2O_7$) in its α form which transforms to a higher temperature form above 1200 ºC[5]. These two first reactions require a high amount of silica. It is unlikely that free silica would be present in such proportions in the silicon introduced in the green mix (98 % Si). However the long processing applied to the materials before firing could potentially cause additional oxidation of the silicon and provide enough silica to feed these reactions.

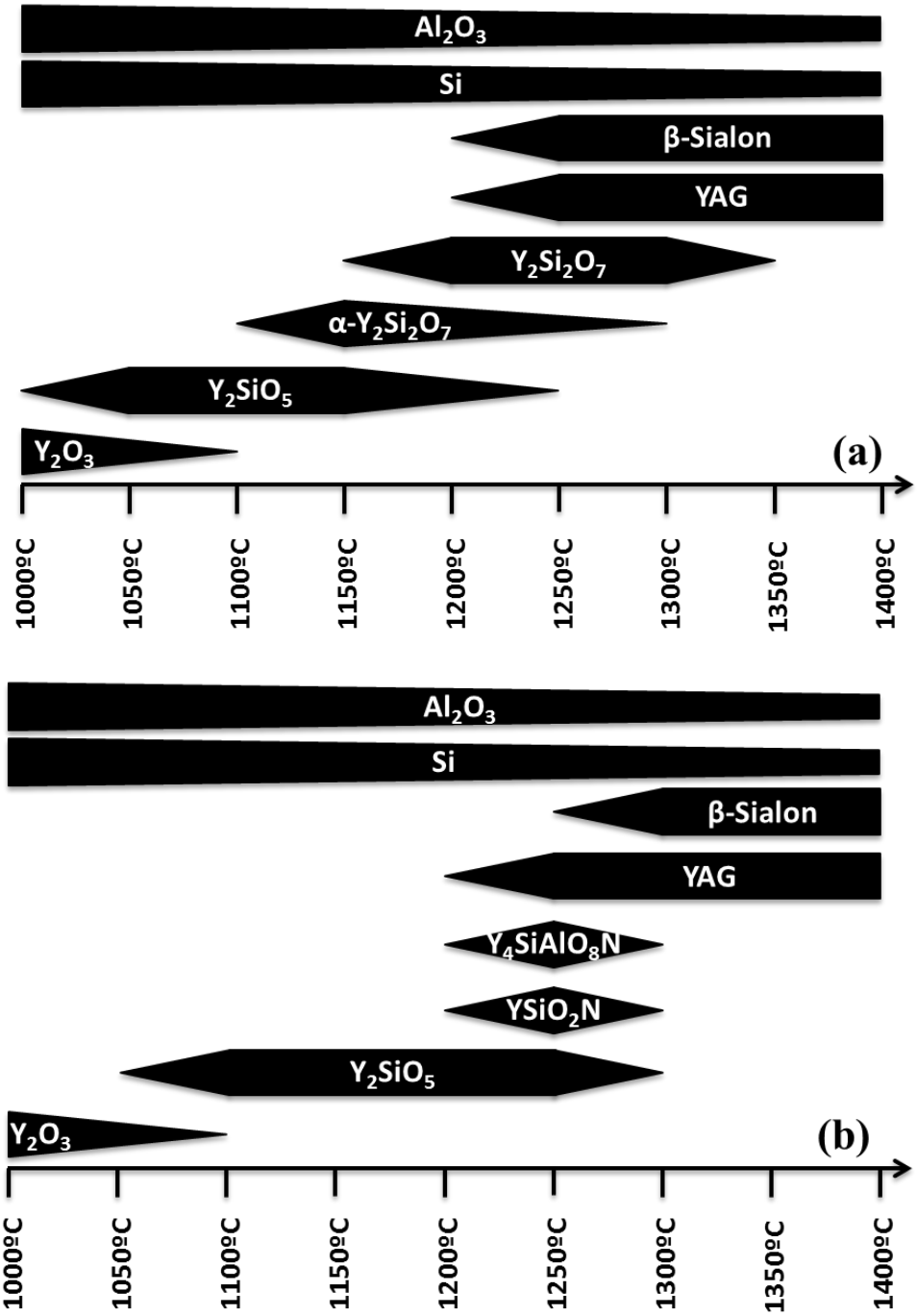

Figure 4.3: Crystalline phase composition of sample 2 (a) on the surface and, (b) in the body.

In the sample body, the yttrium silicate starts reacting at 1250 ºC to form yttrium silicon oxynitride ($YSiO_2N$), often denoted as N-wollastonite[6]. There is no evidence that yttrium disilicate (seen distinctively on the surface of the fired materials) is formed in the sample body. The yttrium silicate could be reacting with either Si_2N_2O formed from the reactants (path a) or silicon and the nitrogen atmosphere (path b) but the latter path may be more likely as this does not require additional free silica to proceed and the Si_2N_2O phase does not appear

in the XRD pattern. Silicon and nitrogen are in such large excess in the reaction environment that the change in their concentration would not be detected by XRD. It is proposed that the $YSiO_2N$ phase immediately reacts with alumina at 1250 ºC to form Y_4SiAlO_8N. This yttrium aluminium silicon oxynitride phase is a possible composition variation of J−Phase[7] ($Y_4Si_{2-x}Al_xO_{7+x}N_{2-x}$ with $x \leq 2$).

Overall, YAG is formed at 1250 ºC in two independent processes, as summarised in these two sets of equations:

On the sample surface:

$$Y_2O_3 + SiO_2 \xrightarrow{1050\ °C,\ N_2} Y_2SiO_5$$

$$Y_2SiO_5 + SiO_2 \xrightarrow{1150\ °C,\ N_2} \alpha - Y_2Si_2O_7$$

$$\alpha - Y_2Si_2O_7 \xrightarrow{1200\ °C - 1300\ °C,\ N_2} Y_2Si_2O_7$$

$$3Y_2Si_2O_7 + 5Al_2O_3 \xrightarrow{1250\ °C,\ N_2} 2Y_3Al_5O_{12} + 6SiO_2$$

In the sample core :

$$Y_2O_3 + SiO_2 \xrightarrow{1100\ °C,\ N_2} Y_2SiO_5$$

Path a :

$$3Si + SiO_2 + 2N_2 \xrightarrow{1250\ °C,\ N_2} 2Si_2N_2O$$

$$Y_2SiO_5 + Si_2N_2O \xrightarrow{1250\ °C,\ N_2} 2YSiO_2N + SiO_2$$

Path b :

$$2Y_2SiO_5 + 3Si + 2N_2 \xrightarrow{1250\ °C,\ N_2} 4YSiO_2N + SiO_2$$

$$8YSiO_2N + Al_2O_3 \xrightarrow{1250\ °C,\ N_2} 2Y_4SiAlO_8N + 3Si_2N_2O$$

$$6Y_4SiAlO_8N + 17Al_2O_3 \xrightarrow{1250\ °C,\ N_2} 8Y_3Al_5O_{12} + 3Si_2N_2O$$

The precipitation of β-Sialon starts at 1250 ºC on the surface and at 1300 ºC progresses to the sample core due to the nitrogen diffusion through the sample. The calculated z-value (approximately 2.35 on the surface and 2.55 in the core - see Annex III) is stable until 1400 ºC then drops homogenously through the sample (to approximately 1.0 on the surface and 1.2 in the core). Figure 4.4 shows backscattered electron images of the white grains of yttrium phases dispersed through the samples. This analysis is supported by the EDS data

provided in Figure 4.5. At 1050 ºC (Figure 4.4a) and at 1200 ºC (Figure 4.4b), larger grains of alumina and silicon can also be seen. At 1400 ºC (Figure 4.4c), the large remaining grains of alumina and mostly silicon are surrounded by small needle shaped grains of β-Sialon that can be observed in the white yttrium phase. This last sample is also very porous as the low CIP pressure (40 MPa) and the nitridation firing temperature are insufficient to obtain a very dense material.

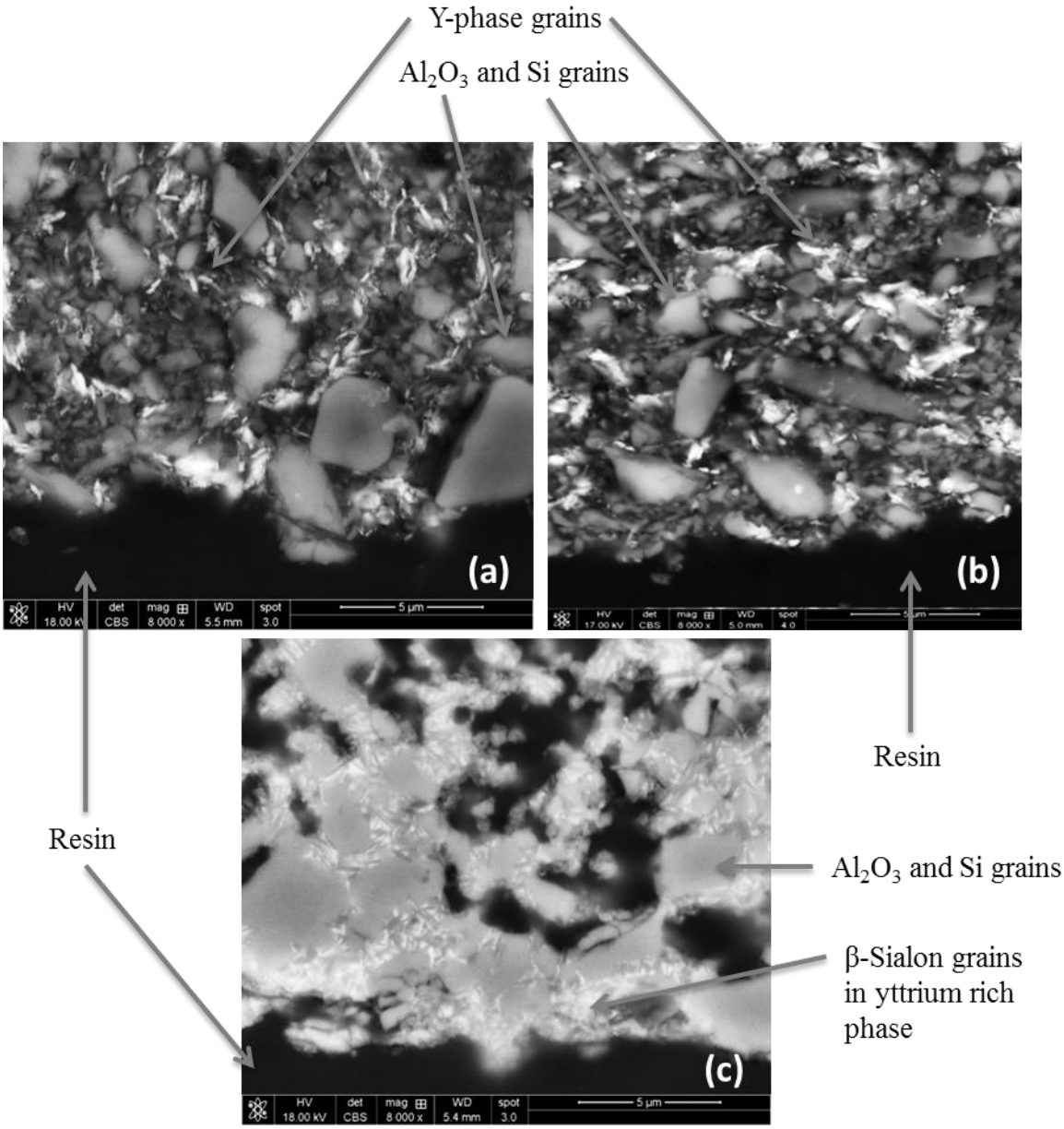

Figure 4.4: SEM backscattering micrographs of the sample cross section at (a) 1050 ºC, (b) 1200 ºC and, (c) 1400 ºC. Scale bars = 5 µm.

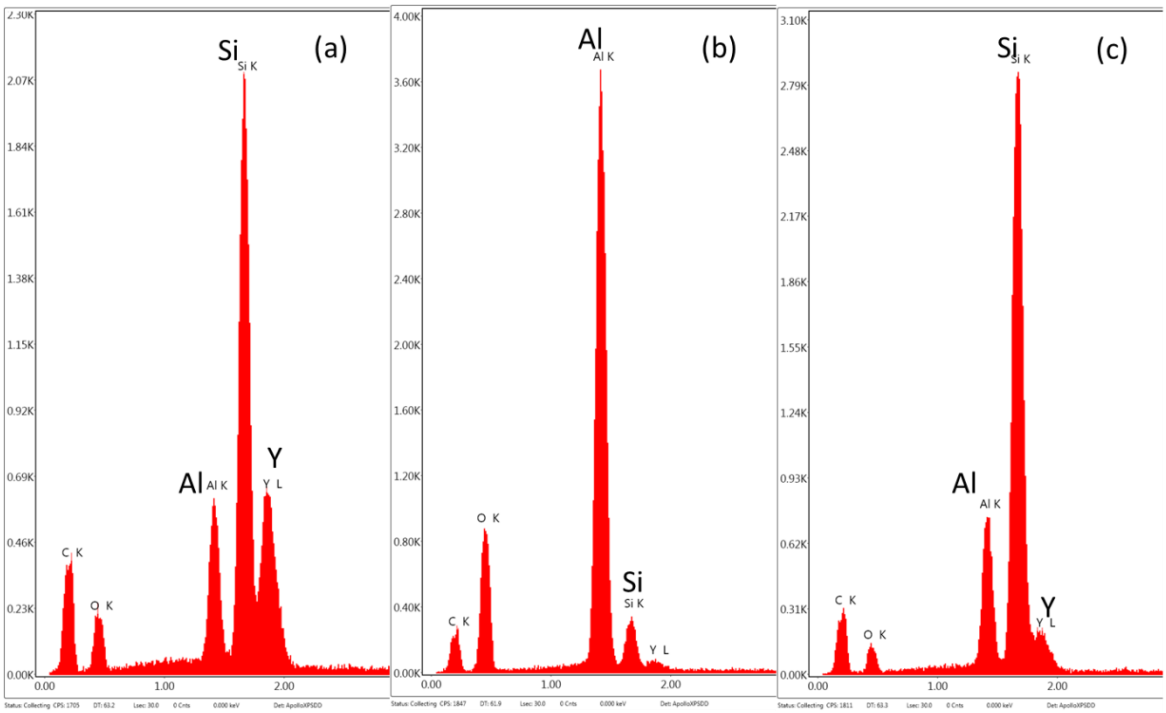

Figure 4.5: EDS analysis of (a) white grains or phase, (b) and (c) larger grains seen in Figure 4.4.

After nitridation the amount of β-Sialon in samples with yttrium oxide additives is higher than in sample 1 (no YAG). Supporting XRD data is displayed in Annex IV. As Brown et al[8] also observed, the reactions with Y_2O_3 break up the silicon oxynitride (Si_2N_2O) and silica skin on the surface of the silicon particles allowing easier access for the nitrogen and enhancing the nitridation reaction.

4.2.1.2 Boron Nitride Behaviour

In this section, it is shown that XRD and EDS analytical methods are not suitable to characterise the coordination and phase behaviour of boron nitride. First, the β-Sialon and BN diffract X-rays at very similar angles (31.2º for the boron nitride main peak and 31.6º for β−Sialon). Second, boron is too light an element to be quantitatively measured by EDS. However, MAS-NMR is a very suitable method for observing the coordination chemistry and short range ordering behaviour of boron materials[9]. ^{11}B is a quadrupolar nucleus with a natural abundance of 80.42 % and a relaxation rate sufficient for the fast acquisition of spectra. The BN used in this study is an hexagonal boron nitride powder (minimum of 99 % BN) from Shenzhen Chinary Co., Ltd. Its main impurity, present with a maximum of 0.1 %, is B_2O_3. The observed spectra are displayed in Figure 4.6.

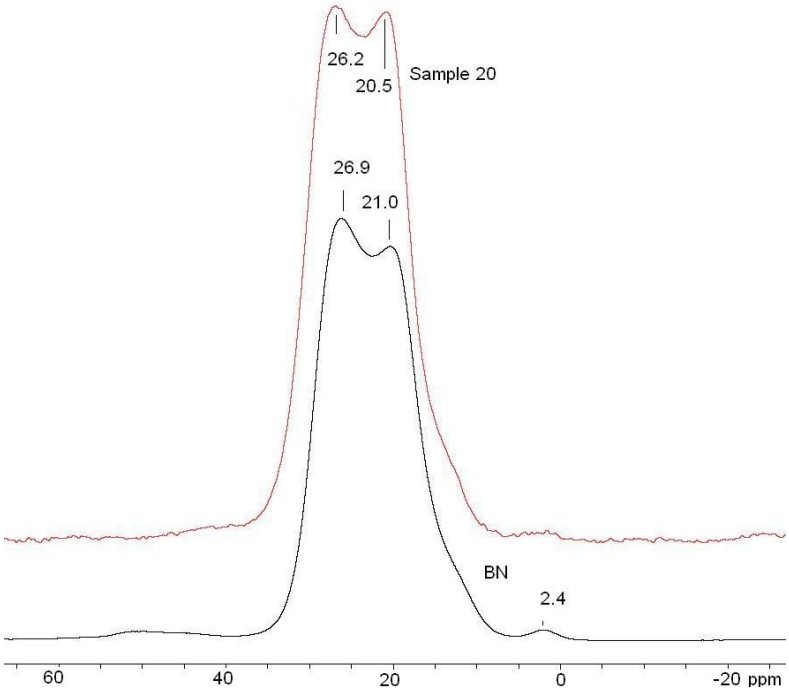

Figure 4.6: ^{11}B MAS NMR spectra of the raw material BN and sample 20 (10.6 wt% BN).

The ^{11}B NMR spectra of the BN powder shows a quadrupolar peak at 26.9-21.0 ppm which corresponds to hexagonal BN[9], and a very small peak at 2.4 ppm which corresponds to boron in a tetrahedral environment (B_2O_3).

Sample 20 was selected for study because it has a high content of BN (10.6 wt%) which improves the sensitivity of the analysis. The quadrupolar peak corresponding to hexagonal BN is present at 26.2-20.5 ppm. Since these peaks are not shifted or modified compared to the BN raw material, it can be concluded that the boron coordination is unchanged in the ceramic, implying that the BN remains unreacted. It is likely to be sited at the Sialon grain boundaries rather than being present in the amorphous phase, where it would most likely react because the boron is a strong glass former. The tetrahedral peak at 2.4 ppm is barely detectable in the fired ceramic.

4.2.1.3 Effect of BN on Sialon Nitridation

An initial experiment aimed to find the approximate BN content which would be acceptable. Samples with increasing BN content were made to test the effect of this material. Samples 3, 4, 5 and 6 contained respectively 0, 1.5, 9 and 18 wt% of BN as a percentage of the final Sialon mass. They were also designed to contain 5 wt% of YAG, added as yttrium oxide and alumina.

Each sample was analysed by XRD. Quantitative analysis of these results revealed the amount of each phase in the ceramic. The compositions achieved were not exactly as expected, with residual corundum in each sample fired at 1600 ºC, while some samples fired at 1700 ºC show less common Sialon phases such as X-Phase or 15-R (an AlN polytype, see Table 2.1).

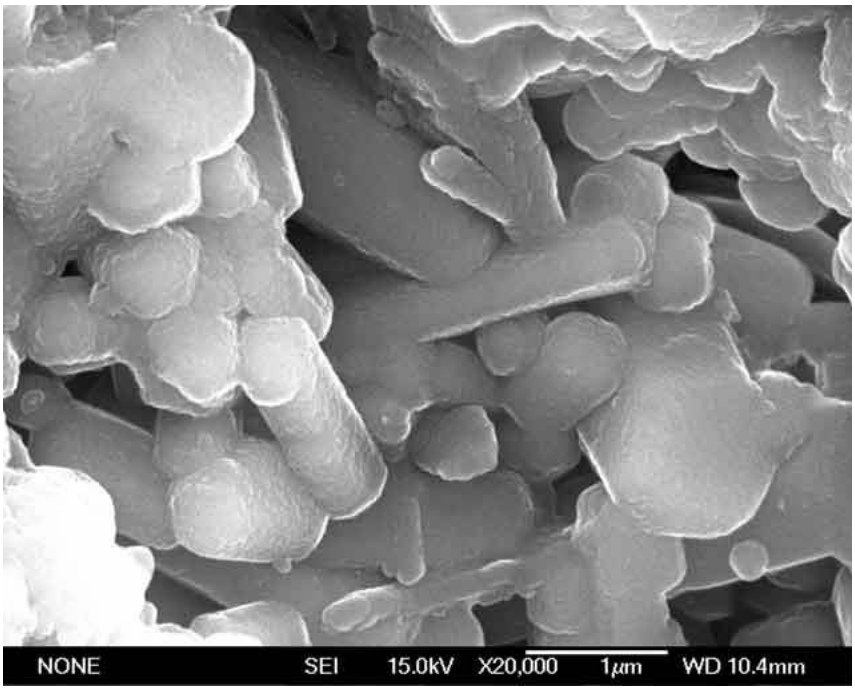

Figure 4.7: SEM micrograph of sample 5 fired at 1600 °C showing β-Sialon grains exposed in an open pore.

SEM analysis clearly confirms the presence of hexagonal β-Sialon grains fused together in these samples. The micrograph in Figure 4.7 shows an example of fused β-Sialon grains. α−Sialon can also develop a hexagonal grain structure[10] but this phase does not appear in the XRD pattern.

The observed z-values (see Table 4.2) for samples 3 to 6 sintered at 1600 ºC range from 0.8 to 1.6, lower than the target value of 2.0, whereas the samples sintered at 1700 ºC gave higher values (2.5−3.7). These observations can be explained by the original composition calculation which has been made on the basis of the behaviour diagram at 1750 ºC whereas the sintering reactions here have been undertaken at 1600 ºC or 1700 ºC. Moreover, for these last samples the higher z-values can also be understood in relation to loss of SiO vapour from the samples at the higher sintering temperature (1700 ºC), in spite of the presence of a protective powder bed.

Sample	Measured z-value at 1600 ºC	Measured z-value at 1700 ºC
3 (5 wt% YAG)	1.55	3.49
4 (5 wt% YAG + 1.5 wt% BN)	1.55	3.68
5 (5 wt% YAG + 9 wt% BN)	1.31	2.5
6 (5 wt% YAG + 18 wt% BN)	0.82	2.5

Table 4.2: Measured z-values for samples 3 to 6 sintered at 1600 ºC and 1700 ºC.

In general, the higher the BN content, the lower the β-Sialon yield and the higher the residual corundum content (see Table 4.3). Increasing BN reduces the reaction yield, probably because of the physical presence of the relatively inert BN which impedes interparticle contact during sintering. The inhibition of sintering results in the sintered bodies having a very high surface area with high SiO loss and high corundum content.

Sample	Composition at 1600 ºC				Composition at 1700 ºC	
	β-Sialon	Corundum	X-Phase	15-R	β-Sialon	Corundum
3 (5 wt% YAG)	100 %	0 %	0 %	0 %	87 %	13 %
4 (5 wt% YAG + 1.5 wt% BN)	82 %	0 %	0 %	18 %	83 %	17 %
5 (5 wt% YAG + 9 wt% BN)	68 %	0 %	32 %	0 %	74 %	26 %
6 (5 wt% YAG + 18 wt% BN)	93 %	7 %	0 %	0 %	70 %	30 %

Table 4.3: Samples 3 to 6 composition by XRD after sintering at 1600 ºC and 1700 ºC.

4.2.1.4 Nitridation Additives

In order to test different additives to improve the Sialon synthesis, the composition with silicon, alumina, 5 wt% of YAG and 9 wt% BN (sample 5) was used as a reference.

The materials added to this starting composition were oxides of calcium, titanium, zirconium, iron, a refractory cement based on calcium hydroxide (CA-25C, see Section 4.1.1 for more details on this material), a mix of premade Sialon (β/O in a ratio 1:2) and the raw material gibbsite ($Al(OH)_3$) substituting for the total alumina raw material. The relevant samples are labelled 7 to 15 in Table 4.1.

After a nitridation firing at 1400 ºC with holds at 1200 ºC and 1350 ºC, the samples were analysed by XRD. Results are displayed in Figure 4.8. The nitrided samples are mainly composed of β-Sialon, O-Sialon and corundum. Two samples showed moderate amounts of X-Phase and there is also mullite present in significant quantities in the 0.7 wt% Fe and 5 wt% TiO_2 samples. The iron-containing samples were only partially reacted after nitridation and show considerable quantities of residual alumina. This is possibly due to incomplete removal of the oxide reaction skin.

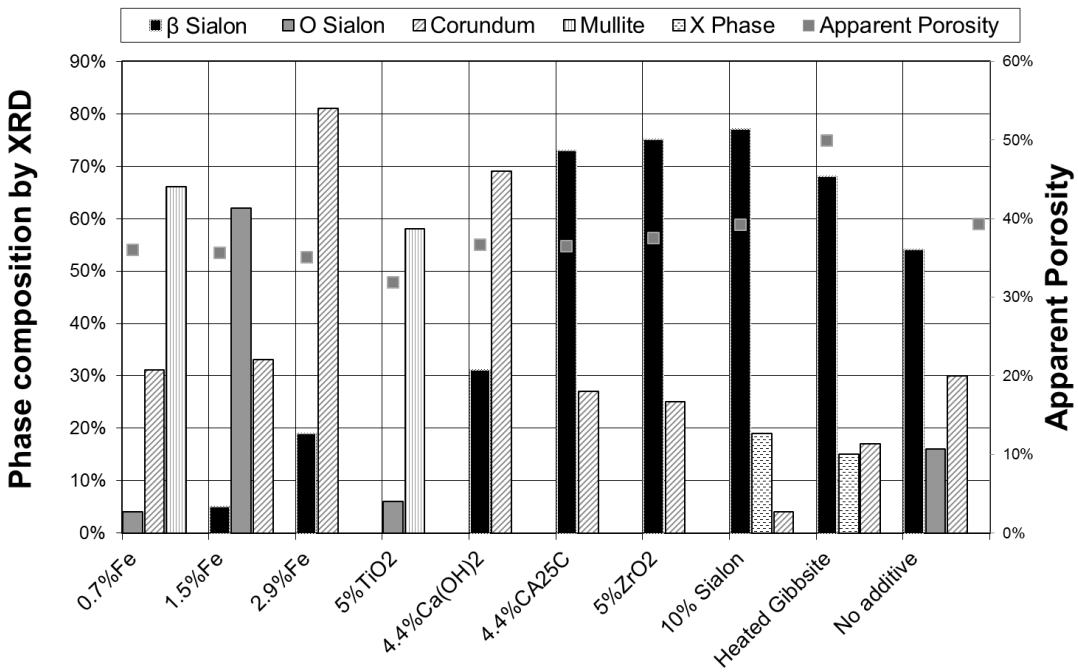

Figure 4.8: Sample compositions after a 1400 ºC nitridation for samples 5 and 7 to 15.

The addition of iron, titanium or calcium hydroxide slows the reaction down. Conversely, adding calcium aluminate cement (CA-25C) or zirconium oxide, premade Sialon or gibbsite enhances the nitridation.

Figure 4.9 shows that after sintering at 1600 ºC, all the samples are composed of β-Sialon and X-Phase in comparable amounts. The proportion of β-Sialon is higher in all the samples where additives have been used than in the sample with no nitridation additives.

The porosity and density of all the 1600 ºC sintered samples was measured using an Archimedes' immersion method (See Section 3.4). The open porosity of the samples containing calcium aluminate cement and calcium hydroxide are close to 2.5 %. The remaining samples have high open porosities of 12 to 35 %.

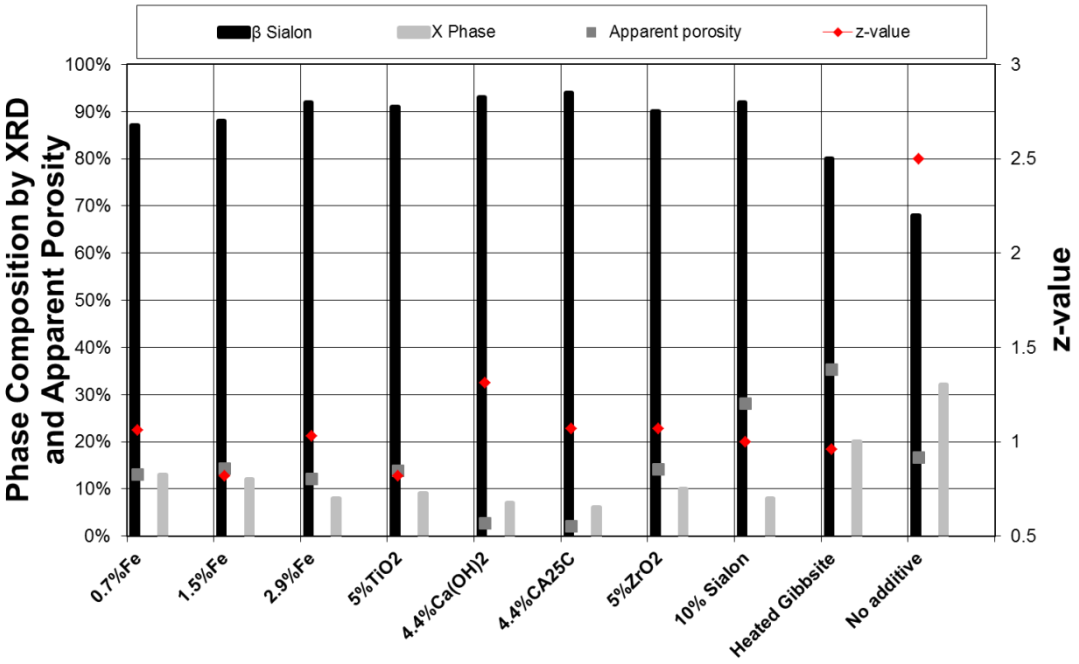

Figure 4.9: Sample compositions after a 1600 ºC sintering for samples 5 and 7 to 15.

As a result, the sample with 4.4 wt% of calcium aluminate cement was selected to study the effect of boron nitride on resistance to thermal shock. It is likely that this material will have a higher green strength before firing than the material with calcium hydroxide alone.

4.2.1.5 Modification of the Nitridation Schedule

Thermogravimetric analysis of each of the previous samples was undertaken. Figure 4.10 shows TGA traces overlaid with the nitridation schedule, showing comparable broad features with distinctive variations resulting from the choice of additive. The samples were heated to 1400 ºC with the nitridation schedule described in the Section 4.1.3 but were not pressed in the CIP, improving the ease of access of nitrogen in the sample. Consequently, the results discussed in this paragraph differ slightly from those summarised in Figure 4.8. The results were plotted as a percentage of the theoretical weight change for the Sialon formation.

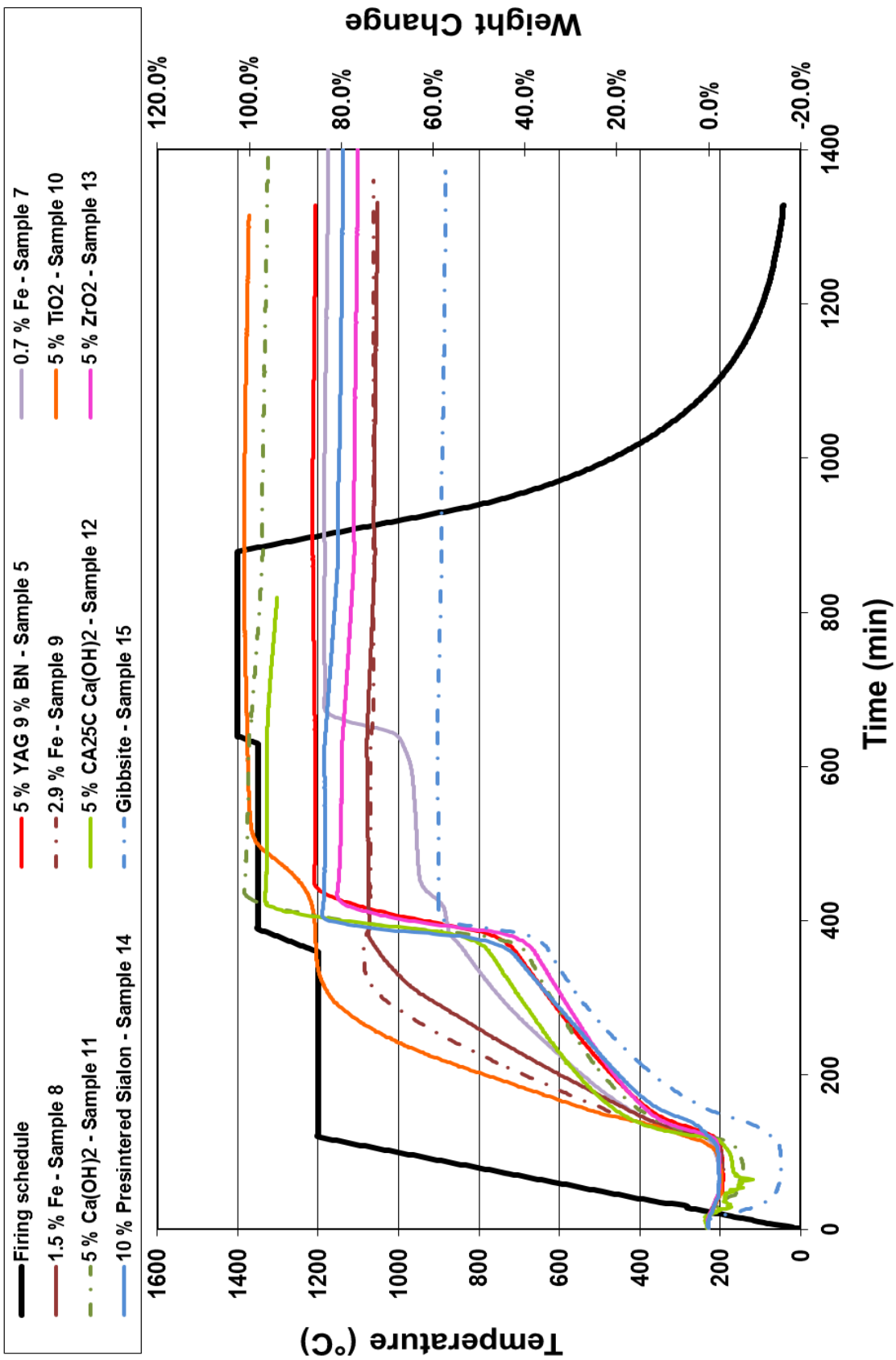

Figure 4.10: TGA results for samples 5 and samples 7 to 15.

When compared to the reference sample 5 (5 % YAG, 9 % BN, no nitridation additive), some additives increase the yield of reaction (TiO_2, $Ca(OH)_2$, and, CA-25C, respectively samples 10, 11 and 12), and some additives increase the rate of the reaction (TiO_2, Fe $\geq$ 1.5 %, $Ca(OH)_2$, CA-25C and presintered Sialon, respectively samples 8, 9, 10, 11, 12, and 14). Iron and TiO_2 additions give the best reaction yield but only the $Ca(OH)_2$ and CA-25C (samples 11 and 12) improve both the yield and the rate of the reaction, pushing the nitridation to 100 % of its theoretical weight change.

In Figure 4.10, the reactions for samples 11 and 12 (calcium additions) are completed well below the melting point of $CaAl_2O_4$, which occurs at 1605 ºC[11]. Thus, there is no direct contribution to nitridation from liquid phase formation due to $CaAl_2O_4$. However, both $CaAl_2O_4$ and free CaO (formed by decomposition of $Ca(OH)_2$ between 400-460 ºC) can react with SiO_2 present on the surface of the silicon metal powder grains to form calcium aluminosilicate and calcium silicate phases, respectively. For example, at 900 ºC, CaO reacts with SiO_2 to form β-Ca_2SiO_4[12], while the CaO-Al_2O_3-SiO_2 phase diagram[11] shows ready uptake of SiO_2 into the calcium aluminate structure at low levels, enabling liquid phase formation as low as 1335 °C. Further, at higher levels of SiO_2 uptake the wider composition region enclosing the Anorthite phase ($CaO.Al_2O_3.2SiO_2$) has liquid states at 1170 °C and 1265 °C. It is certainly a feasible scenario that these liquid phases are contributing to acceleration of the nitridation chemistry. The steep acceleration of weight gain (nitrogen uptake) shown in Figure 4.10 for samples 11 and 12 between 1200 °C and 1350 °C strongly supports this hypothesis. The mechanism by which this occurs is likely to follow a similar path to the formation of YAG and/or $Y_2Si_2O_7$ phases from Y_2O_3, namely, the surface oxide is stripped from the surface of the silicon grains, exposing fresh Si metal surfaces that react promptly with nitrogen. This mechanism has been proposed and validated for acceleration of nitridation in silicon nitride and sialon reaction bonding processes[13] and may be proposed as the likely mechanism for accelerating nitridation in these CaO–based additive systems.

4.2.1.6 Combined Effect of BN and CA-25C

In this section, all the previous results were consolidated to optimise the process variables. Samples with calcium aluminate cement and increasing BN content were prepared. Samples 16 to 20 have respectively 1.5, 4, 5.8, 7.7 and 10.6 wt% BN and 4.4 wt% of calcium aluminate cement CA-25C added as a percentage of the Sialon ceramic volume. They also have 5 wt% of YAG added as yttrium oxide and alumina.

The nitridation program was modified as follows: 1200 ºC was maintained for 6 hours and the hold at 1400 ºC was removed (See Section 4.2.1.5). After sintering at 1600 ºC, the samples were primarily composed of β-Sialon (≈ 90 %) with some X-Phase. The observed z−values were in the range 1.0 to 1.2, lower than the target value of 2.0. This is again potentially due to the use of the 1750 °C Sialon behaviour diagram temperature to calculate the target compositions, whereas the sintering temperature used in this study was typically 1600 ºC.

4.2.2. Mechanical Properties

4.2.1.1 Effect of BN

Samples were tested after nitridation and sintering for density, porosity, shrinkage, elastic modulus, fracture toughness and strength. This section examines the results for samples 3 to 6 sintered at 1600 ºC and 1700 ºC.

Irrespective of the sintering temperature, addition of 18 wt% BN results in very high porosity (11.3 % at 1600 ºC and 8.3 % at 1700 ºC). Moreover, the density is the highest and the porosity the lowest for the samples with 1.5 wt% (0.6 % apparent porosity) and 9 wt% (close to 0 % porosity) BN sintered at 1600 °C. The shrinkage is independent of the BN content.

After the porosity measurement, a sub-sample was quenched to assess resistance to thermal shock. In normal use, ceramic riser tubes in the aluminium casting industry are usually pre−heated at 300 ºC before being placed in contact with the molten aluminium at a temperature of at least 700 ºC. In the laboratory, performing a thermal shock between 700 and 300 ºC is difficult to achieve. In the case of Sialon materials, there is no phase or glass transition in the 0-700 ºC range and therefore the test can be carried out at a different temperature in this range with comparable results[14]. In these experiments, the samples were heated at 420 °C then quenched into water at ambient temperature (ΔT ≈ 400 ºC). An alternative would have been to quench them from 700 ºC which is the maximum thermal shock exposure in operation.

Figure 4.11 shows the compressive strength of quenched and unquenched samples measured by the Brazil test. It is clear that the quenching reduces the strength but even 1.5 wt% BN reduces the *loss in strength*. Increasing the amount of BN does not reduce the strength markedly or improve the resistance to thermal shock.

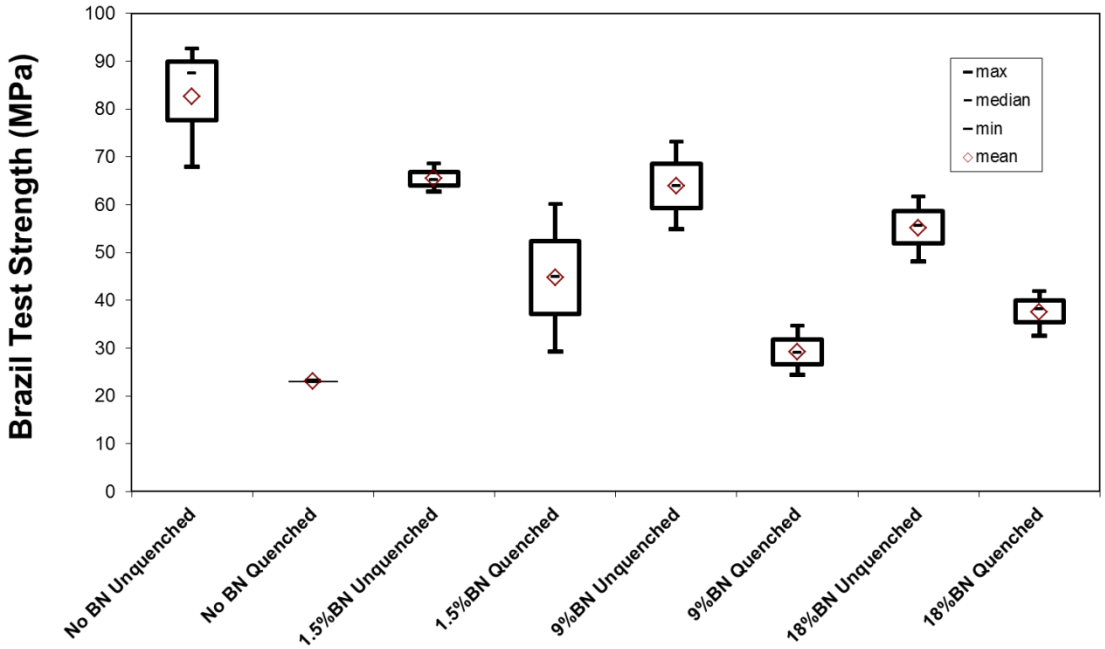

Figure 4.11: Strength of BN samples sintered at 1700 ºC.

Measurement of the elastic modulus of these samples using the ultrasonic technique (See Section 3.7) revealed that BN reduces the modulus thereby improving the elasticity. However 1.5 wt% BN is insufficient to noticeably affect the Sialon elasticity. It had been hoped that the measurement of elasticity[15] would be a rapid non-destructive test method indicator or proxy for resistance to thermal shock. It does appear that elasticity correlates with resistance to thermal shock, but the elasticity is not as sensitive as the Brazil compressive strength test. The elasticity is not sensitive to quenching and is not a good indicator of the damage created by thermal shock as revealed by the Brazil test results.

After sintering, mixes display different levels of toughness (3.73-4.49 MPa.m$^{-1/2}$). The highest value for the samples containing BN was found for the 9 wt% BN samples sintered at 1600 ºC with a toughness of 4.15 MPa.m$^{-1/2}$ but there is a large standard error in these values, due to high levels of residual porosity.

After studying these results, 9 wt% BN was selected for optimising the nitridation additives (See Section 4.2.1.4). The 18 wt% BN sample has been excluded due to its high porosity. Further, the 1.5 wt% BN containing sample was shown to have no effect on the elastic modulus. The sample with 9 wt% BN has an acceptable porosity and density and good toughness at 1600 ºC. The results suggest an optimum BN content in the middle of the range tested. A smaller range of BN content (between 1.5 and 10.6 wt%) was chosen to examine in more detail.

4.2.1.2 Combined Effect of BN and CA-25C

The same physical tests undertaken in the previous section were applied to samples 16 to 20 which contain YAG, CA-25C and a range of BN amount between 1.5 and 10.6 wt% of the final Sialon mass.

The open porosity of these samples is close to zero except for those with 10.6 wt% BN. The bulk density decreases as the BN content increases because the closed porosity increases to almost 5 % (For the calculation method, see Section 3.4). Results are displayed in Figure 4.12.

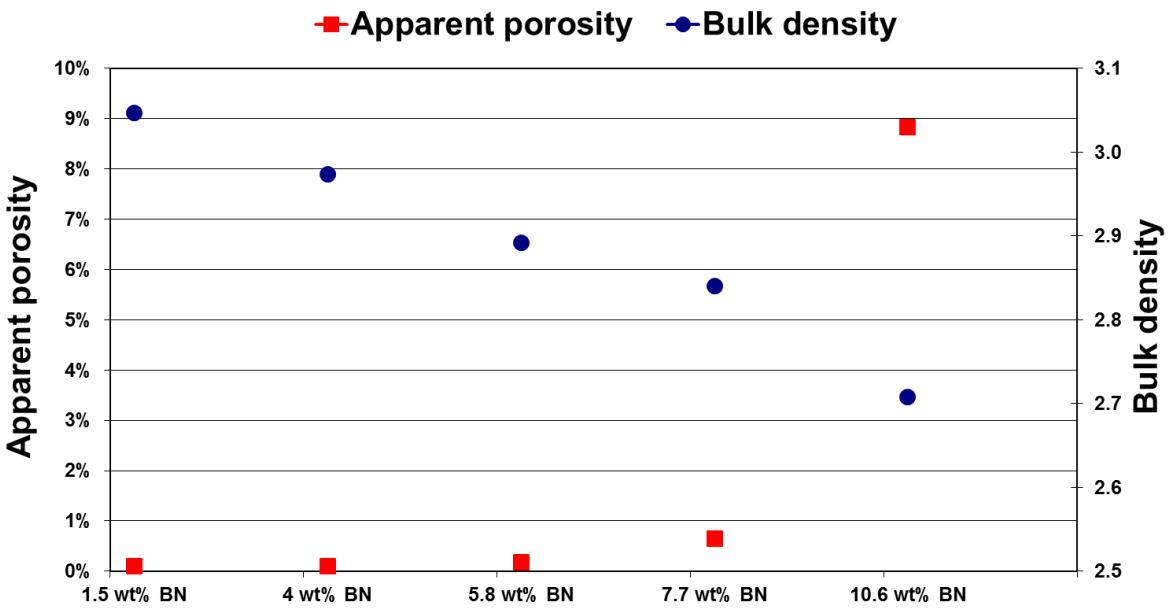

Figure 4.12: Apparent porosity and bulk density for samples 16 to 20 after sintering at 1600 ºC.

These samples were quenched from 420 ºC to allow comparison with the previous tests. The strength before quenching is higher for the samples containing the CA-25C additive than for the samples without the nitridation additive. These samples were sintered at 1600 ºC. After quenching, the strength stabilises around a value close to 30 MPa. The 10.6 wt% BN sample resists the thermal shock well but it already has a low strength before quenching. This observation is due to the increase in porosity (see Figure 4.12) which results in loss of strength, effectively through reducing the cross sectional area of the material. The other samples all display a very similar strength loss. Figure 4.13 shows the results of the Brazil strength test.

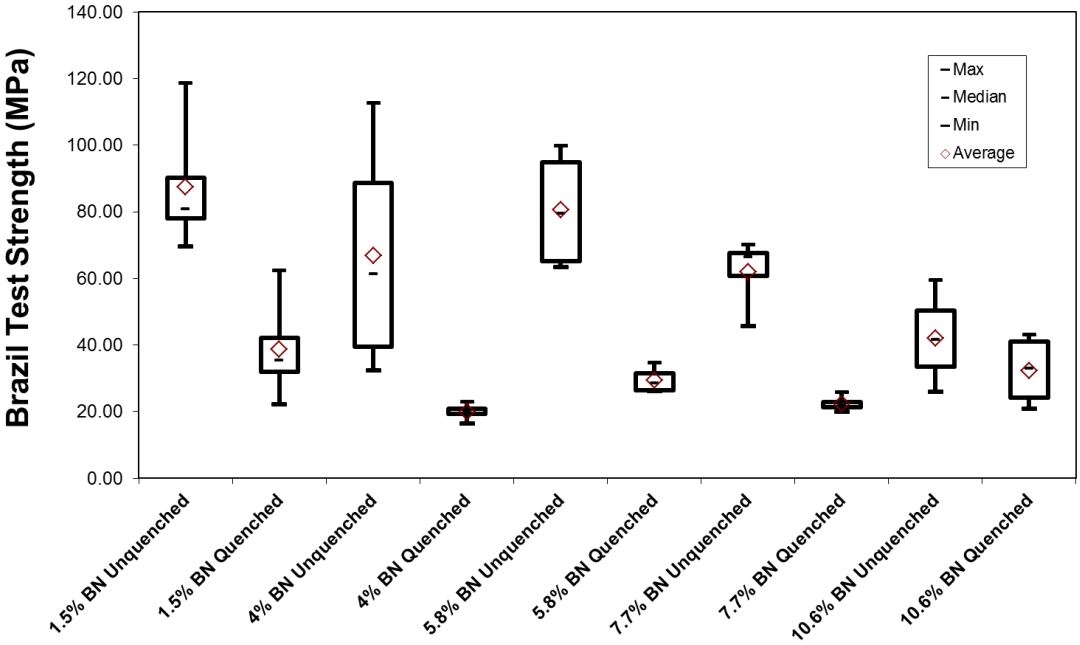

Figure 4.13: Strength of BN and CA-25C samples (16 to 20) sintered at 1600 ºC.

Figure 4.14 shows that the elastic modulus is higher after quenching for all samples except for the one containing 10.6 wt% BN, where the value is unchanged. This observation is contrary to the expectation that quenching might damage the microstructure and potentially reduce the elastic modulus, such as shown by Volkov-Husovic et al[16] in prior work on high alumina refractories or by Aksel et al[17] in studies of magnesia-spinel composites. In the present materials the microstructure is complex due to the multiphase nature of these composites. After 1600 °C firing the microstructure includes a proportion of glass phase material and the presence of the BN phase, which is probably non-wetting and only poorly bonded to the Sialon matrix, creating inherent porosity and local microcracking. Aksel et al.[17] cast doubt on the ability of ultrasonic techniques to give reliable measurements of the Young's modulus in materials containing such microstructures, suggesting a preference for more traditional mechanical test methods. A more extensive examination of this phenomenon is thus required to gain further clarity around these observations. This would include extension of the test regime to observe the impact of repeated quench cycles and potentially the use of mechanical test methods.

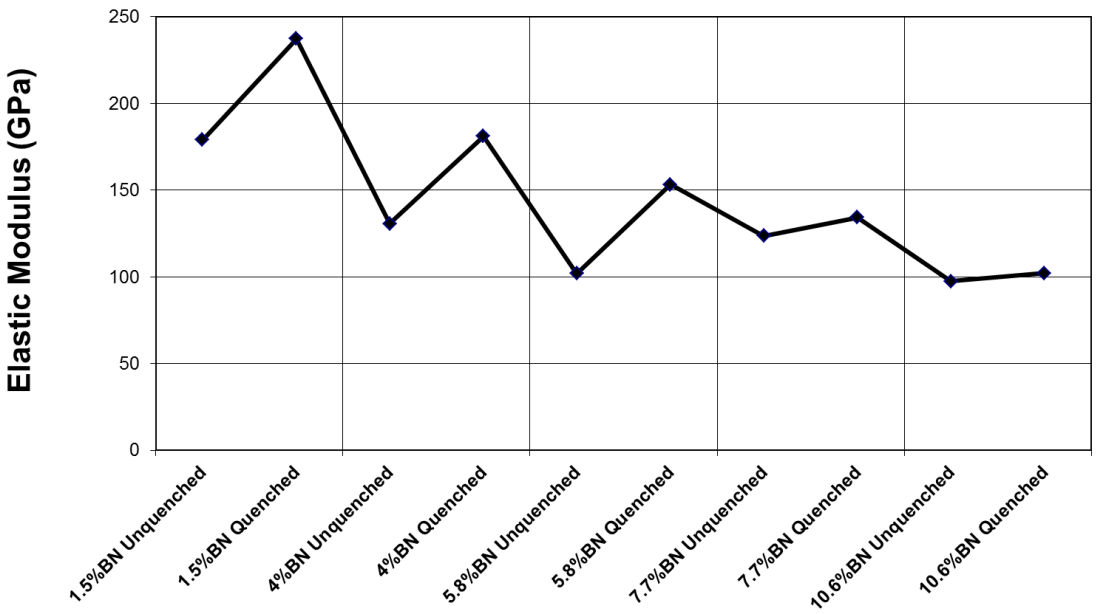

Figure 4.14: Elastic Modulus of samples 16 to 20 sintered at 1600 ºC.

The hardness and toughness tests have been undertaken on polished samples. Results are displayed in Figure 4.15. Toughness increases with the BN content to a value of 4.2 MPa.m$^{-1/2}$ which is a good toughness for these composites. Offsetting this benefit, hardness decreases to a relatively low value of 4.6 GPa.

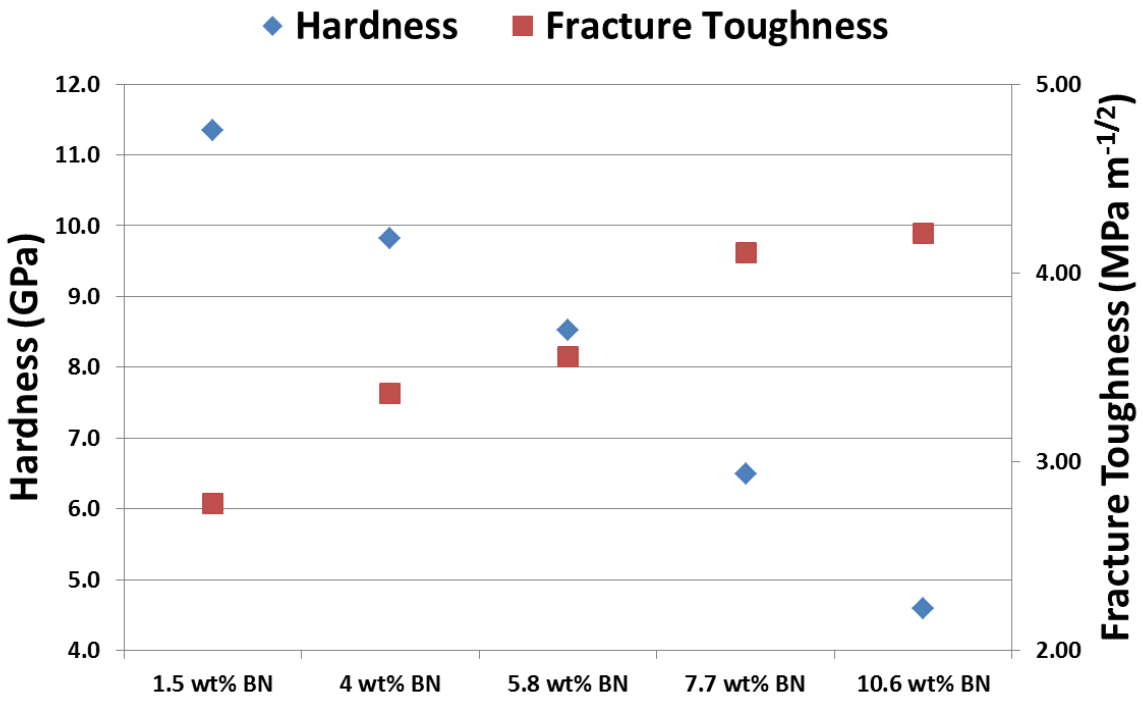

Figure 4.15: Hardness and Fracture Toughness for samples 16 to 20 sintered at 1600 ºC.

In summary, the 10.6 wt% BN composition exhibits high porosity whereas the other BN-containing compositions exhibit very low open porosity and increasing closed porosity with increasing BN content, which is beneficial for thermal shock.

The toughness is improved with increasing additions of BN but the hardness is very low for the 7.7 and 10.6 wt% BN samples. Finally, the BN has no effect on the residual strength after quenching.

4.3 Summary

The aim of this study was to improve the resistance to thermal shock of a β-Sialon composite mix by increasing its fracture toughness. To achieve this, the roles of a range of nitridation and sintering additives have been examined:

- Nitridation additives, designed to improve the yield and the rate of Sialon synthesis, included oxides of calcium, titanium, zirconium, iron, a calcium aluminate refractory cement, a mix of premade Sialon and gibbsite. The most successful nitridation aids, as measured by XRD assessment of the extent of β-Sialon formation, were (in order) 10 % Sialon, 5 % ZrO_2, 4.4 % CA-25C and heated gibbsite. All other additives repressed β-Sialon formation when compared to the 'no additive' result. The reaction mechanism of CaO materials is proposed, supported by thermodynamic data, to react in a similar path to the formation of $Y_2Si_2O_7$ from Y_2O_3 by reacting with the SiO_2 skin on the Si particles and exposing highly reactive Si metal.
- The formation of YAG in these composition and firing conditions occurs in two separate ways on the sample surface and in the sample body, including the formation of yttrium silicate, yttrium disilicate and Sialon phase such as J-Phase. The inhomogeneity observed through the samples is due to heat and nitrogen diffusion rates. The overall effect of the addition of Y_2O_3 and the formation of YAG is the enhancement of the silicon nitridation by removal of the silica skin on its surface and the formation of an intergranular liquid phase at the sintering temperature.
- The results suggest that the nitridation firing schedule could be improved by eliminating the 1400 ºC hold when nitridation additives are used. With CaO materials additives, the 1200 ºC hold could also be replaced by a slow ramp (5 ºC/min) to 1350 ºC and a one hour hold at temperature to complete the nitridation reaction.

- After sintering at 1600 ºC the samples with calcium hydroxide or calcium aluminate cement exhibited the best porosity and density, with the highest conversion to β−Sialon and the least X-sialon impurity phase.
- Boron nitride added to dense Sialons reduces both the elastic modulus and the strength. Samples with 18 wt% of boron nitride were very porous but addition of 1.5 wt% of boron nitride is insufficient to reduce the elastic modulus. BN reduces the strength of the material in proportion to the level of addition. The optimum 7.7 wt% BN addition is a compromise. Solid state ^{11}B NMR indicates that the BN remains unreacted in the fired ceramic body.
- The fracture toughness improved uniformly with BN content but the highest toughness achieved (> 4 $MPa.m^{-1/2}$) does not usefully improve the resistance to thermal shock of the Sialon.

Two key conclusions may be draw from this work. Firstly, it is clear that CaO-based additives have a very strong role in accelerating silicon nitridation processes, particularly in tandem with the use of Y_2O_3. The mechanism of enhancement is proposed to involve reaction with surface silica on the silicon grains to form calcium aluminosilicates and/or calcium silicates which remove surface silica and expose fresh silicon metal surfaces. These CaO-based additives also promote the highest degrees of densification at 1600°C and show the highest reaction conversion to β-Sialon. This may have valuable practical applications for the future design of industrial reaction bonding processes for silicon nitride and sialon composite bodies.

Secondly, the introduction of BN into the sialon composite with a goal of improving thermal shock resistance through reduction of the elastic modulus has been shown to demonstrate only partial success. Although the use of low levels of BN does in fact systematically reduce the elastic modulus as planned, the reduction in refractory performance caused by the increased porosity and reduced strength will limit the extent of industrial uptake of technologies arising from this work.

4.4 Chapter Four Bibliography

1. Tailby, J., *Tougher Sialons - Sialon Composites for Increased Fracture Toughness*. Internal Report, Industrial Research Limited, New Zealand, 2008.
2. O'Meara, C., *Crystallisation and Oxidation of Nitrogen Ceramics in the system Y-Si-Al-O-N*. PhD Thesis, Department of Physics, Chalmers Univeristy of Technology, Gotenborg, Sweden, 1988.
3. Trigg, M.B., *Metastable phase relationship in the yttrium-O'-sialon system*. Rev Chim Miner, 1985, **22**, pp. 449-55.
4. White, G.V., Barris, G.C., Sheppard, C.M., Brown, I.W.M., Yu Chen, C., and Cooper, M., *New Synthesis Routes for Sialon and Sialon-Bonded Ceramics*. J Aust Ceram Soc, 1998, **34**[2], pp. 98-103.
5. Ito, J. and Johnson, H., *Synthesis and study of yttrialite*. Am Mineral, 1968, **53**, pp. 1941-52.
6. Hampshire, S., *Oxynitride glasses, their properties and crystallisation - A review*. J Non-Cryst Solids, 2003, **316**[1], pp. 64-73.
7. Thompson, D.P., Liddell, K., Yu, Z.B., and Gao, L., *J-phase structures in the Y-Si-Al-O-N system*. Proc. 8th Conference and Exhibition of the European Ceramic Society, 2004, **264-268**[pp.1013-16.
8. Brown, I.W.M., Pompe, R., and Carlsson, R., *Preparation of Sialons by the Nitrided Pressureless Sintering (NPS) Technique*. J Eur Ceram Soc, 1990, **6**, pp. 191-200.
9. MacKenzie, K.J.D. and Smith, M.E., In *Multinuclear Solid-State NMR of Inorganic Materials*. Ed. by Pergamon Materials Series, London, 2002, pp. 420-431.
10. Liu, G., Chen, K., Zhou, H., Ning, X.G., Pereira, C., and Ferreira, J.M.F., *Fabrication of yttrium-stabilized α-SiAlON powders with rod-like crystals by combustion synthesis*. J Mater Sci, 2006, **41**[18], pp. 6062-68.
11. In *Phase Diagrams for Ceramists Figure 630*. Ed. by The American Ceramic Society, 1964, pp. 219.
12. MacKenzie, R.C., In *The differential thermal investigation of clays*. Ed. by Mineralogical Society (Clay minerals Group), London, 1957, pp. 238-270.
13. Falk, L.K.L., Pompe, R., and Dunlop, G.L., *Development of microstructure during the fabrication of Si_3N_4 by nitridation and pressureless sintering of Si:Si_3N_4 compacts*. J Mater Sci, 1985, **20**[10], pp. 3545-56.
14. Kingery, W.D., Bowen, H.K., and Uhlmann, D.R., In *Introduction to Ceramics - 16.3 Resistance to Thermal Shock and Thermal Spalling*. Ed. by Wiley-Interscience Publication, New York, 1976, pp. 822-830.
15. Damhof, F., Brekelmans, W.A.M., and Geers, M.G.D., *Experimental analysis of the evolution of thermal shock damage using transit time measurement of ultrasonic waves*. J Eur Ceram Soc, 2009, **29**[8], pp. 1309-22.
16. Volkov-Husovic, T., Jancic, R., and Raic, K., *Relationship Between Mechanical Characteristics and Thermal Shock Stability of Refractories*. Proc. 3rd BMC, 2003, **35**[31], pp.320-25.
17. Aksel, C. and Riley, F.L., *Young's modulus measurements of magnesia-spinel composites using load-deflection curves, sonic modulus, strain gauges and Rayleigh waves*. J Eur Ceram Soc, 2003, **23**[16], pp. 3089-96.

Chapter Five: Formation of a β-Sialon/TiN Composite from a Novel Ti_xAl_y Intermediate – Process and Parameters

Because of their strong covalent bonding characteristic, Sialon materials are extremely difficult to shape using conventional ceramic manufacturing techniques and are restricted to simple shapes such as tubes or rings. It has been reported that the presence of an electrically conductive phase improves the mechanical properties of Si_3N_4 based ceramics[1-4]. It could also open the way to new shaping techniques and new applications for conducting Sialon ceramics.

Titanium species such as TiN or TiCN are the most referenced reinforcing materials for conductive Sialon ceramics. They can be produced *in-situ*[5, 6] or mixed with the Sialon powder before sintering[1, 7]. When produced *in-situ*, the titanium species are usually made from TiO_2 mechanically mixed with Si_3N_4 or pre-made Sialon, or by directly coating the Sialon/Si_3N_4 particles.

This chapter presents a novel technique inspired by the current ceramic and metallurgy literature (See Sections 2.3 and 2.6) which aims to fabricate a Sialon body from an aluminium metal powder with TiN particles made *in-situ*. Aluminium metal is not a common starting material in Sialon ceramic fabrication as its low melting temperature (~ 660 °C) risks melting segregation prior to Sialon formation. Aluminium is usually added as alumina, clay or aluminium nitride. However at high temperature and under inert atmosphere, aluminium metal reduces titania to form alumina and a titanium aluminide intermetallic phase which can then be nitrided to give aluminium nitride and titanium nitride. Finally, after addition of a silicon phase, a Sialon body can be formed by reaction under nitrogen.

5.1 Materials and Methods

5.1.1 Composition

A β-Sialon composite has been prepared with a target composition situated on the β-Sialon line of the phase diagram at the z value of 1.1. This particular composition has been chosen because it corresponds to the intersection point of the O-Sialon, X-Phase and β-Sialon tie lines at 1750 ºC and is a stable composition. The location of this composition, labelled B on the Sialon behaviour diagram is illustrated in Figure 5.1

Some additives have been added to this basic composition: Yttrium Aluminium Garnet (YAG), added as single oxides Al_2O_3 and Y_2O_3; titanium nitride particles have been prepared *in-situ* from titanium isopropoxide in order to create an electrically conductive phase in the Sialon matrix.

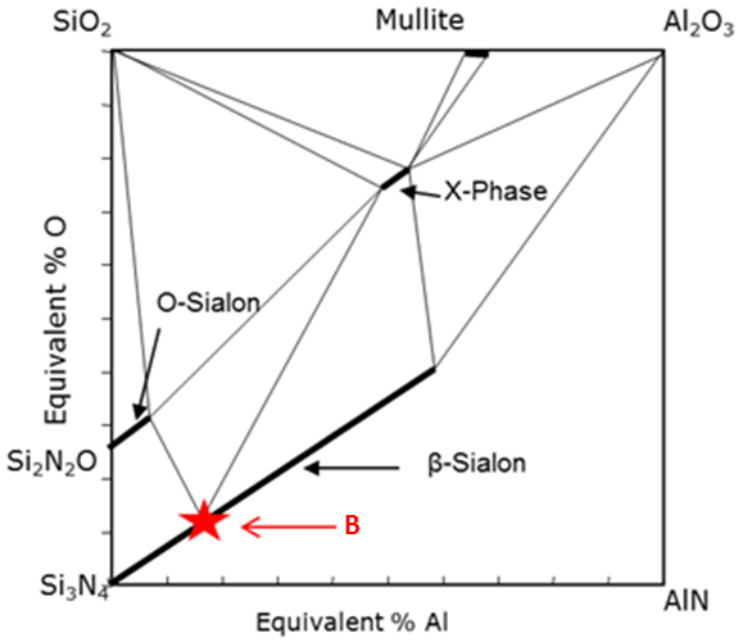

Figure 5.1: Starting composition B on the Sialon behaviour diagram at 1750 ºC.

5.1.2 Powder Preparation and Fabrication of Test Specimens

5.1.2.1 Method Overview

The aim of this study is to fabricate a β-Sialon/TiN composite body by a reaction bonding process, making the TiN particles *in-situ*. The starting powders are aluminium metal powder (99.7 %, TLS Technik GmbH & Co) and silicon metal powder (98.7 %, Sicomill, Grade 4D).

The overall chemical reaction occurs in three steps:

In the reaction 5.1, the aluminium powder is ball milled and chemically coated with titanium dioxide by a sol-gel method (See Sections 3.2.4 and 5.1.2.2) then fired under argon at 800 ºC to form α-alumina and a titanium aluminide whose stoichiometry depends on the initial Al/Ti ratio[8-10] This alloy is nitrided (reaction 5.2) at 1400 ºC to obtain aluminium nitride and titanium nitride. After milling with silicon metal, this last mixture is reacted under nitrogen to form the β-Sialon/TiN composite (reaction 5.3).

$$13Al + 3TiO_2 \xrightarrow{Ar,\ 900\,°C} 2Al_2O_3 + 3Al_3Ti \quad \text{(Eq 5.1)}$$

$$Al_3Ti \xrightarrow{N_2,\ 1400\,°C} 3AlN + TiN \quad \text{(Eq 5.2)}$$

$$Al_2O_3 + AlN + Si + TiN \xrightarrow{N_2, Y_2O_3,\ 1400\,°C} \beta - SiAlON + TiN \quad \text{(Eq 5.3)}$$

5.1.2.2 Aluminium Milling and Coating with TiO_2

During preliminary studies of the reaction between the aluminium and the titania (Eq 5.1), the aluminium melted and part of it, mostly the centre of the grains, coagulated without reacting. The resulting samples contained millimetre-sized balls of aluminium metal (See Figure 5.2) which reacted extremely slowly. The solution proposed was to increase the aluminium powder surface area in order to accelerate the reaction 5.1 (See results in Section 5.2.1).

Figure 5.2: Al-12 wt% TiO_2 in alumina boat (a) on calcined alumina bed before firing and, (b) after 4 hours at 900 ºC under argon with coagulated aluminium balls.

The aluminium powder was weighed into a separate container and transferred into a dry and clean HDPE 250 mL milling bottle with 500 g of 10 mmØ zirconia milling balls (approximately a third of the bottle volume) and 50 g of isopropyl alcohol to cover the balls. The bottle was rotated on the mill for up to 72 hours. After milling, the solvent was not removed so as to prevent spontaneous combustion or oxidation of the aluminium powder and, consequently, the IPA used for the milling was also used for the coating of aluminium.

In order to create a homogeneous network of TiN at the Sialon grain boundaries, the aluminium powder was coated with TiO_2. The sol-gel technique used in this study is based on the techniques previously reported by Gao[5] and Krnel[6] on Si_3N_4 powder.

The aluminium powder, not separated from the IPA used for its milling, was introduced into a round flask with the quantity of titanium isopropoxide (97 %, Aldrich Chemistry) needed to obtain 12 to 120 wt% TiO_2 in the aluminium powder which correspond to 1–10 wt% TiN in the final Sialon. The flask was closed with a rubber top to reduce the contact with the ambient oxygen and water and mixed for about an hour. After opening the flask, distilled water (1Ti:150H_2O) diluted in the same volume of IPA was very slowly added with continuous stirring. The hydrolysis reaction is described by reactions 5.4 and 5.5. The amount of water introduced is very high to avoid the partial hydrolysis with retained organic groups which is favoured by a lack of water[11] (See reactions 5.6 and 5.7). The mixture was stirred for another hour before being vacuum filtered and dried for about 20 hours at 50 ºC under vacuum.

$$Ti(OPr)_4 + 4H_2O \rightarrow Ti(OH)_4 + 4PrOH \quad \text{(Eq 5.4)}$$

$$Ti(OH)_4 \rightarrow TiO_2 + H_2O \quad \text{(Eq 5.5)}$$

$$Ti(OPr)_4 + xH_2O \rightarrow Ti(OH)_x(OPr)_{4-x} + xPrOH \quad \text{(Eq 5.6)}$$

$$Ti(OH)_x(OPr)_{4-x} + Ti(OPr)_4 \rightarrow (OPr)_{4-x}TiO_xTi(OPr)_{4-x} + xPrOH \quad \text{(Eq 5.7)}$$

5.1.2.3 Test Specimen Preparation

Approximately 0.7 g disc samples of 10 mmØ were uniaxially pressed to 15 MPa and held at this pressure for around 30 seconds. The pellets made for the Sialon nitridation reaction (5.3) were transferred to latex balloons and cold isostatically pressed in ethylene glycol at 150 MPa for 60 seconds.

5.1.2.4 Milling and Introduction of Silicon Metal and Yttrium Oxide

After the nitridation reaction of Al_xTi_y (Eq 5.2), silicon metal, plus yttrium oxide (99.9 %, Grade C, HC Starck) and alumina (99.7 %, HPA-0.5, Ceralox) needed for the YAG formation were added to the sample for the Sialon nitridation reaction. Samples resulting from the reaction 5.2 were first placed into a tungsten-carbide bouncing ball grinding system and crushed to a coarse powder (See Section 3.2.2). This powder was introduced in a dry and clean HDPE one litre milling bottle with the other material powders (silicon, yttria and alumina), 700 g of 10 mmØ silicon nitride milling balls (about a third of the bottle volume)

and 150 g of IPA to cover the balls. The bottle was rotated on the mill for approximately 16 hours then the solvent was removed by rotary evaporation.

5.1.3 Firing Techniques

Firings were carried out in a high temperature tube furnace using an alumina boat in an argon or nitrogen atmosphere at a flow rate of 0.1 $L.min^{-1}$. Figure 5.3 shows some samples arranged in an alumina boat before firing.

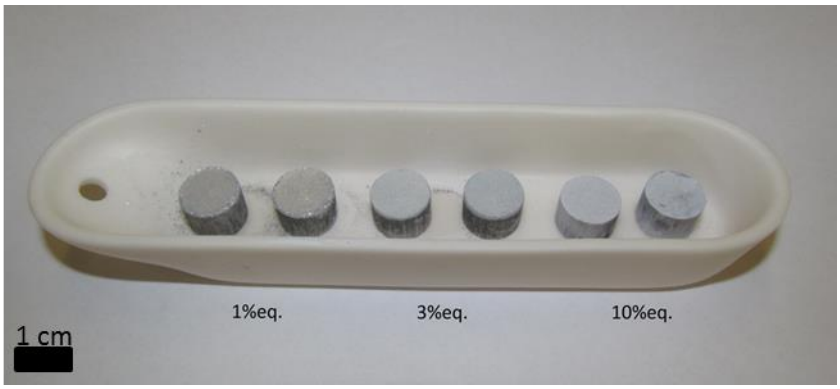

Figure 5.3: Aluminium coated with TiO_2 pressed into 10 mmØ pellets in an alumina boat before firing. Percentages represent the equivalent mass of TiN in the final Sialon mass.

The reaction 5.1 schedule was programmed to be 10 $^{o}C.min^{-1}$ to target temperature, hold 1 to 8 hours then cool to ambient temperature. For this reaction, samples were placed on a coarse calcined alumina powder bed to avoid the possibility that the melted aluminium sticks to the boat.

The reaction 5.2 schedule was programmed to be 10 $^{o}C.min^{-1}$ to target temperature, hold 1 to 3 hours then cool to ambient temperature.

The nitridation firing creates the Sialon phase chemistry and can also densify the sample. It was carried out with a schedule including two holds at 1200 ºC and 1350 ºC taking account of the results obtained in Chapter 4. The samples were nitrided at 1400 ºC on a powder bed layer containing O and β-Sialon in a ratio of 1:2. The nitridation schedule was programmed to be 120 minutes to 1200 ºC, hold 6 hours; 30 minutes to 1350 ºC, hold 4 hours; 10 minutes to 1400 ºC, hold 4 hours; then cool to ambient temperature.

5.1.4 Material Properties Measurement

For more details on this section, refer to Chapter 3.

X-ray diffraction measurements were carried out on a Bruker D8 Advance diffractometer. The 2θ range observed was 10 to 80º or, by exception, to 150º to help distinguish between YAG and TiN phases in some specimens.

Infrared Spectra were taken using a Spectrum One FTIR spectrometer with a diamond ATR module. The 600-4000 cm^{-1} region was scanned with a 4 cm^{-1} resolution.

5.2 Results and Discussion on the Materials Processing

5.2.1 Aluminium Particle Size Distribution

When the as supplied aluminium powder was fired under argon, it melted at about 660 ºC and the centre of the grains aggregated without reacting with the titania, as previously noted in 5.1.2.2. The solution proposed is to increase the surface area of the powder and so enhance the contact between aluminium and TiO_2 to increase the rate of the reaction before the aluminium melting temperature is reached. To achieve this, the aluminium powder was milled for 24, 48 or 72 hours in IPA with zirconia milling balls. The particle size distribution has been measured before and after milling and the grain shape observed by SEM.

The starting aluminium powder has a nominal particle size, measured by the supplier, of −25 µm. Similar results have been obtained with our own equipment. Particle size distribution results are displayed in Table 5.1.

As the milling time increases, the particle size distribution increases. SEM observations show that the aluminium particles, which were spherical before milling (See Figure 5.4a) were now larger and flat (See Figure 5.4b). The milling had beaten the particles flat instead of breaking them down.

The aluminium aggregates in the fired sample completely disappeared when the 48 hours milled aluminium powder was used.

	D_{10} (µm)	D_{50} (µm)	D_{90} (µm)
Supplier (Cilas 920),ultrasonic (60 s)	7.34	16.42	27.36
No milling, ultrasonic (60 s)	10.47	21.33	41.39
1 day milling, ultrasonic (60 s)	19.47	42.18	103.06
2 days milling, ultrasonic (60 s)	22.72	48.61	108.70
3 days milling, ultrasonic (60 s)	31.09	65.23	147.18

Table 5.1: Particle size distribution of the starting aluminium powder

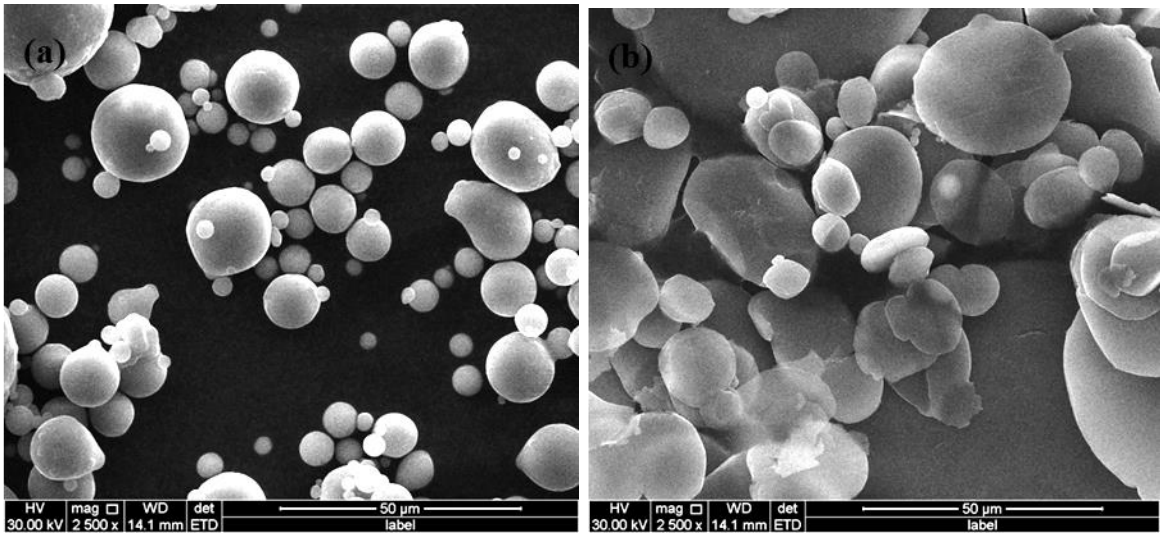

Figure 5.4: SEM micrographs of the aluminium powder (a) before, and (b) after 2 days of milling.

Aluminium is known for its corrosion resistance due to the phenomenon of passivation. This oxide layer at the surface of the aluminium particles would inhibit the reaction between aluminium and titania. The aluminium powder in its milling solvent (IPA) has been observed by a subtractive infrared analysis because the IPA absorbs some infrared frequencies. To distinguish any Al-O bonding absorption caused by the milling process a first measurement has been done on the IPA only and then compared to the results given by the suspension of aluminium in IPA. The two patterns were identical and so this measurement shows that there was no significant trace of Al-O bonding so no oxidation was induced by the milling procedure.

To avoid any oxidation and spontaneous combustion of this highly reactive powder, the aluminium has not been separated from the IPA before the coating, so Solid-State MAS-NMR could not be used to confirm this observation.

5.2.2 Aluminium Coating with TiO_2

The aluminium powder was coated with TiO_2 by the method detailed in Section 5.1.2.2. The quantity of TiO_2 introduced is 12, 37 or 120 wt% (See Annex I). These TiO_2 particles could not be detected by XRD even after a firing in argon atmosphere at 500 ºC for one hour which should normally crystallise them. But when another sample containing 365 wt% TiO_2 was observed after firing, rutile and anatase peaks appeared in the XRD pattern with similar intensities. These peaks had a small intensity compared to those of the aluminium and so it is presumed that the TiO_2 peaks from the sample with lower amounts of TiO_2 were even smaller and hidden in the pattern background.

An SEM observation displayed in Figure 5.5 shows the re-amalgamation of the TiO_2 nano−sized particles. The aluminium is not completely covered with titania which might need to be achieved in order to obtain a continuous network of TiN in the final Sialon body.

An EDS analysis (See Figure 5.6) detects titanium and oxygen in the smaller particles seen in Figure 5.5 on the surface of the bigger aluminium particles. The EDS interaction volume is larger than the TiO_2 particles, therefore aluminium appears on both graphs in Figure 5.6. This confirms the presence of TiO_2 which cannot be seen by XRD due to the relatively low Ti:Al ratio in the sample.

Although the volume of the TiO_2 particles, as represented in Figure 5.5, appears to be sufficient to be detected by XRD, this material has not been fired and it is amorphous. This volume is expected to be much smaller after firing and crystallisation.

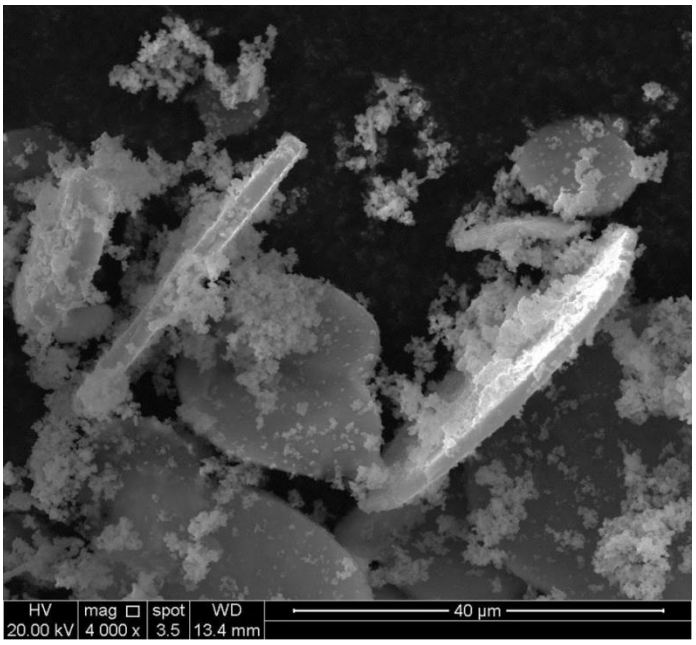

Figure 5.5: Aluminium milled for 48 hours coated with 120 wt% TiO_2.

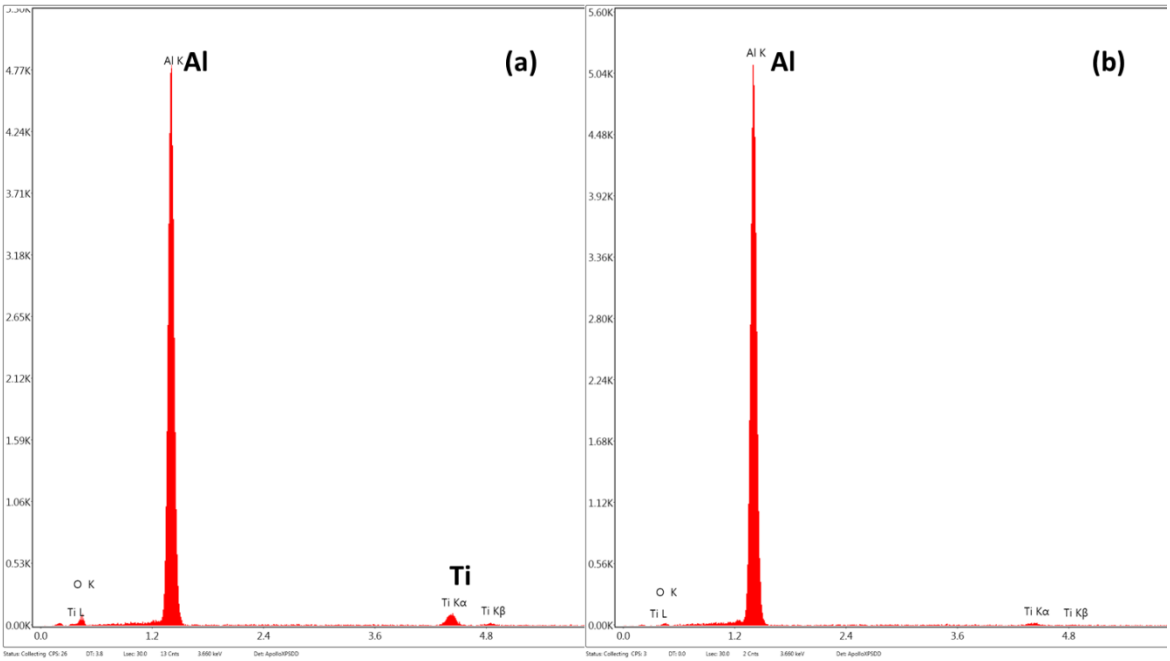

Figure 5.6: EDS analysis of (a) small TiO_2 particles on (b) larger aluminium particles.

5.3 Formation of α-Al_2O_3 and Al_xTi_y

The first reaction (Equation 5.1) between aluminium and titania aims to form α-Al_2O_3 and Al_xTi_y. The titanium aluminide stoichiometry depends on the initial Al:TiO_2 ratio (See Section 1.2.4). The ratios selected for this study are 2.4 and 24.2 (See Annex I) which should form Al_3Ti.

Reaction 5.1 has been reported to start from 500 ºC[9] though Al_2O_3 does not form before 772 ºC[12].

$$13Al + 3TiO_2 \xrightarrow{Ar,\ 900\ ^\circ C} 2Al_2O_3 + 3Al_3Ti \qquad \text{(Eq 5.1)}$$

5.3.1 Preliminary Experiments

Initially, about 0.7 g and 10 mmØ samples of aluminium powder coated with 120 wt% titania were uniaxially pressed at 15 MPa and fired in the Amalgams tube furnace (Figure 3.6c) in a flow of argon (100 mL.min^{-1}) at 900 ºC for one hour resulting in samples deformed by the aluminium melting. These samples were not pressed in the CIP as this part of the Sialon fabrication process does not require densification.

An XRD observation shows that the samples have not reacted. The pattern still shows peaks of aluminium and some very small peaks of rutile, which have resulted from TiO_2 crystallisation.

The same size samples coated with 120 wt% titania were uniaxially pressed at 10 MPa and fired in a flow of argon (100 mL.min^{-1}) at 1200 ºC for one hour. The resulting samples were black, very deformed (due to Al melting at 660 ºC) and stuck to the alumina boat in the absence of a calcined alumina powder bed.

A combined XRD (see Figure 5.7), SEM and EDS (see Figure 5.8) observation of the polished surface of this sample shows that the material is a ceramic-metal composite consisting of a matrix of α-alumina, residual aluminium and TiO which is an intermediate of reaction[8, 10], and Al_3Ti plates which can measure up to 1 mmØ. Titanium aluminide shaped like needles has previously been reported in metal-metal composites [9, 10] after mechanical shaping of the aluminium particles which act as nuclei for growth of the needles. The SEM micrographs in Figure 5.8 show that, in this case, Al_3Ti grows as plates that are much bigger than the aluminium plates (See Section 5.2.1). In this case, it is proposed that the Al plates act as nuclei for the growth of the Al_3Ti plates.

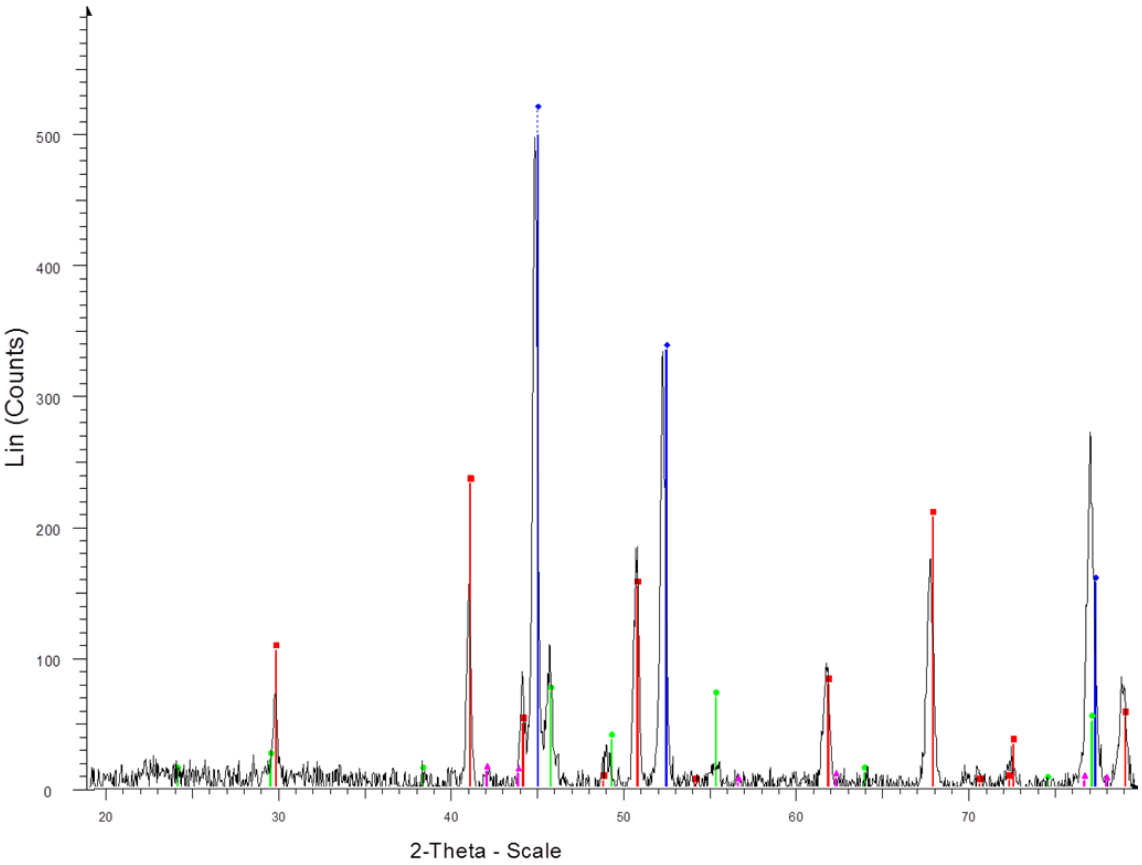

Figure 5.7: XRD pattern of the polished surface of a sample initially containing 120 wt% TiO_2 fired at 1200 ºC for 2 hours. Red: corundum (00-046-1212) ; Blue: aluminium (00-004-0787) ; Green: Al_3Ti (00-037-1449) ; Pink: TiO (00-012-0754).

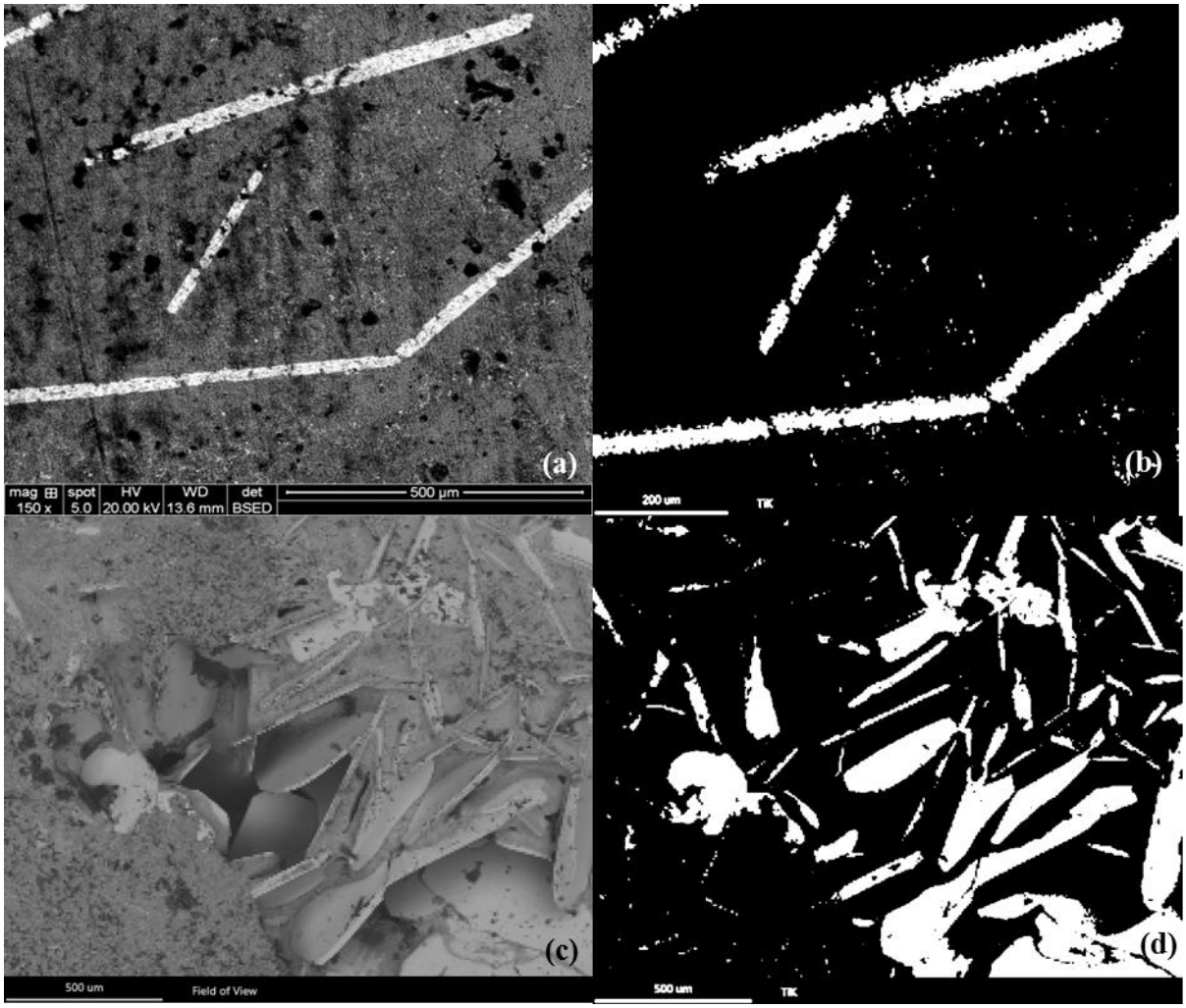

Figure 5.8: SEM micrographs of (a) the polished surface, and (c) an open pore on the sample surface, and the respective titanium EDS mapping (b) and (d) of a sample containing 12 wt% TiO_2 resulting from reaction (5.1) at 1200 ºC showing the Al_3Ti white plates in a grey ceramic-metal matrix.

5.3.2 Optimised Reaction Parameters

The reaction parameters tested in Section 5.3.1 lead to neither a high yield of reaction nor to a successful nitridation of Al_3Ti, as shown in Section 5.4.

Other than temperature, the second parameter that can be modified is the duration of the hold at temperature. As the TiO intermediate needs a temperature equal or higher than 800 ºC to be fully reacted[12], the temperature of 900 ºC used in the previous experiments was chosen to test different hold times. The samples were fired using 4 and 8 hour holds. The XRD composition was the same in both samples: aluminium is still present in non-negligible quantities, Al_2O_3 and Al_3Ti peaks are higher than in the previous experiments, and some TiO_{2-x} phases are detected with $0 > x > 1$. These oxygen-poor titanium dioxide phases are also intermediates of reaction as well as the TiO detected in the shorter firings.

Leaving the samples at temperature for much longer (16 or 24 hours[12]) might complete the reaction but as it is shown in Section 5.4.2, 4 hours at 900 ºC is enough to complete the process of the Sialon/TiN composite formation.

After 4 hours at 900 ºC, the samples are deformed by the aluminium melting and the plate shape of Al_3Ti observed previously at 1200 ºC for 2 hours is not seen. The Al_3Ti particles have no noticeable shape and are homogeneously dispersed in the matrix. Figure 5.9 shows the SEM micrographs of the polished surface of the sample. An EDS analysis (see Figure 5.10) reveals the presence of titanium in the white particles which therefore are inferred to be Al_3Ti, which is the only crystalline titanium containing phase observed by XRD. The grey matrix is composed of aluminium and alumina.

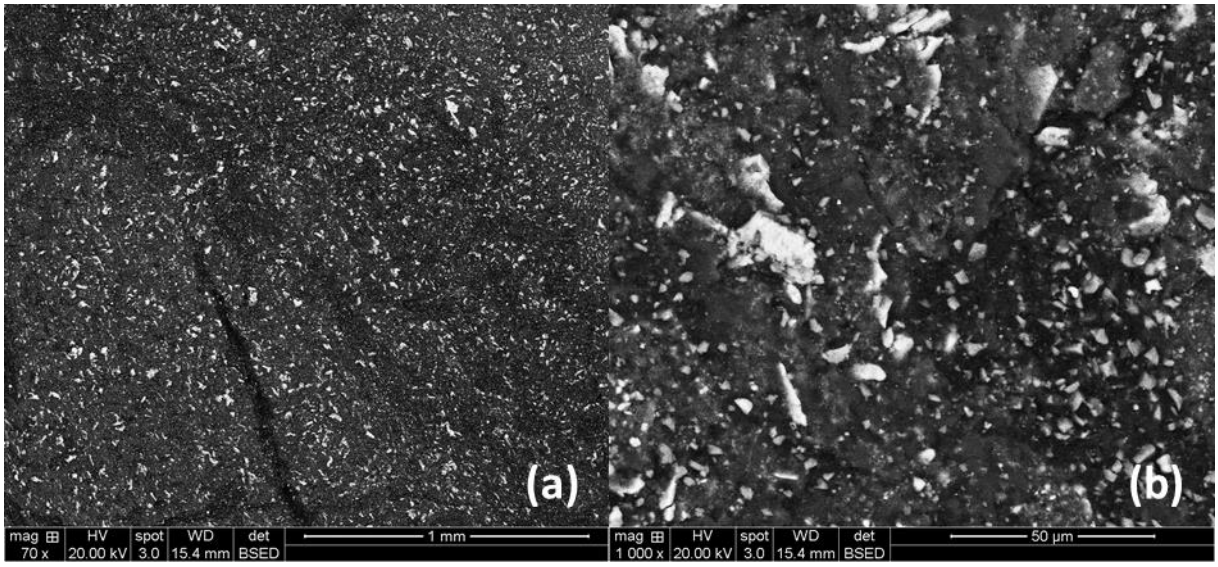

Figure 5.9: SEM micrographs of the polished surface of a sample resulting from reaction 5.1 at 900 ºC for 4 hours showing the white particles of Al_3Ti in an aluminium-alumina matrix at (a) 70 x and (b) 1000 x magnifications.

A bigger batch of samples was prepared to test the mechanical properties of the final Sialon (See Chapter 6), and was fired in the Elatec furnace (Figure 3.6f) that can contain a large number of samples. The samples were contained in alumina boats but the carbon-based structure of the furnace (elements, insulation and furniture consist entirely of graphite) resulted in the samples forming TiC. Consequently the alumina tube furnace was used to fire samples for reaction 5.1. However, this furnace has a small volume capacity and could not contain all the samples in a single firing.

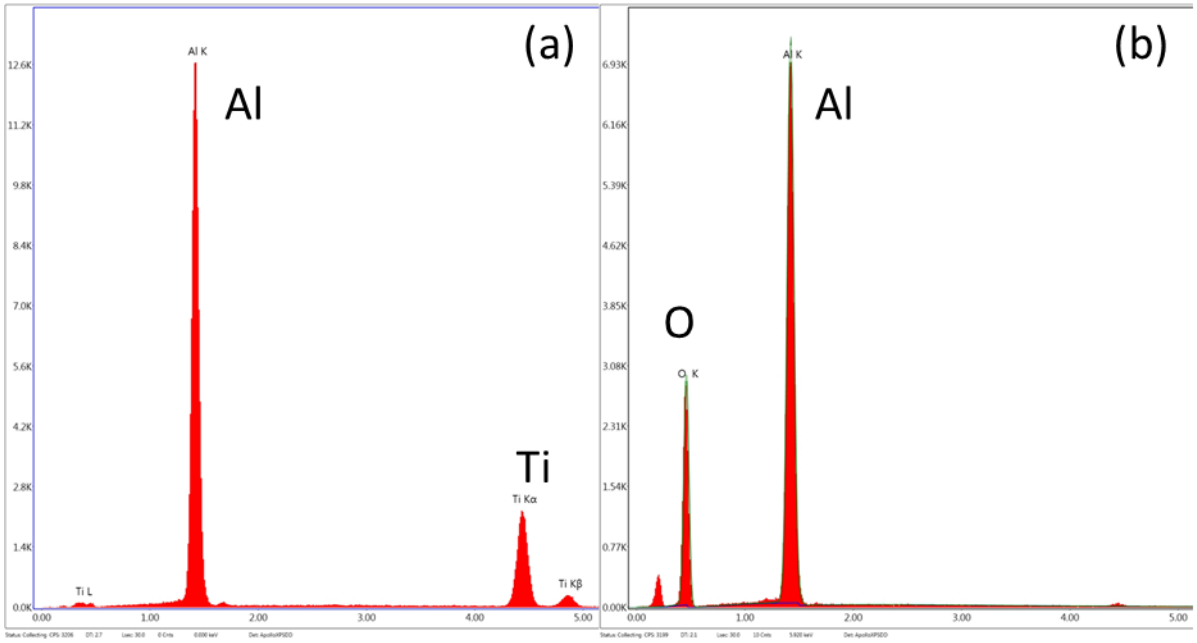

Figure 5.10: EDS analysis on (a) the white particles seen in Figure 5.9 and (b) the matrix around them.

5.4 Nitridation of Al_xTi_y

For the second reaction (Equation 5.2), samples resulting from reaction 5.1 were not processed or modified. The calcined alumina bed was removed from the alumina boat as the samples have been found not to stick even if aluminium metal is still present.

In this reaction, the alumina is chemically inert. Only the titanium aluminide and the remaining aluminium are nitrided by the atmosphere to form aluminium nitride and titanium nitride.

$$Al_3Ti \xrightarrow{N_2,\ 1400\ °C} 3AlN + TiN \qquad \text{(Eq 5.2)}$$

No literature has been found on the nitridation of titanium aluminides. However this reaction is strongly thermodynamically driven by a strongly negative enthalpy of reaction ΔH and a negative free energy of reaction ΔG. Thermodynamic values are displayed in Table 5.2.

T (°C)	ΔH (kJ)	ΔG (kJ)
0	-1129.68	-1025.36
100	-1132.11	-986.706
200	-1132.88	-947.616
300	-1132.67	-908.467
400	-1131.8	-869.414
500	-1130.63	-830.516
600	-1129.35	-791.778
700	-1128.04	-753.189
800	-1126.79	-714.732
900	-1125.65	-676.388
1000	-1124.63	-638.136
1100	-1123.72	-599.96
1200	-1122.92	-561.846
1300	-1122.19	-523.784
1400	-1121.54	-485.766
1500	-1120.94	-447.785
1600	-1120.4	-409.837

Table 5.2: Enthalpy of reaction and free energy of reaction for reaction 4.2[13].

5.4.1 Preliminary Experiments

Initially, samples fired at 1200 ºC under argon (Figure 5.8) have been re-fired under nitrogen at 1200 ºC for one hour, without any physical or chemical alteration prior to firing. The titanium aluminide Al_3Ti needles were still present but they were longer (up to 2 mm) and sometimes looked like they had melted (melting temperature of Al_3Ti is 1220 ºC) during the firing process as shown in Figure 5.11. The cracks observed in the white ribbons are due to the polishing of the sample. The resulting samples were more deformed than the initial samples and have a silvery colour.

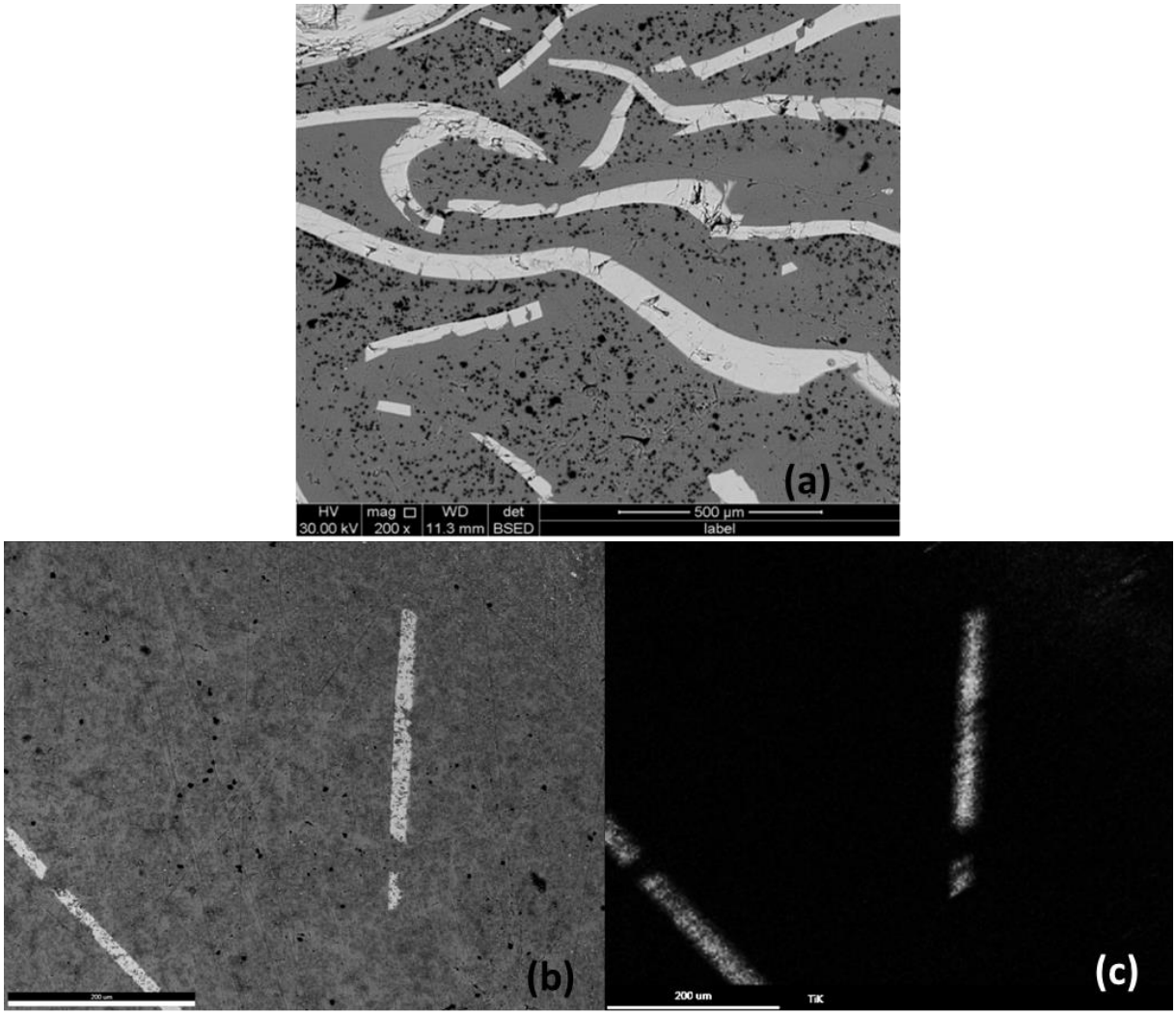

Figure 5.11: SEM micrograph of (a) and (b) the polished surface, and, (c) the titanium EDS mapping of a sample containing 12 wt% TiO_2 resulting from reaction (5.2) at 1200 ºC showing the Al_3Ti white plates in a grey ceramic-metal matrix. Scale bar (a) = 500 µm. Scale bars (b) and (c) = 200 µm.

An EDS and XRD (see Figure 5.12) analysis of the polished surface of the same sample shows the Al_3Ti needles have not been nitrided. There is some clear preferential orientation (see peak at approximately 46º in Figure 5.12) in the XRD pattern of Al_3Ti due to the plate shape of these particles. Titanium and aluminium are clearly seen by EDS in the white plate, aluminium nitride has appeared on the XRD pattern but titanium nitride does not and Al_3Ti peaks are still present. The ceramic matrix contains the unreacted α-alumina and aluminium metal. The presence of AlN in the fired samples can be simply explained by the direct nitridation of aluminium metal by the nitrogen atmosphere. Aluminium melts at 660 ºC and therefore is highly reactive in these firing conditions.

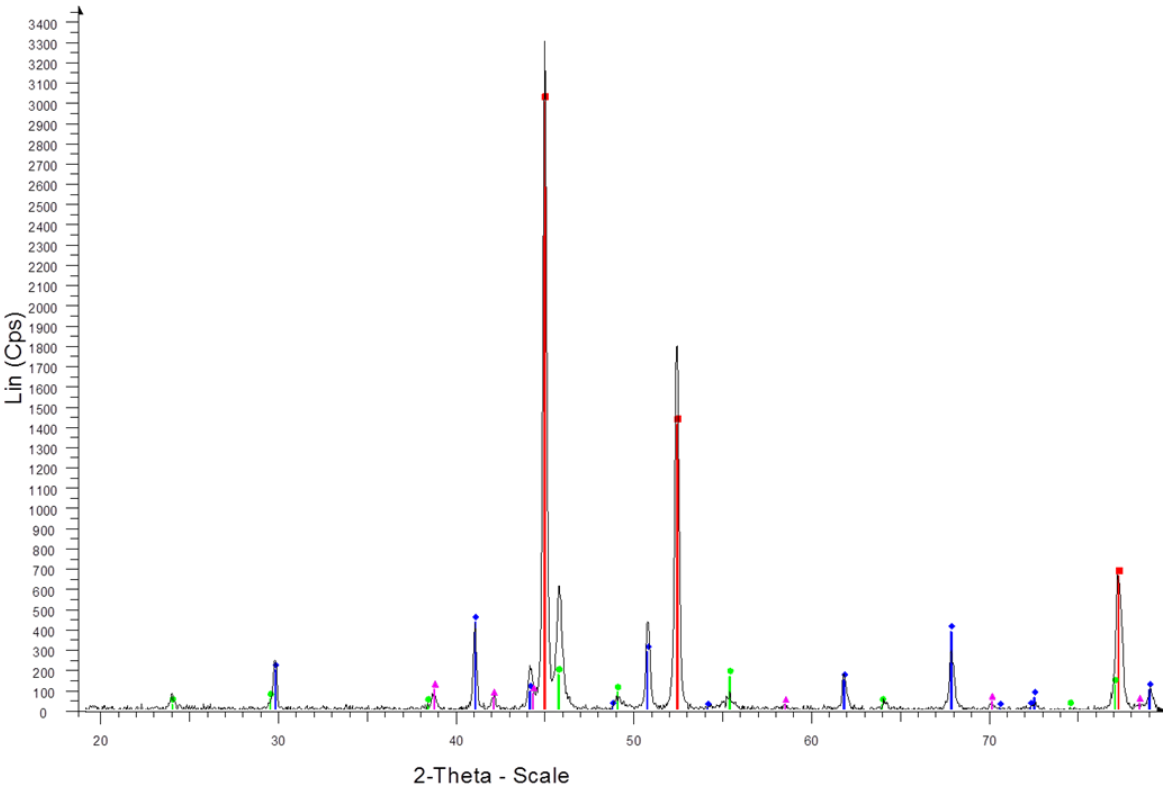

Figure 5.12: XRD pattern of the polished surface of a sample initially containing 120 wt% TiO_2 fired at 1200 ºC for 2 hours in argon then at 1200 ºC for 2 hours in nitrogen. Blue: corundum (00-046-1212); Red: aluminium (00-004-0787); Green: Al_3Ti (00-037-1449); Pink: AlN (00-025-1133).

5.4.2 Optimised Reaction Parameters

Although the thermodynamic data (Table 5.2) predict the nitridation of Al_3Ti at 1200 ºC, it has been shown in the previous section that the kinetics of the reaction are too slow at this temperature.

Samples resulting from reaction 5.1, fired at 900 ºC for 4 hours and 8 hours in argon, have been placed in alumina boats and fired at 1400 ºC for 3 hours in nitrogen in an alumina tube furnace. The XRD (see Figure 5.13) results show, from 4 hours firing, that all the Al and Al_3Ti has been consumed and displayed only α-alumina (unreacted from reaction 5.1), aluminium nitride and titanium nitride peaks. Samples are homogeneously dark and golden, which is a colour characteristic of the presence of TiN.

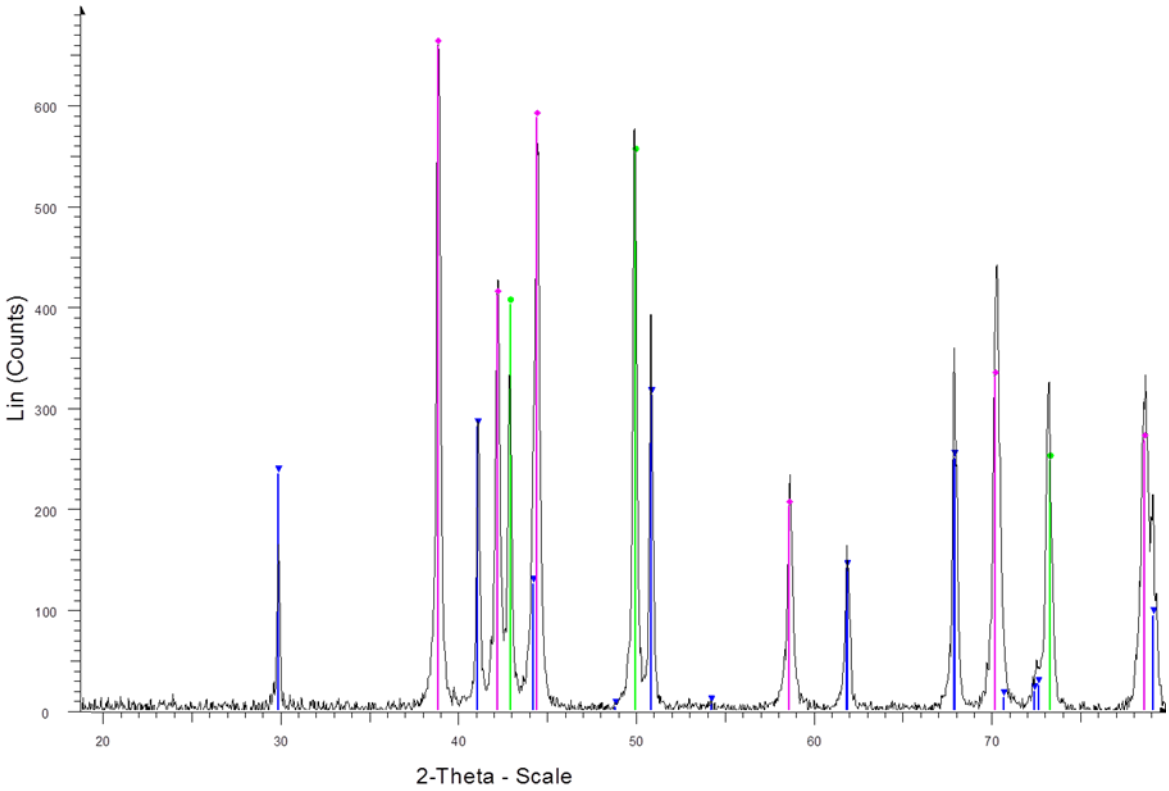

Figure 5.13: XRD pattern of the polished surface of a sample initially containing 37 wt% TiO_2 fired at 900 ºC for 4 hours in argon then at 1400 ºC for 3 hours in nitrogen. Blue: corundum (00-046-1212); Green: TiN (01-087-0633); Pink: AlN (00-025-1133).

Figure 5.14a shows an SEM micrograph of the polished surface of the sample. No particular microstructure can be identified and EDS has insufficient spatial resolution to distinguish the particles, detecting all the elements present uniformly. However, an observation by optical microscopy shows the golden titanium nitride particles homogeneously distributed on the polished surface of the sample (Figure 5.14b). This sample has been polished by hand to a 5 µm finish but it was very fragile and a perfectly flat polishing was not obtained resulting in unequal focusing along an area by optical microscopy. This photo has been obtained using the Extended Focal Imaging (EFI) function of the optical microscope software[14].

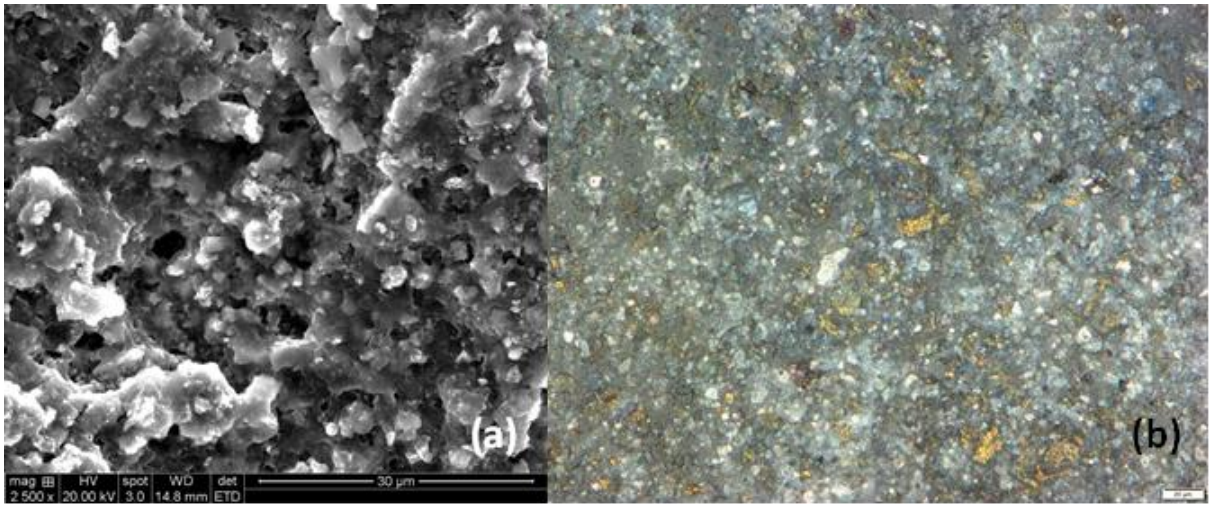

Figure 5.14: Polished surface of a sample resulting from reaction 5.2 at 1400 ºC for 3 hours. (a) SEM micrograph. Scale bar (a) = 30 µm. (b) Optical microscopy photo showing the golden TiN particles dispersed in the sample. Scale bar (b) = 20 µm.

5.5 Sialon Reaction Bonding

A final nitridation reaction allows the formation of the Sialon phase. Samples resulting from reaction 5.2 were ground in a tungsten-carbide bouncing ball system then milled with silicon metal, yttrium oxide and the necessary alumina to form 5 wt% YAG in the final Sialon. After uniaxial pressing and CIP at 150 MPa, the pellets were placed into an alumina boat on a O/β−Sialon powder bed layer. The samples were fired under nitrogen at 1400 ºC for 4 hours including holds for 6 hours at 1200 ºC and 4 hours at 1350 ºC both in the alumina tube furnace then in the Elatec furnace (in graphite pots), giving similar results. Samples were analysed by XRD before firing to confirm that all the phases were still present after processing, especially TiN.

5.5.1 Preliminary Results

Initially, the samples described in Section 5.4.1 were nitrided. These samples had been previously fired at 1200 °C for 1 hour in argon then at 1200 °C for 1 hour in nitrogen before being ground and milled with silicon, yttria and alumina. Thus, before this final nitridation, they were composed of Al, Al_2O_3, Al_3Ti and AlN (plus the added Si and Y_2O_3). The samples were fired according to the schedule noted above in 5.5, then ground to present a grey and uniform surface which was examined by XRD. The XRD results are displayed in Figure 5.15. These fired samples were mainly composed of β-Sialon with a z-value of 1.0 which is close to the target of 1.1. The β-Sialon peaks were split, indicating the presence of a second

β−Sialon phase with a slightly lower z-value. This can be understood by noting that the Sialon reaction remained incomplete after this 1400 °C firing stage and this lower z-value β-Sialon was an intermediate of the reaction. It is not surprising to form Sialon from this initial composition at this temperature. Indeed, silicon, alumina and aluminium nitride are common raw materials for the fabrication of Sialon phases (See behaviour diagram in Figure 5.1); aluminium is easily nitrided to form AlN in these firing conditions as it melts at 660 ºC; and it has been shown in Section 5.4.2 that Al_3Ti is nitrided at 1400 ºC for 3 hours to form AlN and TiN.

The samples nitrided at 1400 °C also contained YAG and α-Si_3N_4 which is a reaction intermediate. Indeed, the first step of a reaction bonding process is the nitridation of silicon (See Section 2.2.4). There is no evidence of any crystalline titanium phase although this may be due either to the low concentration of titanium in the samples or to the fact that YAG and TiN have very similar XRD patterns (see Section 5.5.2).

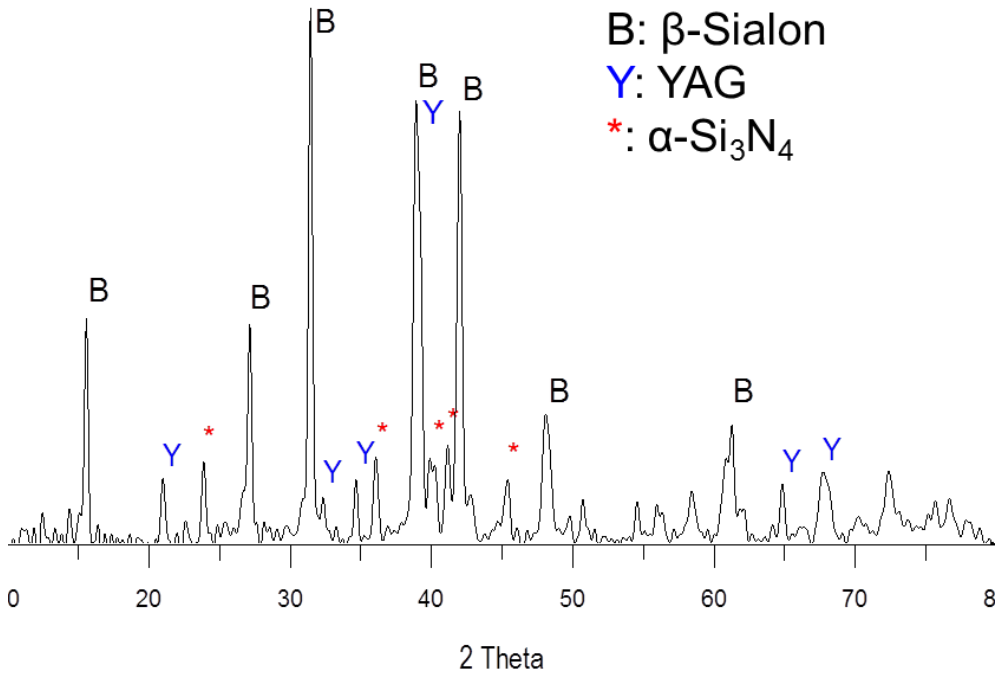

Figure 5.15: XRD pattern of the polished surface of a nitrided sample resulting from preliminary studies. Only major peaks are labelled.

5.5.2 Optimised Reaction Parameters

Samples fired at 900 ºC for 4 hours in argon then at 1400 ºC for 3 hours in nitrogen have been ground and milled with silicon, yttria and alumina and nitrided as described in 5.5 above. Before firing, these samples were composed of alumina, aluminium nitride, residual aluminium, silicon and titanium nitride.

The ground surfaces of the nitrided samples were analysed by XRD and the results for the sample containing 10 wt% TiN are displayed in Figure 5.16. β-Sialon and YAG peaks can easily be identified. However, the TiN peaks are not evident. As can be seen in Table 5.3, the XRD patterns of YAG and TiN are very similar. All the TiN peaks are superimposed on YAG peaks even at high angles ($80^o < 2\theta < 150^o$). However, it can be observed in Figure 5.16 that the YAG peaks (in blue) fit the standard ICDD intensities for the pattern except for the peaks common to TiN (≈ 43º, 50º and 73º). The latter peaks are too intense to be explained by the presence of YAG only.

The TiN peaks were slightly shifted to lower angles, which indicates a larger unit cell. Other cubic phases of titanium compounds such as TiO or TiC have much smaller unit cells, so their peaks are shifted to higher angles. This leads to the conclusion that the shift indicates the formation of vacancies in the TiN structure, which would expand the crystal structure, rather than being due to a chemical change. The unit cell dimensions can be calculated using the Bruker XRD analysis software[15]. The standard ICDD pattern for TiN (00-038-1420) has a unit cell of 4.242 Å, whereas the observed unit cell is 4.258 Å (a 0.4 % linear expansion). This accuracy of the calculation on the unit cell depends primarily on the alignment of the instrument and the quality of the pattern. In these measurement circumstances, both of these parameters gave a small error (0.004 with a measurement step of 0.05º) as the instrument was recently realigned and because TiN has a cubic cell therefore all peaks move together with a unit cell dimension change. The sample containing 3 wt% TiN had a similar pattern with less intense TiN peaks.

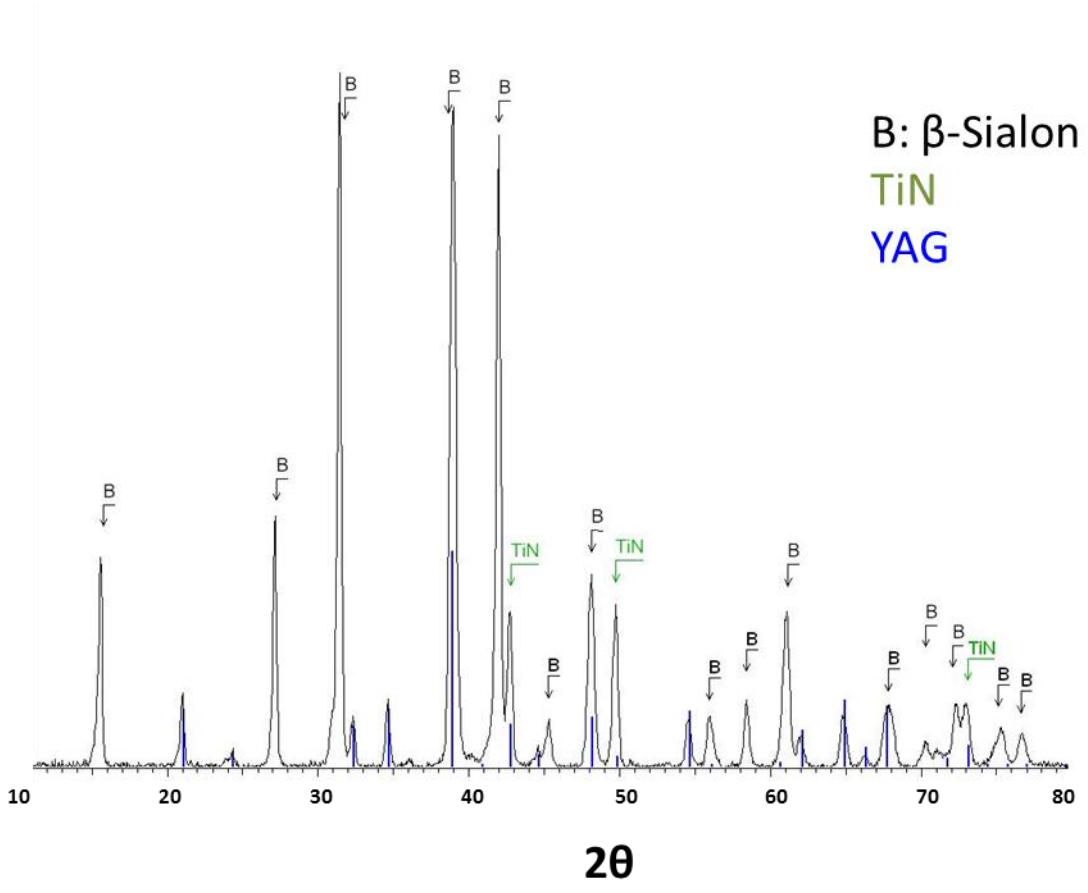

Figure 5.16: XRD Pattern of the polished surface of a nitrided sample containing 10 wt% TiN.

YAG partial pattern (ICDD 33-0040)		TiN full pattern (ICDD 38-1420)	
d(Å)	2θ for Co (λ = 1.79026 Å)	d(Å)	2θ for Co (λ = 1.79026 Å)
2.4520	42.82	2.4492	42.87
2.1220	49.90	2.1207	49.93
1.4780	74.55	1.4997	73.29
1.2800	88.74	1.2789	88.84
1.2257	93.82	1.2245	93.94
1.0616	114.96	1.0604	115.16
0.9741	133.54	0.9730	133.84

Table 5.3: Comparison of partial YAG XRD pattern with the full TiN XRD pattern[15].

The samples have been ground to powder using the tungsten-carbide bouncing ball and analysed by NMR at the University of Warwick (England) by Gregory J. Rees and John V. Hanna with a Bruker Avance II-600 14.1T spectrometer using a 10 mm Bruker static probe. $^{47/49}$Ti NMR spectra were collected using a 3 μs π/4 non-selective pulse in the solid echo

($\pi/4 - \tau - \pi/4$) sequence and with a delay of 0.1 seconds. To increase the excitation a broadband Wideband Uniform Rate and Smooth Truncation-Quadrupolar Carr-Purcell-Meiboom-Gill (WURST-QCPMG) pulse shape was used. This NMR spectroscopy method makes the detection of insensitive nuclei, such as $^{47/49}$Ti, more efficient by uniformly exciting broad spectral regions. All data were referenced to $TiCl_4$, containing ^{49}Ti.

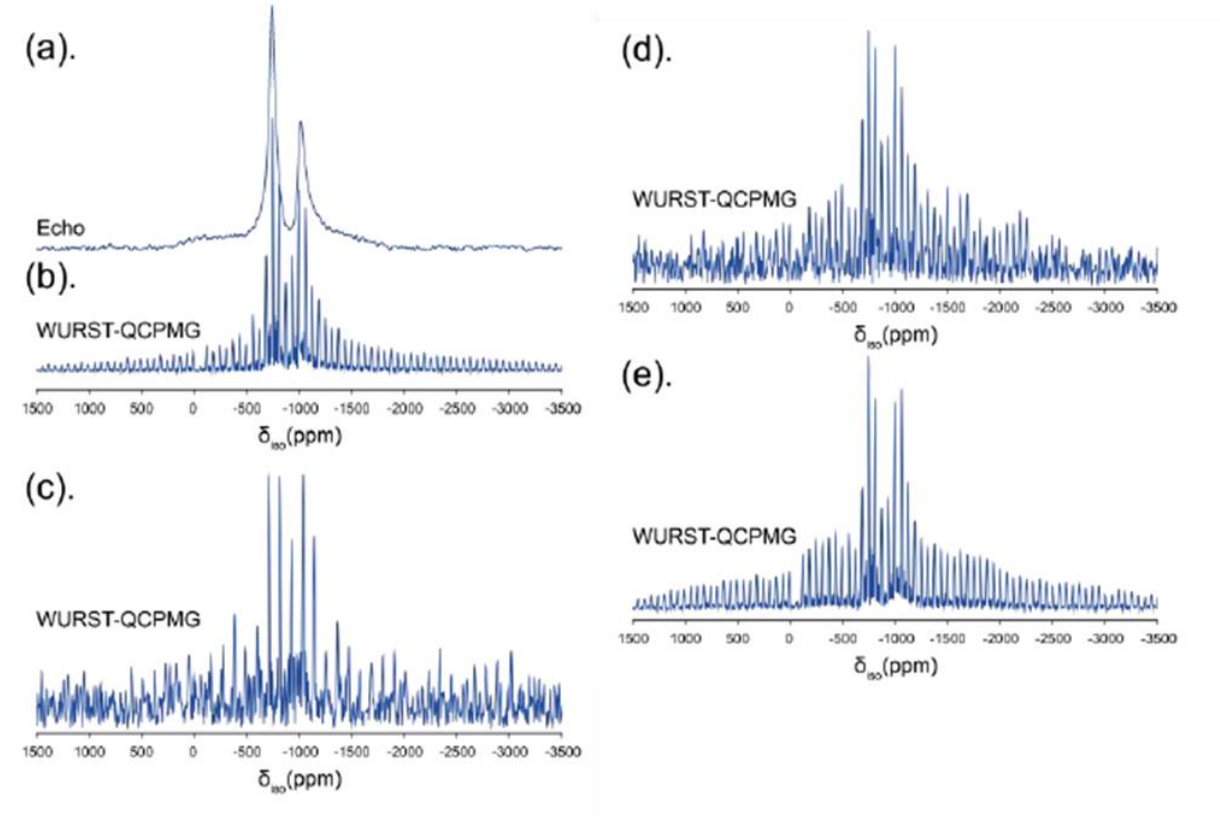

Figure 5.17: $^{47/49}$Ti NMR spectra (a) TiN and (b) the corresponding WURST-QCPMG result, and WURST-QCPMG spectra for (c) Sialon + 1 wt% TiN, (d) Sialon + 3 wt% TiN, and (e) Sialon + 10 wt% TiN. Axis range: 1500 to -3500 ppm.

Figure 5.17 shows the NMR WURST-QCPMG spectra for TiN (Figure 5.17a and b) compared with the spectra for the samples theoretically containing 1, 3 and 10 wt% TiN (Figure 5.17c, d and e, respectively). The signal/noise ratio makes the interpretation of the spectra for the sample containing 1 wt% TiN very difficult but as the concentration of TiN increases, the signal becomes sharper and only the peaks from TiN can be observed.

The combination of the XRD and NMR observations clearly confirm the presence of TiN as the only titanium containing phase in the nitrided samples.

An observation by SEM does not show any noticeable microstructural features such as hexagonal β-Sialon grains but these samples have only been fired at 1400 ºC and such

microstructures would not expected to be found until after processing at higher temperature. The YAG and TiN are uniformly dispersed in the ceramic (see Figure 5.18).

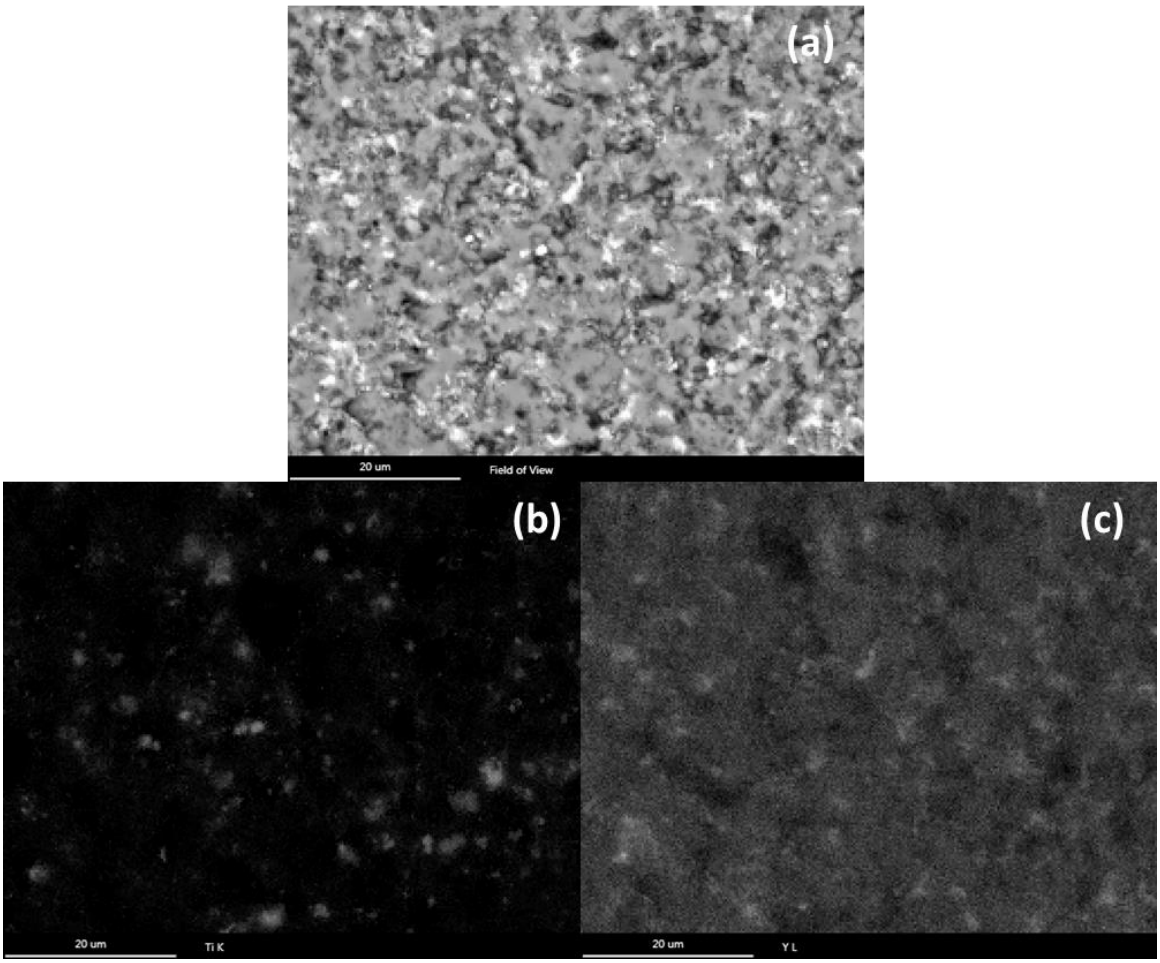

Figure 5.18: (a) SEM backscattering micrograph of the polished surface of a nitrided sample resulting from preliminary studies (fired at 1200 ºC for 2 hours in argon then at 1200 ºC for 2 hours in nitrogen then nitrided at 1400 ºC for 6 hours) showing the white YAG and TiN particles dispersed in a Sialon matrix. (b) Ti and (c) Y EDS maps corresponding to the area represented in (a), showing the homogeneous dispersion of titanium and yttrium phases.

On the other hand, the sample containing 1 wt% TiN showed a somewhat different behaviour with not only the formation of the expected β-Sialon ($z \approx 1$), YAG and TiN but also residual AlN, a Y-α-Sialon close to the β-Sialon line in the behaviour diagram ($m = 1.62$ and $n = 0.81$ – See Figure 2.1) and $Y_3AlSi_2O_7N_2$ (ICDD 00-043-0579), named N-Phase by Inomata[16]. The latter phase was described by Inomata as forming between 1000 and 1400 ºC by decomposition of J-Phase (variously reported as $YSiO_2N$ and Y_4SiAlO_8N, see Section 4.2.1.1). The presence of Y-α-Sialon and N-Phase can be understood with reference to the Sialon behaviour diagram: the amount of alumina formed from aluminium metal during the

process (reaction 5.1) is proportional to the amount of TiO_2 introduced during the aluminium coating. The residual aluminium from reaction 5.1 is then nitrided to form AlN during reaction 5.2, in parallel with the Al_3Ti nitridation. Overall, the less TiO_2 in the green mix, the greater the AlN:Al_2O_3 ratio and the more the composition is shifted to the AlN corner of the Sialon behaviour diagram (See Figure 1.1) where α-Sialon and J-Phase can be found. Note that these phases are not indicated on Figure 1.1 as they exist on another (rare-earth stabilised) plane within the three dimensional phase diagram that includes the simple Sialon behaviour diagram (See Figure 2.1).

5.6 Summary

The aim of this newly developed process was to fabricate a Sialon body with TiN particles made *in-situ*. The starting powder, aluminium metal, was coated with titania by a sol-gel method and reacted at 900 ºC for 4 hours under an inert atmosphere to form α-alumina and Al_3Ti. This titanium aluminide composite was then nitrided at 1400 ºC for 3 hours to form aluminium nitride and titanium nitride. This reaction is strongly thermodynamically driven. XRD evidence shows the complete conversion of Al_3Ti and the formation of AlN and TiN. SEM and EDS evidence shows that the reaction path develops through the formation of uniquely structured plates and ribbon phases.

The agglomeration of the aluminium observed during the first reaction has been solved by milling the powder for 48 hours prior to coating it with titania. The aluminium particles are beaten flat, not fractured, and their particle size distribution increased.

The intermediate product Al_3Ti grows in a plate shape inside the ceramic matrix due to the mechanical pre-shaping of the aluminium particles before the coating. With a longer firing at 1200 ºC in nitrogen, the plates grow longer and can be deformed but are not reacted. The properties of these materials could be investigated in future studies for their reinforcing potential for alumina. Forming the electrically conductive phase with a plate or whisker shape could be a way to minimise the large volume of conductive phase usually needed to create electrical conductivity. To further reduce the percolation threshold, the plates could be aligned by slip casting.

After crushing and mixing this material with suitable silicon phases and yttria as a nitridation and sintering aid, a Sialon body was formed by reaction under nitrogen at 1400 °C. The β−Sialon obtained has a z-value equal to the initial target of 1. YAG has been formed and is homogeneously dispersed in the ceramic matrix. The presence of TiN was confirmed by

observing highly enhanced intensities in the conflicting YAG XRD pattern, and by MAS-NMR.

From an industrial point of view, this newly developed process could be adapted to a less time consuming and less multi-stage process by mixing the silicon and the yttria with the initial Al/TiO_2 powder. The firing schedule could be adapted to a single firing starting in argon up to 900 ºC with a 4 hours hold then in nitrogen to 1400 ºC until the end of the nitridation of Al_3Ti and the Sialon phase. Thermodynamics analysis[13] show that Si and Al would not respectively reduce TiO_2 and Y_2O_3. This method would form a non-densified Sialon/TiN body which would be strongly deformed by the aluminium melting. It would need to be ground and re-pressed before sintering.

5.7 Chapter Five Bibliography

1. Çelik, A., Ayas, E., Halil, E., and Kara, A., *Oxidation behavior of electrically conductive α/β Sialon composites with segregated network of TiCN*. J Eur Ceram Soc, 2012, **32**[7], pp. 1395-403.
2. Duan, R.G., Roebben, G., Vleugels, J., and Van der Biest, O., *Optimization of microstructure and properties of in-situ formed β-O-Sialon-TiN composite*. Mat Sci Eng A-Struct, 2006, **427**, pp. 195-202.
3. Jiang, T., Xue, X.X., Li, Z.F., and Duan, P.N., *High temperature oxidation behavior of electroconductive TiN/O'-Sialon ceramics prepared from high titania slag-based mixture*. T Nonferr Metal Soc, 2011, **21**[12], pp. 2638-43.
4. Shimada, S. and Kato, K., *Coating and spark plasma sintering of nano-sized TiN on Y-α-sialon*. Mat Sci Eng A-Struct, 2007, **443**, pp. 47-53.
5. Gao, L., Li, J., Kusunose, T., and Niihara, K., *Preparation and properties of TiN-Si_3N_4 composites*. J Eur Ceram Soc, 2004, **24**[2], pp. 381-86.
6. Krnel, K., Maglica, A., and Kosmac, T., *β-Sialon/TiN nanocomposites prepared from TiO_2-coated Si_3N_4 powder*. J Eur Ceram Soc, 2008, **28**[5], pp. 953-57.
7. Ayas, E. and Kara, A., *Novel electrically conductive α-β Sialon/TiCN composites*. J Eur Ceram Soc, 2011, **31**, pp. 903-11.
8. Feng, C.F. and Froyen, L., *Formation of Al_3Ti and Al_2O_3 from an Al-TiO_2 system for preparing in-situ aluminium matrix composites*. Compos Part A-Appl S, 2000, **31**, pp. 385-90.
9. Gaus, S.P., Harmer, M.P., Chan, H.M., Caram, H.S., Bruhn, J., and Claussen, N., *Alumina-Aluminide Alloys (3A) Technology: II, Modeling of Ti_xAl_y-Al_2O_3 Composites Formation*. J Am Ceram Soc, 2000, **83**[7], pp. 1606-12.
10. Pan, J., Li, J.H., Kukunaga, H., Ning, X.G., Ye, H.Q., Yao, Z.K., and Yang, D.M., *Microstructural study of the interface reaction between titania whiskers and aluminium*. Compos Sci Technol, 1997, **57**, pp. 319-25.
11. Hanaor, D.A.H., Chironi, I., Karatchevtseva, I., Triani, G., and Sorrell, C.C., *Single and mixed phase TiO_2 powders prepared by excess hydrolysis of titanium alkoxide*. Adv Appl Ceram, 2012, **111**[3], pp. 149-57.
12. Han, C.Z., *Consolidation of Al-TiO_2 and Ti_3Al-Al_2O_3 composite powders*. PhD Thesis, Materials and Process Engineering, The University of Waikato, Hamilton, New Zealand, 2005.
13. Software *HSC Chemistry 7.1*, Outotec. Finland.
14. Software *Stream 1.9*, Olympus. Japan.
15. Software *EVA 1996-2011 17.0.0.2*, Bruker-AXS. Germany.
16. Inomata, Y. and Yasutoshi, H., *Phase Relation in the Compounds Appeared in a System, Si_3N_4 (60 mol%)-Y_2O_3-Al_2O_3-SiO_2 at 1400 ºC*. J Ceram Assoc Jpn, 1977, **85**[987], pp. 533-37. Note: This article has been translated by a proficient Japanese technical translator at Callaghan Innovation.

Chapter Six
Sialon/TiN Composite Properties

In the previous chapter of this thesis, a new fabrication method for Sialon/TiN composites has been presented. It uses unconventional raw materials and a novel methodology to introduce a small volume (0.6-6.5 vol%) of electrically conductive TiN into the ceramic matrix.

This chapter examines the chemical, physical and electrical properties of the material newly fabricated after reaction at 900 ºC in argon then 1400 ºC in nitrogen and sintering at 1600 ºC, namely composition, porosity, density, microstructure, Young's modulus, hardness, fracture toughness, compression strength, resistance to thermal shock and electrical conductivity after sintering at 1600 ºC. The oxidation resistance of these materials is discussed in Chapter 7.

The composition of the samples used to make these measurements and the relevant firing conditions are summarised in Table 6.1.

As seen in Section 5.5.2, sample 22 (composition noted below) shows a different behaviour than the other Sialon/TiN composite samples. Property measurements have been made on this composition but cannot be directly compared to the other samples.

<table>
<tr><th>Sample number</th><th>Sample target composition</th><th>Nitridation conditions</th><th>Sintering conditions</th></tr>
<tr><td>21</td><td>β-Sialon + 5 wt% YAG made from Si, AlN, Al_2O_3, Y_2O_3.</td><td>Reaction bonding at 1400 ºC for 4 hours including holds at 1200 ºC for 6 hours and 1350 ºC for 4 hours, on β/O-Sialon powder bed, in Elatec furnace.</td><td rowspan="4">1600 ºC for 6 hours covered with β/O-Sialon powder bed in Elatec furnace.</td></tr>
<tr><td>22</td><td>β-Sialon + 5 wt% YAG + 1 wt% TiN</td><td rowspan="3">New process detailed in Chapter 5, on calcined alumina bed for reaction 5.1 and β/O-Sialon powder bed for reaction 5.3. Reactions 5.1 and 5.2 were processed in the alumina tube furnace and reaction 5.3 in the Elatec furnace.</td></tr>
<tr><td>23</td><td>β-Sialon + 5 wt% YAG + 3 wt% TiN</td></tr>
<tr><td>24</td><td>β-Sialon + 5 wt% YAG + 10 wt% TiN</td></tr>
</table>

Table 6.1: Samples composition and firing conditions

6.1 Composition, Porosity and Density

6.1.1 Composition by XRD

The unpolished and polished surfaces of each sample have been observed by XRD to determine the chemical composition of the crystalline phases formed after sintering at 1600 ºC. Table 6.2 summarises the samples' composition.

Samples 21, 23 and 24 were composed of β-Sialon (z ≈ 1) and YAG with samples 23 and 24 additionally containing TiN. Sample 24 (10 wt% TiN) also contained a noticeable amount of 15-R Sialon ($SiAl_4O_2N_4$, an AlN polytype – See Figure 6.1 for location on the behaviour diagram).

After the nitridation at 1400 ºC, sample 22 was composed of β-Sialon (z ≈ 1), YAG, TiN, a Y-α-Sialon and $Y_3AlSi_2O_7N_2$ (N-Phase). β-Sialon was the major phase after nitridation. However, after sintering at 1600 ºC, the major phase is Y-α-Sialon with the same compositional parameters measured before sintering (m = 1.62 and n = 0.81). Significant amounts of β-Sialon (z ≈ 1) and 21-R Sialon ($SiAl_6O_2N_6$, an AlN polytype) were also detected. The minor phases are TiN and $Y_2Si_3O_3N_4$, commonly named N-melilite[1]. Yttrium silicon oxynitrides have been previously observed when yttrium oxide is used to promote sintering in silicon nitride and Sialon ceramics[2-4]. Figure 6.1 shows the position of N−melilite in a 3 dimensional representation of the Y-Sialon system.

	β-Sialon (z ≈ 1)	YAG	TiN	15-R	Y-α-Sialon	21-R	N-melilite
Sample 21 (0 wt% TiN)	Major Phase	Minor					
Sample 22 (1 wt% TiN)	Medium		Minor		Major Phase	Medium	Minor
Sample 23 (3 wt% TiN)	Major Phase	Minor	Minor				
Sample 24 (10 wt% TiN)	Major Phase	Minor	Minor	Minor			

Table 6.2: Composition by XRD for samples 21 to 24, following sintering at 1600 °C. White boxes indicate the absence of a species in the corresponding sample.

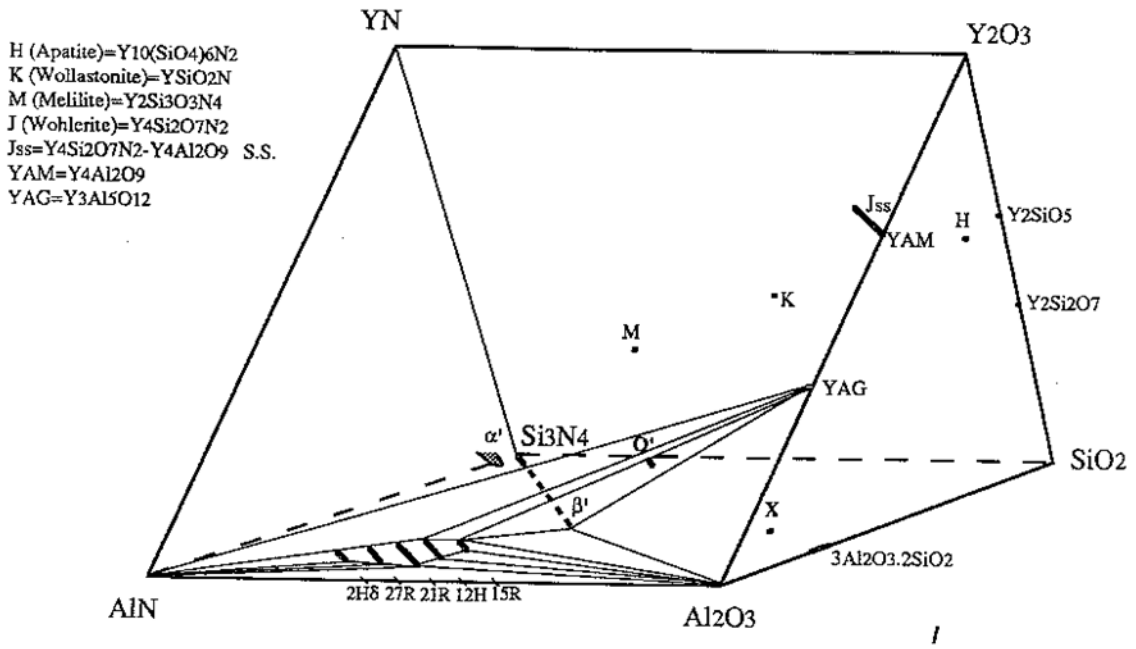

Figure 6.1: Y-Sialon system including the Sialon behaviour diagram[5]. N-melilite is represented by the point M in the YN-Y_2O_3-SiO_2-Si_3N_4 plane.

6.1.2 Porosity and Density

Porosity and density have been measured using the Archimedes' Principle as described in Section 3.4. The samples were carefully cleaned from the residual powder bed and placed under vacuum then impregnated with water. Measurements have been made on 16 samples for each composition. Figure 6.2 shows the evolution of the bulk and apparent densities, as well as the apparent porosity, as a function of the amount of TiN introduced in the Sialon.

The extent of porosity in a ceramic material can vary between 0 and >90 %. The pore size, shape and distribution have a strong influence on many properties[6]. The total porosity includes the open porosity which is connected to the material surface and the closed porosity, where the pores are isolated from one another. In a refractory material, a low porosity is desirable for good strength, load-bearing capacity and corrosion resistance but it may also reduce the fracture toughness as pores may act as 'crack stoppers'. The total porosity can be controlled to achieve desirable mechanical properties but encouraging closed porosity rather than open porosity will enhance the thermal and mechanical properties of refractory materials.

The bulk and apparent densities continuously increase with the amount of added TiN, which has a higher density than Sialon ceramics of approximately 5.2 g.cm^{-3}. The apparent porosity

of Sample 21 (no TiN) was 2.2 %. This figure is low compared to the results obtained in Chapter 3 and can be explained by the higher CIP pressure (150 MPa) used to fabricate these samples. In the 3 wt% TiN and 10 wt% TiN samples (23 and 24), there was almost no residual apparent porosity (less than 0.4 %). This very high densification is due to an increased amount of intergranular phase formed with the introduction of TiN.

Sample 22 (1 wt% TiN) had an apparent porosity of 3.3 %, higher than that of the sample containing no TiN. For this composition, part of the yttrium addition has been incorporated into substitutional sites in the α-Sialon structure, thereby reducing the amount of intergranular phase.

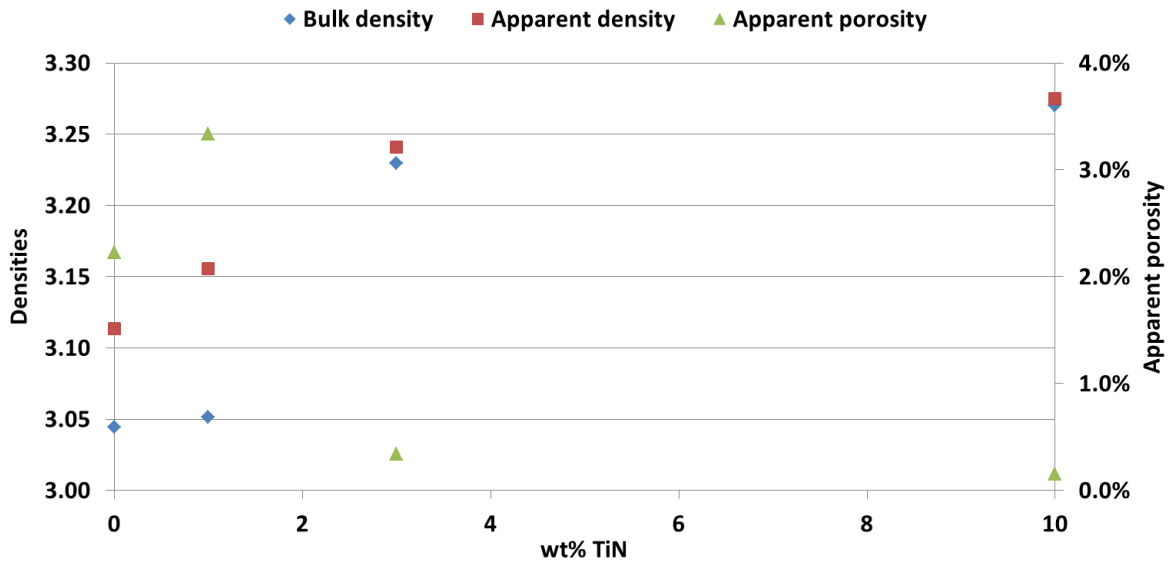

Figure 6.2: Porosity and density of samples 21 to 24 (Sialon + 5 wt% YAG + 0-10 wt% TiN), sintered at 1600 °C.

6.2 Composite Microstructure

Generally, refractories are multiphase materials composed of large grains bound with finer grains and sometimes amorphous phases and pores. The microstructure has a major influence on the properties of a material. For example, elongated grains will increase the fracture toughness (by increasing the crack path length and dispersing the crack energy) whereas the presence of numerous small pores will result in poor strength. Changing pre-firing processing and firing conditions are some of the ways to control the microstructure. Samples have been examined by scanning electron microscopy and its EDS attachment to identify the different phases. Most of the imaging work has been undertaken on the FEI Nova NanoSEM 450 FEG which allows greater magnification than the FEI Quanta 450. It has been found that because

of the high vacuum in the Nova SEM, the use of carbon tape to ensure electrical conductivity and avoid sample charging also increases the sample image drifting. Consequently the carbon tape was replaced by copper tape which creates less outgassing and therefore less drifting. Figure 6.3 shows the SEM micrographs of the polished surfaces of samples 21, 23 and 24.

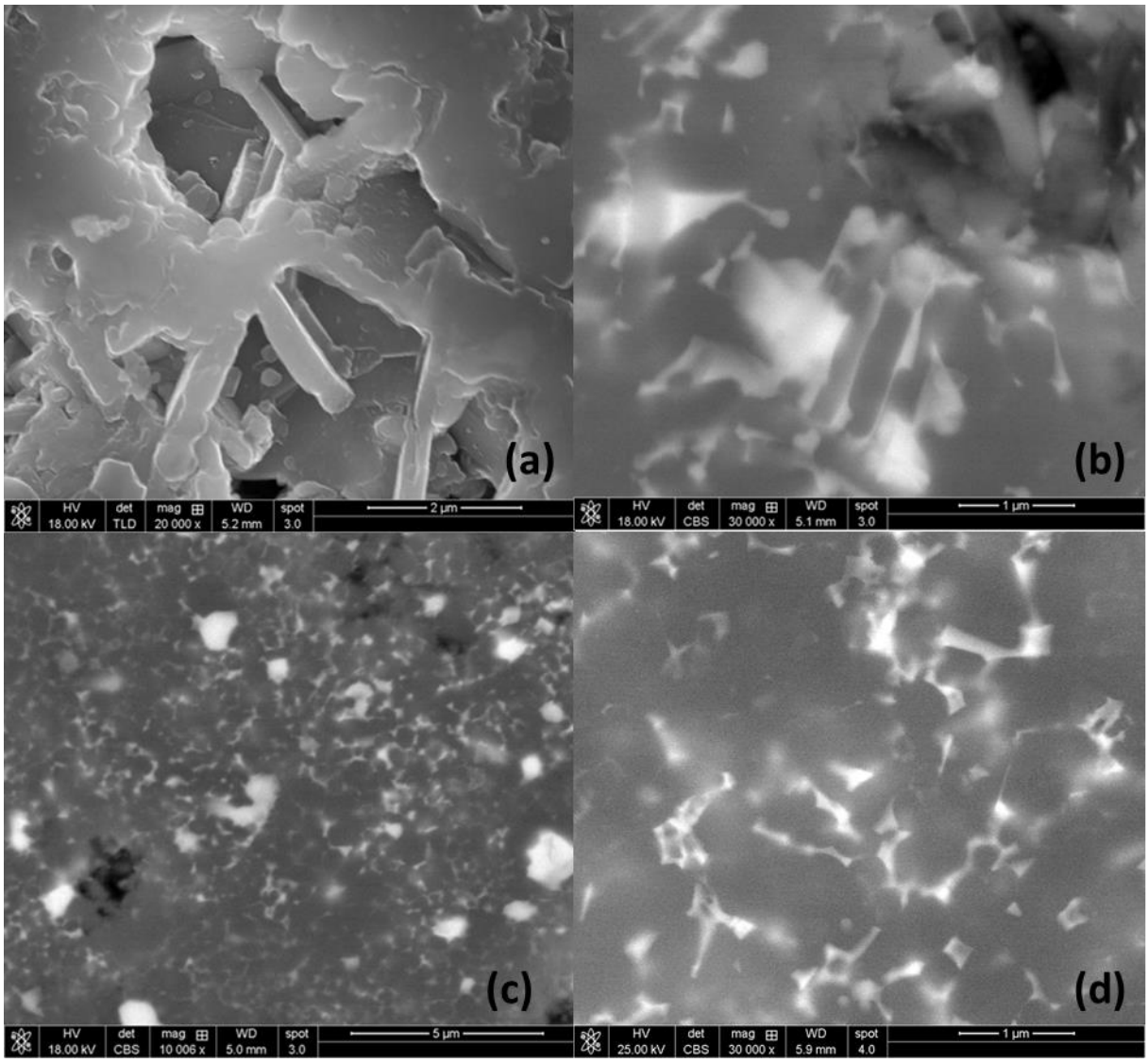

Figure 6.3: SEM micrographs of the polished surface of Sialon/TiN composites samples. (a) Sample 23 showing elongated grains in an open pore, scale bar = 2 µm. (b) Backscattering image of sample 23 showing elongated hexagonal grains of β-Sialon in an yttrium rich intergranular phase, scale bar = 1 µm. (c) Backscattering image of sample 24 showing the β-Sialon grains in the yttrium rich intergranular phase and the larger white grains of TiN, scale bar = 5 µm. (d) Backscattering image of sample 21 showing the β-Sialon grains in the yttrium rich intergranular phase, scale bar = 1 µm.

The characteristic hexagonal shape of β-Sialon was observed in every sample including in open pores (Figure 6.3a and Figure 6.3b). The β-Sialon grains were surrounded by an

intergranular phase which includes the crystalline YAG as shown in Figure 6.3b to Figure 6.3d. The white and larger TiN particles were dispersed in the composite but do not form a continuous network (as can be seen in Figure 6.3c). Figure 6.4 displays the EDS analysis of the white particles observed in Figure 6.3c. Titanium was not detected by EDS in the intergranular phase, although the sample drifting did not allow an accurate analysis on such small areas.

The β-Sialon grains are smaller (< 2 µm) than those observed in Chapter 4 (up to 5 µm) which is typical of β-Sialon with lower z-values[7].

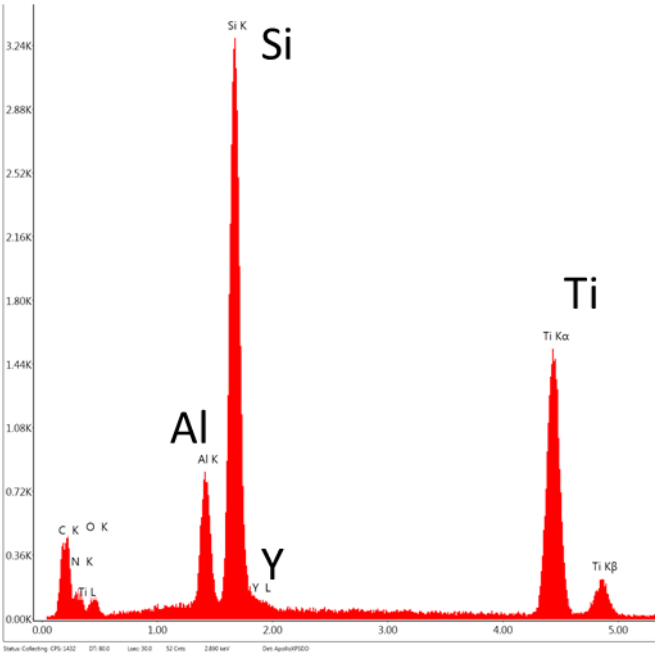

Figure 6.4: EDS analysis of a white particle observed in Figure 6.3c. The large detection of Si is due to the interaction volume of the EDS analysis which is larger than the white particles.

Sample 22 reveals a large amount of porosity. The polished sample surface observed in the micrographs (See Figure 6.5) reveals a combination of open and closed porosity. The formation of α-Sialon requires the absorption of yttrium into structural sites in the Sialon phase and therefore reduces the amount of intergranular phase, which substantially increases the porosity of the material.

The matrix of this sample was formed from the Sialon phases (in Figure 6.5, β-Sialon is dark grey, Y-α-Sialon is light grey), including the Sialon 21-R polytype. The different Sialon phases are identified by both a visual estimation of their volume compared with the XRD peak intensities and their colour in backscattering images: the light grey phase appears larger and the average atomic number ($\bar{Z}$) of the best matching ICDD pattern α-Sialon

($Y_{0.54}Si_{9.57}Al_{2.43}O_{0.81}N_{15.19}$, $\bar{Z} = 10.49$) is higher than that of the β-Sialon (Si_5AlON_7, $\bar{Z} = 10$). The N-melilite has agglomerated in patches as shown in Figure 6.5 (large white particles) dispersed through the sample. The TiN particles also appeared white in the micrographs but they were smaller and more discrete than those of the N-melilite. (See Figure 6.6 for EDS analysis of the white particles observed in Figure 6.5).

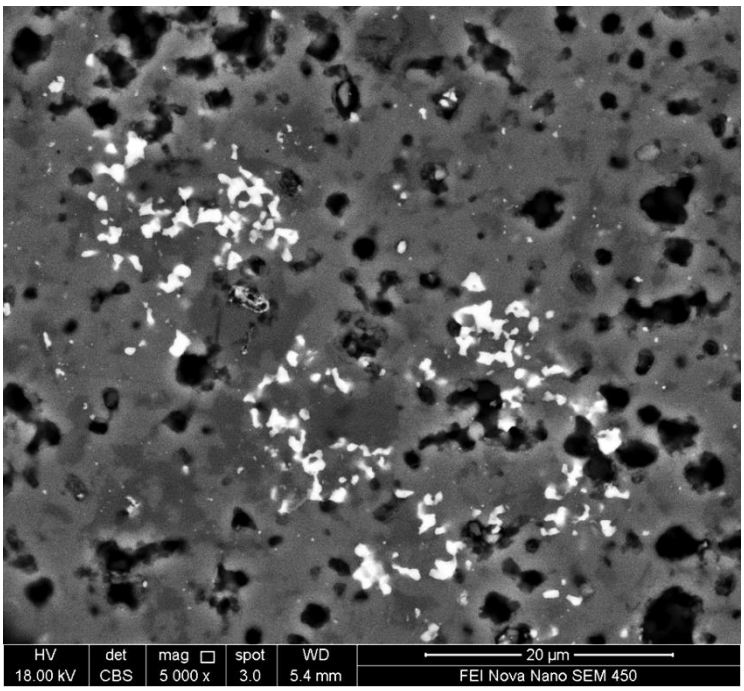

Figure 6.5: SEM micrograph of the polished surface of sample 22 showing the white N-melilite and TiN particles in the Sialon matrix, and pores.

On the polished surface, some large golden coloured particle agglomerates were visible, measuring about 1 mm long. The golden colour indicates a high concentration of TiN which was confirmed by EDS. Figure 6.7 shows the SEM micrographs of one of these particles and reveals how the TiN particles were dispersed through it. The white grains of TiN were heterogeneously dispersed (see Figure 6.7) in a high aluminium content Si-Al-O-N phase as shown in Figure 6.8. This phase is likely to be 21-R ($SiAl_6O_2N_6$) because it is the crystalline phase detected by XRD with the highest Al:Si ratio. In Figure 6.8, small EDS peaks of titanium and carbon appeared. The former is a consequence of the depth of the EDS analysis beam which may penetrate further than the analysed grains, thereby revealing deeper subsurface grains. The latter was due to the sample being coated with carbon to ensure electrical conductivity in the SEM.

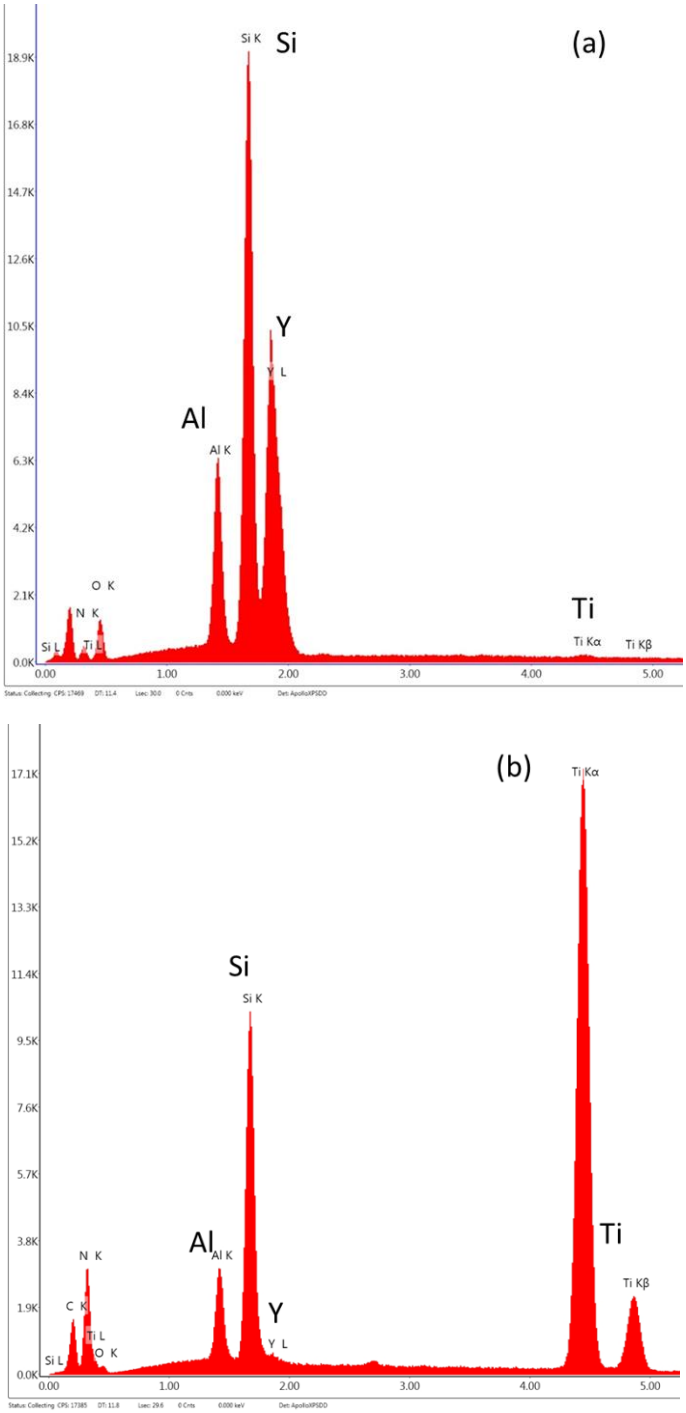

Figure 6.6: EDS analysis on (a) the large agglomerated and (b) the small dispersed white particles observed in Figure 6.5.

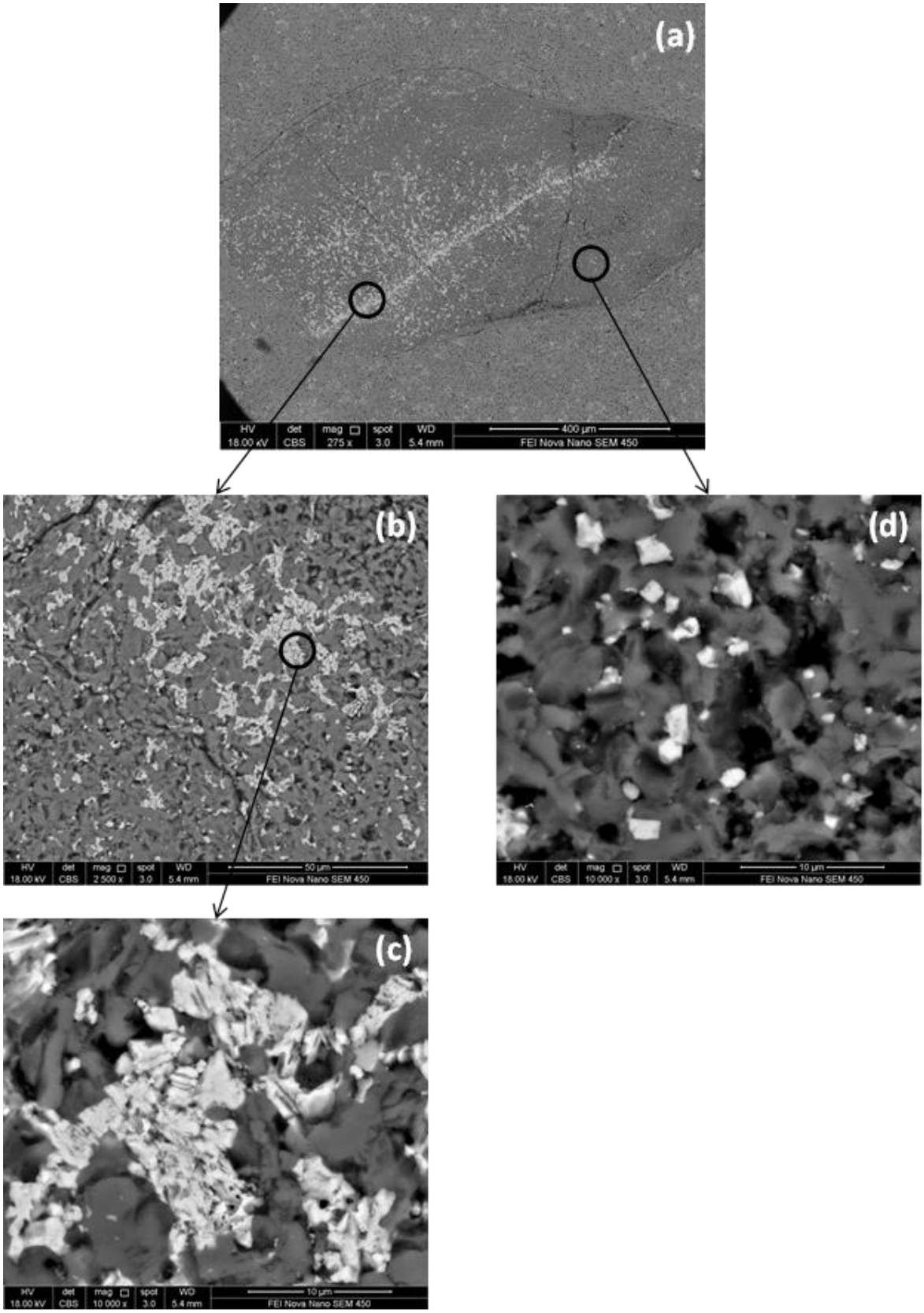

Figure 6.7: SEM Micrographs of the polished surface of sample 22 showing (a) a golden particle on the surface, (b) and (c) a TiN high density area, and (d) a TiN-rich low density area.

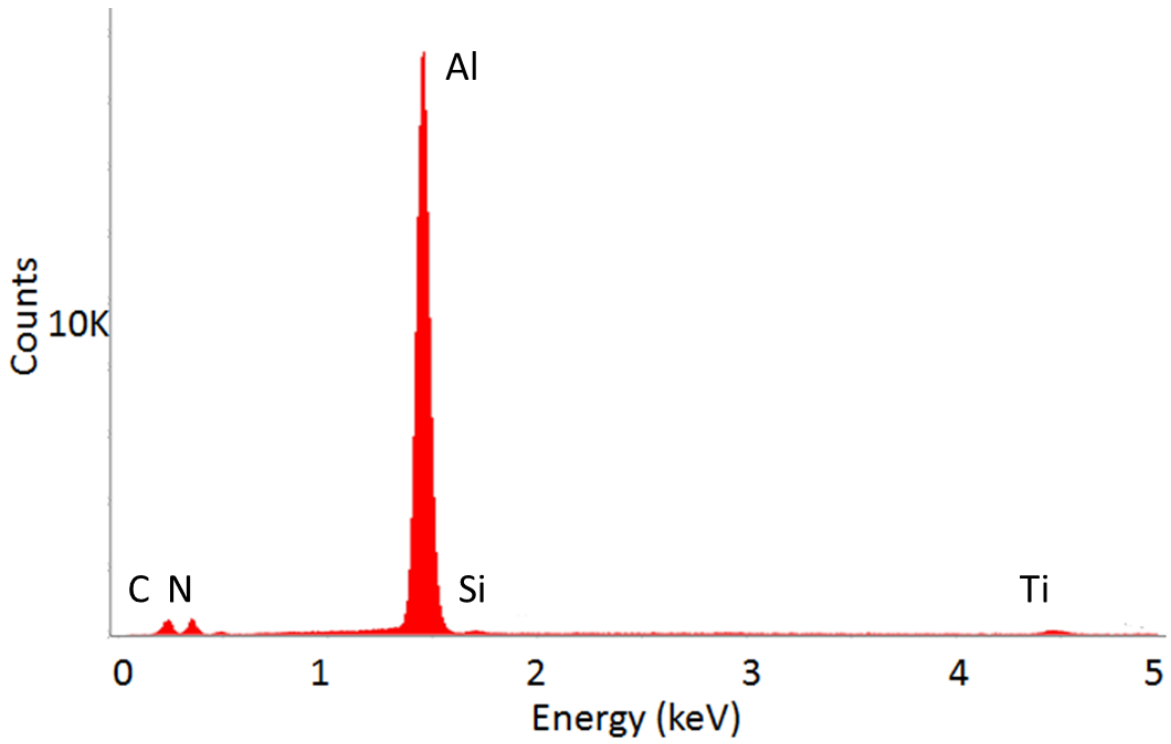

Figure 6.8: EDS analysis of the dark phase surrounding the TiN grains in the golden particles (see Figure 6.7).

6.3 Hardness and Toughness by Vickers Indentation

6.3.1 Young's Modulus Measurement

Young's modulus or Elastic modulus quantifies the ability of a material to elastically resist the stress of a load. This is an important mechanical property for refractories, especially those which have to withstand the weight or the mechanical shock of molten metal.

The Young's modulus of these samples must be measured as this value is included in the toughness calculation (Equation 3.12). The longitudinal wave transit time was measured on seven samples per composition and Young's modulus was calculated using Equation 3.7. The Poisson's ratio was estimated to be 0.27[8, 9]. The Young's modulus results are displayed in Figure 6.9.

Kokmeijer[10] measured the mechanical properties of a hot-pressed β-Sialon with CaO or CeO_2 additives and reports other values found in the literature. All the authors mentioned, including Kokmeijer, found that the nature and concentration of the additive have no influence on the Young's modulus of β-Sialon ceramics. It appears that the Young's modulus of the β−Sialon/TiN composites (samples 21, 23 and 24) observed in this study greatly increased with the amount of TiN. This increase cannot be explained by the observation made

by Vepřek[11] that the smaller the TiN grains the higher the Young's modulus of a TiN/Si_3N_4 composite: a SEM observation of the samples showed that the TiN grains are the same size and more numerous as the concentration increases. The Young's Modulus of pure TiN has been reported to be up to 600 GPa[12], much greater than that of Sialon ceramics. The particles of TiN are dispersed discretely in the Sialon matrix (See Figure 6.3). It is clear that increasing the amount of TiN has a noticeable effect on the Young's modulus of the composite. However, this is not a linear increase as the degree of TiN particles dispersion and contact have an impact on the overall material modulus.

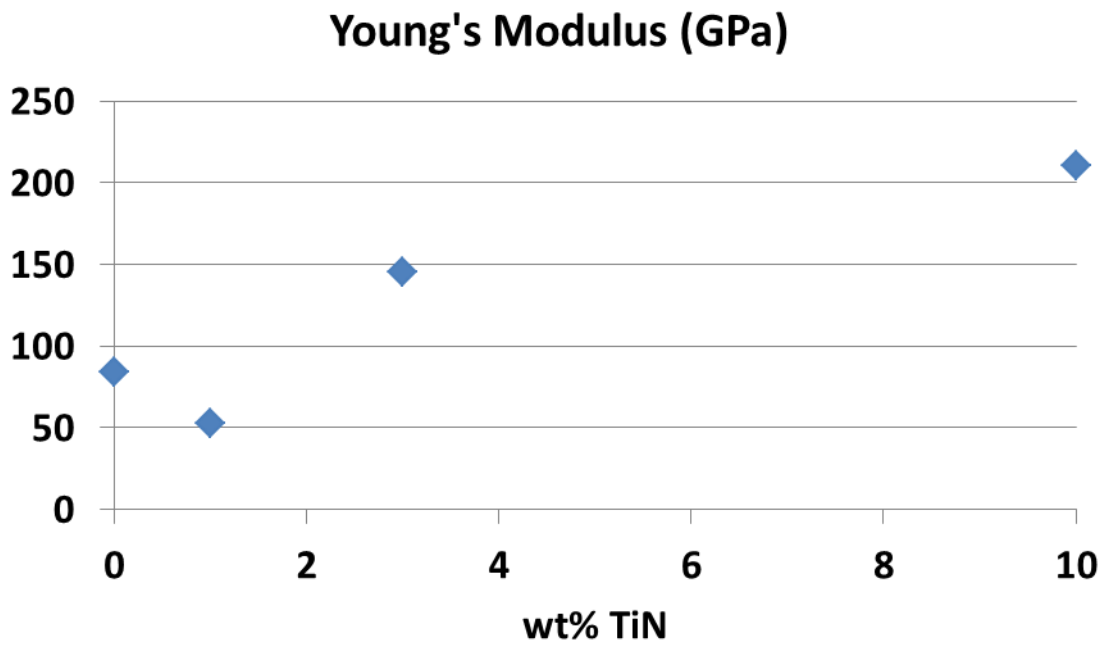

Figure 6.9: Evolution of the Young's modulus as a function of the TiN concentration.

It has been shown in Chapter 4 that the measurement of Young's modulus was not suitable to assess the resistance to thermal shock of these samples. This measurement was therefore only used to calculate the fracture toughness by Vickers indentation.

6.3.2 Hardness and Fracture Toughness Measurement

Hardness and fracture toughness are properties that are usually considered together as the former measures the capacity to resist surface penetration while the latter is related to the resistance to crack propagation. Both properties are industrially important: for refractory applications, materials need to resist loads and cracks created by thermal expansion; cutting tools and milling media are required to be harder than the material that they must cut or mill

and to have a high fracture toughness to resist mechanical shocks and thermal expansion in cutting conditions.

Hardness and fracture toughness have been measured by Vickers indentation under a 10 kg load as described in Section 3.10, and calculated using Equations 3.11 and 3.12. Three samples for each composition were polished to a 3 µm finish and five indents have been made on each sample. When the diamond had not indented the surface properly (because of misplacement of the sample on the equipment or a surface not being perfectly flat), the result was ignored resulting on a minimum of twenty values for each composition. Moreover, the only indenter available had a small crack on the edge of the diamond resulting in slightly higher hardness results. Calibration has been made on a calibration block with a theoretical hardness of 726HV10 or 7.12 GPa. The measured hardness was 743HV10 or 7.29 GPa.

The hardness and fracture toughness results are displayed in Figure 6.10.

The hardness of samples 21, 23 and 24 increased with the amount of TiN from 16±2 to 17.7±1.2 GPa which are high values for the β-Sialon phase. This observed increase was mostly due to the decrease of the apparent porosity (See Figure 6.2) but also to the contribution from the very high hardness of TiN (up to about 49 GPa[11]). Sample 22 exhibited a hardness of 16.1±1.7 GPa. α-Sialons are known for their higher hardness amongst the Sialon phases and this value was reduced by the presence of β-Sialon and 21-R Phase.

The fracture toughness of samples 21, 23 and 24 was also shown to increase with the amount of TiN from 1.6±0.3 to 3.3±0.1 $MPa.m^{-1/2}$. Although it is usually observed that hardness and fracture toughness evolve in opposite ways, these values were improved by a lower porosity and a higher grain/intergranular phase volume ratio as the TiN concentration increased. The more grains in the material the more the propagation of cracks through the weaker intergranular phase is constrained. The fracture toughness for sample 22 was measured as 1.7±0.5 $MPa.m^{-1/2}$ but the porosity of this sample was high (See Figure 6.5) and most cracks ended in a pore. The area containing golden grains observed on the sample surface and shown in Figure 6.7 was not included in the measurement and therefore the measured area contained less than 1 wt% TiN. There is a caveat on this result as the crack propagation was prematurely stopped in the pores rather than finishing in the solid material.

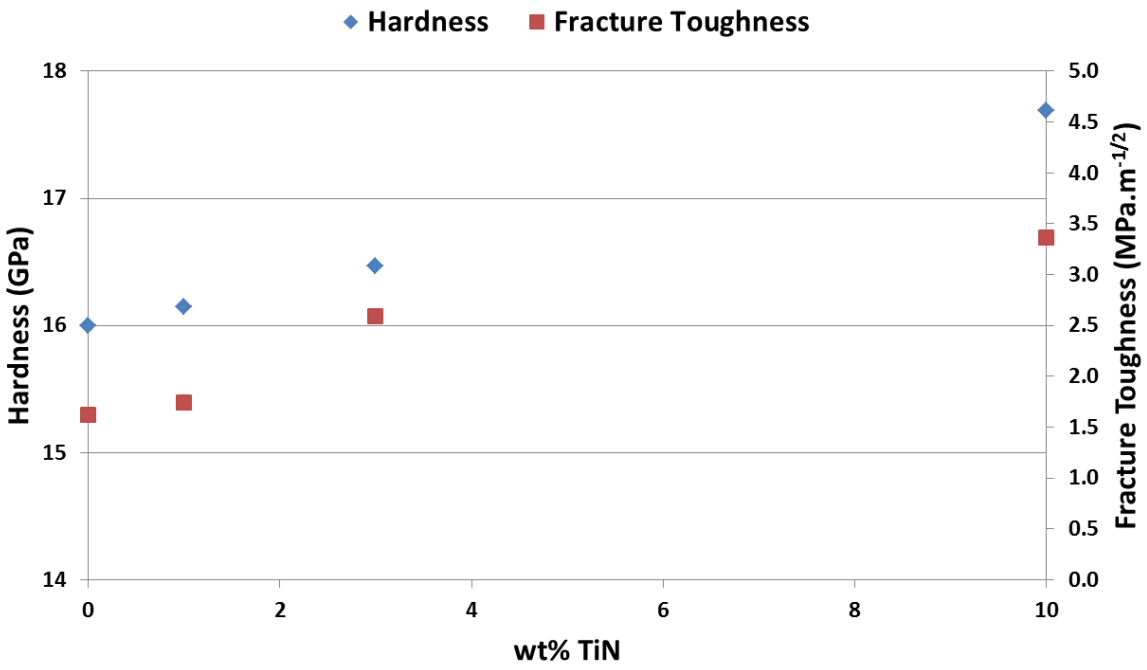

Figure 6.10: Hardness and fracture toughness by Vickers indentation for samples 21 to 24. Measurement and reproducibility errors are indicated in the text.

6.4 Compressive Strength and Resistance to Thermal Shock

A high compressive strength gives materials a good resistance to heavy loads. This is an essential requirement for refractory materials for aluminium processing which are exposed to mechanical pressure from the molten metal and from the static loading of multiple layers of refractory blocks. This characteristic also needs to be retained during sustained thermal exposure.

Compressive strength measurements were undertaken on at least ten samples per composition as described in Section 3.11. Half of the samples were exposed to a thermal shock of 400 ºC using a vertical tube furnace (See Figure 3.6d) set to 420 ºC prior to the test. Samples for this measurement have been carefully selected, avoiding any obvious defects such as cracks or deformation created during prior processing.

Results for the unquenched and quenched samples are shown in Figure 6.11.

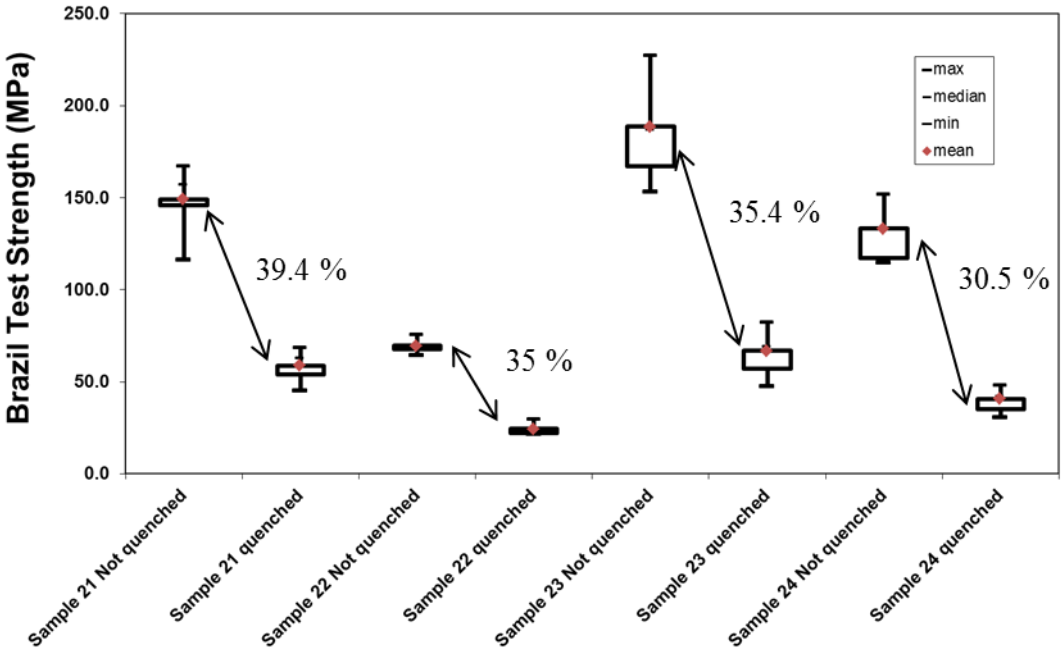

Figure 6.11: Compressive strength and effect of thermal shock on Sialons/TiN composites. Percentages represent the strength loss.

The presence of TiN does not have a substantial effect on the compressive strength before quenching. The lower value for sample 22 (1 wt% TiN) can be understood by its different composition (primarily Y-α-Sialon rather than β-Sialon) and higher porosity. Micro-cracks, visible only by optical microscopy, and pores have an impact on the compressive strength and also explain the dispersion of results.

The measured strength loss is similar for all the samples which means that the presence of such small volumes of TiN has no significant effect on the resistance to thermal shock of these β-Sialon composites.

6.5 Electrical Conductivity

6.5.1 Electrical Conductivity Measurement

Electrical conductivity has been measured at ambient temperature because electrical discharge machining (see Section 2.4.1) is normally undertaken in these conditions. In the present experiments, silver paste was applied as the electrode material and dried at 110 ºC for an hour.

D.C. conductivity measurement has been undertaken with the assembly schematically described in Figure 6.12. One of the electrodes was guarded to measure a volume conductivity rather than a surface conductivity along the sample edge. Because this

measurement is very temperature sensitive, the sample was placed into an oven (Delta 9023) equipped with source (Keithley 230 Programmable Voltage Source) and ampere-meter (Keithley 485 Autoranging Picoammeter) adapter to keep the sample at constant temperature (20−150 ºC). The voltage sent through the sample was 100 V, the maximum voltage delivered by the source. No D.C. measurement was obtained at ambient temperature as Sialon ceramics are very strong insulators and the capacitance seen was lower than the ampere-metre limit of a few pF.

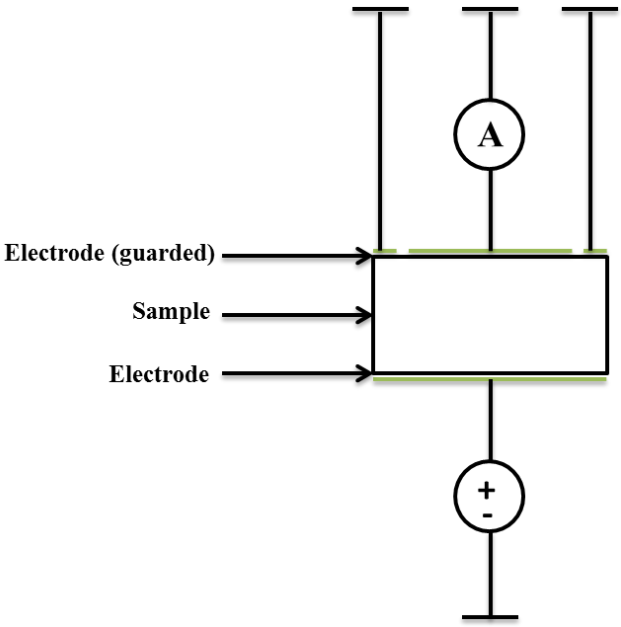

Figure 6.12: D.C. conductivity measurement.

The A.C. electrical conductivity of samples 21 to 24 was measured by a two-probe method (See Section 3.12) using a Agilent 4294A Precision Impedance Analyser and a Hewlett-Packard 16047D Test Fixture. The A.C. current was set to 1 V which is the maximum voltage delivered by the analyser and measurements were made at 40 and 500 Hz at ambient temperature. The band width was set to a high setting (small band width) to obtain a higher precision on low frequency results.

The electrical permittivity was calculated using the following equation:

$$\varepsilon = (C * H)/(\varepsilon_0 * S) \qquad \text{(Eq 6.1)}$$

Where ε is the permittivity of the material in $F.m^{-1}$, C is the capacitance in F, H is the sample height in m, ε_0 is vacuum permittivity with $\varepsilon_0 = 8.85 \times 10^{-12}$ $F.m^{-1}$, and S is the sample surface area in m^2.

Permittivity of samples 21 to 23 reached the value of about 9.5 $F.m^{-1}$, which is in the high range for these Sialon ceramics[13]. The effect of TiN is only visible for sample 24 (10 wt% TiN) which had a permittivity of 10.8 $F.m^{-1}$.

For the A.C. electrical conductivity measurement, the analyser was set by default to model the measured material with a series circuit and the measurements were collected this way. But this kind of circuit has no conductivity at low frequencies and is therefore not suitable to model this ceramic material. It is possible to convert the resistance and reactance of the series circuit model (R_S and X_S, respectively) to those of a parallel model (R_P and X_P, respectively) with Equations 6.7 and 6.8. Figure 6.13 explains the calculation details.

The introduction of a small volume of TiN (0.6-6.5 vol%) in these samples was insufficient to improve the electrical conductivity of these Sialon/TiN composites. The electrical conductivity was measured for all the samples in the range of 10^{-7} $S.m^{-1}$ at 40Hz and 10^{-4} $S.m^{-1}$ at 500Hz.

If the charge carriers in the material are dominating the electrical conductivity measurement, the conductivity would be higher at low frequency where charged species have more time to move through the sample. If the dielectric loss is the dominating mechanism, the conductivity would be higher at high frequency which enhances the effect of the species polarity. The very low D.C. conductivity measurement showed that the dielectric loss is the prevailing phenomenon in these materials and therefore the electrical conductivity was expected to be lower at low frequency.

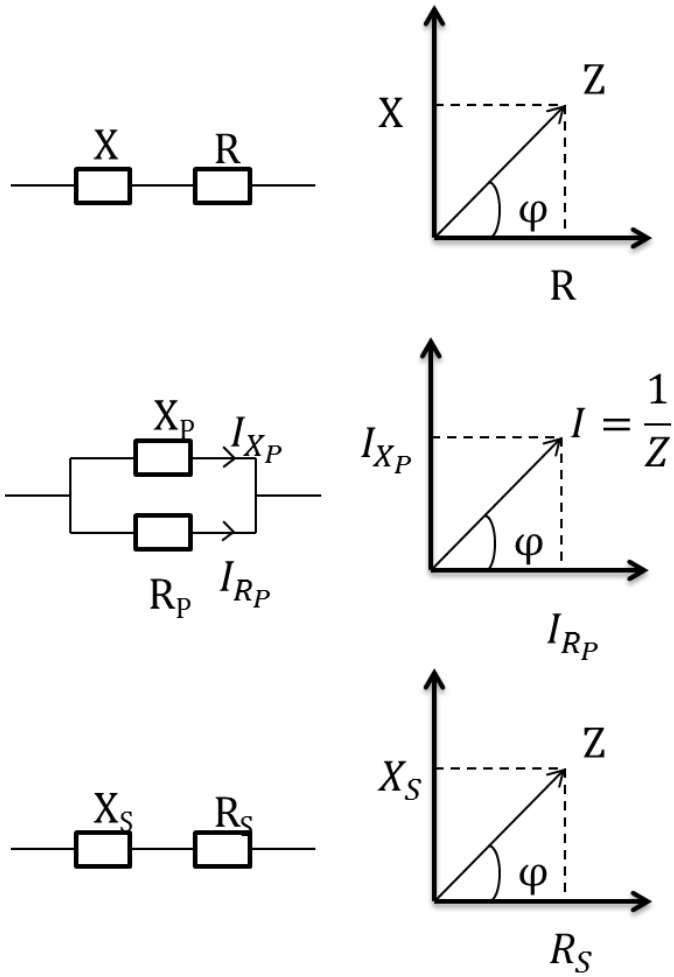

$$Z = R + iX \quad \textbf{(Eq 6.2)}$$

$$Z^2 = R_S{}^2 + X_S{}^2 \quad \textbf{(Eq 6.3)}$$

$$I_{X_P} = \frac{1}{Z}\tan\varphi \quad \textbf{(Eq 6.4)}$$

$$I_{R_P} = \frac{1}{Z}\cot\varphi \quad \textbf{(Eq 6.5)}$$

$$\tan\varphi = \frac{X_S}{R_S} \quad \textbf{(Eq 6.6)}$$

Figure 6.13: Calculation details for conversion from series circuit model to parallel circuit model.

By combining all the previous equations, R_S and X_S can be converted to R_P and X_P:

$$X_P = \frac{1}{I_{X_P}} = \frac{z}{\tan\varphi} = \frac{\sqrt{X_S{}^2 + R_S{}^2}}{X_S/R_S} \quad \text{(Eq 6.7)}$$

$$R_P = \frac{1}{I_{R_P}} = \frac{z}{\cot\varphi} = \frac{\sqrt{X_S{}^2 + R_S{}^2}}{R_S/X_S} \quad \text{(Eq 6.8)}$$

6.5.2 Electrical Conductivity Improvement

The low level of addition of electrically conductive particles (up to 6 vol% TiN) does not noticeably improve the electrical conductivity of these Sialon composites. For these micron-sized particles, the literature reports a percolation threshold of 20 vol% TiN[14]. Therefore a simple way to improve the electrical conductivity of these composites would be to increase the added volume of TiN. However, the more TiO_2 that is introduced in the starting mix the more Al_2O_3 is produced. This alumina excess would need to be counterbalanced to obtain the

desired z-value. It could be achieved, up to the desired amount, by further addition of yttria with no addition of the extra alumina required to form YAG.

Another solution to increase the electrical conductivity without achieving the percolation threshold would be to modify the particles shape and size. Ayas et al.[15] fabricated an electrically conductive Sialon-TiCN composite with only 5 vol% nano-sized TiCN. Forming the electrically conductive phase with a plate, whisker or fibre shape could be a way to get around the large volume of conductive phase needed to create electrical conductivity. To further reduce the percolation threshold, these asymmetric particles would need to be aligned, for example by slip casting.

6.6 Summary

In this chapter, the chemical, mechanical and electrical properties of the material fabricated by the newly developed processed described in Chapter 5 have been measured. These properties have been compared with those of a β-Sialon, including 5 wt% YAG, fabricated by reaction bonding from a mix of alumina, aluminium nitride, silicon and yttria at 1600 ºC.

The reference sample fabricated by reaction bonding was composed of the expected β-Sialon and YAG, as well as the samples containing 3 and 10 wt% TiN. The latter also contained some 15-R Phase. The microstructure of these samples was similar with hexagonal grains of β-Sialon surrounded by an intergranular phase containing YAG and TiN. The apparent porosity decreases to a very low level (< 0.4 %) for the 3 and 10 wt% TiN materials.

The sample containing 1 wt% TiN reacted to form Y-α-Sialon as well as β-Sialon, 21-R Phase, TiN and N-melilite ($Y_2Si_3O_3N_4$). The apparent porosity of this sample was relatively high (3.3 %) and polishing revealed an even greater amount of closed porosity. In this sample, the microstructure developed in an unusual way with agglomeration of the N-melilite and TiN and no observable Sialon characteristic microstructure.

Table 6.3 summarises the results obtained for the physical and electrical properties

	Young's modulus (GPa)	Hardness by Vickers 10 kg (GPa)	Fracture Toughness ($MPa.m^{-1/2}$)	Compressive strength (MPa)	Compressive strength after 400 ºC thermal shock (MPa)	A.C. Electrical conductivity 500Hz ($S.m^{-1}$)
Sample 21 (0 wt% TiN)	84±19	16±2	1.6±0.3	149±22	58±12	$4.40x10^{-4}$
Sample 22 (1 wt% TiN)	53±15	16.1±1.7	1.7±0.5	69.6±4.5	24.4±3.6	$2.29x10^{-4}$
Sample 23 (3 wt% TiN)	145±16	16.46±1.41	2.6±0.3	188±33	67±16	$8.18x.10^{-4}$
Sample23 (10 wt% TiN)	210±11	17.7±1.2	3.3±0.1	133±19	41±8	$4.43x10^{-4}$
YAG	-	-	-	-	-	$4.64x10^{-4}$
TiN	600[12]	49[11]	7[16]	-	-	-

Table 6.3: Physical and electrical properties of the studied materials.

6.7 Chapter Six Bibliography

1. Fang, C.M., De Wijs, G.A., De Groot, R.A., Metselaar, R., Hintzen, H.T., and De With, G., *O/N ordering in $Y_2Si_3O_3N_4$ with the melilite-type structure from first-principles calculations*. Chem Mater, 2000, **12**[4], pp. 1071-75.
2. Rae, A.W.J.M., Thompson, D.P., Pipkin, N.J., and Jack, K.H., *The Structure of Yttrium Silicon Oxynitride and its Role in the Hot-Pressing of Silicon Nitride with Yttria Additions.* In Special Ceramics **6**, 1975, ed. by P.Popper, publ. BCRA, Stoke-on-Trent, pp. 347-60.
3. Cheng, Y. and Thompson, D.P., *Aluminum-containing nitrogen melilite phases*. J Am Ceram Soc, 1994, **77**[1], pp. 143-48.
4. Sun, W.Y., Tien, T.Y., and Yen, T.S., *Solubility of a'-SiAlON Solid Solutions in the System Si,Al,Y/N,O*. J Am Ceram Soc, 1991, **74**[10], pp. 2547-50.
5. Sun, W.Y., Tien, T.Y., and Yen, T.S., *Subsolidus Phase Relationship in Part of the System Si,Al,Y/N,O: The System Si_3N_4-AlN-YN-Al_2O_3-Y_2O_3.* J Am Ceram Soc, 1991, **74**[11], pp. 2753-58.
6. Kingery, W.D., Bowen, H.K., and Uhlmann, D.R., In *Introduction to Ceramics - 11. Microstructure of Ceramics*. Ed. by Wiley-Interscience Publication, New York, 1976, pp. 540-548.
7. Hyuga, H., Yoshida, K., Kondo, N., Kita, H., Sugai, J., Okano, H., and Tsuchida, J., *Fabrication of presureless sintered dense β-SiAlON via a reaction-bonding route with ZrO_2 addition*. Ceram Int, 2009, **35**[5], pp. 1927-32.
8. Fukuhara, M. and Yamauchi, I., *Temperature dependence of the elastic moduli, dilational and shear internal frictions and acoustic wave velocity for alumina, (Y)TZP and β'-sialon ceramics*. J Mater Sci, 1993, **28**[17], pp. 4681-88.
9. Shimada, S., Aoki, T., Mackenzie, K.J.D., Okutani, T., and Shimokawa, K., *Oxidation and mechanical behavior of carbothermal β-SiAlON ceramics*. J Ceram Soc Jap, 1999, **107**[9], pp. 786-90.
10. Kokmeijer, E., de With, G., and Metselaar, R., *Microstructure and mechanical properties of β'-$Si_3Al_3O_3N_5$ ceramics*. J Eur Ceram Soc, 1991, **8**[2], pp. 71-80.
11. Vepřek, S., Reiprich, S., and Shizhi, L., *Superhard nanocrystalline composite materials: The TiN/Si_3N_4 system*. Applied Physics Letters, 1995, **66**, pp. 2640.
12. Vijgen, R.O.E. and Dautzenberg, J.H., *Mechanical measurement of the residual stress in thin PVD films*. Thin Solid Films, 1995, **270**[1-2], pp. 264-69.
13. Kim, D.K., Kim, H.N., Seong, Y.H., Baek, S.S., Kang, E.S., and Baek, Y.G., *Dielectric properties of SiAlON ceramics*. Key Eng Mat, 2009, **403**, pp. 125-28.
14. Gao, L., Li, J., Kusunose, T., and Niihara, K., *Preparation and properties of TiN-Si_3N_4 composites*. J Eur Ceram Soc, 2004, **24**[2], pp. 381-86.
15. Ayas, E. and Kara, A., *Novel electrically conductive α-β Sialon/TiCN composites*. J Eur Ceram Soc, 2011, **31**, pp. 903-11.
16. Holmberg, K., Laukkanen, A., Ronkainen, H., Wallin, K., and Varjus, S., *A model for stresses, crack generation and fracture toughness calculation in scratched TiN-coated steel surfaces*. Wear, 2003, **254**[3–4], pp. 278-91.

Chapter Seven: Oxidation Resistance of Sialon/TiN Composites

Nitrogen ceramics are thermodynamically unstable compared to their oxides[1]. However, a protective oxide film can be formed, through which diffusion is slow. This has the effect of increasing the failure temperature of the material. In industrial conditions, Sialon objects can be exposed to highly oxidising atmospheres such as in high temperature refractory use or at the contact points of cutting tools in engineering applications. To evaluate their resistance to such conditions, Sialon and Sialon/TiN composite samples have been fired in an oxidising atmosphere (air at atmospheric pressure and humidity) in a tube furnace at temperatures in the range 900 to 1300 ºC for two hours. Loosely packed Kaowool® fibre was placed in the ends of the furnace tube to reduce thermal radiation losses, while maintaining an open air atmosphere.

Usually the oxidation behaviour is quantified by measuring the weight gain and calculating the oxidation constant from the parabolic increase of the weight gain with time[2]. In this study, to evaluate the surface damage caused by the oxidising atmosphere, the elemental density on the surface of the samples was observed by Ion Beam Analysis (IBA) techniques at GNS Science, Lower Hutt. The ion beam dimension is 2 mm in diameter. To prepare samples for IBA, 20 mmØ sample discs were polished down to 1 µm finish then cut in quarters with the diamond saw.

Nuclear analysis techniques are very efficient tools to characterise the composition of matter at the atomic level. These techniques are usually non-destructive although a prolonged exposure to the beam could make significant changes in the material surface by the removal of atoms.

Ion beams are produced from an accelerator with energy in the range of tens of keV to a few MeV. Accelerated ions can include protons ${}^{1}_{1}\mathrm{H}^{+}$, deuterons ${}^{2}_{1}\mathrm{H}^{+}$, single charged helium ions ${}^{4}_{2}\mathrm{He}^{+}$ and, α-particles ${}^{4}_{2}\mathrm{He}^{2+}$.

Samples were mounted on sample holders with carbon tape as shown in Figure 2.13c to ensure electrical conductivity and placed into the chamber under a 10^{-5} mbar vacuum.

In this chapter, the sample numbers refer to Table 6.1, namely 21 (0 wt% TiN), 22 (1 wt% TiN), 23 (3 wt% TiN) and 24 (10 wt% TiN).

7.1 Ion Beam Analysis Techniques

This study applies three IBA techniques to analyse surface changes in the Sialon ceramic composition following their controlled oxidation. These techniques - Rutherford Backscattering (RBS), Nuclear Reaction Analysis (NRA) and Particle-Induced Gamma Emission (d-PIGE) - offer different elemental analysis targets covering the full range of elements of interest in this study namely, Si, Al, O, N, Y and Ti. The IBA techniques typically have a depth of analysis of a few microns.

RBS observes the elastic scattering of the particle beam from the target nuclei. It was performed with a 2 MeV ^{4}He incident beam. This technique has good sensitivity for the heavier elements in the sample, and was therefore used to characterise silicon, aluminium, titanium and yttrium. Particles are collected at a backscattering angle at 165º with a silicon surface barrier (SSB) detector after collision with the sample. Energy calibration was made using the following materials: solid Si20Ag and Si_3N_4 formed by chemical vapour deposition (CVD). The Ag, Si and N edges in the spectra were used for energy calibration and solid (x-axis)-angle.

NRA examines the reactions that can occur between the target nuclei and the particles in the beam which result in the emission of discrete ions that have a characteristic energy. It is sensitive for detecting light elements (Z = 1-15). In this study, the ^{14}N(d, α_0) reaction was observed using a 1.4 MeV deuteron beam. At low energy levels (< 7.5 keV), the α-induced reactions of silicon, carbon and oxygen create interferences and make the lower energy reactions unsuitable for analysis. To remove the flux of the elastically scattered primary beam, a Mylar filter of 14 µm was placed in front of the detector to allow only the most energetic particles to pass through and avoid saturation of the detector. This filter allows the detector to be moved closer to the sample to get a higher count rate however it also has the effect of reducing the achievable depth resolution. A TiN sample was used as the N standard.

The d-PIGE technique refers to gamma-rays produced when an incident beam of protons interacts with the nucleus of an element which emits gamma-ray photons of characteristic energy. This detector enables the detection of ^{16}O in the sample. The oxygen concentration is calculated from the yield from the 871 keV gamma ray peak. A SiO_2 sample was used as the oxygen standard.

Table 7.1 summarises the different detector characteristics.

Detector	Detection angle	Filter	Species detected
RBS – SSB	165º	-	Si, Al, Ti, Y
NRA – SSB	150º	14 µm Mylar	N
PIGE – High purity Ge	90º	-	O

Table 7.1: Detectors used for IBA

7.2 Oxidation Process Observed by SEM Imaging & XRD

7.2.1 Sample Appearance and Microstructure

The samples appearance changed substantially as the firing temperature increased. All compositions followed the same time/temperature oxidation scheme but shell layers did not appear at the same temperature and with the same intensity. In Figure 7.1a, the mirror polished surface (1 µm finish) of an unfired sample can be seen beside the most extreme change observed: after the firing at 1300 ºC, Sample 23 was covered with bubbles which strongly suggest the formation of a liquid phase during the oxidation process. These bubbles were first observed at 1250 ºC on all the samples. From 1100 ºC for Sample 21 and 1200 ºC for the other samples, a shell layer can be observed on the samples as shown in Figure 7.1b. Figure 7.2 illustrates the different regions of the samples described in this chapter: the top surface polished before oxidation firing and the unpolished edge resulting from a sample cut after the sintering at 1600 ºC but prior to the oxidation firing. Both regions of the sample have been exposed to the same oxidising conditions. The unpolished edge is composed of two zones: the shell which is chemically identical to the top surface, and the core which was inside the sample during the sintering but, following cutting, formed an external surface during the oxidation firing.

The IBA techniques have a depth of analysis of a few microns, therefore the layer analysed by this method is much thinner than the shell formed by the oxidation (see Figure 7.3).

After the oxidation firing the samples were observed by scanning electron microscopy using the FEI Nova NanoSEM 450 FEG instrument. In order to protect the oxidation layer, the samples were not polished or coated, resulting in surface charging. To reduce this phenomenon, the SEM was set to a low voltage (10 kV). Such acquisition conditions also increase the topography on the surface, decrease the depth of analysis and make focused images harder to obtain.

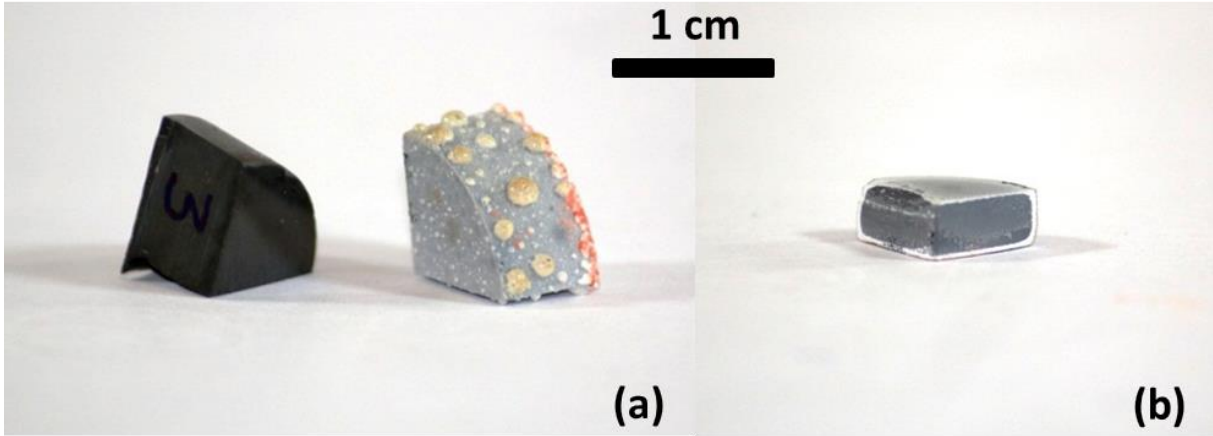

Figure 7.1: Samples resulting from firing in oxidising conditions. (a) Sample 23 before firing and after two hours in air at 1300 ºC and, (b) Sample 24 after two hours in air at 1200 ºC. Photos by The MacDiarmid Institute for Advanced Materials and Nanotechnology.

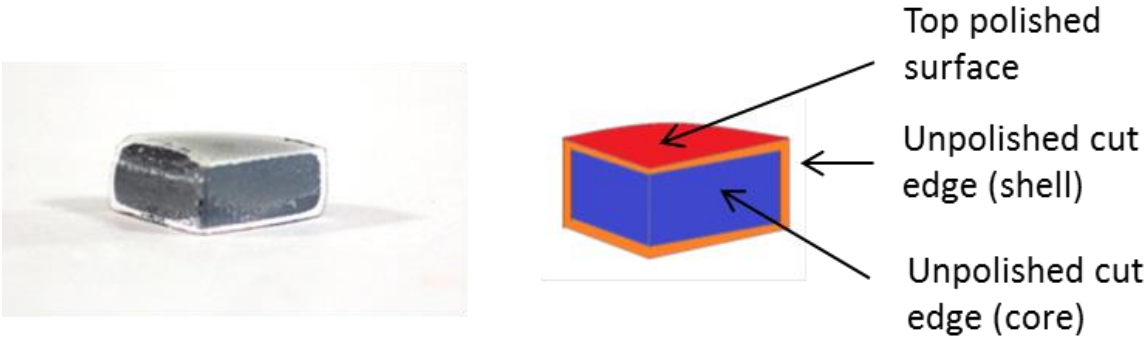

Figure 7.2: Illustration of the different regions observed and described in this study: top polished surface (red), shell of the unpolished cut edge (orange) and the core of the unpolished cut edge (blue).

The micrographs corresponding to the samples shown in Figure 7.1 can be seen in Figure 7.3. The unpolished surfaces of all the unfired samples showed little to no porosity as seen for Sample 23 in Figure 7.3a. The dark area on this figure is caused by surface charging and is not part of the observed surface.

From 1100 ºC for Sample 21 and from 1200 ºC for Samples 22 to 24 for two hours in air, a visible surface layer was formed. This has an irregular height on the sample edge with a minimum thickness of 100 µm as shown in Figure 7.3b. This oxidation layer covered the entire sample surface at 1300 ºC (see Figure 7.1a and Figure 7.3d). The evolution of this surface layer was not made through the sample core or on the top polished surface but along the non-polished oxidised sample edge. The difference in oxidation behaviour between the

shell layer and the sample's edge can be understood by SiO loss taking place during the sample nitridation and sintering, which has slightly reduced the oxygen content of the outside surface of the original samples. The cut made to obtain the samples for oxidation measurement (as noted in the introductory paragraph of this chapter) was made after sintering but prior to the oxidation firing. Therefore the top surface and the cut edges of the sample, which were in the sample core during nitridation and sintering, have a small oxygen content difference, making the oxygen-poor top surface less resistant to oxidation. This observation is confirmed by high heterogeneity in the porosity distribution on the polished surface of oxidised samples between the surface 70 microns and the sample core (see Figure 7.4). The ZAF-corrected EDS analysis (see Table 7.2) of the porous surface and the denser core (areas indicated in Figure 7.4) shows that the surface is deficient in silicon. The light element data (oxygen and nitrogen) includes non-negligible errors and cannot be readily interpreted.

Observing these cut edges where the oxidation reaction was slower provides additional information on the oxidation process.

The oxidation layer is very porous and the shape of the pores (seen in Figure 7.3b and Figure 7.3d) suggests the formation of a liquid phase which is sufficiently viscous to trap gas bubbles. The lowest eutectic known in the Y-Si-Al-O-N system is approximately 1365 ºC but a liquid phase at a lower temperature has already been proposed by Vickridge et al.[3].

Figure 7.3c shows the microstructure of Sample 24 at the interface between the oxidation layer and the less oxidised region of the sample edge. This area is part of the oxidised surface but, as noted above, oxidation occurred at different rates in both areas. Two types of particles can be seen: 500 nm sized particles appearing white on the micrograph and, grey and flat particles measuring up to approximately 10 µm. These particles are also present at lower concentrations on the oxidation layer and polished surface (top area out of focus in Figure 7.3b) and would therefore feature in the XRD results discussed in Section 7.2.2.

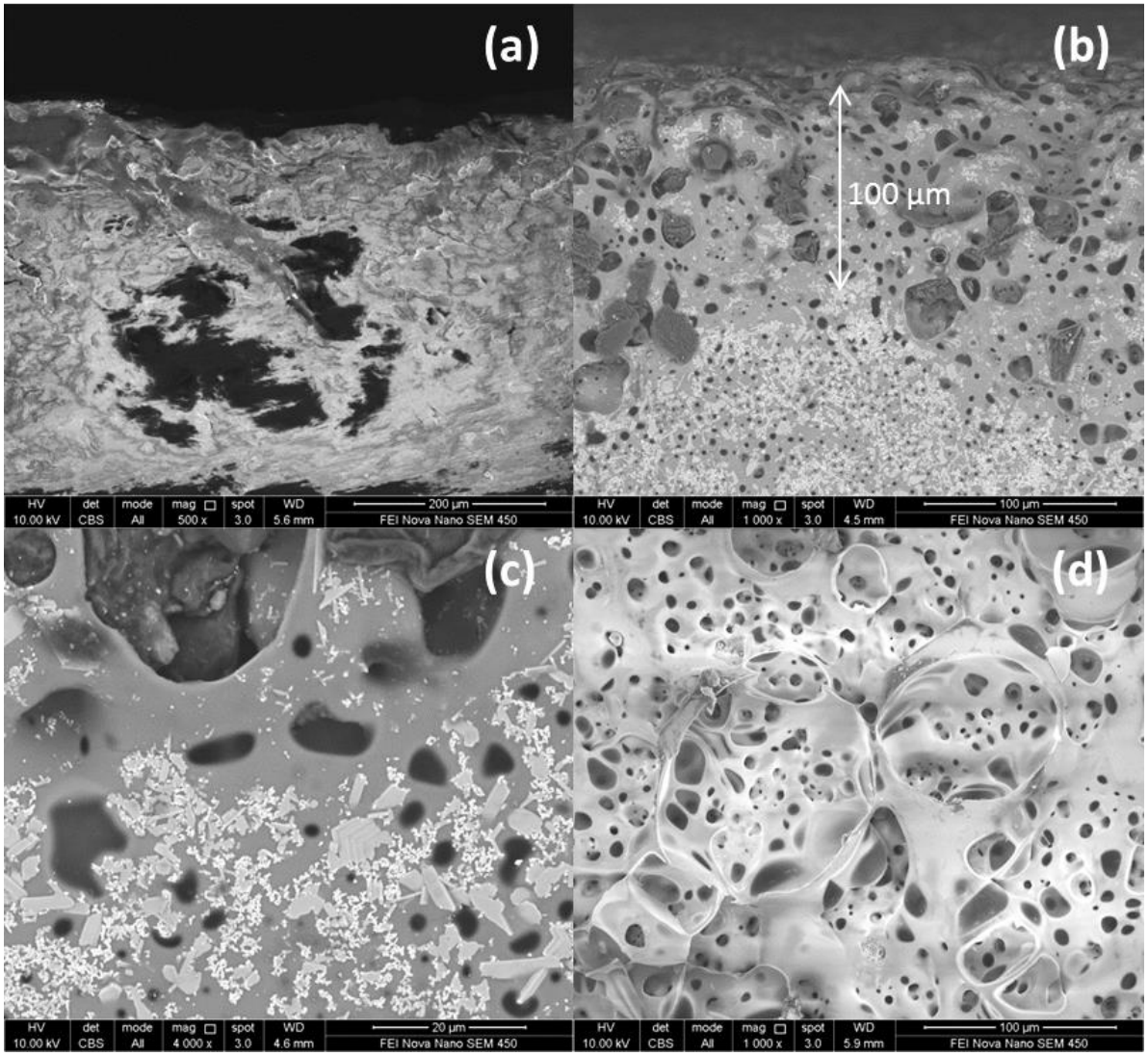

Figure 7.3: SEM Micrographs of the unpolished edges of (a) Sample 23 before firing (scale bar = 200 µm), (b) and (c) Sample 24 (10 wt% TiN) fired at 1200 ºC for 2 hours in air (scale bar = 100 µm for (b), scale bar = 20 µm for (c)), and, (d) Sample 23 (3 wt% TiN) fired at 1300 ºC for 2 hours in air (scale bar = 100 µm). All the micrographs in this figure have been collected on the edge of the sample (the orange and blue areas in Figure 7.2). The dark area on picture (a) is due to sample charging.

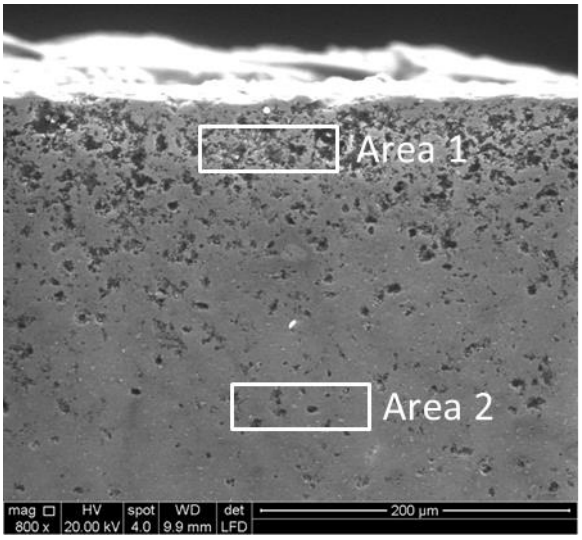

Figure 7.4: SEM Micrograph of the polished surface of sample 23 before oxidation showing heterogeneous distribution of the porosity. Due to the specimen/instrument orientation the true specimen surface commences where the white surface zone meets the grey porous area.

	Element	Atomic %	Error %		Element	Atomic %	Error %
Area 1	N K	47.7	13.4	Area 2	N K	47.2	14.2
	O K	16.4	16		O K	9.9	17.4
	Al K	6.9	5.3		Al K	7.9	4.8
	Si K	27.9	4.1		Si K	33.7	3.9
	Y L	0.6	15.7		Y L	0.6	15.9
	Ti K	0.6	21.7		Ti K	0.8	17.9

Table 7.2: ZAF-corrected EDS analysis of Area 1 and Area 2 indicated in Figure 7.4.

Sample 24 (10 wt% TiN) fired at 1200 ºC for two hours in air was analysed at the Titanium Industry Development Association (TiDA, Tauranga) who operate a Zeiss Evo MA25 (2010) SEM with an INCA Analyser (Oxford Instruments). EDS analysis was performed on a similar area to that shown in Figure 7.3c, on the small white particles and on the larger grey particles as shown in Figure 7.5. EDS spectra are shown in Figure 7.6. As described in Section 7.2.2, XRD analysis show that at 1200 ºC, Sample 24 contains the original β-Sialon, YAG and TiN, as well as TiO_2 and $Y_2Ti_2O_7$. The volume of YAG and TiN phases has decreased. The two new crystalline phases can be identified by comparing the Ti and Y peaks on the EDS spectra. Both elements appear in the spectra of both particles because the EDS beam area is larger than these particles. However, in Figure 7.6a, the atomic Ti:Y ratio is very

high (approximately 45 after ZAF correction) suggesting that the large grey particles are TiO_2. In Figure 7.6b, the ratio is close to 1 (after ZAF correction), which shows that the small white particles are $Y_2Ti_2O_7$. This observation aligns with the particles' colours in the SEM micrographs, as the heavier the element (the heaviest in the particle) the whiter the particle appears.

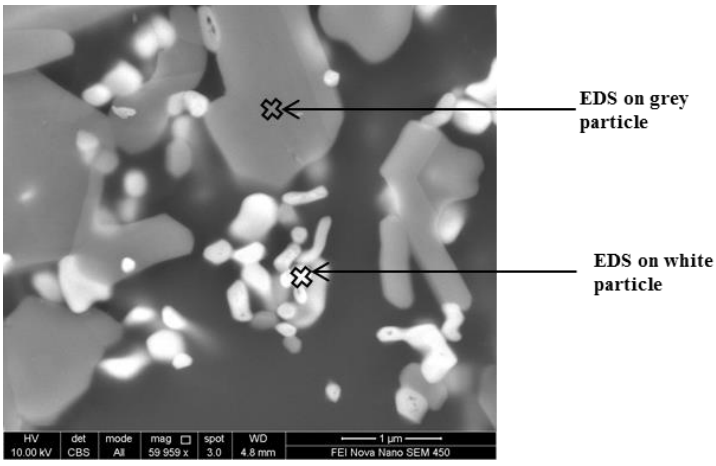

Figure 7.5: Position of EDS analysis on Sample 24 fired at 1200 ºC for two hours in air. Scale bar = 1 µm.

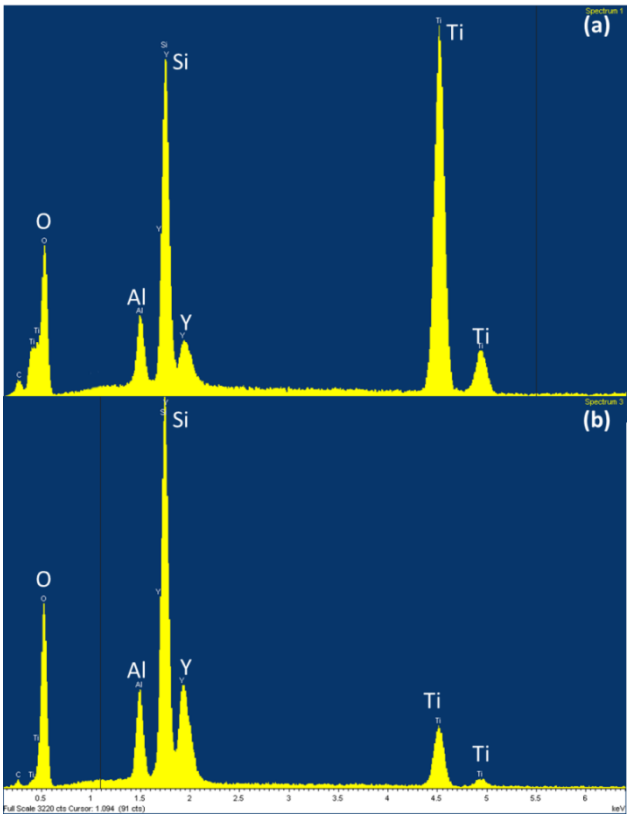

Figure 7.6: EDS spectra collected from (a) large grey particles and, (b) small white particles observed in Figure 7.3b and c and, Figure 7.5. Scale ranges from 0 to 5.5 keV.

7.2.2 Sample Composition by XRD

The top surface of each sample (polished prior to firing) has been analysed by XRD after the oxidation firing to compare with the elemental spectra obtained using the IBA techniques. Because all the samples of the same composition were of a very similar size and have been analysed with the same methodology, the peak intensities can be compared between XRD patterns. Figure 7.7 to Figure 7.10 show the accumulated XRD peak intensities of the crystalline phases present at the surface of the oxidised samples. Selected XRD patterns are displayed in Annex IV. The depth of analysis, with a 5º incident beam, has a maximum of approximately 20 µm, deeper than that analysed by the IBA techniques. The analysis depth slightly decreases with the density of the analysed sample. Therefore, when the shell layer is formed (approximately 100 µm, see Figure 7.3), only its phase composition appears in the XRD patterns. A single peak per phase has been selected with the criterion that it does not match any other pattern than that of the other observed phases (except for TiN for which the peak matching the smallest of the YAG peaks was chosen to minimise the potential for conflicting XRD peaks). Therefore these graphs do not imply any absolute phase volume in the sample but only an increase or decrease of the independent volume of each phase as a function of temperature.

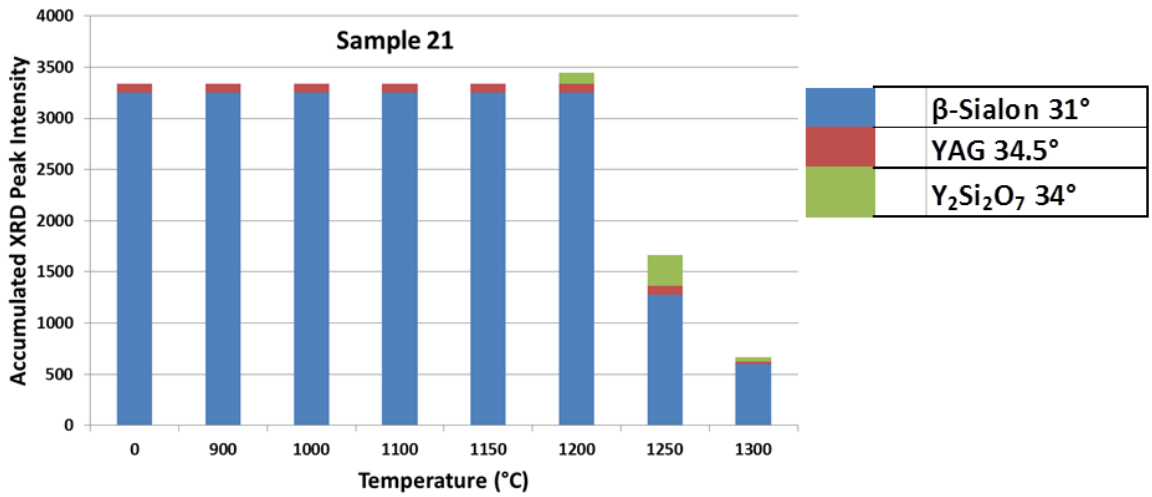

Figure 7.7: XRD peaks intensity and observed peak position for Sample 21 (0 wt % TiN).

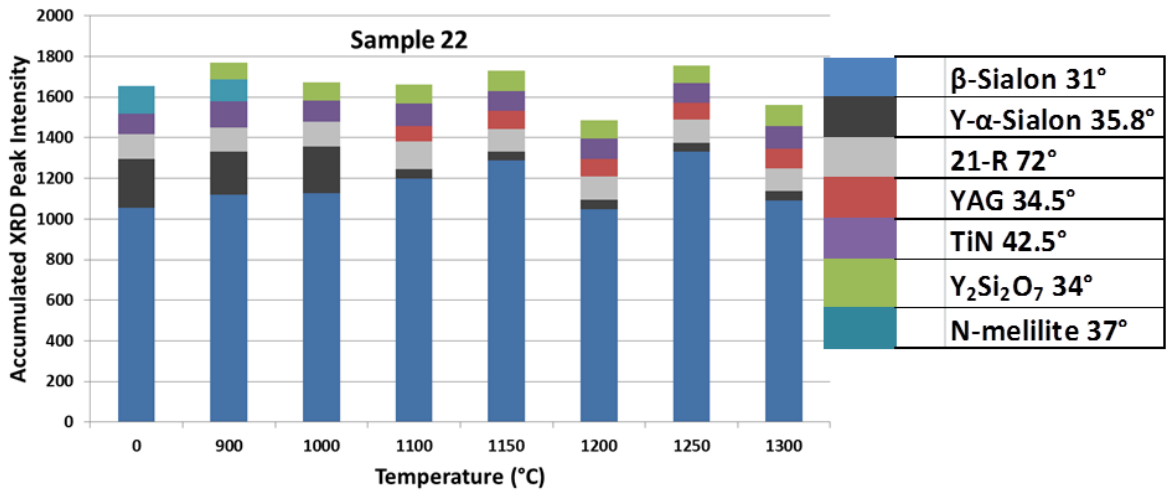

Figure 7.8: XRD peaks intensity and observed peak position for Sample 22 (1 wt % TiN).

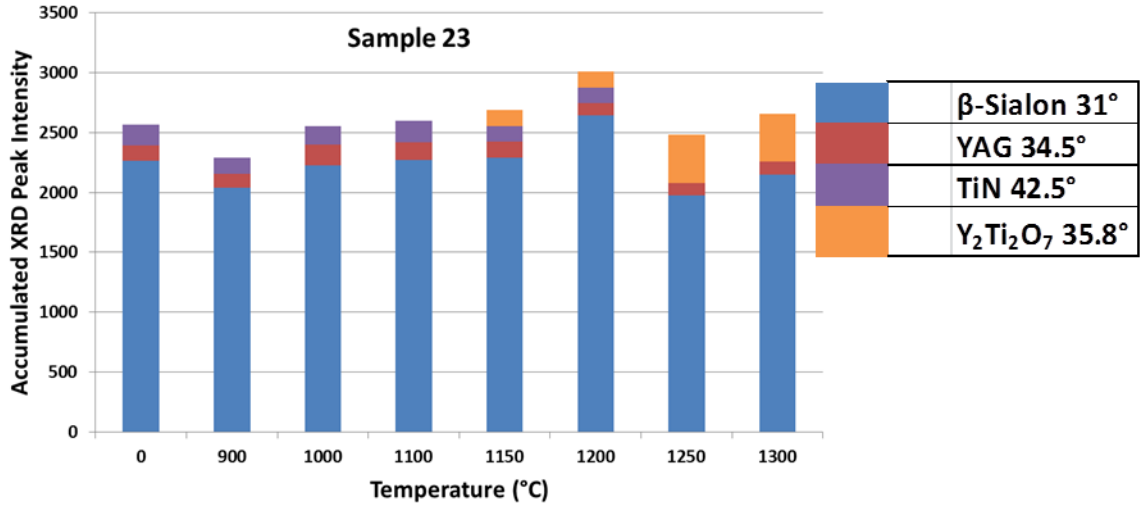

Figure 7.9: XRD peaks intensity and observed peak position for Sample 23 (3 wt % TiN).

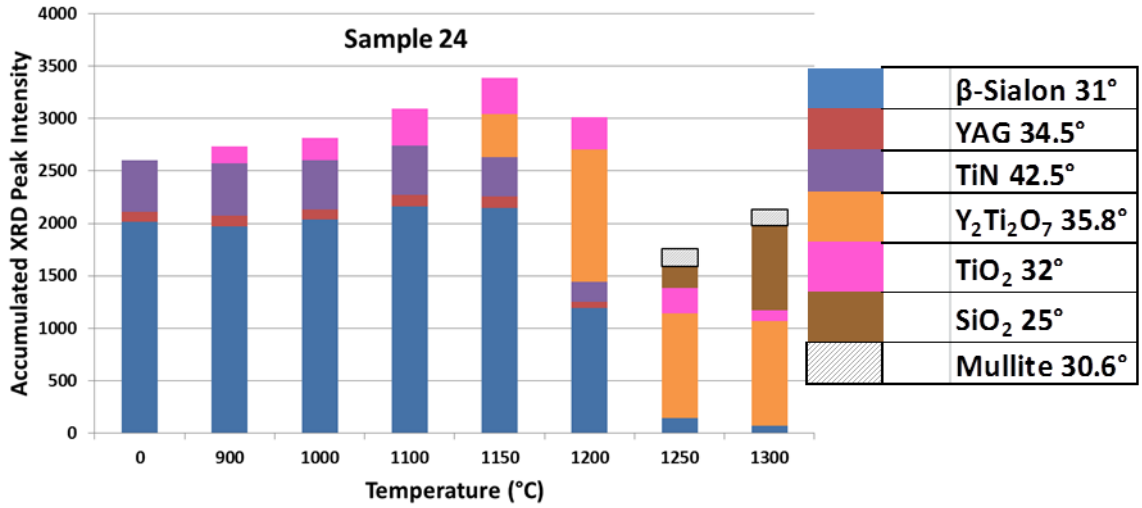

Figure 7.10: XRD peaks intensity and observed peak position for Sample 24 (10 wt % TiN).

Despite the formation of a very small shell layer at 1100 ºC, no changes were observed in the crystalline composition of Sample 21 until 1200 ºC. This layer was caused by surface SiO loss during the sintering firings and oxidised more rapidly than the cut faces of the sample, potentially because of its oxygen deficiency. Oxidation of this layer below 1200 ºC was not detected by XRD despite the visible colour change. At 1200 ºC, y-$Y_2Si_2O_7$ appeared. This yttrium silicate phase, also referred to as low yttrialite, has previously been crystallised from Y-Sialon glass[4]. These results are in accordance with the studies by Vickridge et al.[3] and Brown et al.[5] on α/β-Sialon composites. These studies also report the formation of crystalline silica (SiO_2) from 1200 ºC. In the present case, no crystalline silica phases were observed and there is no XRD evidence to suggest the presence of amorphous silica. The β−Sialon and YAG peaks were not affected until 1250 ºC at which point their intensity dropped dramatically.

In Sample 22, the β-Sialon, 21-R and TiN phases were not attacked by the atmosphere at 1000 ºC but the N-melilite ($Y_2Si_3O_3N_4$) has disappeared to be replaced by $Y_2Si_2O_7$. From 1100 ºC, the Y-α-Sialon phase was substantially reduced and YAG appeared.

Samples 23 and 24 reacted to the oxidation in similar ways up to 1150 ºC. The amount of β−Sialon remained constant and TiN was partially oxidised to TiO_2. It is difficult to draw conclusions on the oxidation behaviour of TiN in Sample 23 as the potential TiO_2 peaks were not visible above the background. At 1150 ºC, $Y_2Ti_2O_7$ was formed from the partial oxidation of both YAG and TiN. At 1250 ºC, TiN has completely been oxidised in both samples as well as YAG in Sample 24 due to the larger amount of TiN in this sample. In Sample 24 β-Sialon started to decompose from 1200 ºC, decaying to a very low level at 1300 ºC with the appearance of mullite and cristobalite (SiO_2) from 1250 ºC.

The unexpected resistance of TiN to oxidation up to 1200 ºC in Samples 23 and 24 and 1300 ºC in Sample 21 suggests that a protective TiO_2 skin is formed on the TiN. It is likely that TiO_2 was not detected in Sample 22 and 23 because of the low level of TiN addition.

The oxidation process does not affect the measured z-value of the β-Sialon in any of the samples (see Annex III).

7.3 Use of IBA to Observe the Oxidation Process

Diffusion through the covalent structure of Sialon is very slow. The glassy phase surrounding the Sialon grains is the weakness of this material as it will partially melt at temperatures below 1400 ºC, forming the liquid phase that enhances the Sialon sintering but which is also responsible for deformation, creep and mechanical failure. In oxidising conditions, it is also this inter-granular phase which allows a much faster diffusion of the oxygen and other elements through the material. It is the principal diffusion pathway for both gaseous and atomic species in these materials at elevated temperatures.

7.3.1 Concentration and distribution of Y, Ti, Si, Al, O and N by RBS

Figure 7.11 shows the RBS spectra for Y, Ti, Si, Al, O and N for Samples 21 to 24.

RBS spectra are obtained by counting the number of light atomic particles (in this case ^{4}He) which are backscattered with a given kinetic energy from the analysed samples and towards a detector. The kinetic energy and angle of the backscattered particle is a function of the mass of the atoms with which the particle interacts. Incident particles which have interacted with atoms from the materials surface will have a well tabulated energy which results from the kinematics of the collision. If the interaction occurs deeper in the material, the backscattered particle will arrive at lower energies because of energy loss within the material. The amplitude of the signal is a function of the atomic concentration of the atoms, the higher the concentration the higher the amplitude, and of the interaction cross-section which can be pictured as the “size” of the atom seen from the fast moving interacting particle perspective. This technique allows the identification of changes in the material composition and the observation of elemental migration, in particular for yttrium as detailed below. Typically, an RBS spectrum provides an immediate visual estimate of the depth distribution of the different atoms by identifying the edge of the peak, which corresponds to the sample surface, for the different atoms in the materials, and measuring variations in the signal intensity for lower energies. For instance, if the atomic concentration remains the same, then the RBS signal will be a plateau. It is common, although not technically accurate, to directly refer to RBS spectra as a ‘depth profile’. However, a depth scale can be inferred from the data by using composition simulation software.

The Sialon elemental masses are too similar to each other to readily distinguish them. The difference in atomic mass is too small between nitrogen and oxygen and between silicon and

aluminium for the technique to properly distinguish these species. Hence the surface peak and subsequent plateau for silicon and aluminium create one single data envelope. Further, the scattering from the deep layers of oxygen as well as multiple scattering at low energy obscures the nitrogen profile. Nevertheless, nitrogen and oxygen can easily be distinguished by NRA and PIGE, respectively, as discussed later in this chapter. The scattering signals from the deep layers of yttrium overlay slightly with the titanium spectrum but the mass difference is sufficient so that the signals can be resolved. However, to calculate the titanium depth profile it is necessary to subtract the contribution from the yttrium signal.

The first detection of yttrium movement can be seen at 1000 ºC, similar to that observed by Brown et al.[5] for α/β-Sialons with high levels of yttrium addition. Except for Sample 22 where $Y_2Si_2O_7$ appears on the surface, this first yttrium movement happens exclusively in the glassy phase. In the absence of TiN (Sample 21), the yttrium enrichment starts slowly; whereas in the presence of TiN, the outer 0.05 μm is yttrium rich at 1100 ºC. By 1200 ºC (or 1150 ºC for Sample 24), the outer 0.1 μm has been enriched in all the samples, following which the signal decreases rapidly as the temperature rises.

Movement of titanium is only very lightly detected for Sample 23 from 1100 ºC. No crystalline titanium containing phase other than TiN was detected by XRD or NMR at this temperature (see Chapter 5) which suggests that a small amount of TiO_2, not detectable by XRD, may be formed. IBA techniques have effectively a low detection threshold (a few ppm). On the other hand, in Sample 24, titanium peaks are detected from 1000 ºC and the outer 0.1 μm is enriched in titanium by 1150 ºC.

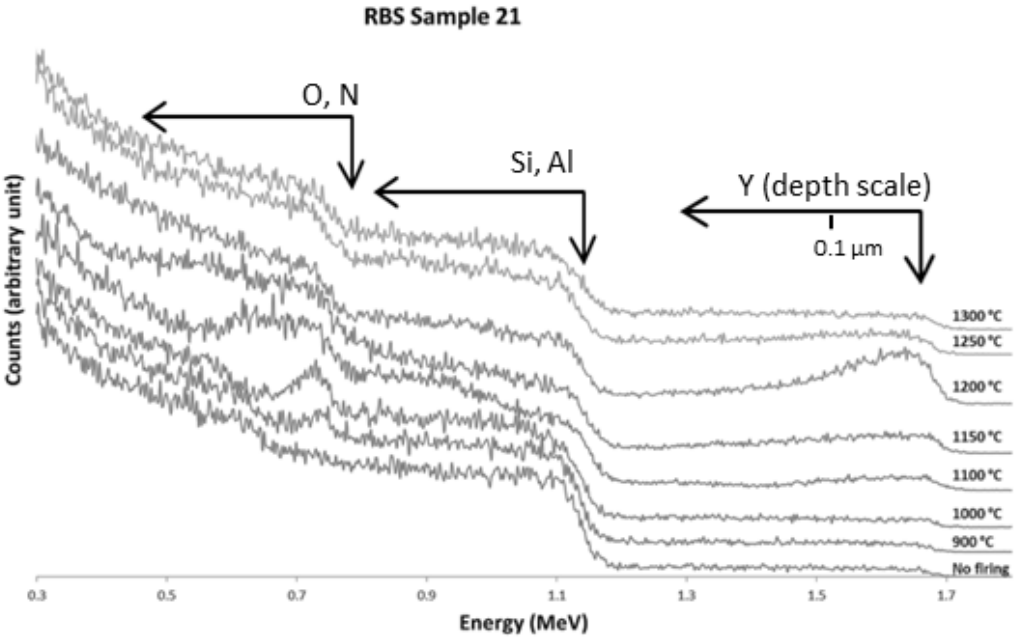

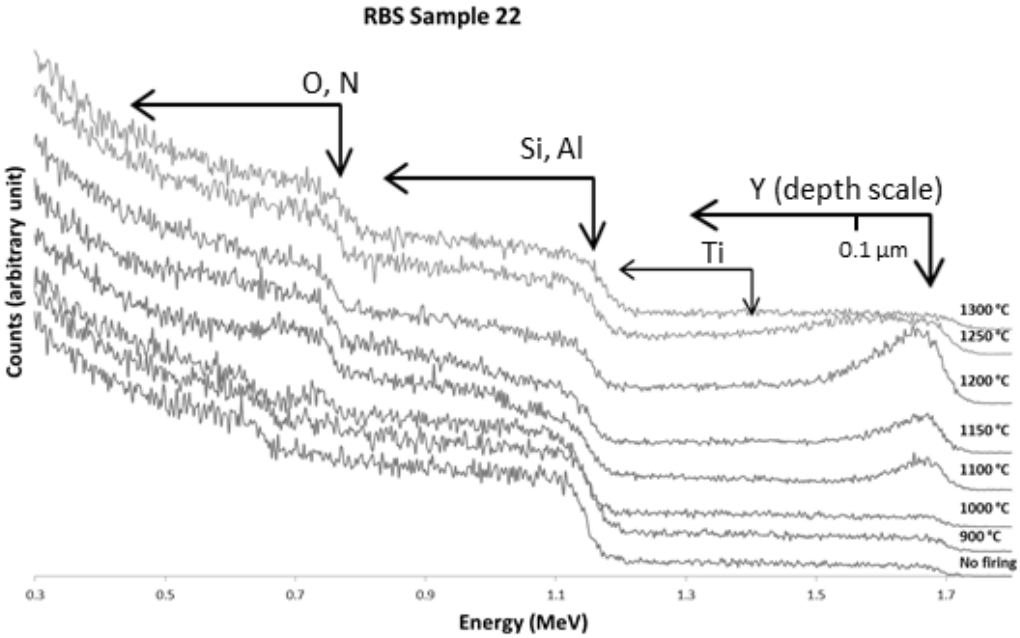

Legend is on the following page.

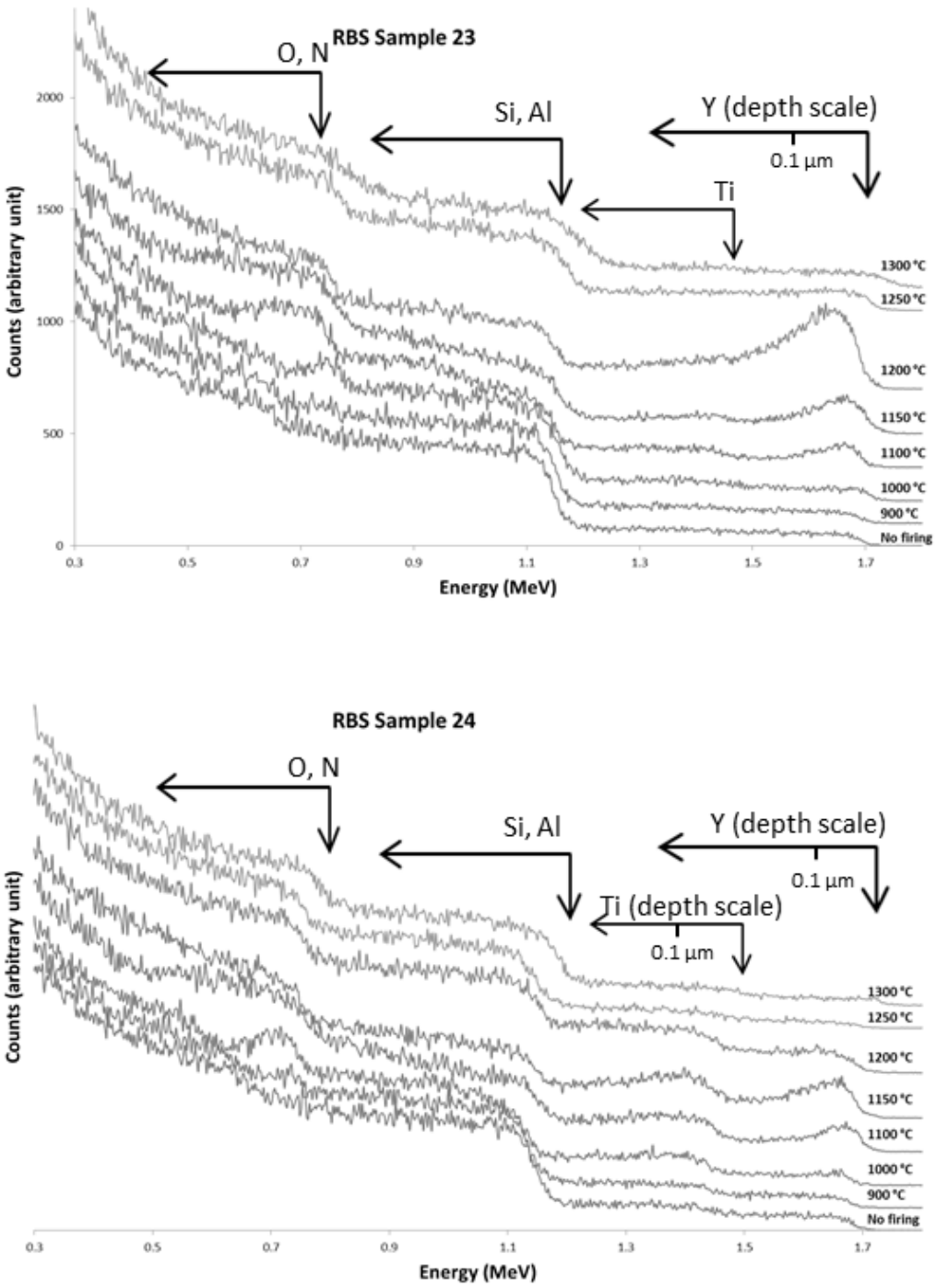

Figure 7.11: RBS spectra of oxidised Samples 21 to 24, showing depth profiling for yttrium and titanium. Vertical arrows indicate the position of the edge of the peak, corresponding to the surface of the sample while horizontal arrows show the depth scale for each element.

To calculate the depth profiles for yttrium and titanium, each spectrum has been independently simulated using the software package RUMP[6, 7]. This software is used to simulate Rutherford scattering spectra by calculating the backscattering yield for each atom composing the material from the experimental parameters (geometry, incident ion, energy,

accumulated charge) and hence calculating a model of the analysed material. Figure 7.12 shows an example of a RUMP RBS spectrum simulation (in red) best fitting the experimental data (in black) made on Sample 24. The software simulation is based on a layered sample composition in atomic areal density (in atoms.cm^{-2}) for each element. When the layered composition gives the best match to the measured data, it is possible to obtain an areal density (see Figure 7.13) of the analysed volume (in atoms.cm^{-2}) for yttrium and titanium. The areal density of titanium is calculated by subtraction of that of yttrium as the two elements interact slightly with each other. These areal densities can then be converted (see Equation 7.1) to a calculated depth (in nm) by estimating the density of the material (using a tabulated value of a similar material or via another experiment). In this case the density of mullite was chosen to be representative of the oxidation layer of the samples (ρ = 3.19 g.cm^{-3} = 9.47x10^{22} atoms.cm^{-3}).

$$thickness\ (\mu m) = \frac{areal\ density\ (atom.cm^{-2}).10^{15} * \overline{Z}\ (g.mol^{-1})}{d\ (g.cm^{-3}) * N_a\ (atom.mol^{-1})} * 10^{-4} \qquad \text{(Eq. 7.1)}$$

The combination of the RUMP simulation of the RBS spectra and the application of the Equation 7.1 enables the calculation of the depth profiles for yttrium and titanium indicated in Figure 7.11 for samples 21 to 24.

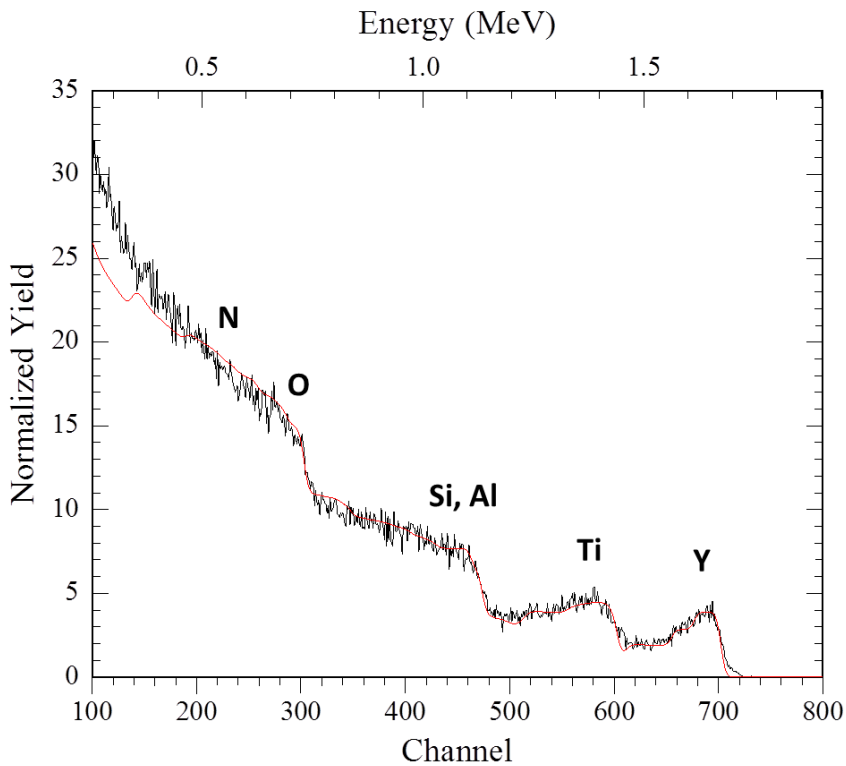

Figure 7.12: RBS spectrum for Sample 24 fired for two hours in air at 1150 ºC and computer simulation made with RUMP[6, 7].

The simulation accuracy varies with the following parameters:

the peak width at half-height which is dependent on the energy measured by the detectors. In this study, all the chosen detectors have a resolution of 15 keV (equivalent to approximately 10 nm),

and the density used to convert the areal density to a calculated depth.

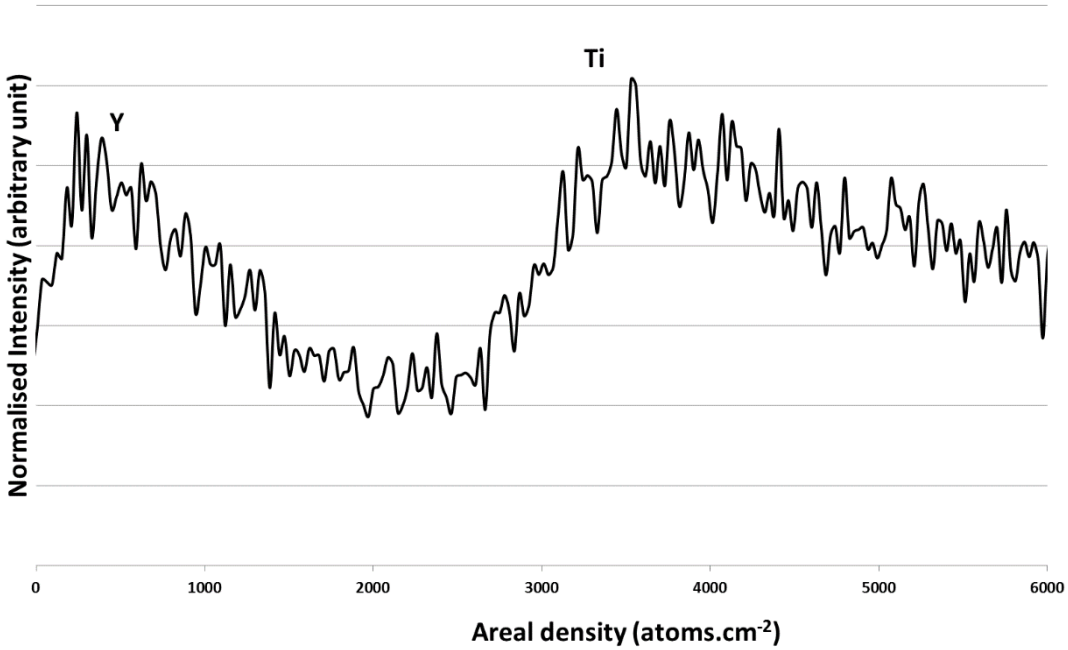

Figure 7.13: Areal density of yttrium and titanium from the surface of sample 24 (10 wt% TiN). The shift from the sample surface (0 atoms.cm^{-2}) is due to multiple-scattering.

7.3.2 PIGE Spectra for Oxygen

Figure 7.14 shows the peak intensities measured by PIGE which confirm observation of the diffusion of oxygen into the sample surface. The first change in oxygen concentration is observed at 1000 ºC in all the samples. Sample 21 (no TiN) is more heavily oxidised with increasing temperature until 1200 ºC where all the samples have a similar oxygen concentration at the surface. By 1300 ºC, the oxygen concentration in the analysed zone has been at least doubled in all the samples. Sample 22 has the smallest increase of oxygen at its surface which can be understood by the smaller volume of glassy phase in this sample, from which yttrium has been incorporated into the α-Sialon structure. At 1100 ºC, when the Y−α−Sialon decomposes the oxygen is incorporated into YAG (see Figure 7.8). The β-Sialon phase stays stable in this sample because the temperature is too low for an α/β

transformation[8]. The silicon from the α-Sialon may be incorporated in the glassy phase while the nitrogen is removed from the sample as seen in the NRA results (see Section 7.3.3).

From 1250 ºC to 1300 ºC, the oxygen level slightly decreases in Samples 23 and 24 due to SiO loss by volatilisation from the glassy phase.

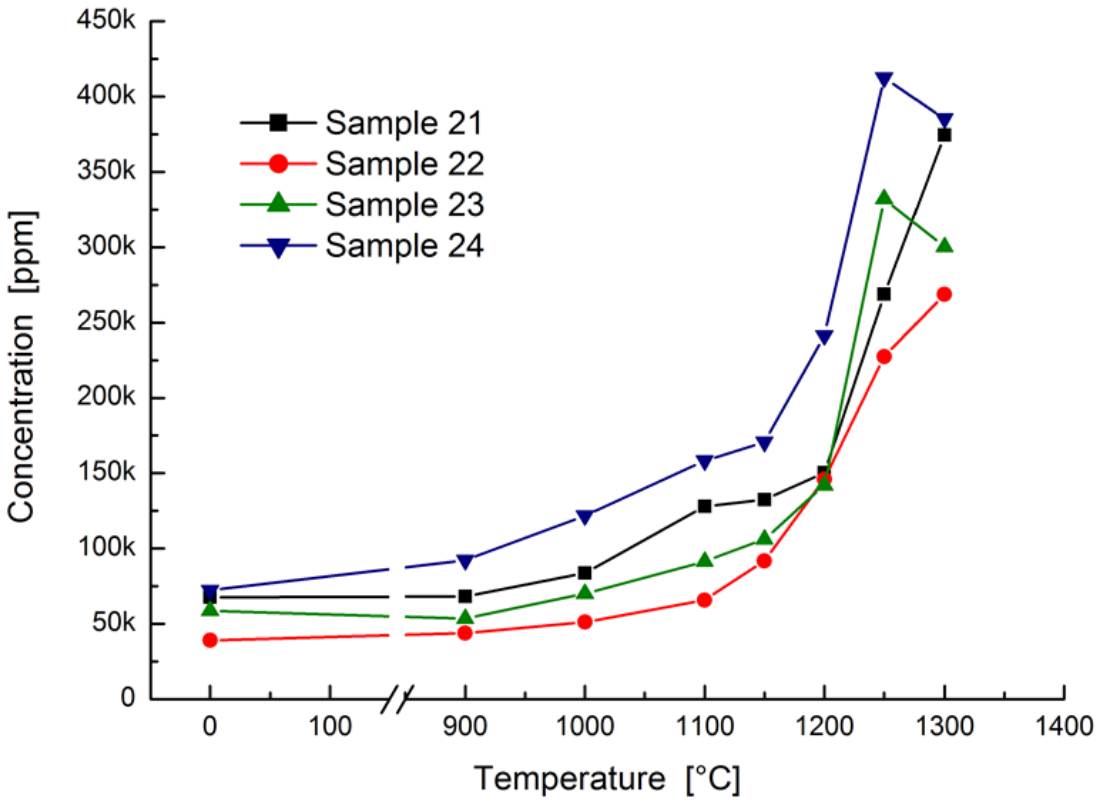

Figure 7.14: PIGE peaks intensities as a function of temperature for oxidised Samples 21 to 24.

7.3.3 NRA Spectra for Nitrogen

Figure 7.15 shows the NRA spectra for nitrogen for Samples 21 to 24. The complete NRA spectra display several other peaks for nitrogen but also multiple scattering and superimposed peaks for silicon, aluminium and oxygen. The $^{14}N(d, \alpha_0)$ reaction can be observed independently from other reactions between approximately 8 and 9 keV.

By simulating the nuclear reaction spectra with the software SIMNRA[9], the structure of the samples was modelled to provide composition information of the outer layers. As for RUMP, this software requires modelling the atomic composition for several packed layers by comparing simulated spectra with the measured spectra. The modelled composition is performed in atomic areal density (atoms.cm^{-2}) which is then converted to depth (nm) by using the density of mullite (ρ = 3.19 g.cm^{-3} = 9.47x10^{22} atoms.cm^{-3}) in the depth conversion.

An example of a simulation made on Sample 22 fired at 1100 ºC can be seen in Figure 7.16. To quantify the depth of the oxidation and diffusion layers, every NRA spectrum was simulated with SIMNRA. Perfect agreement between the simulated and measured spectra on the left part of the NRA spectrum (below approximately 760 channels / 85 keV) is difficult to obtain as this part of the peak contains some multiple scattering and the depth calculations are made only on the outer layers represented on the high energy side of the peak in the spectrum. The complete NRA simulation results can be found in Annex V. The calculated depth of the nitrogen depletion is indicated in Figure 7.15 for each starting composition. The point of calculation is positioned at the half-height of the peak of the most depleted layer where nitrogen, in its original concentration, is still present in the total analysis volume (1200 ºC). The nitrogen depletion in the samples oxidised at 1250 and 1300 ºC has occurred deeper than the IBA depth of analysis and these peak are therefore not included in the depth calculation.

In Sample 21, the replacement of nitrogen by oxygen starts at 1100 ºC as observed by Brown et al.[5]. This observation does not correspond to any crystalline change (see Figure 7.7) and therefore happens in the glassy phase, up to 0.7 µm deep at 1200 ºC. Then at 1250 ºC, the nitrogen concentration drops drastically even in the deeper layers of the surface, whose thicknesses are hard to calculate because of the very low slopes of the NRA spectra. This can be correlated to the decomposition of β-Sialon observed by XRD.

Nitrogen movement also starts at 1100 ºC in Sample 22 but it corresponds to the Y-α-Sialon decomposition. The rest of the oxidation process for nitrogen is the same as for Sample 21 but with a thicker oxidation layer (up to 1.1 µm at 1200 ºC).

In Samples 23 and 24 (3 wt% and 10 wt% TiN respectively), the oxidation of TiN to TiO_2 (not detected by XRD in Sample 23), is confirmed by the first shift in the nitrogen spectrum to lower energy at 900 ºC (approximately 40 keV) then the mechanism continues as temperature increases. In Sample 23, the nitrogen-poor oxidised layer is 0.6 µm thick by 1200 ºC. In Sample 24, the oxidation mechanism is faster due to the higher level of TiN addition: at 1150 ºC, $Y_2Ti_2O_7$ appears and the nitrogen-poor layer is 1.5 µm thick, while the oxidation starts to affect the deeper layer from 1200 ºC.

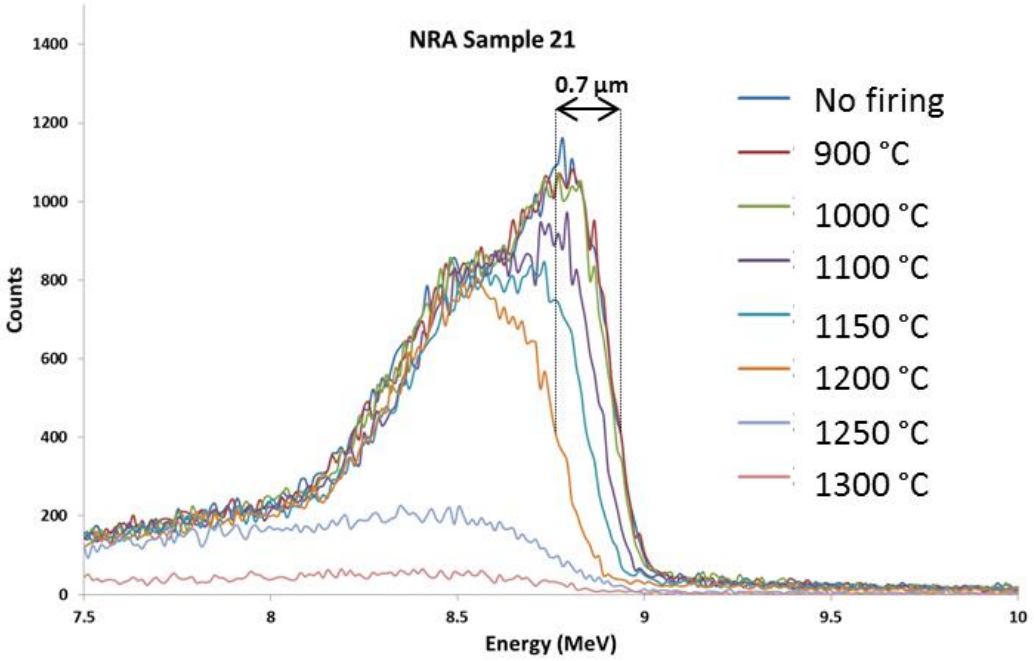

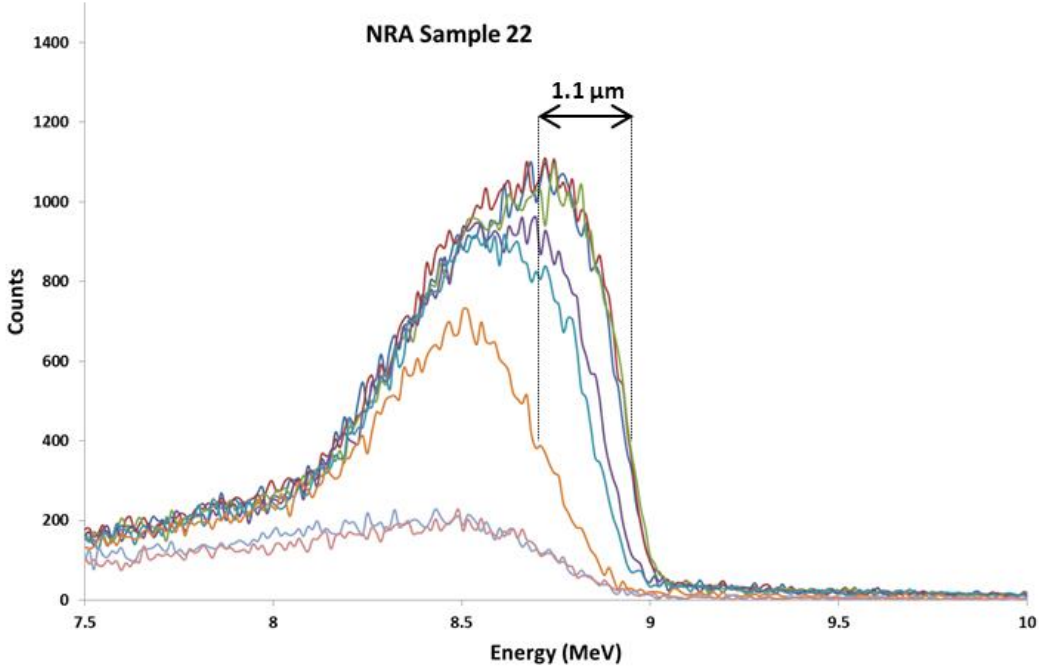

Legend is on the following page.

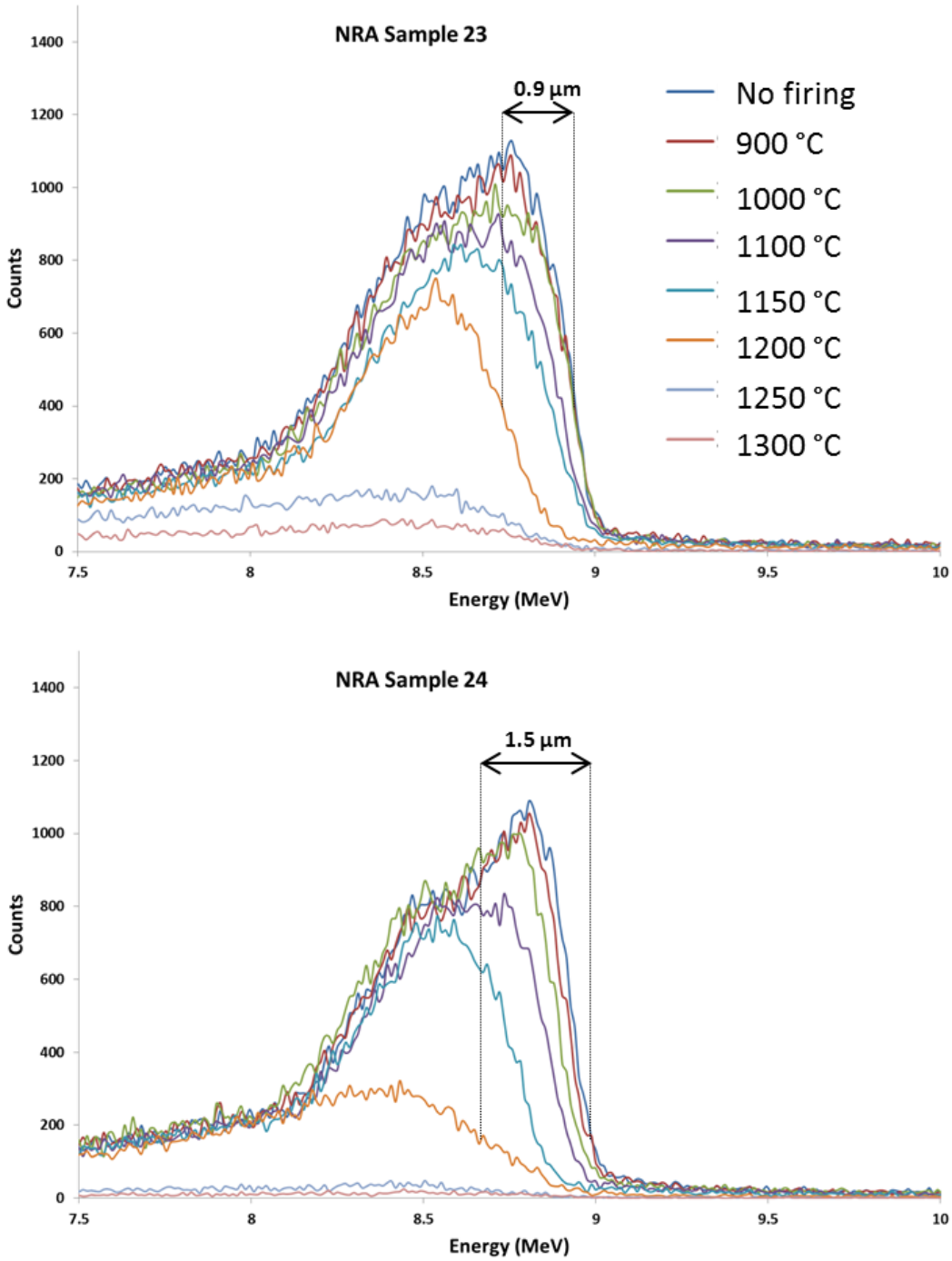

Figure 7.15: NRA spectra of nitrogen at the surface of oxidised Samples 21 to 24 and the nitrogen depth profile for the first simulated layer up to 1200 ºC. Legend is common to all the graphs.

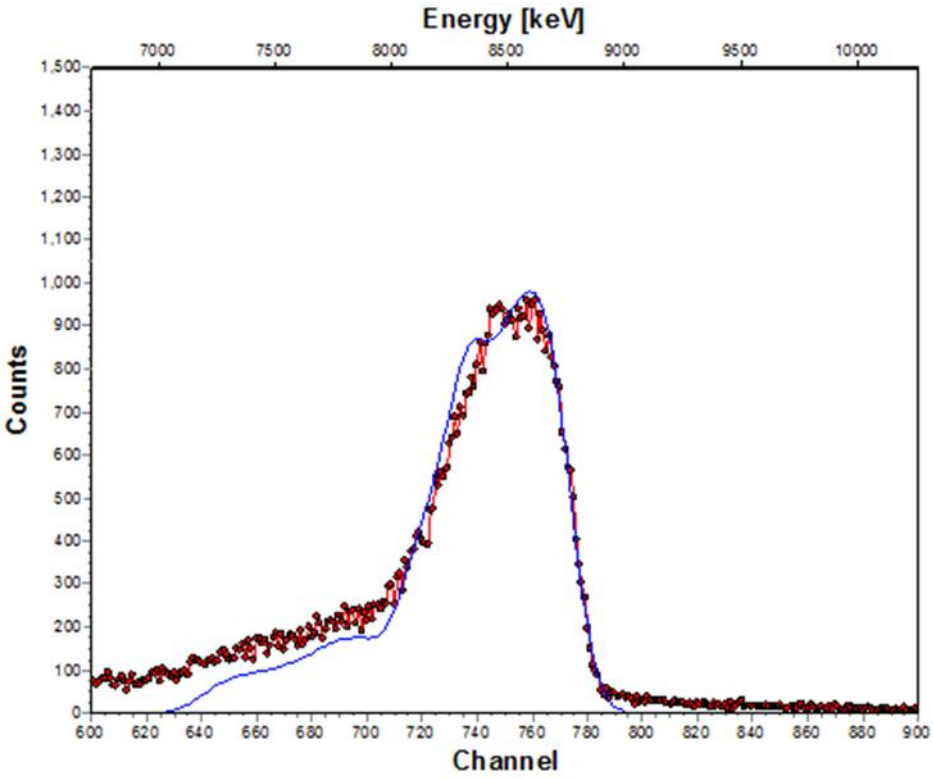

Figure 7.16: NRA spectrum for Sample 22 fired for two hours in air at 1100 ºC and computer simulation made with SIMNRA[9].

7.4 Summary

In this chapter, the oxidation resistance of β-Sialon/TiN composites (0 to 10 wt% TiN) has been measured by XRD, SEM and IBA techniques. The diffusion behaviour of Si, Al, Y and Ti was measured by RBS; O diffusion by PIGE; and N diffusion by NRA. Figure 7.17 illustrates schematically the comparative analysis depth of the characterisation techniques used in this study.

In Sample 21 (0 wt% TiN), the first elemental movement was observed at 1000 ºC with the surface enrichment of oxygen to a depth of at least 9 µm, the maximum analysis depth for the PIGE technique. Yttrium and nitrogen were mobile from 1100 ºC which corresponds to the first visual change, with the outer 0.1 µm enriched in Y and the outer 0.3 µm depleted in N. At 1200 ºC, the oxidised layer (nitrogen-poor, yttrium and oxygen-rich) was 0.7 µm thick, consistent with XRD observation of $Y_2Si_2O_7$. These results are in accordance with the studies by Brown et al.[5] on α/β-Sialon composites with high yttrium additive levels, although the formation of crystalline silica was only observed at the highest TiN doping levels (10 wt%) in the present studies. The oxidation induced changes to the sialon chemistry and structure are

limited to a near surface zone of a maximum of 100 µm, in accordance with previous studies on the oxidation of silicon nitride-based ceramics[1, 10-12].

In the TiN containing samples, IBA shows that yttrium and titanium are very mobile at temperatures as low as 1000 ºC and surface nitrogen was totally depleted to a depth of 1.5 µm by 1200 ºC. The XRD and IBA evidence indicates that the combined presence of YAG and TiN has protected the β-Sialon phase from oxidation due to the mobile Y and Ti species forming an oxygen-rich crystalline barrier layer to inhibit oxygen ingress. The oxidation of TiN formed both TiO_2 and $Y_2Ti_2O_7$ which suggests that elemental silicon (both from the glassy phase and the β-Sialon) has been protected from oxidation by the titanium phases. This is especially clear in the samples with lower TiN doping levels up to 3 wt % which show an absence of silica phases such as cristobalite at temperatures up to 1300 °C. Only at the highest doping level of 10 wt% TiN is the oxidation protection compromised, with the β-Sialon decomposing above 1200 °C to form cristobalite (SiO_2) and mullite ($3Al_2O_3.2SiO_2$), while continuing to sustain the TiO_2 and $Y_2Ti_2O_7$ titanium oxidation products.

At a microstructural level, the progression of the oxidation process, such as that shown for sample 24 (10 wt% TiN) in Figure 7.3b and Figure 7.3c, can be drawn as a series of schematics or cartoons, such as Figure 7.18. Here we see the representation of a pore space surrounded by a matrix of β-Sialon, with surface crystallisation of TiO_2 and $Y_2Ti_2O_7$. Whereas most of the surface zone phase information is captured by the XRD analysis, the differing degrees of penetration of the IBA techniques provide more selective analyses. While these IBA analyses may not be fully representative of the ‘bulk’ they provide exceptional detail of the near surface diffusion and phase transformation within the sialon composite body.

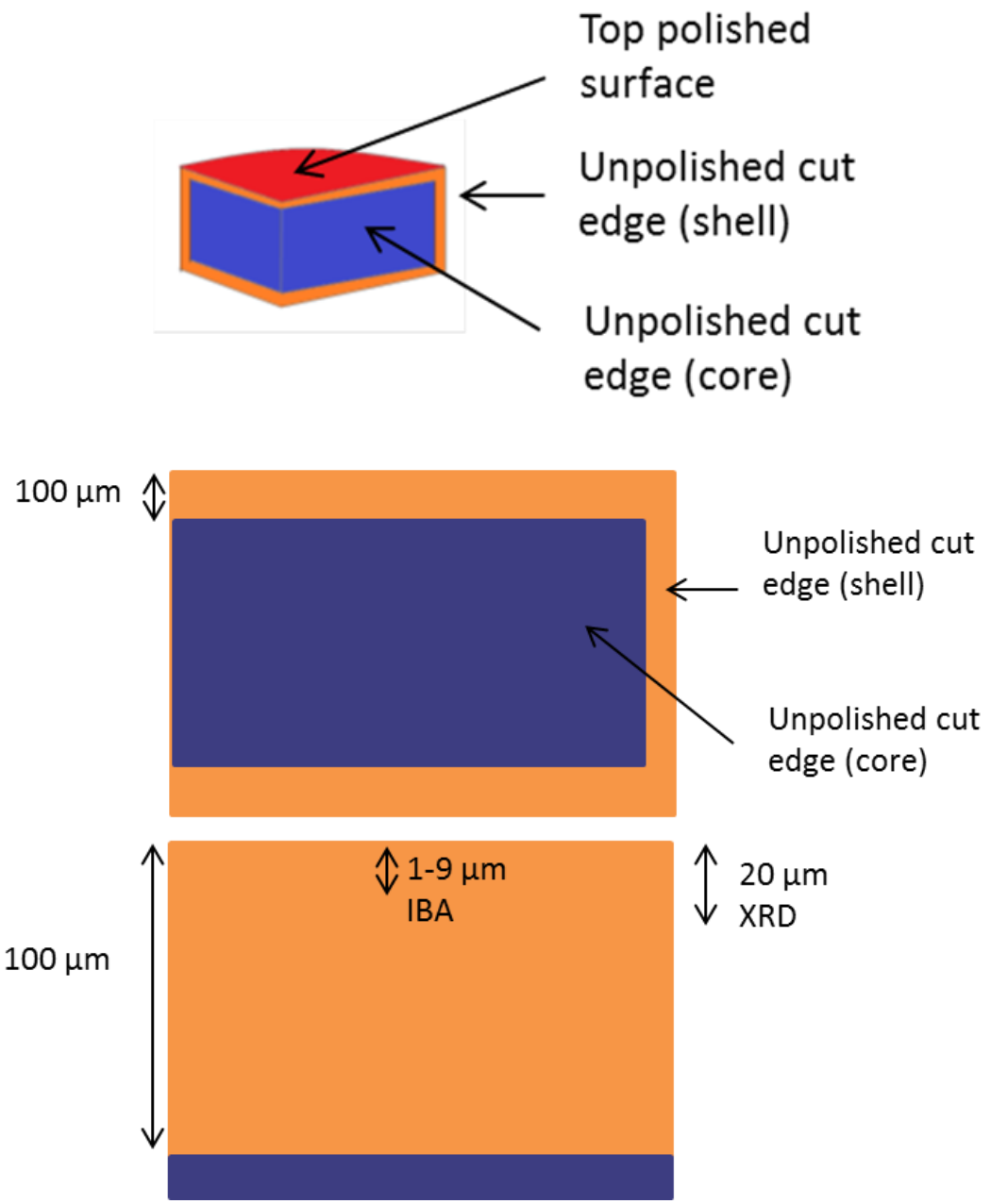

Figure 7.17: Comparative analysis depth of IBA and XRD characterisation techniques on the edge of a sample as represented in Figure 7.2.

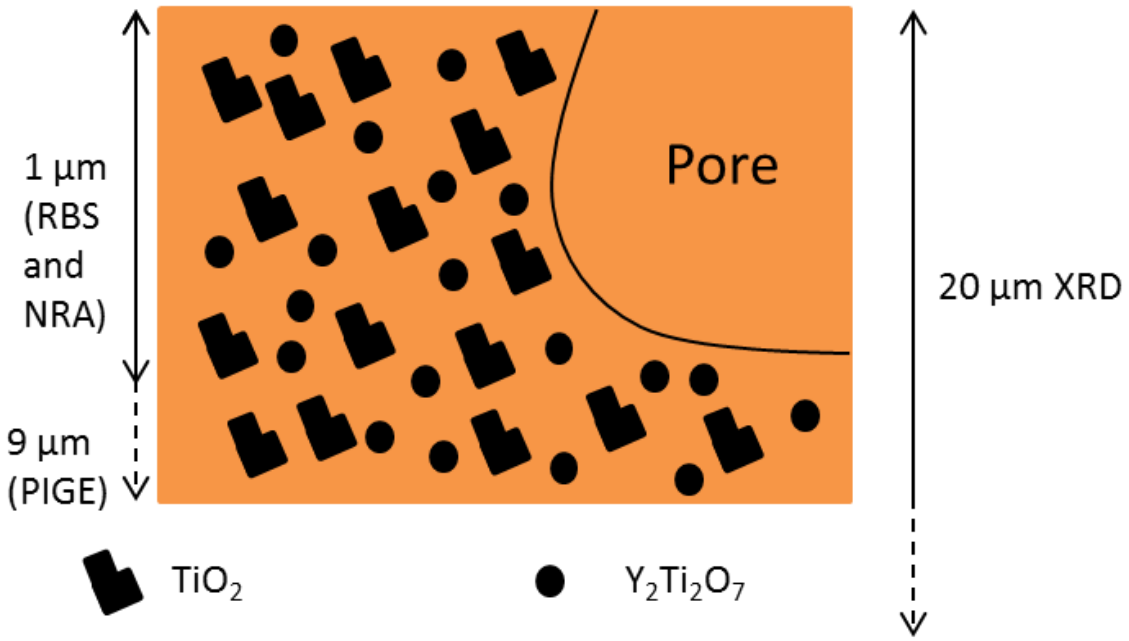

Figure 7.18: Schematic of the oxidation process for sample 24 (10 wt% TiN). Orange area: β-Sialon + SiO_2 + Mullite + amorphous phase; oxygen, yttrium and titanium enriched; nitrogen depleted.

To conclude, the oxidation mechanism for β-Sialon/TiN composites proceeds by a combination of movement of yttrium and titanium, creating surface enrichment of Y/Ti phases, replacement of nitrogen by oxygen in the glassy intergranular phase, and major crystalline and chemical changes in an outer layer of about 100 µm thickness at 1200 ºC which result in the formation of protective crystalline phases TiO_2 and $Y_2Ti_2O_7$. The detailed development of individual oxidation phases is best summarised at the macroscopic level by the XRD sequences detailed in Figure 7.10. Using sample 24 (10 wt% TiN) as an exemplar, a précis of the individual oxidation transformations is as follows:

$$\mathrm{TiN} \xrightarrow{900\,^{\circ}\mathrm{C}} \mathrm{TiO_2} \xrightarrow{1150\,^{\circ}\mathrm{C}} \mathrm{Y_2Ti_2O_7} \qquad \text{(Eq 7.2)}$$

$$\mathrm{YAG} \xrightarrow{1150\,^{\circ}\mathrm{C}} \mathrm{Y_2Ti_2O_7} \qquad \text{(Eq 7.3)}$$

$$\beta - \mathrm{Sialon} \xrightarrow{1250\,^{\circ}\mathrm{C}} \mathrm{Mullite} + \mathrm{Cristobalite} \qquad \text{(Eq 7.4)}$$

7.5 Chapter Seven Bibliography

1. Clarke, D.R. and Lange, F.F., *Oxidation of Si//3N//4 Alloys: Relation to Phase Equilibria in the System Si//3N//4-SiO//2-MgO*. J Am Ceram Soc, 1980, **63**[9-10], pp. 586-93.
2. Klemm, H. and Schubert, C., *Silicon Nitride/Molybdenum Disilicide Composite with Superior Long-Term Oxidation Resistance at 1500°C*. J Am Ceram Soc, 2001, **84**[10], pp. 2430-32.
3. Vickridge, I.C., Brown, I.W.M., Ekstrom, T.C., and Trompetter, W.J., *Ion Beam analysis of sialon ceramics*. Nucl Instrum Meth B, 1996, **118**, pp. 608-12.
4. Liddell, K. and Thompson, D., *X-ray Diffraction Data for Yttrium Silicates*. Trans J Br Ceram Soc, 1986, **85**, pp. 17-22.
5. Brown, I.W.M., Barris, G.C., Sheppard, C.M., Trompetter, W.J., and Vickridge, I.C., *Use of IBA techniques for the measurement of oxidation processes in sialon ceramics*. Mod Phys Lett B, 2001, **15**[28-29], pp. 1305-13.
6. Software *RUMP-RBS Analysis and Simulation Package 4.00*, Doolittle, L.R. and Thompson, M.O. with assistance from R.C. Cochran. Cornell University, NY, United States.
7. Doolittle, L.R., *A semiautomatic algorithm for rutherford backscattering analysis*. Nucl Instrum Meth B, 1986, **15**[1-6], pp. 227-31.
8. Mandal, H. and Thompson, D.P., *Mechanism for Alpha to/from Beta Sialon Transformation*. Proc. Fourth ECerS, 1995, **2**[2], pp.2-6.
9. Software *SIMNRA 6.05*, Mayer, M. Max-Planck-Institut for Plasma Physics, Germany.
10. Kiehle, A.J., Heung, L.K., Gielisse, P.J., and Rockett, T.J., *Oxidation Behavior of Hot-Pressed Si//3N//4*. J Am Ceram Soc, 1975, **58**[1-2], pp. 17-20.
11. Singhal, S.C., *Thermodynamics and kinetics of oxidation of hot-pressed silicon nitride*. J Mater Sci, 1976, **11**[3], pp. 500-09.
12. Tripp, W.C. and Graham, H.C., *Oxidation of Si//3N//4 in the Range 1300 Degree to 1500 Degree C*. J Am Ceram Soc, 1976, **59**[9-10], pp. 399-403.

Chapter Eight: Conclusions and Recommendations for Future Work

The overall goal of this thesis is to examine how selected ceramic additives, including titanium nitride (TiN), impact upon the "chemistry ↔ microstructure ↔ properties" relationship to enable control of industrially important thermal, electrical and engineering properties of β-Sialon based ceramics. These additives have been shown to strongly influence nitridation and sintering behaviour and their impact upon the ceramic microstructure results in systematic changes to porosity, density, Young's modulus, hardness, fracture toughness, compressive strength, resistance to thermal shock, electrical conductivity and resistance to oxidation.

A novel reaction path has been developed to incorporate TiN additives into β-Sialon/TiN composites. In this new process, the TiN is fabricated *in situ* through reduction of titania by aluminium metal.

8.1 Conclusions

The observation that selected additives have a significant effect on the chemistry, microstructure and physical properties of β-Sialon and β-Sialon-TiN composites has led to the following conclusions:

8.1.1 Effect of Nitridation Aids

- The nitridation additives tested on a β-Sialon/X Phase composite were Fe (as Fe_2O_3), TiO_2, $Ca(OH)_2$ (pure or from a calcium aluminate cement CA-25C), ZrO_2, ground pre−sintered Sialon and heated $Al(OH)_3$. After nitridation firing at 1400 ºC, the most successful nitridation aids, as measured by XRD assessment of the extent of β-Sialon formation, were, in order, the pre-sintered Sialon, ZrO_2, CA-25C and heated $Al(OH)_3$. All other additives repressed β-Sialon formation. After sintering at 1600 ºC, all additives improved the β-Sialon yield, with $Ca(OH)_2$ additives achieving the best densification, as measured by their porosity and density.
- The reaction mechanism for enhancing nitridation using CaO-based additives is proposed, supported by thermodynamic data, to proceed by a similar path to the formation of $Y_2Si_2O_7$ from Y_2O_3 by reacting with the SiO_2 skin on the Si particles and exposing highly reactive Si metal to the nitrogen gas.
- Boron nitride added to dense Sialons reduced both the Young's (elastic) modulus and the strength. Samples with 18 wt% of boron nitride addition were very porous but addition of 1.5 wt% of boron nitride was insufficient to reduce the elastic modulus.

Overall, BN reduced the strength of the material but increased the fracture toughness (up to approximately 4 $MPa.m^{-1/2}$) in proportion to the level of addition. The optimum 7.7 wt% BN addition is a compromise. BN did not improve the resistance to thermal shock of the Sialon composite. Solid state ^{11}B NMR indicates that the BN remains unreacted in the fired ceramic body.

- The formation of refractory YAG phases in β-Sialon/X Phase composites, under the firing conditions of this study, occurred via two separate reaction paths on the sample surface and in the sample body. These paths included the formation of yttrium silicate, yttrium disilicate and J-Phase Sialon.

8.1.2 Development of a New Reaction Path

- A new reaction path has been developed to fabricate a β-Sialon/TiN composite. Raw materials are aluminium metal, silicon metal and titanium isopropoxide. YAG, added as single oxides yttria and alumina, has been used as a sintering aid. The well documented reaction between aluminium and titania was undertaken under argon at 900 ºC for 4 hours forming Al_3Ti, as predicted by thermodynamic models. Although strongly thermodynamically driven at lower temperatures, kinetic constraints required the nitridation of this titanium aluminide to be completed at 1400 ºC for 3 hours, forming AlN and TiN.
- To reduce the agglomeration of aluminium particles during firing, due to its low melting point, the powder was milled extensively prior to coating with titania, with an optimum at 48 hours. The aluminium particles were beaten flat, not fractured, and their particle size distribution increased. This mechanical pre-shaping induced the formation of Al_3Ti with a microstructure consisting of uniquely structured plates and ribbon phases.
- After addition of a suitable silicon phase, a β-Sialon/TiN/YAG composite was formed from the nitrided Al_2O_3-AlN-TiN precursor at 1400 ºC and densified at 1600 ºC. The $^{47/49}Ti$ MAS-NMR spectra, as well as enhanced XRD peak intensities in the YAG pattern have confirmed the *in situ* formation of TiN. With the addition of 1 wt% TiN (0.6 vol%), the Sialon formation route took an unexpected turn to form a Y-α-Sialon as well as β-Sialon, 21-R and TiN. The yttrium containing phase was N−melilite ($Y_2Si_3O_3N_4$) rather than YAG. This composition has been obtained because of the small amount of alumina produced (directly related to the amount of titania

introduced), which resulted in a compositional shift toward the AlN corner of the Sialon behaviour diagram.

- This newly developed process could be adapted to an industrially viable process by reducing the number of steps to a single firing starting in argon up to 900 ºC with a 4 hours hold then in nitrogen to 1400 ºC until the completion of the nitridation of Al_3Ti and the precipitation of the Sialon phase. Thermodynamic analyses show that Si and Al would not respectively reduce TiO_2 and Y_2O_3. This method would form a non-densified Sialon/TiN body which would be strongly deformed by the aluminium melting. The reaction product would need to be ground and re-pressed before sintering, typically at 1600 °C.

8.1.3 Effect of TiN on β-Sialon Physical Properties

- The addition of TiN has reduced the material porosity by providing a larger volume of intergranular phase. However with low levels of addition, when Y-α-Sialon was formed, the porosity increased because of uptake of the yttrium component of the intergranular phase to stabilise the α-Sialon matrix.
- Young's modulus, hardness, fracture toughness and compressive strength were generally improved or not significantly reduced with the presence of any amount of TiN. However the presence of TiN had no impact on the resistance to thermal shock of the β-Sialon.
- The small volume of TiN introduced (0.6-6 vol%) was insufficient to improve the A.C. conductivity of the composites but the largest volume of TiN significantly increased the permittivity of the material.

8.1.4 Oxidation of β-Sialon/TiN Composites

- Yttrium and titanium were very mobile from 1100 ºC, with a 0.1 µm thick enrichment layer formed by 1150 ºC for the sample containing 10 wt% TiN, and formed at 1200 ºC for the other samples. These elemental movements create an oxygen-rich layer composed of crystalline $Y_2Ti_2O_7$ and TiO_2, which acts as a barrier to protect the β-Sialon phase from oxidation up to a minimum temperature of 1250 ºC.
- The replacement of nitrogen by oxygen in the samples was observed from 1100 ºC to form an nitrogen-poor layer, whose thickness ranged between 0.7 and 1.5 µm at 1200 ºC. This thickness increases with the amount of TiN additive as this is partially

converted to TiO_2. However, the TiN resistance to oxidation has been observed up to 1300 ºC. It is likely to be protected by a TiO_2 skin which forms from 900 ºC.

- In the case of low TiN addition (1 wt%), the N-melilite and Y-α-Sialon were oxidised with the formation of $Y_2Si_2O_7$ at 900 ºC and the recrystallisation at 1100 ºC of YAG, which had previously transformed into N-melilite during the sintering.
- The SiO loss during the nitridation and sintering firings is critical in determining the oxidation resistance of β-Sialon/TiN composites as it creates an oxygen-poor and oxidation-prone layer on the SiO-depleted outer surface.
- A low addition of TiN (approximately 3 wt%) improves the oxidation resistance without sacrificing hardness or fracture toughness and could have significant industrial applications, for example in the context of improving the performance of Sialon cutting tools.

8.2 Recommendations for Future Work

Considering the outcomes achieved in this thesis, the author would recommend further studies in the following areas:

- β-Sialon samples could be annealed after more elevated sintering at 1700 ºC to crystallise the amorphous phase around the Sialon grains, which should improve the mechanical properties. A study of the combined effect of yttria and calcium aluminate sintering aids would inform this experiment.
- Results suggest that the nitridation firing schedule could be improved by eliminating the 1400 ºC hold, and reducing the duration of the 1350 ºC hold. This should be examined for β-Sialon/TiN composites.
- The reinforcing potential of Al_3Ti plates in Sialon ceramics could be investigated.
- Synthesis and properties of β-Sialon/TiN composites in the range 6-30 vol% TiN has not been examined within the current literature nor in this study. Introducing a high volume of TiN via the newly developed process would produce a large amount of alumina which would push the composition toward higher z-value β-Sialons or even β-Sialon/X-Phase composites. It could be compensated, to a certain extent, by not adding any extra alumina for the formation of YAG. At approximately 30 vol% TiN the percolation threshold will be achieved at which point a dramatic change in the electrical and thermal conductivity behaviour might be expected.

Annexes

Annex I Aluminium Coating with Titania: Aluminium, Titanium Isopropoxide $Ti(OPr)_4$ and, Water Ratios

The sol-gel coating of aluminium powder by titania is described in Section 3.2.4 and discussed in Section 5.3.2. Table I.1 details the calculation of the green composition for the aluminium powder coated with TiO_2 equivalent to x % TiN in the final Sialon and Table I.2 gives the added masses of each compound to make the powder mixes for x = 1, 3 and 10, as well as the equivalent wt% of TiO_2 in the aluminium powder mentioned in Chapter 5.

β-Sialon z-value	1.1
wt% TiN in final Sialon	x%
Initial mass of Al (g)	y

Legend	Desired amount
	Weight of compounds to introduce

M (Sialon)	281.6
n (Sialon)	n(Al)/z-value
m (Sialon)	M(Sialon)/*n(Sialon)

M TiN	61.9
n TiN	M(Sialon)*x%/M(TiN)
m TiN	M(Sialon)*x%

$M(TiO_2)$	79.9
$n(TiO_2)$	n(TiN)
$M(TiO_2)$	$M(TiO_2)*n(TiO_2)$

w% TiO_2 in the Al powder	$m(TiO_2)/y$

	Al	Ti	$Ti(OPr_4)$
M	27.0	47.9	284.2
n	m(Al)/M(Al)	n(TiN)	n(TiN)
m	y	n(Ti)*M(Ti)	$n(Ti(OPr_4))*M(Ti(OPr_4))$

H_2O for 1Ti:150H_2O
$n(Ti)*150*M(H_2O)$

Ti:Al	n(Ti)/n(Al)
Al:TiO2	$n(Al)/n(TiO_2)$

Table I.1: Calculations for aluminium coated with titania green mix. Masses are expressed in grams and quantities in mol.

wt% TiN in final Sialon	1	3	10
m(Al)	10	10	10
$m(Ti(OPr_4))$	4.36	13.07	43.56
$m(H_2O)$	41.38	124.13	413.78
Ti:Al	4/100	12/100	41/100
Al:TiO_2	24.2	8.1	2.4
wt% TiO_2 in Al	12.2%	36.7%	122.4%

Table I.2: Added compounds in the aluminium coated with titania green mix for 1, 3 and 10 wt% TiN in the final Sialon.

Annex II Phase Ratio: Calculation from XRD Highest Peak Intensity

The phase ratios reported in Figure 4.7 and 4.8 have been calculated by using the intensity ratios recorded in the International Centre for Diffraction Data (ICDD) database following equation II.1 and II.2. Table II.1 reports the data for the phases observed in these two figures.

$$I_{Phase} = Peak\ count_{Phase} / (\frac{I}{I_C})_{Phase} * Reference\ Intensity_{Phase} \quad \text{(Eq II.1)}$$

$$\%Phase = \frac{I_{Phase}}{\sum_{k=All\ present\ phases} I_k} * 100 \quad \text{(Eq II.2)}$$

Equation II.1 calculates the intensity of the most intense peak from the read intensity count on the XRD pattern and the reference intensity ratio (RIR) I/I_C. If the highest peak for a phase was overlapped with the peak of another phase the corrected height was calculated from a lower peak by multiplying by the reference intensity (equal to 100 % for the highest peak). The RIR and reference intensities were found in the ICDD database.

It is important to note that this semi-quantitative method does not account for preferential orientation which may enhances some peaks in an XRD pattern. Very little preferential orientation has been observed in this work and therefore calculating phase proportions on a single peak is still relevant. Moreover, it is assumed that all the peaks are the same width.

There are two kinds of errors on the calculation: the manual reading and the counting uncertainty (statistical noise) on the measured pattern, which is the square root of the number of counts.

Phase (ICDD number)	I/I_C	Peak (intensity compared to the most intense peak)
β-Sialon (48-1615)	1.2	38° (99 %)
O-Sialon (42-1492)	1.5	22° (33 %)
Corundum (10-173)	1	41° (90 %)
Mullite (15-776)	0.8	19° (50 %)
X-Phase (35-23)	Estimated at 1.2	28° (100 %)

Table II.1: ICDD data for observed phases in samples 5 and 7 to 15.

Annex III Z-value Calculation

The β-Sialon z-value calculation used in this thesis has been developed at Industrial Research Limited from the study by Ekström et al.*. In this study the z-value dependencies on the a and c cell parameters (in Å) have been calculated to be:

$$z = (a-7.603)/0.0296 \quad \text{(Eq III.1)}$$

$$z = (c-2.907)/0.0255 \quad \text{(Eq III.2)}$$

From these calculated values, for $0 \leq z \leq 4$, the z-value dependency on the position of the (101) β-Sialon peak (found between 38 and 39° 2θ) and on the position of the (100) β-Sialon peak (found between 15 and 16° 2θ) can be obtained with Equations III.1 to III.5.

$$d_{(101)} = 1/\sqrt{\frac{4}{3a^2} + \frac{1}{c^2}} \quad \text{(Eq III.3)}$$

$$d_{(100)} = \frac{\sqrt{3}a}{2} \quad \text{(Eq III.4)}$$

$$2\theta_{(hkl)} = \frac{360}{\pi} * \arcsin\left(\frac{\lambda}{2d_{(hkl)}}\right) \text{ with } \lambda = 1.7906 \text{ Å for CoK}\alpha \quad \text{(Eq III.5)}$$

By plotting z as a function of $2\theta_{(101)}$ and $2\theta_{(100)}$, Equations III.6 and III.7, respectively, are obtained.

$$z = 124.76 - 3.174*2\theta_{(101)} \quad \text{(Eq III.6)}$$

$$z = 259.26 - 16.588*2\theta_{(100)} \quad \text{(Eq III.7)}$$

Finally, by plotting z as a function of $(2\theta_{(101)} - 2\theta_{(100)})$, Equation III.8 was obtained and then used to calculate the z-value.

$$z = 92.75396 - 3.91326*(2\theta_{(101)} - 2\theta_{(100)}) \quad \text{(Eq III.8)}$$

*Ekström, T., Käll, P.O., Nygren, M., and Olsson, P.O., *Dense single-phase β-sialon ceramics by glass-encapsulated hot isostatic pressing*. J Mater Sci, 1989, **24**[5], pp. 1853-61.

Annex IV Selected XRD Patterns from Section 4.2.1.1

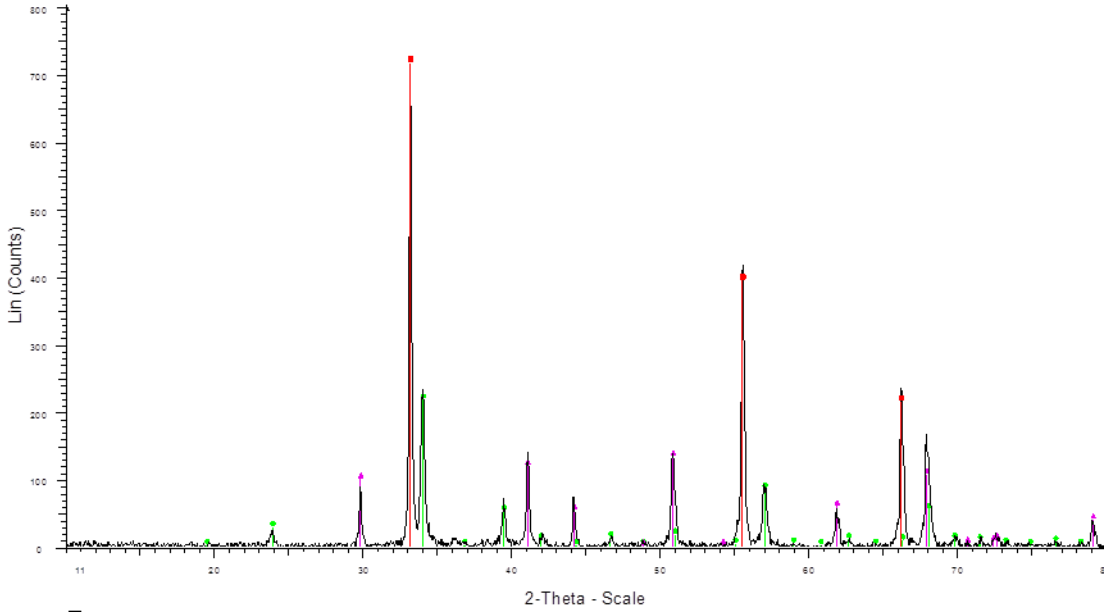

Figure IV.1: XRD pattern of the polished surface of Sample 2 fired at 1000 ºC for 1 hour. Red: Silicon (ICDD 00-027-1402); Pink: Corundum (ICDD 00-010-0173); Green: Y_2O_3 (ICDD 00-041-1105).

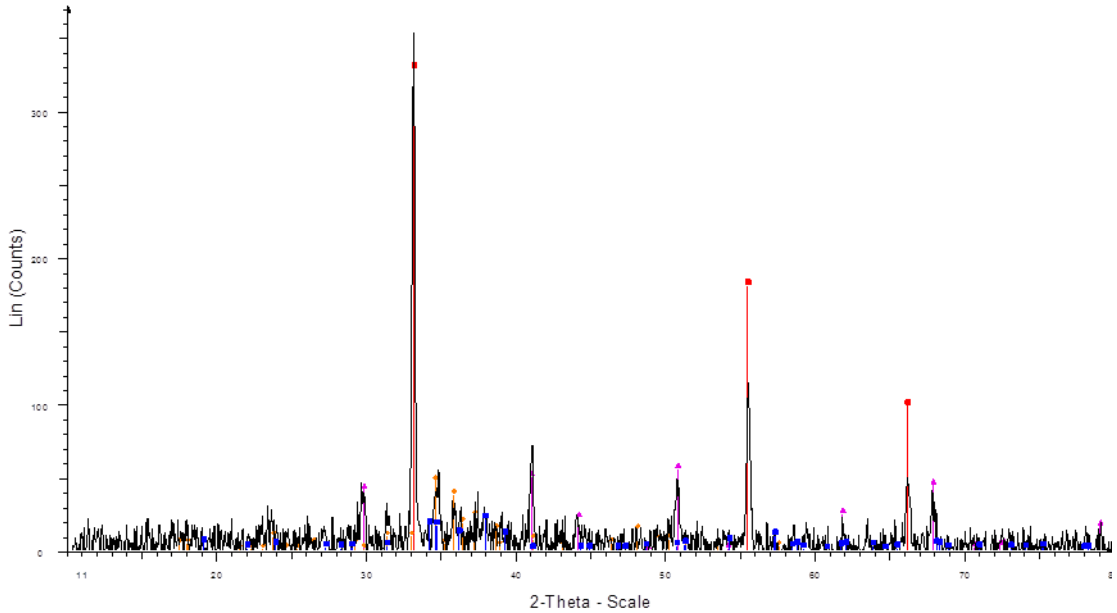

Figure IV.2: XRD pattern of the unpolished surface of Sample 2 fired at 1150 ºC for 1 hour. Red: Silicon (ICDD 00-027-1402); Pink: Corundum (ICDD 00-010-0173); Blue: Y_2SiO_5 (ICDD 00-052-1810); Orange: α-$Y_2Si_2O_7$ (ICDD 00-038-0223).

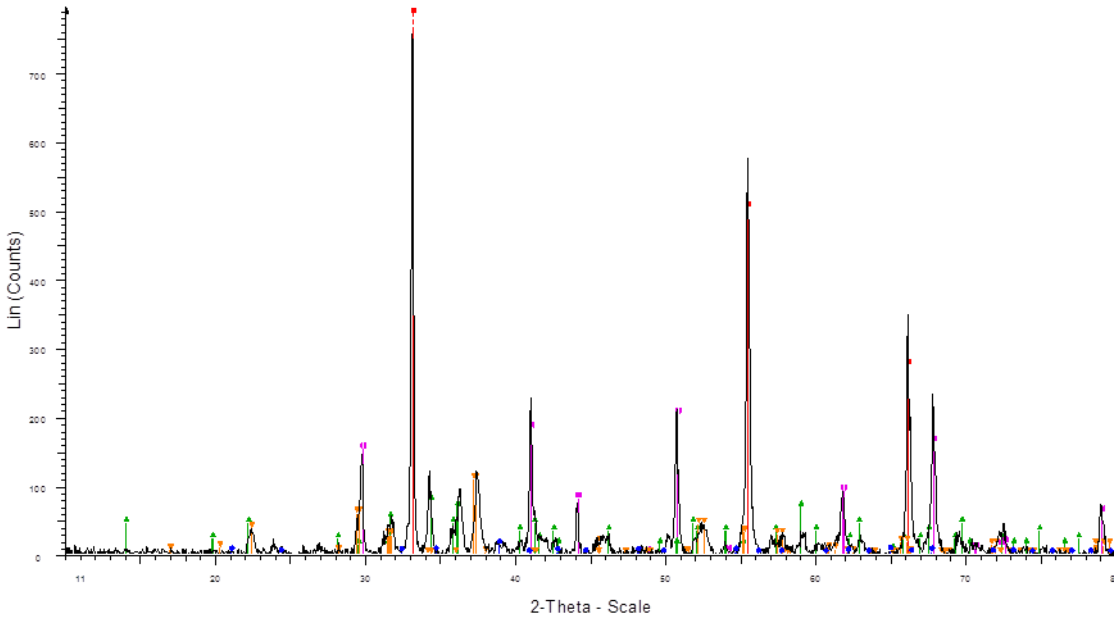

Figure IV.3: XRD pattern of the polished surface of Sample 2 fired at 1250 ºC for 1 hour. Red: Silicon (ICDD 00-027-1402); Pink: Corundum (ICDD 00-010-0173); Green: Y_4SiAlO_8N (ICDD 00-048-1630); Orange: $YSiO_2N$ (ICDD 01-089-3502); Blue: YAG (ICDD 00-033-0040).

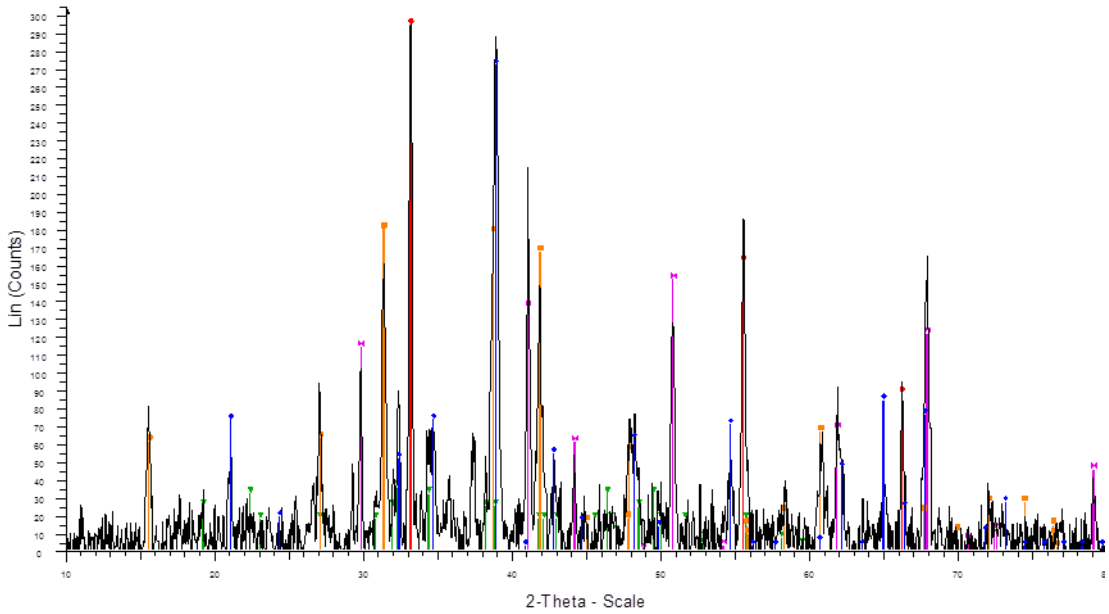

Figure IV.4: XRD pattern of the unpolished surface of Sample 2 fired at 1300 ºC for 1 hour. Red: Silicon (ICDD 00-027-1402); Pink: Corundum (ICDD 00-010-0173); Green: $Y_2Si_2O_7$ (ICDD 00-038-0440); Blue: YAG (ICDD 00-033-0040); Orange: β-Sialon (ICDD 00-048-1616).

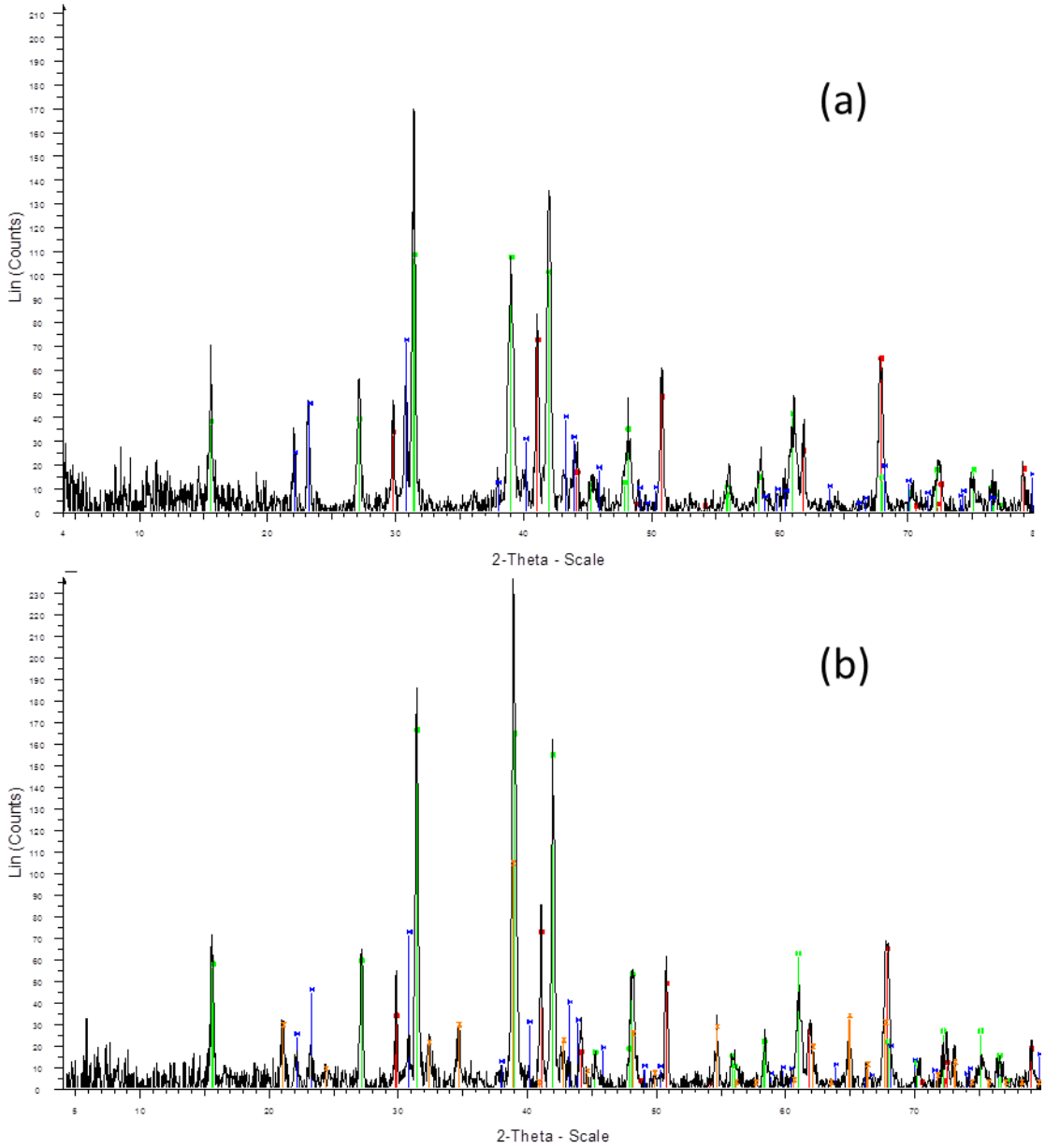

Figure IV.5: XRD patterns of (a) Sample 1 and (b) Sample 2 after nitridation at 1400 ºC for 6 hours. Red: Corundum (ICDD 00-046-1212); Blue: O-Sialon (ICDD 00-042-1492); Green: β-Sialon (ICDD 00-048-1615); Orange: YAG (ICDD 00-033-0040).

Annex V Selected XRD Patterns from Figure 7.5 to Figure 7.8

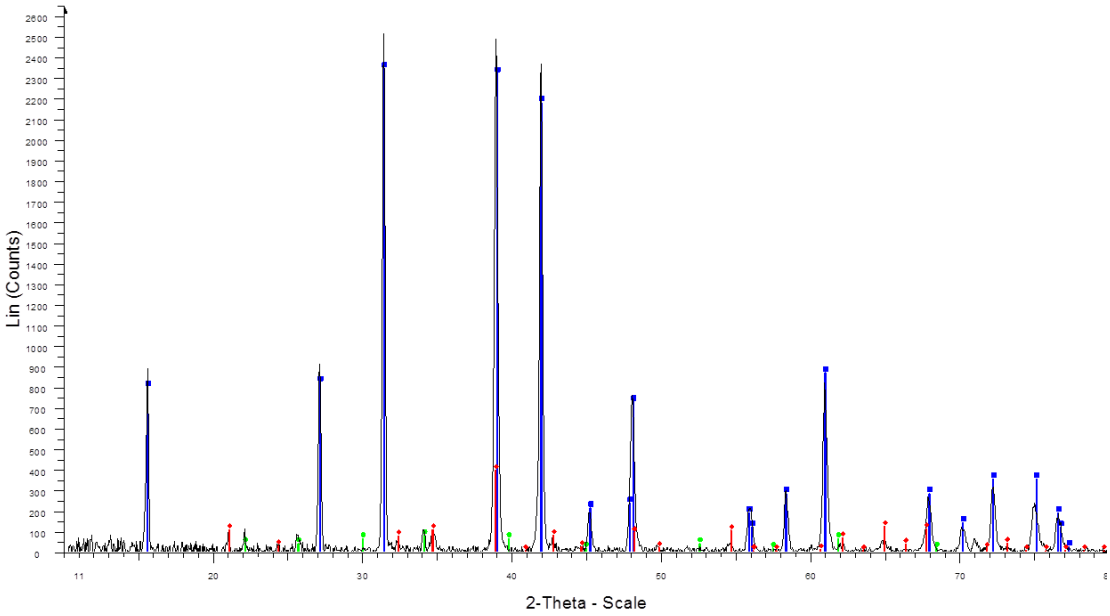

Figure V.1: XRD pattern of the polished surface of Sample 21 oxidised at 1200 ºC for 2 hours. Blue: β-Sialon (ICDD 00-048-1615); Red: YAG (ICDD 00-033-0040); Green: Yttrium silicate $Y_2Si_2O_7$ (ICDD 00-045-0042).

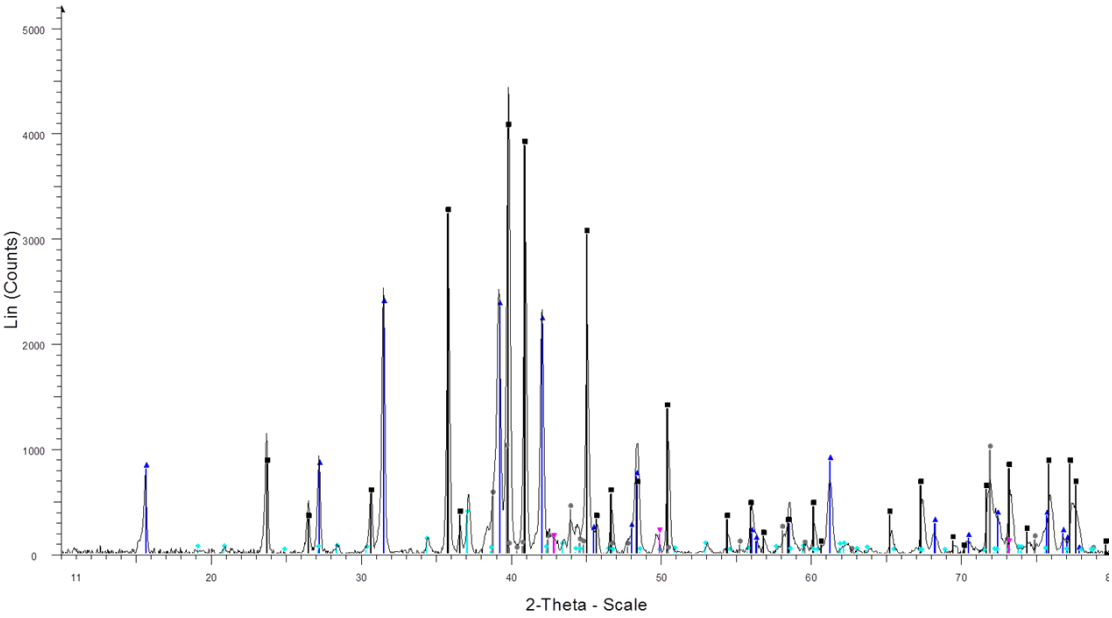

Figure V.2: XRD pattern of the polished surface of Sample 22 before oxidation. Blue: β-Sialon (ICDD 00-048-1615); Black: Y-α-Sialon (ICDD 00-042-0251);Grey: 21-R Phase (ICDD 00-053-1012); Pink: TiN (ICDD 00-038-1420); Turquoise: N-melilite (ICDD 01-070-3557).

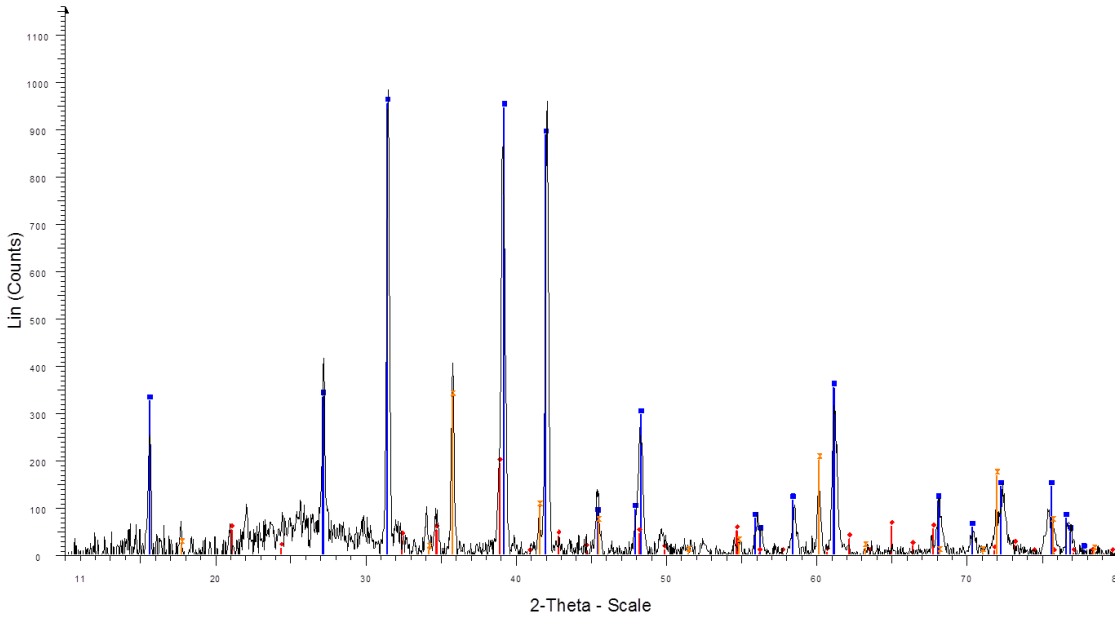

Figure V.3: XRD pattern of the polished surface of Sample 23 oxidised at 1250 ºC for 2 hours. Blue: β-Sialon (ICDD 00-048-1615);Red: YAG (ICDD 00-033-0040); Orange: $Y_2Ti_2O_7$ (ICDD 00-042-0413).

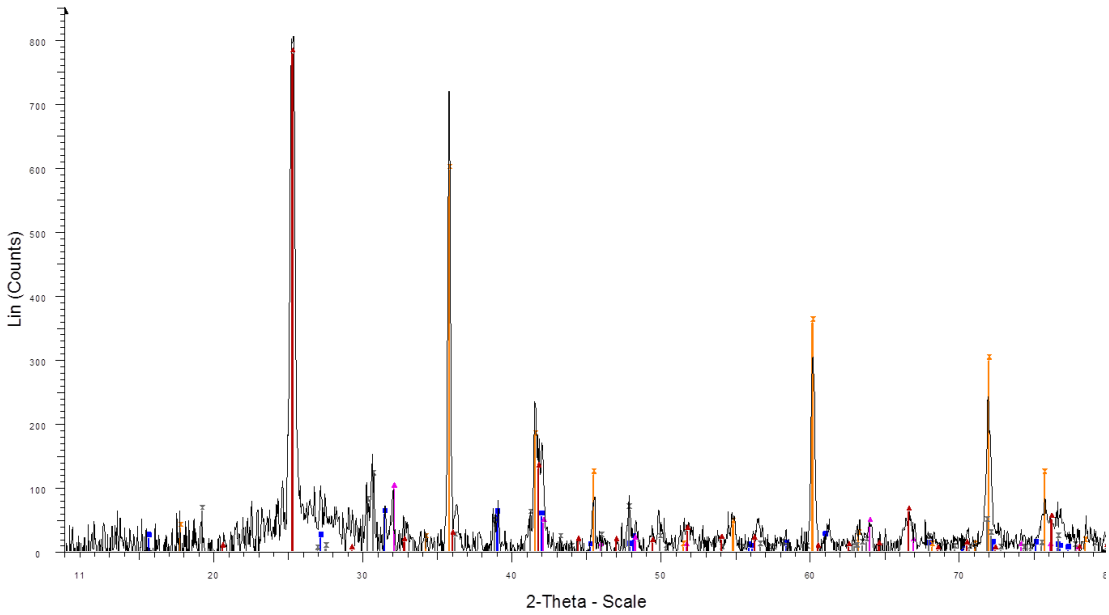

Figure V.4: XRD pattern of the polished surface of Sample 24 oxidised at 1300 ºC for 2 hours. Blue: β-Sialon (ICDD 00-048-1615); Orange: $Y_2Ti_2O_7$ (ICDD 00-042-0413); Pink: TiO_2 (ICDD 03-065-1119); Brown: SiO_2 (ICDD 01-085-0621); Grey: Mullite (ICDD 01-082-0037).

Annex VI NRA Simulation of Layer Composition

NRA simulation was performed with the software SIMNRA as described in Section 7.3.3. The levels of elemental silicon (38 %) and aluminium (12 %) were kept constant, assuming that nitrogen is replaced by oxygen. Therefore the level change of nitrogen was balanced with that of oxygen. The following tables report the simulations of NRA profiles for all the samples studied in the oxidation resistance experiment described in Chapter 7 (Sample 21 to 24 – 0 to 10 wt% TiN - fired from 0 to 1300 ºC in air for two hours). When two or more profiles were identical only the lowest temperature simulation is reported.

For the depth calculation indicated in Figure 7.10, for Samples 22 and 23, the calculated thickness of the first layer did not maintain linearity between the energy range on the profile and the thickness of layer 1 in the other samples. The thickness of these first layers was calculated using the data for layer 1 and half of layer 2. Another solution would have been to separate the second layer in two different layers, the first of which would have had a very low level of nitrogen.

	Layer 1		**Layer 2**	**Layer 3**
	[0 % N]		**[N%]**	**[N%]**
Temperature (°C)	**Thickness x 10^{15} (atoms.cm^{-2})**	**Thickness Layer1**	**Thickness x 10^{15} (atoms.cm^{-2})**	**Thickness x 10^{15} (atoms.cm^{-2})**
0	0	0 nm	0	0
1000	500	53 nm	0	0
1100	1800	190 nm	8000 [40]	0
1150	4000	422 nm	8500 [40]	0
1200	6700	707 nm	9000 [37]	0
1250	6700		8000 [7]	20,000 [13]

Table VI.1: NRA simulation with SIMNRA. Simulated layers composition for Sample 21 (β-Sialon + 0 wt% TiN).

Temperature (°C)	Layer 1 [0 % N] Thickness x10^{15} (atoms.cm^{-2})	Thickness Layer1	Layer 2 [N%] Thickness x 10^{15} (atoms.cm^{-2})	Layer 3 [N%] Thickness x 10^{15} (atoms.cm^{-2})	Layer 4 [N%] Thickness x 10^{15} (atoms.cm^{-2})	Layer 5 [N%] Thickness x 10^{15} (atoms.cm^{-2})
0	0	0 nm	0	0	0	0
1100	500	53 nm	4000 [15]	8000 [45]	0	0
1150	1000	106 nm	4000 [13]	8000 [41]	0	0
1200	3000	317 nm	7000 [10]	4000 [28]	17000 [45]	0
1250	3500		8000 [5]	3000 [8]	16000 [14]	6000 [22]

Table VI.2: NRA simulation with SIMNRA. Simulated layers composition for Sample 22 (β-Sialon + 1 wt% TiN).

Temperature (°C)	Layer 1 [0 % N] Thickness x10^{15} (atoms.cm^{-2})	Thickness Layer1	Layer 2 [N%] Thickness x10^{15} (atoms.cm^{-2})	Layer 3 [N%] Thickness x10^{15} (atoms.cm^{-2})	Layer 4 [N%] Thickness x10^{15} (atoms.cm^{-2})	Layer 5 [N%] Thickness x10^{15} (atoms.cm^{-2})
0	0	0 nm	0	0	0	0
1100	1000	105 nm	8000 [33]	0]	0	0
1150	1500	158 nm	6000 [25]	7000 [42]	0	0
1200	5500	580 nm	6000 [22]	4000 [44]	0	0
1250	5500		8000 [5]	1000 [8]	17000 [11]	4000 [20] Layer 6: 4000 [28] Layer 7: 15000 [38]

Table VI.3: NRA simulation with SIMNRA. Simulated layers composition for Sample 23 (β-Sialon + 3 wt% TiN).

Temperature (°C)	Layer 1 [0 % N] Thickness x10^{15} (atoms.cm^{-2})	Thickness Layer1	Layer 2 [N%] Thickness x10^{15} (atoms.cm^{-2})	Layer 3 [N%] Thickness x10^{15} (atoms.cm^{-2})	Layer 4 [N%] Thickness x10^{15} (atoms.cm^{-2})
0	0	0 nm	0	0	0
1100	2500	264 nm	4500 [33]	6000 [38]	0
1150	1150	633 nm	5500 [25]	4000 [42]	0
1200	1200	1.47 µm	10000 [6]	15000 [19]	8000 [34]

Table VI.4: NRA simulation with SIMNRA. Simulated layers composition for Sample 24 (β-Sialon + 10 wt% TiN).